

THÈSE DE DOCTORAT DE

L'ÉCOLE NATIONALE SUPÉRIEURE MINES-TÉLÉCOM ATLANTIQUE
BRETAGNE PAYS DE LA LOIRE - IMT ATLANTIQUE

ÉCOLE DOCTORALE N° 596

Matière, Molécules, Matériaux

Spécialité : *Physique Subatomique et Instrumentation Nucléaire*

Par

Víctor Valencia Torres

Investigation of J/ψ collectivity in Pb-Pb collisions using multi-particle cumulants technique with ALICE detector and exploration of cold nuclear matter effects with Drell–Yan production

Thèse présentée et soutenue à Nantes, le 18/11/2025

Unité de recherche : Laboratoire SUBATECH, UMR 6457

Thèse N° : 2025IMTA0497

Rapporteurs avant soutenance :

Rapporteur :	Giulia MANCA	Professeure Associée de l'Université de Cagliari, Cagliari, Italie
Rapporteur :	Cvetan CHESHKOV	Directeur de Recherche CNRS, IP2I, Lyon, France

Composition du Jury :

Président :		
Examineurs :	David d'ENTERRIA	Physicien senior, CERN, Genève, Suisse
	Raphaëlle BAILHACHE	Physicienne senior à l'Université Goethe, Frankfurt am Main, Allemagne
	François ARLEO	Directeur de Recherche CNRS, SUBATECH, Nantes, France
Dir. de thèse :	Ginés MARTINEZ	Directeur de Recherche CNRS, SUBATECH, Nantes, France
Encadrant :	Marie GERMAIN	Chargée de Recherche CNRS, SUBATECH, Nantes, France
Encadrant :	Maxime GUILBAUD	Maître de conférences IMT Atlantique, SUBATECH, Nantes, France

Invité(s) :

Pol-Bernard GOSSIAUX	Professeur IMT Atlantique, SUBATECH, Nantes, France
----------------------	---

Dedico esta tesis a mi abuela y a mi padre, con profunda gratitud por su cariño, su fortaleza y la inspiración que han sembrado en mi vida.

Contents

Thesis structure	9
1 Introduction	13
1.1 Standard model and the strong interaction	13
1.1.1 Quantum chromodynamics	17
1.2 Hadronic matter phase diagram and the quark-gluon plasma (QGP)	22
1.3 Ultrarelativistic heavy-ion collisions	24
1.3.1 Initial stage of the collisions	25
1.3.1.1 The Glauber model and centrality	25
1.3.1.2 Nuclear parton distribution functions (nPDFs) . . .	27
1.3.1.3 Kinematic variables	30
1.3.2 History of a HIC	33
1.3.3 Observables and probes of the QGP	35
1.4 Relativistic fluid theory of QGP	37
1.4.1 Non-interacting ideal QGP	37
1.4.2 Relativistic viscous fluid dynamics	41
1.5 Collective behaviour in heavy-ion collisions	45
1.5.1 Expansion dynamics toward equilibrium	46
1.5.2 Radial flow	49
1.5.3 Eccentricity and anisotropic flow	50
1.5.4 Experimental methods to extract flow	54
1.5.5 Gaussian models for flow fluctuations	57
1.5.6 Elliptic flow and fluctuation ratio of light hadrons	67
2 Charmonium collectivity	73
2.1 Quarkonia as hard probe	74
2.1.1 Decay channels of J/ψ	75
2.1.2 Charmonium production in hadronic collisions	76
2.1.2.1 Hard-scattering	77

2.1.2.2	Phenomenological production models	80
2.1.2.3	Prompt and non-prompt J/ψ	82
2.1.2.4	Photo-production of J/ψ in AA collisions	83
2.1.3	Cold nuclear matter (CNM) and QGP in-medium effects on charmonium	84
2.1.3.1	Cold nuclear matter effects in pA collisions	84
2.1.3.2	QGP effects in AA collisions	87
2.1.3.3	Characteristic timescales of charm thermalisation	87
2.1.4	In-Medium quarkonium models in the QGP	93
2.2	Flow in the heavy-sector	96
2.2.1	Flow of J/ψ at LHC and RHIC	96
2.2.2	Flow of open heavy flavor and quarkonia in Run 3	99
3	Experimental setup	103
3.1	The Large Hadron Collider	103
3.2	A Large Ion Collider Experiment (ALICE)	111
3.2.1	Central barrel	112
3.2.2	Forward and backward detectors	116
3.2.3	The muon spectrometer	118
3.3	Continuous readout and data Processing	123
3.4	Muon reconstruction and quality assurance	126
3.4.1	Data taking and track reconstruction in MCH	127
3.4.2	Cluster map display	128
4	Multi-particle cumulant J/ψ analysis	133
4.1	Data sample and event selection	133
4.1.1	Data sample	133
4.1.2	Event Selection	134
4.1.2.1	Centrality determination	135
4.2	Track and muon selections	136
4.2.1	Barrel track selections	136
4.2.2	Muon and dimuon selection criteria	138
4.3	Multi-particle cumulant method	139
4.3.1	Q-vectors	139
4.3.2	Multi-particle correlation	140
4.3.2.1	2-particle correlations	140

4.3.2.2	4-particle correlations	142
4.3.3	Event-averaged correlators	143
4.3.4	Cumulants	144
4.4	Elliptic flow coefficients with ALICE detector	145
4.4.0.1	Flow vectors using Non-Uniform Acceptance (NUA) weights	146
4.4.0.2	Reference correlators (REF) with NUA weights	147
4.4.0.3	Particle of interest (POI) correlators with NUA weights	149
4.4.0.4	REF and POI cumulants	150
4.5	v_2^{REF} and $v_2^{\mu\mu}$ using cumulants with Run 3 data	151
4.5.1	REF flow at mid-rapidity	151
4.5.2	POI flow at forward rapidity	156
4.5.2.1	Invariant mass of dimuons	156
4.5.2.2	Elliptic flow of dimuons	158
4.5.2.3	Statistical error estimation of $v_2^{\mu\mu}$	161
4.6	Event mixing procedure	162
4.6.1	Application of event mixing to flow methods	164
4.7	J/ψ v_2 Signal Extraction	168
4.7.1	Systematic uncertainties study	173
4.7.1.1	Uncertainties of J/ψ yield	173
4.7.1.2	Uncertainties from $v_2^{J/\psi}$ extraction	176
4.8	J/ψ flow results	179
4.9	2D representation of flow fluctuations	188
5	Study of cold nuclear matter effects with Drell-Yan production	193
5.1	Drell-Yan in high-energy collisions	193
5.1.1	Isospin effects in pA	195
5.1.2	Antiquark flavor asymmetry in the nucleon sea	197
5.1.3	Gluon shadowing in pPb collisions	199
5.2	Drell-Yan analysis	201
5.2.1	From PDF to cross sections and R_{pA}	202
5.2.2	Model and DY pseudo-data	205
5.2.3	Reweighting nuclear PDFs using DY pseudo-data	207
5.2.4	Results	209
6	Conclusion and perspectives	211

7	Résumé en français	215
7.1	Flot elliptique du J/ψ dans les collisions Pb-Pb	215
7.2	Étude des effets de matière nucléaire froide avec le processus Drell-Yan	222
A	Mathematical framework	227
B	Flow analysis with cumulants	243
C	Cold nuclear matter effects and nPDF	267

Thesis structure

This thesis presents a detailed investigation of collective charm dynamics and cold nuclear matter effects in high-energy nuclear collisions at the Large Hadron Collider (LHC), focusing respectively on J/ψ production in Pb–Pb collisions and the Drell–Yan (DY) process in pPb collisions. The study of J/ψ production includes a measurement of its azimuthal anisotropy, with particular emphasis on the elliptic flow v_2 and its event-by-event fluctuations, quantified using multi-particle cumulant techniques. On the cold-nuclear-matter side, the thesis presents theoretical predictions for DY production in pPb collisions, exploiting the clean nature of the DY process to probe initial-state effects. The DY results are also used to constrain nuclear parton distribution functions (nPDFs), thereby improving our understanding of nuclear modifications to partonic structure. The thesis is organized into six main chapters, each addressing a specific aspect of the research:

Chapter 1 - Introduction: This chapter establishes the theoretical foundations of the Standard Model, with particular emphasis on the strong interaction and Quantum Chromodynamics (QCD). It introduces the concept of the quark–gluon plasma (QGP), a deconfined state of matter created in ultra-relativistic heavy-ion collisions, and discusses the key observables used to characterize this exotic phase of matter. A central focus is placed on the role of relativistic hydrodynamics in describing the evolution of the QGP. The emergence of collective flow is presented as one of the most compelling signatures of strongly interacting QGP matter. In particular, the chapter highlights the importance of flow fluctuations, which arise from event-by-event variations in the initial-state geometry. Two common interpretations of these fluctuations (based on one-dimensional and two-dimensional Gaussian distributions of the underlying flow vector) are introduced and contrasted. By motivating the hydrodynamic description and the study of anisotropic flow and its fluctuations, the chapter provides the essential background needed to understand the physics motivations behind the experimental measurements presented in

subsequent chapters.

Chapter 2 - Charmonium collectivity: Building upon the introduction, this chapter focuses specifically on quarkonia as hard probes of the QGP. It reviews the properties of charmonium states, their production mechanisms in hadronic collisions, and the various theoretical frameworks used to describe their behavior in nuclear environments. The chapter distinguishes between cold nuclear matter effects (observed in proton–nucleus collisions) and QGP effects (in nucleus–nucleus collisions), setting the stage for understanding how charmonium collectivity can reveal information about the QGP properties. This chapter is essential for readers who need to understand the physics context before diving into the experimental analysis.

Chapter 3 - Experimental setup: This chapter provides a detailed description of the experimental apparatus used for the measurements. It begins with an overview of the Large Hadron Collider and its main experiments, before focusing specifically on the ALICE detector. The chapter covers the detector subsystems, data acquisition systems, and analysis frameworks that are crucial for understanding the technical aspects of the measurements.

Chapter 4 - Multi-particle cumulant J/ψ analysis: This chapter presents the main experimental analysis of this thesis: the measurement of J/ψ elliptic flow and flow fluctuations in Pb–Pb collisions using multi-particle cumulant techniques. It details the data sample, event selection criteria, signal extraction methods, and the cumulant analysis framework. The chapter reports the first measurements of J/ψ elliptic flow using this technique, providing insights into the collective behavior of heavy quarks in the QGP. This is the core experimental contribution of the thesis and should be read carefully by those interested in the analysis methodology and results.

Chapter 5 - Study of cold nuclear matter effects with Drell–Yan production: This chapter presents a complementary phenomenological study focused on constraining nuclear parton distribution functions (nPDFs) using Drell–Yan production in proton–lead collisions. It introduces the Drell–Yan process, discusses isospin effects and antiquark flavor asymmetry, and presents a detailed analysis using reweighting techniques to assess the potential impact of DY pseudodata on nPDF determinations. This chapter addresses a different but related aspect of nuclear physics, focusing on initial-state effects rather

than final-state QGP modifications.

Chapter 6 - Conclusion and perspectives: The final chapter synthesizes the main findings of both analyses, discusses their implications for our understanding of QGP physics and nuclear structure, and outlines future directions for research. It highlights the key achievements and identifies areas for improvement in future measurements.

Chapter 1

Introduction

1.1 Standard model and the strong interaction

The standard model is describing all known particles of our universe and their fundamental interactions. The model is composed of 12 particles of matter called fermions, 6 quarks (up, down, charm, strange, top and bottom) and 6 leptons (electron, muon, tau with their associated neutrinos [1], as shown in figure 1.1).

All these matter particles are anti-symmetric states (with half-integer spin) that follow Fermi-Dirac statistics, they all respect the Pauli's exclusion principle that imposes that two fermions can never be in the same quantum state [2]. The vector bosons (with integer spin) are the particles associated to forces: the photon is the boson of the electromagnetic interaction. The W and Z bosons are the mediators of the weak interaction responsible for beta decays, the decays of many hadrons (such as the neutron and strange particles), and the decays of many fundamental particles like the muon. The gluons (g) are the particle's mediators of the strong nuclear interaction, which confines quarks in a color singlet state called hadrons. All bosons obey Bose-Einstein statistics. The Standard Model (SM) uses Quantum Field Theories (QFT) to describe mathematically the different interactions. The three fundamental forces (electromagnetic, weak and strong) are related to different gauge symmetries that are internal transformations under which a Lagrangian is invariant [3].

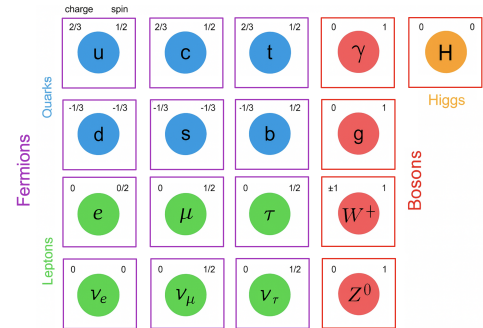


FIGURE 1.1 – Fermions and bosons of the standard model.

$U(1)$ is the gauge symmetry group of electromagnetism, $SU(2)$ is the group for the weak interaction, and $SU(3)$ for the strong interaction. In the SM, the electromagnetic and weak interactions are unified in a single framework called the electroweak (EW) theory, based on the gauge symmetry group $SU(2)_L \times U(1)_Y$, which is spontaneously broken to $U(1)_{\text{em}}$ by the Higgs mechanism [2, 4, 5]:

$$SU(2)_L \times U(1)_Y \longrightarrow U(1)_{\text{em}}. \quad (1.1)$$

This spontaneous reduction of symmetry is called spontaneous symmetry breaking (SSB), and according to the Goldstone theorem [6], it gives rise to new massless scalar bosons, called Goldstone bosons¹.

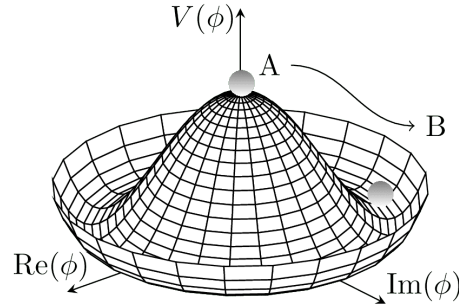


FIGURE 1.2 – Illustration of the Higgs potential (Mexican hat), with state A (before SSB) and state B (after SSB).

Before SSB, the EW sector of the SM is described by the following gauge-invariant Lagrangian:

$$\begin{aligned} \mathcal{L}_{\text{EW}}^{\text{sym}} = & \bar{\psi}_L i\gamma^\mu D_\mu \psi_L + \bar{\psi}_R i\gamma^\mu D_\mu \psi_R - \frac{1}{4} W_{\mu\nu}^a W^{a,\mu\nu} - \frac{1}{4} B_{\mu\nu} B^{\mu\nu} \\ & + (D_\mu \Phi)^\dagger (D^\mu \Phi) - V(\Phi). \end{aligned} \quad (1.2)$$

where $\psi_{L,R}$ denote the left- and right-handed fermion fields². The left-handed fields ψ_L form $SU(2)_L$ doublets, such as $L_{\alpha L} \equiv (\nu_\alpha, \ell_\alpha)_L^T$, and $Q_{iL} \equiv (u_i, d_i)_L^T$, where $\alpha = e, \mu, \tau$ labels the lepton families and $i = 1, 2, 3$ labels the quark generations³.

1. The Goldstone theorem states that whenever a continuous global symmetry is spontaneously broken, new massless scalar excitations (Goldstone bosons) appear. In the electroweak theory, however, these Goldstone bosons are not observed as physical particles: they are absorbed by the gauge fields, providing the longitudinal degrees of freedom of the massive W^\pm and Z bosons.

2. A fermion field can be decomposed into left- and right-handed components using the chirality projection operators: $\psi = P_L \psi + P_R \psi = \psi_L + \psi_R$, where $P_{L,R} = \frac{1}{2}(1 \mp \gamma^5)$.

3. Explicitly, $(u_1, u_2, u_3) \longleftrightarrow (u, c, t)$ and $(d_1, d_2, d_3) \longleftrightarrow (d, s, b)$.

The superscript T denotes the transpose, meaning that the fields are arranged as column vectors. The right-handed fields ψ_R are singlets like e_R, u_R , and d_R . The operator D_μ is the covariant derivative, introducing the gauge fields W_μ^a and B_μ in the following way: $D_\mu = \partial_\mu - ig\frac{\sigma^a}{2}W_\mu^a - ig'\frac{Y}{2}B_\mu$, with g and g' the gauge couplings and σ^a the Pauli matrices. The terms $W_{\mu\nu}^a$ and $B_{\mu\nu}$ are the field strength tensors of the gauge fields (for $SU(2)_L$ and $U(1)_Y$, respectively). The scalar field Φ is the Higgs doublet, defined as $\Phi = (\phi^+, \phi^0)^T$. The Higgs field has a hypercharge⁴ $Y = \frac{1}{2}$ and the Higgs potential takes the form $V(\Phi) = \mu^2 \Phi^\dagger \Phi + \lambda (\Phi^\dagger \Phi)^2$, where the parameter $\mu^2 < 0$ triggers SSB and $\lambda > 0$ ensures that the potential is bounded from below (see Figure 1.2). After the Higgs field acquires a vacuum expectation value⁵ $\langle \Phi \rangle = (0, v/\sqrt{2})^T$, the EW gauge symmetry is spontaneously broken by the Higgs mechanism, which explains how the W and Z bosons acquire mass while leaving the photon massless. Additionally, the same mechanism is responsible for giving mass to fermions through Yukawa couplings with the Higgs field.

Thus, the scalar Higgs boson (spin 0) is not a specific mediator of a given force but is responsible for giving mass to all the elementary particles [5]. After SSB, the electroweak Lagrangian can be understood as a sum of different terms, each of which has a clear physical role:

$$\begin{aligned} \mathcal{L}_{\text{EW}}^{\text{SSB}} = & \mathcal{L}_K + \mathcal{L}_N + \mathcal{L}_C \\ & + \mathcal{L}_H + \mathcal{L}_{\text{HV}} + \mathcal{L}_{\text{WWV}} \\ & + \mathcal{L}_{\text{WWVV}} + \mathcal{L}_Y, \end{aligned} \quad (1.3)$$

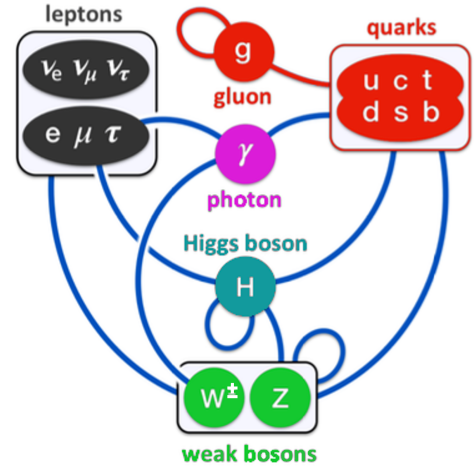


FIGURE 1.3 – Interactions allowed in the SM.

where, \mathcal{L}_K contains the kinetic energy and mass terms for all the fundamental fields. The neutral current interactions, encoded in \mathcal{L}_N , describe how fermions couple to the photon and the Z boson. Complementary to this, \mathcal{L}_C governs the charged current interactions mediated by the W^\pm bosons. The Higgs sector itself contributes several distinct terms. The self-interactions of

4. In the electroweak theory the hypercharge operator of $U(1)_Y$ is $Y = Q - T_3$, where $T_3 = \frac{1}{2} \text{diag}(1, -1)$ for an $SU(2)_L$ doublet and Q is the charge operator of $U(1)_{\text{em}}$.

5. The vacuum expectation value is $v = \sqrt{-\mu^2/\lambda}$, implying a nonzero vacuum energy, and is related to the Fermi constant by $v = (\sqrt{2}G_F)^{-1/2} \simeq 246 \text{ GeV}$.

the Higgs boson, such as cubic (h^3) and quartic (h^4) couplings, are collected in \mathcal{L}_H . The interactions between the Higgs and the massive vector bosons (hWW and hZZ) are contained in \mathcal{L}_{HV} . The gauge fields also interact among themselves. The Lagrangian piece \mathcal{L}_{WWV} describes the triple vertices involving two W bosons and either a photon or a Z , while \mathcal{L}_{WWVV} accounts for the quartic vertices involving two W bosons and two additional gauge bosons, such as $WW\gamma\gamma$ or $WWZZ$. Finally, \mathcal{L}_Y collects the Yukawa interactions, which generate fermion and boson masses and describe the direct couplings between the Higgs boson and fermions ($h\psi\bar{\psi}$). In addition, the SSB of $[SU(2)_L \times U(1)_Y]$ by the Higgs doublet transmits flavor violation to the weak interaction, encoded in the following expression

$$\mathcal{L}_C = \frac{g}{\sqrt{2}} \left[\bar{\nu}_{iL} \gamma^\mu U_{\alpha i}^* \ell_{\alpha L} W_\mu^+ + \bar{u}_{iL} \gamma^\mu V_{ij} d_{jL} W_\mu^+ \right] + \text{h.c.}, \quad (1.4)$$

where g is the $SU(2)_L$ gauge coupling and "h.c." denotes the Hermitian conjugate, which restores the corresponding W^- interactions. The Pontecorvo–Maki–Nakagawa–Sakata (PMNS) matrix $U_{\alpha i} \equiv U_{\text{PMNS}}$ encodes the mixing between charged-lepton flavor eigenstates⁶ $\ell_\alpha = (e, \mu, \tau)$ and neutrino mass eigenstates $\nu_i = (\nu_1, \nu_2, \nu_3)$. The flavor index $\alpha = e, \mu, \tau$ corresponds to the charged leptons, while $i = 1, 2, 3$ labels neutrino mass eigenstates. The Cabibbo–Kobayashi–Maskawa (CKM) matrix, $V_{ij} \equiv V_{\text{CKM}}$, encodes the misalignment between up- and down-type quark mass eigenstates⁷. In the charged-current interaction, it determines how an up-type quark mass eigenstate $u_i = (u, c, t)$ couples to linear combinations of down-type quark mass eigenstates $d_j = (d, s, b)$. The indices $i, j = 1, 2, 3$ label quark generations. The structure of \mathcal{L}_C highlights two key features of the weak interaction: it involves only left-handed fermions, and it allows for flavor-changing transitions. A direct example is the neutron β -decay:

$$n(udd) \xrightarrow{d \rightarrow u} p(uud) + e^- + \bar{\nu}_e. \quad (1.5)$$

Which at a quark level corresponds to a down quark decaying to up. These

6. Notice that a flavor eigenstate created in a weak process is a linear superposition of mass eigenstates. By consequence, when neutrinos propagate, because these superpositions evolve differently in time, the flavor composition of the state changes, giving rise to the neutrino oscillations.

7. The diagonal elements of V_{CKM} correspond to transitions within the same generation and are close to unity, reflecting that such processes dominate in weak interactions. In contrast, the non-diagonal elements of V_{CKM} describe intergenerational flavor-changing transitions, which are suppressed in magnitude. This structure interestingly underlies phenomena such as K^0 – \bar{K}^0 mixing, giving rise to the long- and short-lived states K_L and K_S .

processes illustrate how the charged–current interaction mediated by W^\pm bosons is responsible for weak⁸ decays that change the flavor of matter constituents.

Finally, by incorporating the electroweak interaction together with the strong interaction, one arrives at the framework of the SM. This unification can also be expressed in terms of gauge symmetries $SU(3)_C \times SU(2)_L \times U(1)_Y$, under which the Lagrangian of the Standard Model \mathcal{L}_{SM} is invariant [7]. All interactions allowed in the SM between quarks, leptons, gauge bosons, and the Higgs boson are illustrated in Figure 1.3. We remark that even if this model explains a wide variety of phenomena, there are still many unanswered questions beyond the SM, such as: how does gravity behave in Quantum Mechanics? Where has all the antimatter gone? Or how do dark energy and dark matter exactly work?

1.1.1 Quantum chromodynamics

Quantum Chromodynamics (QCD) is the QFT of the strong interaction. It describes the dynamics and interactions between partons (quarks and gluons) [8]. In close analogy, Quantum Electrodynamics (QED) is the QFT of the electromagnetic interaction, where the fundamental conserved quantity is the electric charge, while in QCD the corresponding conserved quantity is the color charge. The quark fields have 3 quantum color numbers and 6 different flavors, and the dynamics of parton interactions are controlled by the following Lagrangian⁹ [9]:

$$\mathcal{L}_{\text{QCD}} = \sum_{q=1}^{N_f} \bar{\psi}_{q,a} \left(i\gamma^\mu \partial_\mu \delta_{ab} - g_s \gamma^\mu t_{ab}^C A_\mu^C - m_q \delta_{ab} \right) \psi_{q,b} - \frac{1}{4} G_{\mu\nu}^C G^{C,\mu\nu}. \quad (1.6)$$

Here, $\psi_{q,a}$ denotes a quark field of flavor q with color index $a \in \{r, g, b\}$ and mass m_q . The gluon fields are represented by A_μ^C , with $C = 1, \dots, 8$ labeling the adjoint representation of the color group. The γ^μ are Dirac matrices, and t^C are the 3×3

8. The weak interaction coupling strength is small compared to the strong and electromagnetic forces. This weakness manifests in comparatively long lifetimes of particles that decay via the weak interaction. For instance, a free neutron in vacuum survives on average about 15 minutes before undergoing β -decay. Even much longer lifetimes occur in nuclei such as ^{14}C , whose β -decay with a half-life of about 5730 years forms the basis of radiocarbon dating.

9. Analogously to QCD, the QED Lagrangian is $\mathcal{L}_{\text{QED}} = \bar{\psi}(i\gamma^\mu \partial_\mu - e\gamma^\mu A_\mu - m)\psi - \frac{1}{4}F_{\mu\nu}F^{\mu\nu}$, where ψ is the fermion (Dirac) field and A_μ is the electromagnetic gauge field. $F_{\mu\nu}$ is the electromagnetic field strength tensor, that can be written as $F_{\mu\nu} = \partial_\mu A_\nu - \partial_\nu A_\mu$, which reflects the Abelian structure of the $U(1)$ group.

generators of the $SU(3)$ algebra. The object $G_{\mu\nu}^C$ stands for the gluon field strength tensor. The parameter g_s is the QCD coupling constant, which controls the strength of the interaction between quarks and gluons. QCD is a non-abelian gauge theory because $G_{\mu\nu}^A$ transforms in a special way to conserve the invariance of \mathcal{L}_{QCD} [10]:

$$G_{\mu\nu}^C = \partial_\mu A_\nu^C - \partial_\nu A_\mu^C + g_s f^{CDE} A_\mu^D A_\nu^E, \quad (1.7)$$

where f^{CDE} are the structure factors of the $SU(3)$ algebra, appearing in the commutation relations of the generators $[t^C, t^D] = if^{CDE}t^E$. As a consequence of the non-abelian structure of QCD, the mediators of the interaction (gluons) carry color charge themselves. This leads to additional interaction terms, such as gluon-gluon interactions (like gluon + gluon \rightarrow gluon) which have no analogue in abelian gauge theories like QED. Equation 1.7 follows a non-commutative algebra, the last term allows vertices of 3 and 4 gluons in the theory [11].

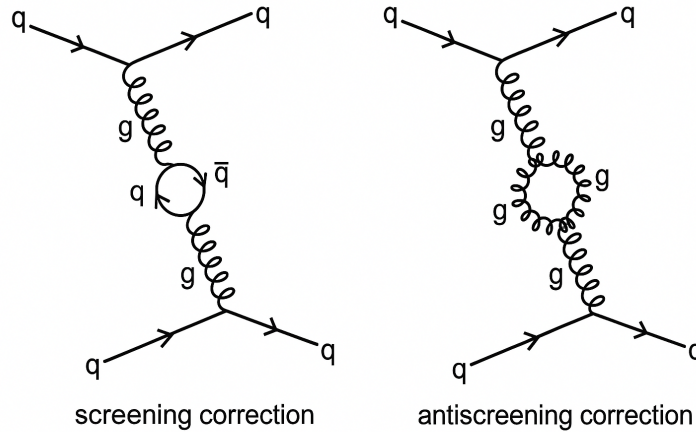


FIGURE 1.4 – At left, the gluon exchanged by two colored particles splits into a virtual quark pair. In this case, the interaction between two partons is screened. At right, the gluon splits into a virtual gluon pair (gluon self-interaction), and an anti-screening effect occurs (this diagram does not exist in QED) [12].

In QCD, as a consequence of the self-interacting nature of gluons, new Feynman diagrams¹⁰ involving 3- and 4-gluon vertices appear at next-to-leading order

10. In quantum field theory, each fundamental interaction can be represented by a Feynman diagram. Beyond being a pictorial shorthand, a Feynman diagram encodes the terms contributing to the transition amplitude (matrix element) of a given process. Squaring the absolute value of this amplitude, and including appropriate phase-space and flux factors, yields measurable quantities

(NLO), as illustrated in Figure 1.4. These quantum processes induce specific properties in the theory, leading to the scale dependence of the coupling g_s . One usually introduces the QCD running constant¹¹ α_s , defined as $\alpha_s = \frac{g_s^2}{4\pi}$. The scale dependence of $\alpha_s(Q)$ is determined by the QCD renormalization group equation [13], which can be written as:

$$\alpha_s(Q^2) = \frac{4\pi N_c}{(11N_c - 2N_f) \ln(Q^2/\Lambda_{QCD}^2)} \quad \text{if } Q^2 \gg \Lambda_{QCD}^2, \quad (1.8)$$

where, Q^2 is the four-momentum transfer squared, Λ_{QCD} is the characteristic energy scale of QCD, $N_c = 3$ is the number of colors and $N_f = 6$ is the number of quark flavours. Notice that $11N_c - 2N_f > 0$, which implies that α_s decreases with increasing Q^2 .

In Figure 1.5, the evolution of α_s as a function of Q is shown, the experimental points are consistent with QCD predictions. The theory possesses 2 principal regimes separated by Λ_{QCD} . The first one takes place at large running constant (low energies $\Lambda_{QCD} > Q$), it is explained by non-perturbative physics, where effective field theories are needed to describe for example, hadron states, hadron-hadron interactions, nuclei and nuclear interactions [8]. The second regime, at small running constant (high energies $\Lambda_{QCD} < Q$) concerns highly energetic partons described by perturbative Quantum Chromodynamics (pQCD).

There are three main important properties in QCD:

The **asymptotic freedom** ($\Lambda_{QCD} \ll Q$) is an interesting property that implies a reduction in the strength of the QCD interaction between quarks and gluons when the energy scale increases and the length scale decreases [13].

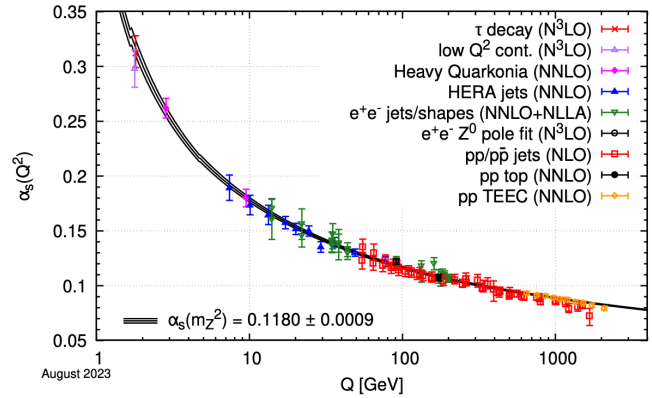


FIGURE 1.5 – Running QCD coupling constant as a function of the energy scale Q [1].

such as cross sections and decay rates.

11. In close analogy with QED, where the strength of the electromagnetic interaction is given by the fine-structure constant α_{em} , defined as $\alpha_{em} = \frac{e^2}{4\pi}$.

These hadrons are overall color-neutral states built primarily from valence quarks, which determine the hadrons conserved quantum numbers (such as electric charge, baryon number...). In addition to these, the strong interaction generates a dynamic background of gluons and sea quarks (quark–antiquark pairs) arising from quantum vacuum fluctuations, because the energy of the vacuum is not zero. According to the Heisenberg uncertainty principle $\Delta E \Delta T \geq \hbar/2$, an energy fluctuation ΔE can occur during a short time interval ΔT , allowing virtual particles, including massive

quark–antiquark pairs, to appear inside a hadron¹². Hadrons can be classified into two types¹³: the quark–antiquark pairs ($q\bar{q}$), called mesons, and the three-quark states (qqq), called baryons (see examples of different mesons and baryons and their quark content in Figure 1.6). Notice that, in addition to hadrons shown in Figure 1.6, heavier hadrons containing b quarks (such as B^0 , B^+ , B_s^0 , B_c^+ , Υ , Λ_b^0 , Ξ_b^- , etc.) can also be formed. The heaviest quark, the top, decays via the weak interaction so rapidly that it does not hadronize¹⁴.

The last interesting property is the **chiral symmetry breaking**, more specific the spontaneous symmetry breaking of a global symmetry of quarks [19]. Chiral symmetry reflects the invariance between quarks of left- and right-handed chirality. A quark is said to be right-handed when its spin is aligned with its momentum, and left-handed when the spin is oriented in the opposite direction. In the theoretical limit of massless quarks ($m_q \approx 0$), the QCD Lagrangian treats left- and right-handed quarks independently, thereby conserving chiral symmetry. In vacuum, however, this symmetry does not remain intact and it is spontaneously broken through the formation of the chiral condensate:

$$\langle \bar{\psi}\psi \rangle = \langle \bar{\psi}_L\psi_R + \bar{\psi}_R\psi_L \rangle, \quad (1.9)$$

which links left- and right-handed components. Equation 1.9 is derived in detail in Appendix A. The nonvanishing expectation value $\langle \bar{\psi}\psi \rangle \neq 0$ indicates the breaking of chiral symmetry. This mechanism generates the masses for pseudo-scalar hadrons. At sufficiently high temperatures or energy densities, the restoration of chiral symmetry takes place, leading to $\langle \bar{\psi}\psi \rangle \sim 0$. This restoration occurs primarily for the light quarks (u, d, s), whereas for heavy quarks (c, b, t) the explicit mass terms in the QCD Lagrangian remain dominant and prevent restoration.

It is important to note that many of the nonperturbative features of QCD can be studied within a powerful framework known as lattice QCD (lQCD) [20]. In this approach, a gauge theory is formulated on discretized space and (imaginary) time, represented by a lattice of points. The QCD Lagrangian is then evaluated

12. These sea quarks and gluons play an important role in the hadron's mass and momentum distribution. Quantum numbers of a hadron are fixed solely by its valence quark content.

13. In addition to conventional mesons and baryons, exotic multiquark states (also color-neutral) such as tetraquarks ($qq\bar{q}\bar{q}$) and pentaquarks ($qqqq\bar{q}$) have been observed experimentally, notably by the LHCb Collaboration [16, 17].

14. Nevertheless, intriguing measurements by the CMS Collaboration hint at the possible existence of rare, massive bound states, such as toponium [18].

numerically using Monte Carlo simulations, with the full continuum solutions of QCD recovered in the limit where the lattice spacing is reduced to zero and the lattice volume grows to infinity. Lattice QCD enables quantitative calculations of hadron masses, as well as a wide range of other insights into the strongly interacting regime of QCD.

1.2 Hadronic matter phase diagram and the quark-gluon plasma (QGP)

An exponential mass spectrum, proposed in the 1960s by Hagedorn, predicts that the density of hadronic states increases exponentially with mass [21]:

$$\rho(m) \sim m^{-a} e^{m/T_H}, \quad (1.10)$$

where m is the mass of a hadron, T_H is the Hagedorn temperature and a is a model-dependent constant controlling the low-mass behavior. Equation 1.10 suggests that above the temperature T_H , hadronic matter cannot be heated further. This behavior marks the transition to a new phase of matter in which quarks are no longer confined [22], as illustrated in the left panel of Figure 1.7.

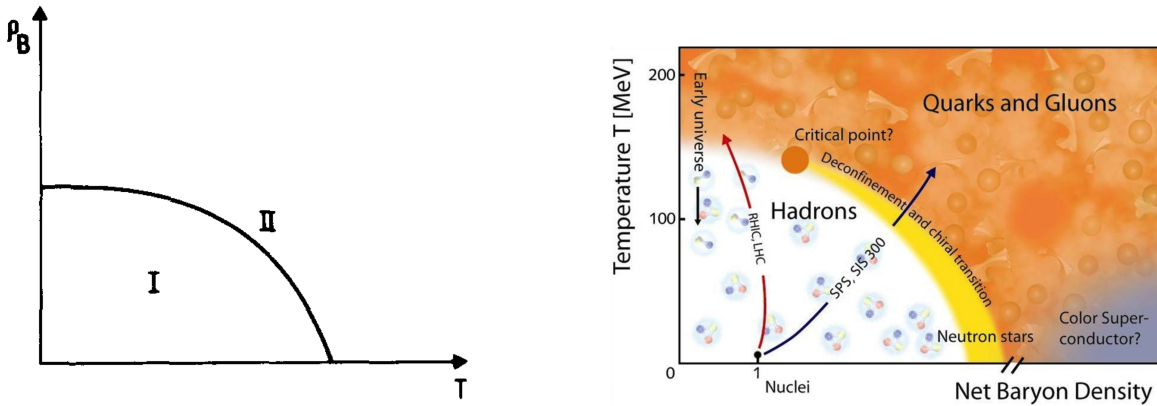


FIGURE 1.7 – Left: Schematic representation of the early phase diagram proposed by Cabibbo and Parisi [23], where quarks are confined in phase I and deconfined in phase II (baryon number density ρ_B vs temperature T). Right: More recent version of the QCD phase diagram showing the various phases of strongly interacting matter (temperature vs net baryon density) [24].

The transition temperature was estimated to be on the order of the pion mass, $k_B T_c \sim m_\pi$, where k_B is the Boltzmann constant. The right panel of Figure 1.7 shows a more complete version of the QCD phase diagram. It outlines the current understanding of different states of QCD matter [25], including the hadronic phase, the QGP, and the color-superconducting phases at high baryon densities. The diagram is parameterized by temperature T and the net baryon density ρ_B . At low values of temperature and net baryon density, partons are confined in the form of hadrons. The white area represents the zone of confinement. As the net baryon density increases, the parton density rises, and with increasing temperature, the interactions between partons weaken. When certain values of both parameters (temperature and net baryon density) are reached, a phase transition occurs. In this new regime, where the color charge density is large, the interaction between partons becomes screened, and free states of partons are predicted by QCD theory. These states are located in the orange region of the diagram, where the QGP is formed. This QGP matter is predicted to have existed during the first moments of the universe ($\sim 10^{-6}$ s after the Big Bang) and may also exist in the core of neutron stars [26]. Two types of phase transitions are predicted to exist in the phase diagram of strongly interacting matter [27, 28]:

- A first-order phase transition¹⁵, characterized by a discontinuous change in the state of matter. Strictly speaking, it appears as a line in the QCD phase diagram. However, due to experimental uncertainties, it is depicted as a yellow band in the right panel of Figure 1.7.
- A crossover transition at low baryon chemical potential, where the properties of matter change continuously between the hadronic and QGP phases (this is not a true phase transition in the thermodynamic sense).

Experimentally, to explore the QCD phase diagram and investigate the region where the QGP may form, heavy-ion collisions are employed to reach extremely high temperatures and energy densities. At the LHC, these collisions allow the study of the region characterized by high temperature and very low net baryon density, which corresponds to the crossover region of the phase diagram. There is no unique critical temperature for this crossover, instead, it occurs over a range of temperatures. The temperature at which the transition appears for vanishing baryon chemical potential, it typically lies in the range of about 140–190 MeV. The

¹⁵ A comprehensive discussion of the various types of phase transitions is provided in appendix A.

point that separates the crossover region from the first-order phase transition line at higher baryon densities is not precisely known and is referred to as the critical point. In addition, at low temperatures and extremely high net baryon density, theoretical predictions suggest the possible existence of a color superconducting phase.

1.3 Ultrarelativistic heavy-ion collisions

Under normal conditions of nuclear matter, quarks remain confined within bound states. Heavy-ion collisions (HICs), however, can generate the extreme temperatures and densities required to form a QGP.

The experimental HIC program began in the 1990s at the **Alternating Gradient Synchrotron (AGS)** at Brookhaven National Laboratory (BNL) and the **Super Proton Synchrotron (SPS)** at CERN, reaching maximum center-of-mass energies of $\sqrt{s_{NN}} = 4.75\text{GeV}$ and $\sqrt{s_{NN}} = 17.2\text{GeV}$, respectively. These pioneering measurements provided the first experimental indications of deconfinement [30, 31]. Since 2000, the **Relativistic Heavy Ion Collider (RHIC)** at BNL has enabled collisions of gold nuclei at $\sqrt{s_{NN}} = 200\text{GeV}$ [32–34]. The conditions achieved at RHIC proved to be optimal for producing and characterizing a strongly coupled QGP, establishing it as an ideal environment to study the properties of deconfined matter. Beginning

in 2010, the **Large Hadron Collider (LHC)** at CERN extended these investigations to significantly higher energies, with Pb–Pb collisions (see Figure 1.8) reaching $\sqrt{s_{NN}} = 2.76\text{TeV}$ [35, 36]. At the LHC, the QGP is produced at higher temperatures, larger energy densities, and with a longer lifetime compared to RHIC. Notice that heavy-ion experiments also typically perform measurements on smaller systems, such as proton–proton (pp) or proton–lead (pPb) collisions (where QGP formation is not expected) to provide essential baselines. Comparisons of HICs with small colliding systems help to isolate QGP-specific signatures and clarify the transition from confined to deconfined matter. Nevertheless, several QGP-like

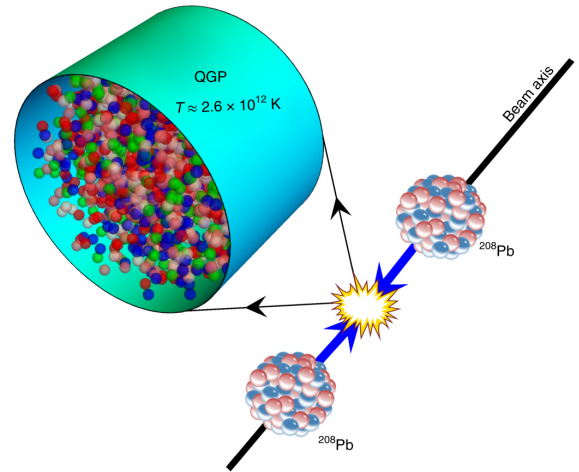


FIGURE 1.8 – Schematic illustration of the creation of QGP in Pb–Pb collisions at the LHC. Figure from [29].

signatures have already been observed in small systems at the LHC (and RHIC).

1.3.1 Initial stage of the collisions

1.3.1.1 The Glauber model and centrality

In nucleus-nucleus collisions, the initial geometry is characterized by the impact parameter b , which is the distance between the paths of the two heavy-ions (see Figure 1.9). The value of b determines the degree of overlap between the two nuclei: for small b , the overlap is large (central collisions), while for large b , the overlap becomes small (peripheral collisions). In the ultra-peripheral regime, b is so large that the nuclei do not overlap at all. To characterize the initial geometry and estimate quantities such as the number of binary (nucleon-nucleon) collisions, a realistic description of the initial state is needed. The Glauber model [37] provides a geometric framework to simulate this configuration using a probabilistic treatment of independent nucleon–nucleon interactions. Each nucleus is sampled according to a density profile, typically the Woods–Saxon distribution:

$$\rho(r) = \rho_0 \cdot \frac{1 + w(r/R)^2}{1 + \exp[(r - R)/a]}, \quad (1.11)$$

where R is the nuclear radius, a the surface diffuseness, and w accounts for deformation. Equation 1.11 is particularly relevant in the so-called optical approximation, where continuous nuclear densities are used to compute the elementary binary collisions between constituent nucleons. Figure 1.9 visualizes the Glauber Model geometry, with the impact parameter b and the position in the transverse plane \mathbf{s} .

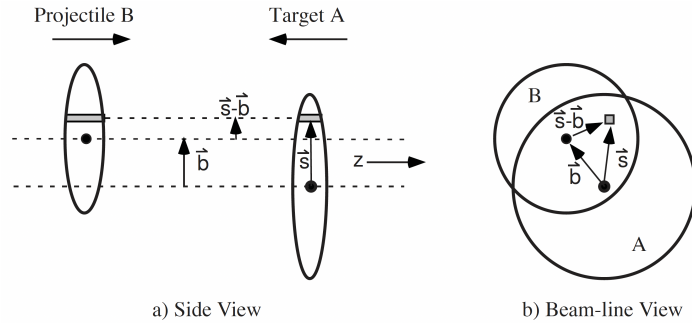


FIGURE 1.9 – Schematic representation of the Glauber Model geometry, with transverse (a) and longitudinal (b) views [37].

The two nucleons are assumed to collide if their transverse separation is smaller

than $\sqrt{\sigma_{NN}^{\text{inel}}/\pi}$, where $\sigma_{NN}^{\text{inel}}$ is the inelastic nucleon–nucleon cross section. Based on this geometrical criterion, the following key quantities can be computed within the Glauber model:

- N_{part} : the number of nucleons that participate in at least one collision.
- N_{coll} : the total number of binary nucleon–nucleon collisions.
- N_{ch} : the number of charged particles produced in the final state.

Figure 1.10 illustrates the relation between N_{part} , b and the multiplicity N_{ch} of a Pb–Pb collision, determining the collision centrality.

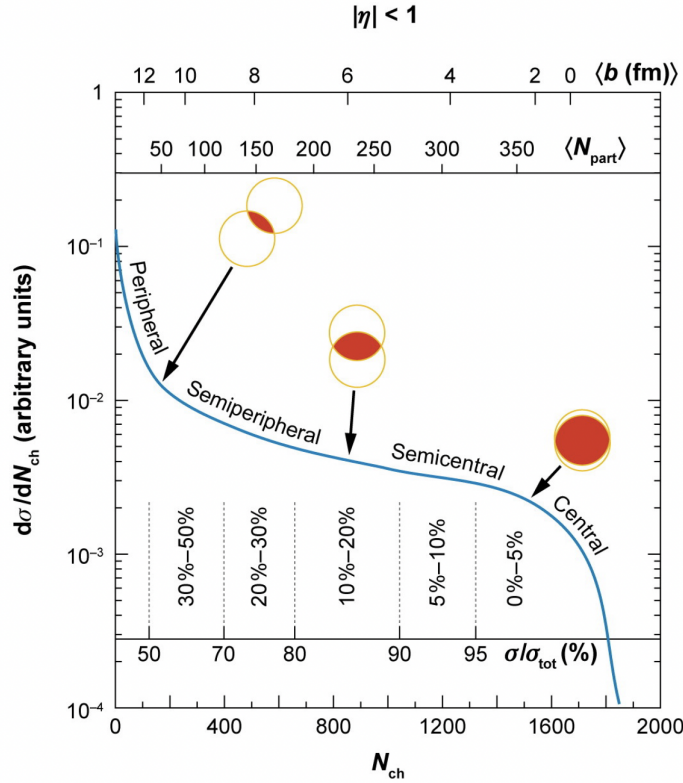


FIGURE 1.10 – Centrality determination using the Glauber model. The figure illustrates the charged-particle multiplicity distribution $d\sigma/dN_{\text{ch}}$ (in arbitrary units) as a function of the charged-particle multiplicity N_{ch} . Centrality classes are defined by percentiles of the total inelastic cross section $\sigma/\sigma_{\text{tot}}$ [37].

The centrality of a collision is thus correlated to the impact parameter and is usually expressed as a percentile of the total inelastic cross section. It can be approximated as:

$$c(b) \sim \frac{\pi b^2}{\sigma_{\text{inel}}}, \quad (1.12)$$

where, σ_{inel} is the total inelastic scattering cross section. For example, a centrality $c = 10\%$ corresponds to the most central collisions (smallest b), while $c = 70\%$ corresponds to more peripheral collisions.

To quantify the spatial overlap, one defines the nuclear overlap function:

$$T_{AA}(b) = \int d^2s T_A(\mathbf{s}) T_A(\mathbf{s} - \mathbf{b}), \quad (1.13)$$

where, $T_A(\mathbf{s}) = \int dz \rho_A(\mathbf{s}, z)$ is the nuclear thickness function. T_{AA} relates to N_{coll} via:

$$N_{coll}(b) = T_{AA}(b) \cdot \sigma_{NN}^{inel}, \quad (1.14)$$

Glauber simulations provide initial geometric quantities used to characterize centrality and spatial eccentricity. A simplified classification of heavy-ion collisions according to the initial geometry and event type is presented below.

Classification of collisions:

- Central Collisions (CC): 0 – 10% (large overlap, high N_{part})
- **Mid-Central Collisions (MCC):** 10–50% (intermediate overlap).
- **Peripheral Collisions (PC):** 50–100% (small nuclear overlap, characterized by low multiplicities and few participating nucleons).

In addition, Ultra-Peripheral Collisions (UPC) are defined as a type of collision in which two nuclei pass by each other without overlapping, preventing hadronic interactions. The process is dominated by the intense electromagnetic fields produced by nuclei large charges. Notice that in smaller colliding systems (like pp or pA), alternative descriptions such as the Color Glass Condensate (CGC) may offer a more suitable representation of the initial state [38].

1.3.1.2 Nuclear parton distribution functions (nPDFs)

In high-energy hadronic and nuclear collisions, the structure of the incoming projectiles (protons or nuclei) is encoded in Parton Distribution Functions (PDFs). These functions describe the probability of finding a parton (quark or gluon) carrying a momentum fraction x of the parent nucleon's momentum, evaluated at a given resolution scale Q^2 . PDFs are non-perturbative quantities which has to be determined experimentally and they are a crucial component of the initial-state description [39].

PDF

PDFs are supposed to be universal, they are typically extracted in (eA, γ A, pA) [40] at different Q^2 . Most of the proton PDFs are constrained with HERA Data, Tevatron and LHC colliders [41]. Different collaborations like: MMHT2014 [42], CTEQ [43], CT14 [44], NNPDF [45] uses these experimental data to fit and extract the PDFs. The PDFs estimation from different collaborations are regularly updated as new experimental data become available.

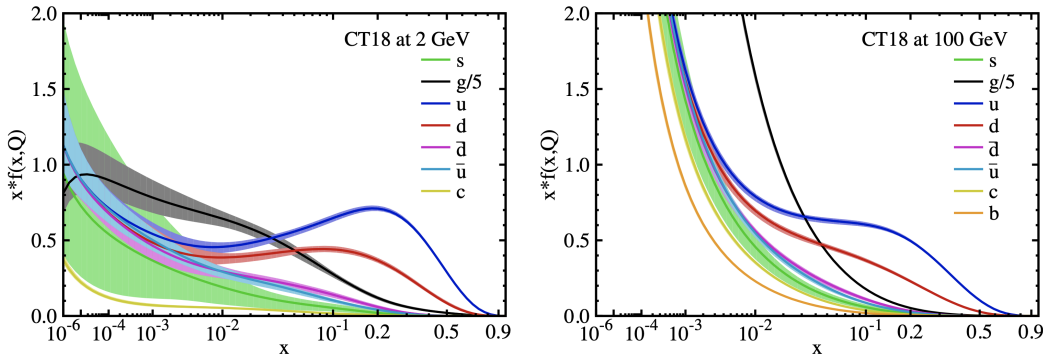


FIGURE 1.11 – Representation of the proton PDF at $Q = 2$ GeV (left) and $Q = 100$ GeV (right). The CT18 parton distribution functions for $u, \bar{u}, d, \bar{d}, s = \bar{s}$ [46].

At low values of x-Bjorken, the predominant components are gluons and sea quarks. As the energy increases, these contributions become increasingly significant. The evolution of the PDFs depending of Q^2 follows the Dokshitzer-Gribov-Lipatov-Altarelli-Parisi (DGLAP) evolution equations [47–49]:

$$\frac{dq_i}{d \ln Q^2} = \frac{\alpha^2}{2\pi} \frac{dx_0}{x_0} \left[q_i(x_0, Q^2) P_{qq} \left(\frac{x}{x_0} \right) + g(x_0, Q^2) P_{qg} \left(\frac{x}{x_0} \right) \right], \quad (1.15)$$

$$\frac{dg}{d \ln Q^2} = \frac{\alpha^2}{2\pi} \int_x^1 \frac{dx_0}{x_0} \left[q_i(x_0, Q^2) P_{gq} \left(\frac{x}{x_0} \right) + g(x_0, Q^2) P_{gg} \left(\frac{x}{x_0} \right) \right]. \quad (1.16)$$

where the splitting functions P_{ij} represents the probability for partons i, j , $q_i(x, Q^2)$ is the quark distribution function of flavour i and $g(x, Q^2)$ is the gluon distribution. We can see in these equations (1.15 and 1.16) that quarks PDFs for a given (x, Q^2) are linked to the gluons PDFs at the same (x, Q^2) . The splitting functions are calculated with perturbative QCD (see Figure 1.12).

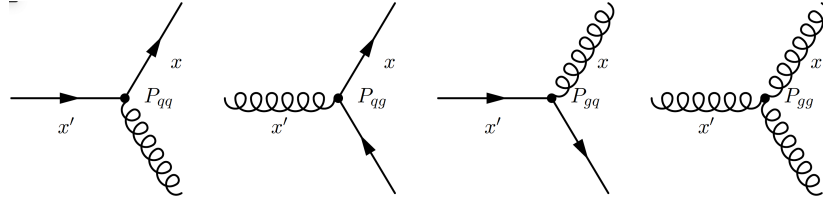


FIGURE 1.12 – Illustration at Leading Order (LO) of different parton splitting functions.

The DGLAP equations are solved numerically when the PDFs $f_i(x, Q_0^2)$ at given scale Q_0^2 , are provided as input. The PDFs are determined with a global fit of experimental data (evolution from Q_0^2 to Q^2).

nPDF

In the case of nuclei targets, the parton distribution functions (PDFs) are modified due to several nuclear effects [50]. These modifications are encoded in nuclear PDFs (nPDFs), which extend the proton PDF framework to nuclei. The nuclear modification is commonly expressed through the ratio:

$$R_f^{(A)}(x, Q) \equiv \frac{f^{(N/A)}(x, Q)}{\frac{Z}{A}f^{(p)}(x, Q) + \frac{A-Z}{A}f^{(n)}(x, Q)}, \quad (1.17)$$

where $f^{(N/A)}(x, Q)$ denotes the parton distribution function of flavor f in a bound nucleon inside a nucleus of mass number A , and $f^{(p)}(x, Q)$, $f^{(n)}(x, Q)$ refer to the same flavor PDFs in a free proton and a free neutron, respectively. The denominator represents the isospin-averaged parton density of a free nucleon in the nucleus, weighted by the number of protons Z and neutrons $A - Z$. The ratio $R_f^{(A)}$ quantifies how much the nuclear environment modifies the distribution of partons compared to what would be expected from a simple superposition of free nucleons. A deviation from unity in this ratio signals the presence of nuclear effects. Several global nPDF fits have been developed using experimental data from deep inelastic scattering experiments (DIS) involving nuclei. Figure 1.13 illustrates one example of such a global analysis [51], where two different results of $R_f^{(A)}$ (with and without the inclusion of D -mesons) are shown.

Even though a substantial amount of D -meson data from LHCb experiment is available [52], one should be cautious when using them as a probe to constrain nPDFs. As emphasized in Ref. [53], the suppression of D -mesons in pPb collisions at

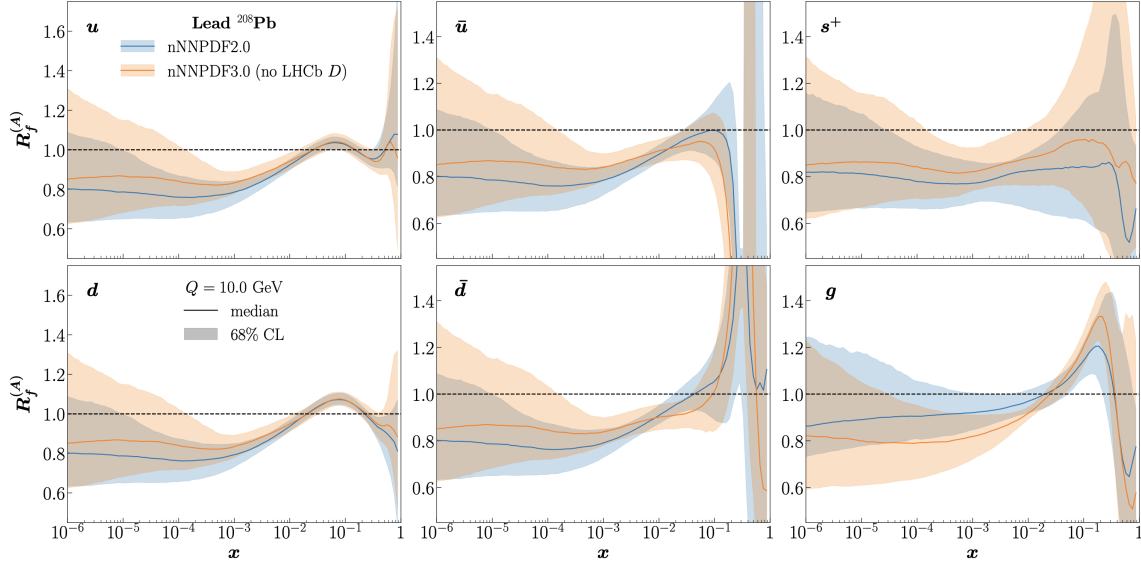


FIGURE 1.13 – $R_f^{(A)}$ as a function of x for various parton species, computed with nPDFs from the nNNPDF3.0 fit [51].

the LHC is not solely driven by nuclear effects such as gluon shadowing or saturation¹⁶. Other medium-induced gluon radiation effects have also been identified to be important, such as fully coherent energy loss (FCEL) effect [54] (see Section 2.1.3.1 in Chapter 2 for more details). Consequently, D -meson measurements cannot be regarded as a robust probe for constraining nPDFs. In contrast, Drell-Yan (DY) production can be considered as a cleaner probe [55], since it is a purely electromagnetic process at leading order. In Chapter 5 of this thesis, we show results on constraining $R_f^{(A)}$ using reweighting techniques with DY pseudo-data¹⁷ in the LHCb kinematic region, obtaining improved trends consistent with those shown in Figure 1.13.

1.3.1.3 Kinematic variables

In experimental particle physics, fundamental kinematic variables are measured to characterize the particles produced in high-energy collisions.

16. At low x , non-linear gluon recombination processes ($g + g \rightarrow g$) are expected to reduce the gluon density in nuclear PDFs, a phenomenon known as saturation. The resulting suppression observed in $R_g^{(A)}$ is referred to as gluon shadowing.

17. Pseudodata refers to artificially generated data that mimics real data but is not collected from actual experiments. It is often used to make predictions.

We consider the Cartesian coordinate system shown in Figure 1.14, where the z -axis represents the beam axis and the two nuclei entering into collision.

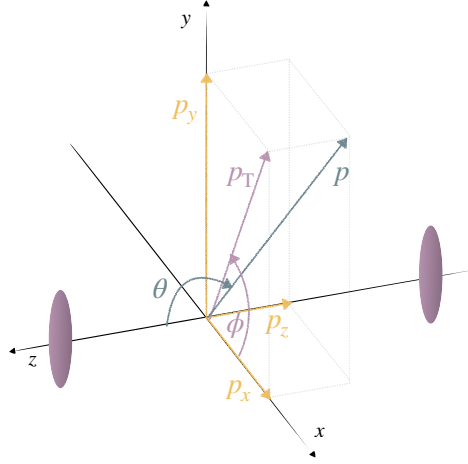


FIGURE 1.14 – Coordinate system of a particle produced in a collision [56].

— **Transverse momentum:**

$$p_T = \sqrt{p_x^2 + p_y^2}. \quad (1.18)$$

The transverse momentum p_T is the component of a particle's momentum perpendicular to the beam axis [1]. It is a Lorentz-invariant quantity under boosts along the z -direction, meaning it remains unchanged by longitudinal motion or relativistic contraction along the beam axis.

— **Rapidity:**

$$y = \frac{1}{2} \ln \left(\frac{E + p_z}{E - p_z} \right). \quad (1.19)$$

Rapidity is a dimensionless value related to velocity [57]. The equation for the transformation of rapidity is $y' = y - \arctan \beta_z$ where $\beta_z = \frac{v_z}{c}$. Two particles ejected after the collision with rapidities y_1 and y_2 in a certain frame of reference respects always:

$$y'_1 - y'_2 = (y_1 - \tanh^{-1}(\beta_z)) - (y_2 - \tanh^{-1}(\beta_z)) = y_1 - y_2. \quad (1.20)$$

The difference is an invariant quantity with respect to the Lorentz boost along

the beam axis. In the context of parton distribution functions [58], rapidity is directly related to the x-Bjorken variable, which represents the momentum fraction carried by a parton in the incoming nuclei. In two-particle to two-particle processes, the relation between Bjorken-x and the rapidity y of a produced particle of mass M in a hadronic collision at center-of-mass energy \sqrt{s} is:

$$x_{1,2} = \frac{M}{\sqrt{s}} e^{\pm y}, \quad (1.21)$$

where, x_1 and x_2 are the momentum fractions of the partons from the two incoming hadrons. This relation illustrates how forward rapidity ($y \gg 0$) corresponds to probing small x in one of the colliding hadrons and large x in the other, making rapidity a key variable in accessing different parton kinematics. The detailed derivation of equation 1.21 can be found in appendix 1.

— **Pseudorapidity:**

$$\eta = -\ln \left(\tan \frac{\theta}{2} \right) = \frac{1}{2} \ln \left(\frac{|\vec{p}| + p_L}{|\vec{p}| - p_L} \right). \quad (1.22)$$

Pseudorapidity is a spatial coordinate describing the angle of a particle relative to the beam axis and p_L is the component of the longitudinal momentum ($p_L = p_z$) and θ is the angle between the particle trajectory and the positive direction of the beam axis. Particles with high pseudorapidity values are generally lost escaping from the acceptance zone in the detector. Notice that if the mass of the particle is negligible compared to momentum $|p| \gg m$ and $E \approx |p|$, pseudorapidity and rapidity become the same observable $y \approx \eta$.

- **Invariant Mass:** The invariant mass is a fundamental quantity in relativistic physics, representing the mass of a particle or system of particles in any inertial frame. It is a Lorentz-invariant quantity, allowing the identification of resonances regardless of the observer's frame of reference. For a single particle, the invariant mass corresponds to its rest mass and is derived from the energy-momentum relation¹⁸:

$$m = \sqrt{E^2 - \mathbf{p}^2}. \quad (1.23)$$

18. This energy-momentum relation, commonly known as the Einstein-Pythagorean equation: $E^2 = (pc)^2 + (mc^2)^2$. In natural units where $c = 1$, this simplifies to $E^2 = p^2 + m^2$.

For a system of two particles, the invariant mass of the combined system is given by:

$$M = \sqrt{m_1^2 + m_2^2 + 2(E_1 E_2 - p_1 p_2 \cos \theta)}, \quad (1.24)$$

where, m_1, m_2 are the rest masses, E_1, E_2 the energies, p_1, p_2 the magnitudes of the momenta, and θ the angle between the momentum vectors of the two particles.

1.3.2 History of a HIC

The study of heavy-ion collisions at ultrarelativistic energies has greatly advanced our understanding of strongly interacting matter under extreme conditions. Experiments at the RHIC first provided compelling evidence for the creation of a strongly coupled QGP. Building upon these discoveries, the LHC has extended the energy frontier, allowing us to explore the QGP at higher temperatures and higher energy densities, as well as over an extended QGP lifetime [36].

During the initial instants of the HIC, hard scattering processes take place (production of high- p_T partons and heavy quarks...), these processes are calculated within the pQCD framework [60].

At LHC, around $t \sim 1 \text{ fm}/c$, the system reaches approximately thermal equilibrium [61] and the hydrodynamic expansion of the QGP takes place. Inside the hot medium, all color charges are free, meaning that partons (quarks and gluons) are deconfined. The QGP expands and cools, driving the system toward the hadronization phase.

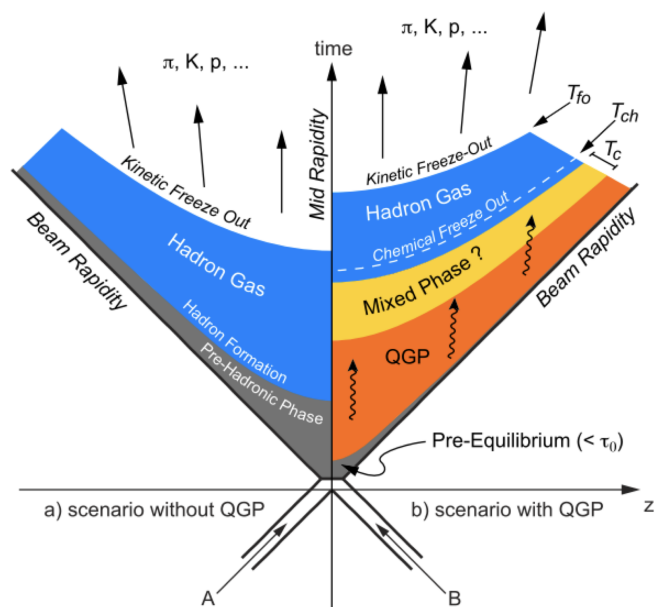


FIGURE 1.15 – Björken scenario with and without the QGP phase. Figure from [59].

At $t \sim 10 \text{ fm}/c$, when the transition temperature is lower than a certain T_C critical value (150 - 160 MeV), a phase transition occurs where all partons hadronize into pions, Kaons, protons, etc. These final-state hadrons may continue to scatter (potentially altering their chemical composition) or decay into other states. The resulting products are what experiments ultimately observe. Figure 1.15 shows the time and space evolution of the entire HIC. The whole QGP formation process can be simplified into four main phases, as illustrated in Figure 1.16.

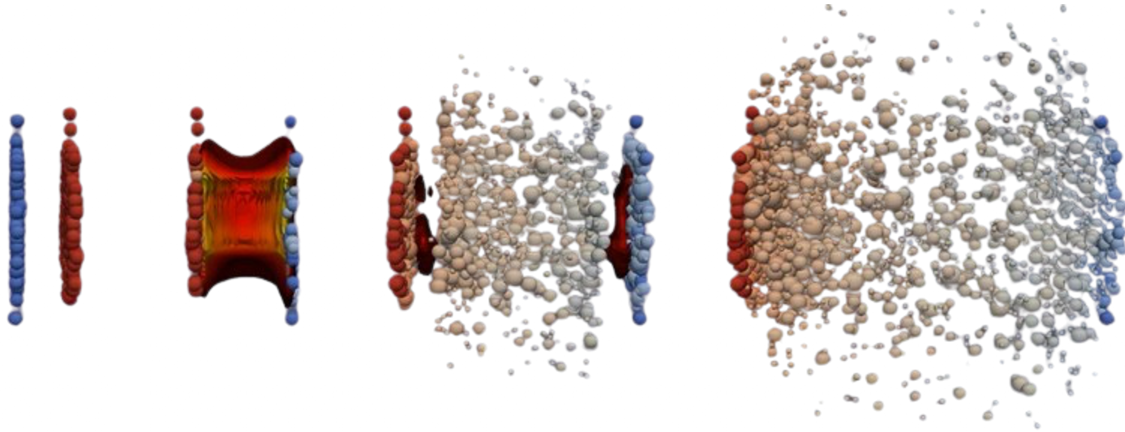


FIGURE 1.16 – Simulation of the dynamical evolution of a central heavy-ion collision, illustrated through four stages: (1) two Lorentz-contracted lead nuclei approaching impact, (2) the onset of pre-equilibrium dynamics after the collision, (3) the subsequent hydrodynamic expansion of the quark–gluon plasma (QGP), and (4) the final hadronisation of the system into observable particles. Figure from Ref. [62].

1. Initial conditions phase:

Before the collision, heavy-ions travelling at almost the speed of light suffer a large Lorentz contraction, taking a pancake shape in the lab's reference frame. The crossing time of the nuclei can be estimated as

$$\tau_{\text{cross}} = \frac{2R}{\gamma}, \quad (1.25)$$

where γ is the Lorentz factor¹⁹ and R the radius of the nucleus.

2. Pre-equilibrium phase:

Shortly after the collision, the system enters a pre-equilibrium stage lasting on

19. In special relativity, γ is the Lorentz factor, defined as $\gamma = \frac{1}{\sqrt{1-v_z^2/c^2}}$, where v_z is the longitudinal component of the particle velocity along the beam axis and c is the speed of light.

the order of 1 fm/c [63]. During this period the medium has not yet reached thermal equilibrium, and the earliest hard processes occur [64].

3. The hydrodynamic expansion phase:

At this level, numerous particles in a very small volume are produced. The temperature after the collision is so high that quarks and gluons are deconfined and form a QGP, which rapidly thermalizes. This state, produced in Pb-Pb collisions at the LHC, is the hottest droplet of liquid with the lowest viscosity ever known (almost a perfect fluid) [36]. The hydrodynamic plasma medium expands very fast and it last up ~ 10 fm/c depending of its size. The Plasma progressively cools down until a critical temperature T_C is reached and the crossover happens (see figure 1.15).

4. The hadronic phase:

In this phase, the hadronic gas formed continues to lower its temperature and under a threshold temperature T_{ch} , the gas reaches a first chemical freeze-out, where inelastic collisions stop. Finally, when the gas temperature arrive at T_{fo} a kinetic freeze-out will take place. In this last phase, momentum of hadrons remains constant (elastic collisions stops) and hadrons propagate towards the detectors.

1.3.3 Observables and probes of the QGP

To study the QGP produced in HIC, one must rely on QGP observables. These are measurable quantities that encode information about the formation and evolution of the deconfined medium (e.g., nuclear modification factor R_{AA} , anisotropic flow coefficients v_n , etc.). Among these, the information from different types of particle probes is particularly valuable. Understanding how these probes are modified by the QGP requires comparing their behavior across different collision systems. The Proton-proton (pp) collisions, where no QGP is expected, provide a baseline, while proton-nucleus (pA) collisions help isolate cold nuclear matter effects (nuclear phenomena unrelated to QGP). These comparisons are crucial for interpreting observations in nucleus-nucleus (AA) collisions, such as Pb-Pb. Interestingly, the discovery of QGP-like signatures in high-multiplicity pp and pA collisions at the LHC has challenged the notion that QGP forms only in large systems. Note that particle probes can be classified into:

Soft probes: The majority of particles produced in HIC are soft hadrons with low transverse momenta p_T respect to Λ_{QCD} . These final-state hadrons reflect the collective behavior of the expanding QGP at the moment of kinetic freeze-out. Their distributions carry information about the medium thermodynamic properties and transport coefficients. In particular, soft probes reveal collective flow phenomena, presented in detail through the study of anisotropic flow in section 1.5.2. Another important bulk observable is strangeness enhancement [65], where the yield of strange and multi-strange hadrons (such as Λ , Ξ , and Ω) is found to be significantly higher in AA collisions than in pp collisions at the same energy. This enhancement is interpreted as a consequence of the high gluon density in the deconfined phase, which facilitates strange quark pair production via processes like $gg \rightarrow s\bar{s}$. Interestingly, similar trends have been observed in high-multiplicity pp and pA collisions [66], raising new questions about the possible onset of collectivity in small systems.

Hard probes: These probes originate from early hard scatterings and are characterized by a large momentum and/or mass compared to $\Lambda_{\text{QCD}} \sim 200$ MeV, such as jets, heavy-flavor hadrons and quarkonia originate from hard partonic scatterings in the earliest stages of the collision. These objects are particularly useful to study QGP properties because their initial production is well described by perturbative QCD (pQCD). As they traverse the medium, energetic partons lose energy through both collisional and radiative processes. This energy loss leads to observable effects such as the suppression of high- p_T hadrons and jets compared to proton-proton baselines [67]. Heavy-flavor hadrons (containing charm or bottom quarks) are also key observables, as heavy quarks are produced early and experience the full evolution of the medium. Their in-medium energy loss, mass-dependent dynamics, and hadronization mechanisms provide insights into the transport properties of the QGP [68].

Electroweak probes: Particles that interact only electromagnetically or via the weak force have minimal interactions with the strongly-coupled QGP and can thus traverse it largely unaffected. This category includes dileptons, photons, as well as electroweak bosons such as Z^0 and W^\pm . While weak bosons are produced in initial hard scatterings, real and virtual photons can be emitted at all stages of the collision. In particular, thermal radiation from the QGP phase leads to an excess of low-mass dileptons and low- p_T direct photons over expectations from hadronic sources. These emissions carry information about the temperature and space-time evolution

of the medium, providing a unique window into the QGP's early stages [69].

The comprehensive study of such diverse signatures (spanning a wide range of momentum scales) is essential for characterizing the formation and properties of the QGP.

1.4 Relativistic fluid theory of QGP

The foundations of relativistic hydrodynamics in high-energy physics were established by Landau [70], well before the discovery of QCD. Decades later, experiments at RHIC and the LHC provided data demonstrating its effectiveness in describing the strongly interacting matter produced in heavy-ion collisions. This chapter introduces the fundamental concepts for studying the QGP within relativistic fluid dynamics. We begin with the thermodynamic properties of an ultrarelativistic ideal gas, estimating the energy density in this limit and comparing it to a simple geometric estimation (at collider energies) to highlight the relevant orders of magnitude. The discussion then moves from non-interacting to interacting systems, introducing key dimensionless numbers (Knudsen, Reynolds, and Mach) that define the regimes of collectivity in a system. These quantities provide the justification for applying relativistic hydrodynamics as an effective description for the QGP created in heavy-ion collisions. We finally outline the formulation of second-order hydrodynamic theories and viscous relativistic fluids, emphasizing transport properties such as shear viscosity.

1.4.1 Non-interacting ideal QGP

In the ultrarelativistic regime [57], where particle masses are negligible compared to the thermal energy ($T \gg m$), the energy-momentum relation simplifies²⁰ to $E_{\vec{p}} = |\vec{p}|$. This limit is relevant for describing an ideal QGP at sufficiently high temperatures, where quarks and gluons behave as effectively massless, deconfined particles [69]. The system can be treated as an ideal gas of massless relativistic particles in thermal equilibrium. If we consider a dilute gas of identical particles (bosons or fermions), the average occupation number of a single-particle state with

20. The relativistic energy relation $E^2 = (pc)^2 + (mc^2)^2$ can be approximated for ultra-relativistic particles as $E \approx pc$ when $pc \gg mc^2$ (and using natural units, $c = 1$).

momentum \vec{p} at equilibrium is given by:

$$f_{\text{BE}}(\vec{p}) = \frac{1}{e^{(E_{\vec{p}} - \mu)/T} - 1} \quad (\text{bosons}), \quad f_{\text{FD}}(\vec{p}) = \frac{1}{e^{(E_{\vec{p}} - \mu)/T} + 1} \quad (\text{fermions}) \quad (1.26)$$

Here, $E_{\vec{p}}$ is the single-particle energy, μ is the chemical potential, and T is the temperature. The minus sign in the Bose-Einstein distribution [71, 72] reflects the tendency of bosons to bunch together, allowing several particles to occupy the same state (Bose einstein condensate). In contrast, the plus sign in the Fermi-Dirac distribution [73, 74] enforces the Pauli exclusion principle, restricting fermions to at most one particle per state. In the context of an ideal QGP, the energy density and pressure in the baryonless limit $\mu = 0$ are given by:

$$\epsilon^{\text{ideal}} = g \int \frac{d^3 p}{(2\pi)^3} |\vec{p}| \cdot \frac{1}{e^{|\vec{p}|/T} \pm 1}, \quad (1.27)$$

$$p^{\text{ideal}} = \frac{g}{3} \int \frac{d^3 p}{(2\pi)^3} |\vec{p}| \cdot \frac{1}{e^{|\vec{p}|/T} \pm 1}. \quad (1.28)$$

By switching to spherical coordinates and using $p = |\vec{p}|$, we obtain:

$$p^{\text{ideal}} = \frac{g}{6\pi^2} \int_0^\infty \frac{p^3 dp}{e^{p/T} \pm 1}. \quad (1.29)$$

With the change of variable $x = p/T$, the integral becomes a standard statistical integral of Bose–Einstein or Fermi–Dirac type [75]:

$$\int_0^\infty \frac{x^n dx}{e^x \pm 1} = \Gamma(n+1) \cdot \zeta(n+1) \times \begin{cases} 1 & (\text{bosons}) \\ 1 - 2^{-n} & (\text{fermions}) \end{cases} \quad (1.30)$$

where $\Gamma(n+1)$ and $\zeta(n+1)$ denote Euler’s gamma and Riemann zeta functions at order $n+1$. For $n = 3$, this yields:

$$p_{\text{boson}}^{\text{ideal}} = \frac{g}{6\pi^2} T^4 \cdot \Gamma(4) \cdot \zeta(4) = \frac{g\pi^2}{90} T^4, \quad (1.31)$$

$$p_{\text{fermion}}^{\text{ideal}} = \frac{g}{6\pi^2} T^4 \cdot \Gamma(4) \cdot \left(1 - \frac{1}{2^3}\right) \zeta(4) = \frac{7}{8} \cdot \frac{g\pi^2}{90} T^4. \quad (1.32)$$

For an ideal QGP consisting of $N_c^2 - 1$ gluons and N_f massless flavors of quarks,

the total number of relativistic degrees of freedom can be computed as follows.

- **Gluons:** Gluons are massless vector bosons that transform under the adjoint representation of the gauge group $SU(N_c)$. In QCD theory, $N_c = 3$, corresponding to three color charges (red, blue and green). Since gluons have two transverse polarization states, the total number of bosonic degrees of freedom is $g_b = 2 \times (N_c^2 - 1) = 2 \times 8 = 16$.
- **Quarks:** As spin- $\frac{1}{2}$ fermions, quarks contribute $g_f = 2 \times 2 \times N_c \times N_f$, where the factors account for spin degeneracy, particle–antiparticle symmetry, color, and flavor, respectively. In the high-temperature regime of the QGP, only the three lightest quark flavors (up, down, and strange) can be considered as massless ($N_f = 3$), since $T_{QGP} \gg m_q$ for these species. Thus, the total number of fermionic degrees of freedom becomes $g_f = 2 \times 2 \times 3 \times 3 = 36$.

Since fermionic contributions to thermodynamic quantities are weighted by a factor of $7/8$ relative to bosons as shown in equation 1.32, the total effective number of degrees of freedom becomes

$$g_{\text{eff}} = g_b + \frac{7}{8}g_f = 16 + \frac{7}{8} \cdot 36 = 47.5. \quad (1.33)$$

Thus, the pressure and energy density of an ideal QGP are:

$$p^{\text{ideal}} = \frac{\pi^2}{90} \cdot g_{\text{eff}} \cdot T^4, \quad (1.34)$$

$$\epsilon^{\text{ideal}} = \frac{\pi^2}{30} \cdot g_{\text{eff}} \cdot T^4 \quad (1.35)$$

This Stefan–Boltzmann-like behavior confirms that the QGP, in this limit, behaves as an ultrarelativistic fluid. For massless particles such as photons, gluons, or ultrarelativistic quarks, the pressure and energy density are related by the expression:

$$p^{\text{ideal}} = \frac{\epsilon^{\text{ideal}}}{3}. \quad (1.36)$$

By combining equations 1.34 and 1.35, one can easily show this relation. Equation 1.36 plays a key role in hydrodynamic modeling of heavy-ion collisions and early-universe cosmology [76]. Nevertheless, the approximation holds for an ideal QGP at high temperatures where interactions are weak.

Energy density estimates

Although the energy-density expression in Equation 1.35 is derived for an ultrarelativistic ideal gas, it provides a reliable order-of-magnitude estimate of the energy densities expected in ultrarelativistic heavy-ion collisions. At the LHC and RHIC, the nucleon–nucleon center-of-mass energies are $\sqrt{s_{NN}} \sim 5$ TeV and $\sqrt{s_{NN}} \sim 200$ GeV, respectively, corresponding to beam Lorentz factors $\gamma^{\text{LHC}} \sim 2500$ and $\gamma^{\text{RHIC}} \sim 100$. A rough geometric estimate of the initial energy density can be obtained by approximating the rest energy of the two colliding ions (each with A nucleons of mass m) as $E \simeq 2A mc^2$. Each nucleus is Lorentz-contracted to a slab of thickness $2R/\gamma$ along the beam and has transverse area πR^2 . So the initial volume for two nucleus can be approximated as $V \sim 2(\pi R^2) \cdot (2R/\gamma) = 4\pi R^2(R/\gamma)$. The corresponding energy density within this approximation is

$$\varepsilon_{\text{geom}} \equiv \frac{E}{V} \sim \frac{2A mc^2}{4\pi R^2 (R/\gamma)}. \quad (1.37)$$

Among the inputs, we approximate the mass of a nucleon as 1 GeV ($m_p = 0.938$ GeV, $m_n = 0.939$ GeV). We use a nuclear radius $R \sim 7$ fm for Pb at the LHC and for Au at RHIC.²¹ The energy density of an ideal QGP was estimated using the Stefan–Boltzmann law (shown in Equation 1.35), taking an effective temperature of $T_{\text{QGP}} \sim 0.3$ GeV. Finally, the Table 1.1 presents estimates of the energy densities $\varepsilon_{\text{QGP}}^{\text{ideal}}$, $\varepsilon_{\text{geom}}^{\text{RHIC}}$, and $\varepsilon_{\text{geom}}^{\text{LHC}}$. For comparison of orders of magnitude, the estimated energy density of water $\varepsilon_{\text{water}}$, is also included.

The following hierarchy of energy densities is shown in Table 1.1:

$$\varepsilon_{\text{water}} \ll \varepsilon_{\text{QGP}}^{\text{ideal}} \sim \varepsilon_{\text{geom}}^{\text{RHIC}} < \varepsilon_{\text{geom}}^{\text{LHC}} \quad (1.38)$$

The simple geometric estimate $\varepsilon_{\text{geom}}^{\text{RHIC}}$ is of the same order of magnitude as $\varepsilon_{\text{QGP}}^{\text{ideal}}$, reflecting the extreme initial energy densities in heavy-ion collisions. As expected, the energy density at the LHC is higher than at RHIC ($\varepsilon_{\text{geom}}^{\text{LHC}} > \varepsilon_{\text{geom}}^{\text{RHIC}}$). By contrast, the energy density of water in normal conditions²² is $\sim 10^{20}$ J/m³, many orders of

21. Empirically, nuclear densities are nearly constant across the chart of nuclides, which implies $V = \frac{4}{3}\pi R^3 \propto A$. With the scaling $R \simeq R_0 A^{1/3}$, where $R_0 \simeq 1.2$ fm, one finds for lead and gold ($A_{\text{Pb}} = 208$, $A_{\text{Au}} = 197$): $R_{\text{Pb}} \approx 1.2 \text{ fm} \times 208^{1/3} \approx 7 \text{ fm}$ (LHC), $R_{\text{Au}} \approx 1.2 \text{ fm} \times 197^{1/3} \approx 7 \text{ fm}$ (RHIC).

22. Normal conditions refer to liquid water at standard temperature and pressure: 0°C (273.15 K) and 1 atmosphere (101.325 kPa).

Energy density	GeV/fm ³	J/m ³	Parameters
$\varepsilon_{\text{QGP}}^{\text{ideal}} \sim \frac{\pi^2}{30} g_{\text{eff}} T^4$	$\mathcal{O}(10^1)$	$\mathcal{O}(10^{36})$	$g_{\text{eff}} = 50, T \sim 0.3 \text{ GeV}$
$\varepsilon_{\text{geom}}^{\text{RHIC}} \sim \frac{2A mc^2}{4\pi R^2(R/\gamma)}$	$\mathcal{O}(10^1)$	$\mathcal{O}(10^{36})$	$A = 197, \gamma^{\text{RHIC}} \sim 100$
$\varepsilon_{\text{geom}}^{\text{LHC}} \sim \frac{2A mc^2 \gamma}{4\pi R^2(R/\gamma)}$	$\mathcal{O}(10^2)$	$\mathcal{O}(10^{37})$	$A = 208, \gamma^{\text{LHC}} \sim 2500$
$\varepsilon_{\text{water}} \sim \rho c^2$	$\mathcal{O}(10^{-16})$	$\mathcal{O}(10^{20})$	$\rho = 10^3 \text{ kg/m}^3$

TABLE 1.1 – Order-of-magnitude comparison of energy densities: For an ideal QGP ($\varepsilon_{\text{QGP}}^{\text{ideal}}$), simple geometric estimates (for the LHC and RHIC) based on Lorentz-contracted nuclear overlap ($\varepsilon_{\text{geom}}^{\text{RHIC}}$ and $\varepsilon_{\text{geom}}^{\text{LHC}}$), and water rest-mass energy density ($\varepsilon_{\text{water}}$).

magnitude smaller than the $\sim 10^{36}\text{--}10^{37} \text{ J/m}^3$ characteristic QGP scales.

While the ideal QGP reproduces the correct order of magnitude of the energy density, it fails to capture other measured properties, most notably the viscosity η , which diverges in the non-interacting (ideal QGP) limit, $\eta \rightarrow \infty$. Current experimental signatures of collective behaviour, such as flow measurements, indicate that the QGP is strongly coupled. This necessitates a relativistic viscous hydrodynamic description, where particles strongly interact. In the next chapter, we derive a more general expression for the energy density by contracting the energy–momentum tensor associated to a viscous fluid, and we also present the shear and bulk viscosities, along with the lower bound on the shear-viscosity-to-entropy-density ratio associated with the near-perfect-fluid limit.

1.4.2 Relativistic viscous fluid dynamics

Relativistic hydrodynamics provides a framework for describing strongly coupled systems in local thermodynamic equilibrium, whose pressure and temperature vary in both space and time and which are not globally at rest [77]. To assess the applicability of the relativistic hydrodynamic formalism to an expanding QGP, one typically evaluates a set of dimensionless parameters. More generally, in order to justify the use of fluid dynamics and to characterize the nature of the flow in any physical system, three dimensionless numbers are commonly introduced:

$$\left\{ \begin{array}{l} \text{Knudsen number: } K_n \equiv \frac{\lambda}{R} \Rightarrow K_n \ll 1 \text{ (hydrodynamic limit).} \\ \text{Mach number: } Ma \equiv \frac{v}{c_s} \Rightarrow Ma \ll 1 \text{ (incompressible flow).} \\ \text{Reynolds number: } Re \equiv \frac{Rv}{\eta/\rho} \Rightarrow Re \gg 1 \text{ (inviscid flow).} \end{array} \right. \quad (1.39)$$

Here, λ is the mean free path, R a characteristic system size, v a flow velocity of a given fluid, c_s the speed of sound, η the shear viscosity, and ρ the density. Notice that only if $K_n \ll 1$, the hydrodynamic description is valid²³. For incompressible flow, we have $Ma \ll 1$, meaning density fluid variations negligible. The limit of the Reynolds number, $Re \gg 1$, implies that viscous forces are negligible, corresponding to an inviscid regime, where turbulence takes place. At low values of Re , the flow is typically laminar. Notice that transport theory gives the ratio $\eta/\rho \sim \lambda c_s$, leading to the following compact relation between the three dimensionless numbers:

$$Re \times K_n \sim Ma. \quad (1.40)$$

In heavy-ion collisions, the applicability of hydrodynamics is governed by K_n number, estimated to be $K_n \sim 0.1$ in central Au–Au collisions at RHIC [78]. This small value justifies treating K_n as a perturbative parameter, allowing the particle distribution function $f(x, p)$ to be expanded in powers of K_n :

$$f(x, p) = \underbrace{f_{\text{eq}}^{(0)}}_{\text{Euler term}} + \underbrace{K_n f^{(1)}}_{\text{Navier-Stokes term}} + \underbrace{K_n^2 f^{(2)}}_{\text{Burnett term}} + \dots \implies p^\mu \partial_\mu f = C[f], \quad (1.41)$$

where, $C[f]$ is the collision kernel of the Boltzmann equation²⁴. At zeroth order, one recovers inviscid hydrodynamics. The first-order correction introduces dissipative effects, giving rise to the Navier–Stokes equations. The second-order correction defines the Burnett equations [79]. However, Burnett equations are known to be acausal and unstable in the relativistic regime.

23. $K_n \ll 1$ is a condition for local thermodynamic equilibrium, meaning that the mean free path of a particle between two collisions is much smaller than the characteristic dimension of the system.

24. The Boltzmann equation describes the evolution of the particle distribution function $f(x, p)$ under the combined effect of free streaming, $p^\mu \partial_\mu f$, and interactions, encoded in the collision kernel $C[f]$. The kernel vanishes in local equilibrium, $C[f_{\text{eq}}] = 0$, while out of equilibrium it drives the system back toward equilibrium through scattering processes.

Second-Order Hydrodynamics (Israel-Stewart theory)

To incorporate dissipative effects and respect causality, second-order theories such as the Israel-Stewart framework introduce relaxation-type dynamics for dissipative currents [80]. These modifications render the equations hyperbolic, ensuring causal and stable behavior. In a general viscous fluid, the energy-momentum tensor is written as:

$$T^{\mu\nu} = \varepsilon u^\mu u^\nu - \mathcal{P} \Delta^{\mu\nu} + \pi^{\mu\nu}, \quad (1.42)$$

where, $\Delta^{\mu\nu} = (g^{\mu\nu} - u^\mu u^\nu)$ is the local 3-metric, u^μ denotes here the local flow velocity ($u^\nu u_\nu = 1$). By contracting each term we obtain the following definitions:

$$\varepsilon = u_\mu T^{\mu\nu} u_\nu \quad (\text{energy density}), \quad (1.43)$$

$$\mathcal{P} = (P + \Pi) = -\frac{1}{3} \Delta_{\mu\nu} T^{\mu\nu} \quad (\text{hydrostatic + bulk pressure}), \quad (1.44)$$

where, $\pi^{\mu\nu}$ and Π are the shear and bulk stress tensors, respectively. The energy-momentum tensor $T^{\mu\nu}$ can be split into two parts: an ideal part and a correction due to viscosity (bulk and shear). This decomposition is written as

$$T^{\mu\nu} = T_{\text{ideal}}^{\mu\nu} + \delta T^{\mu\nu} = (\varepsilon \cdot u^\mu u^\nu - P \Delta^{\mu\nu}) + \delta T^{\mu\nu}, \quad (1.45)$$

Here, the correction term $\delta T^{\mu\nu}$ includes viscous effects. The flow velocity u^μ is defined as the time-like eigenvector of the ideal part $T_{\text{ideal}}^{\mu\nu}$. The entropy current is defined as $S^\mu = s \cdot u^\mu$, where s is the scalar entropy density in the local rest frame of the fluid. Multiplying the divergence of the entropy current by the temperature T , we obtain

$$T \partial_\mu S^\mu = u_\nu \partial_\mu T_{\text{ideal}}^{\mu\nu} = -u_\nu \partial_\mu \delta T^{\mu\nu} = \pi^{\mu\nu} \cdot \nabla^{\langle\mu} u^{\nu\rangle} - \Pi \cdot \partial_\mu u^\mu, \quad (1.46)$$

where, the new projection operator is defined as $\nabla^\mu = (g^{\mu\nu} - u^\mu u^\nu) \partial_\nu$. In Equation 1.46, two types of thermodynamic forces appear: $\nabla^{\langle\mu} u^{\nu\rangle}$, related to shear viscosity and $\partial_\mu u^\mu$ related to bulk viscosity. The symmetrized and traceless combination is defined as $\nabla^{\langle\mu} u^{\nu\rangle} \equiv \nabla^\mu u^\nu + \nabla^\nu u^\mu - \frac{2}{3} \Delta^{\mu\nu} \nabla_\alpha u^\alpha$. We consider here a viscous hydrodynamic case with both shear and bulk viscosity, but neglect heat conduction (since $\mu_B \approx 0$). Also, for massless particles, the bulk viscosity can be ignored. The viscous corrections can be modeled as:

$$\pi^{\mu\nu} = 2\eta \cdot \nabla^{\langle\mu} u^{\nu\rangle} \quad (\text{shear stress tensor}), \quad \Pi = -\zeta \cdot \partial_\mu u^\mu \quad (\text{bulk pressure}), \quad (1.47)$$

where, η and ζ are the shear and bulk viscosities, respectively, with the bulk viscosity typically smaller than the shear viscosity. Viscosity reflects the internal friction that resists the relative motion of different fluid layers. In microscopic terms, viscosity quantifies how momentum is transported across the fluid.

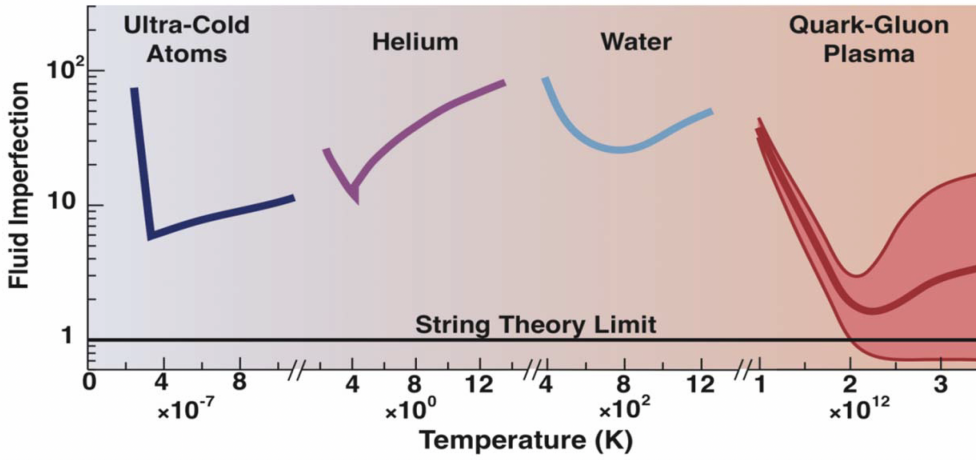


FIGURE 1.17 – Temperature dependence of viscosity for various forms of matter, from common liquids to the quark–gluon plasma (QGP). The curve illustrates how, at extreme temperatures, the QGP exhibits an exceptionally low viscosity, approaching the nearly perfect fluid limit.

Figure taken from [81].

Figure 1.17 shows the temperature dependence of viscosity for ultra-cold atoms, helium, water and the QGP. As temperature increases, the QGP approaches a “nearly perfect fluid” regime, where viscosity is minimal. A simple kinetic-theory can already estimate the shear viscosity of the QGP, using $\eta \sim n \langle p \rangle \lambda$, where n is the particle density, $\langle p \rangle$ the average momentum, and λ the mean free path²⁵. Since $s \sim n \sim T^3$ in a relativistic dilute gas, one finds:

$$\frac{\eta}{s} \sim \langle p \rangle \lambda. \quad (1.48)$$

Invoking the Heisenberg uncertainty principle: $\Delta x \Delta p \geq \frac{\hbar}{2} = \frac{h}{4\pi}$, and identifying²⁶

25. The mean free path λ is the average distance a particle travels before undergoing a collision. In the absence of interactions, $\lambda \rightarrow \infty$, which implies that the shear viscosity also diverges, $\eta \rightarrow \infty$.

26. This identification is heuristic, since $\langle p \rangle$ and λ are not strictly conjugate variables, but the

$\Delta x \sim \lambda$ and $\Delta p \sim \langle p \rangle$, using natural units, one obtains $\langle p \rangle \lambda \sim \frac{1}{4\pi}$. Using Eq. 1.48, we can finally write [82]:

$$\frac{\eta}{s} \sim \frac{1}{4\pi}. \quad (1.49)$$

A more refined AdS/CFT²⁷ calculation [83], applied to strongly coupled supersymmetric Yang–Mills theories, has also found $\frac{\eta}{s} = \frac{1}{4\pi}$, which has been conjectured as a universal lower bound for conformal gauge theories. Heavy-ion collision experiments suggest that the ratio η/s (shear viscosity over entropy density) [84] lies in the range

$$\frac{\eta}{s} \approx 0.08 - 0.20. \quad (1.50)$$

Surprisingly, these values are quite close to the AdS/CFT estimation, indicating that the QGP may be the most perfect fluid ever observed in nature. Several hydrodynamic aspects of a QGP have been studied in detail using both weak and strongly coupled fluid approaches. Weak coupling approaches rely on perturbative methods and kinetic theory [85], while strong coupling approaches employ non-perturbative techniques [27]. Nevertheless, it is important to note that $\eta/s \sim 0.20$ does not necessarily indicate genuine non-perturbative effects, recent results [86] suggest that it may rather be understood within resummation-improved perturbative QCD.

1.5 Collective behaviour in heavy-ion collisions

Signs of collectivity in heavy-ion collisions first emerged in the light hadron sector at RHIC. Early measurements [87] revealed substantially stronger thermalization than at lower energies, and multiple observables exhibited flow-like motion of the produced matter. By 2005, the QGP was characterized as a nearly “perfect” fluid with very low viscosity. Higher-energy measurements at the LHC later reinforced this fluid picture, confirming collective dynamics in an even hotter QGP.

In this chapter, we present the dynamics of longitudinal and transverse expansion [78] in heavy-ion collisions, including sound wave propagation and the first measurement of the speed of sound in QGP. We also introduce the major areas of

argument captures the correct scale.

27. A conformal field theory (CFT) is a quantum field theory invariant under conformal transformations, and therefore possesses no intrinsic mass scale. In contrast, QCD is not conformally invariant, since the theory is characterized by the dynamical scale Λ_{QCD} . Nevertheless, the mathematical representation of the conformal group in a five-dimensional anti-de Sitter (AdS) space can be used to construct a useful first approximation to the theory.

study within this framework: the initial spatial anisotropies, radial flow, and final anisotropic flow, as well as the principal experimental techniques used to extract flow signals, with careful treatment of non-flow contributions. In addition, we provide a detailed discussion of event-by-event fluctuations and present results in the light-quark sector in both light- and heavy-ion collisions.

1.5.1 Expansion dynamics toward equilibrium

The early evolution of ultra-relativistic heavy-ion collisions is governed by the dynamics of an out-of-equilibrium system characterized by strong anisotropies in momentum space [88]. This evolution is well described by relativistic hydrodynamics [78]. The thermalization process has been extensively studied. In particular, the energy-momentum tensor displays a marked imbalance between the longitudinal pressure P_L , aligned with the beam axis, and the transverse pressure P_T , which governs expansion in the transverse plane:

$$P_L = \int \frac{p_z^2}{p^0} f(p) d^3p, \quad P_T = \frac{1}{2} \int \frac{p_x^2 + p_y^2}{p^0} f(p) d^3p. \quad (1.51)$$

Here, $f(p)$ denotes the one-particle distribution function, p^0 is the energy of a particle, and p_x, p_y, p_z are the components of the momentum vector. In Figure 1.18, the pressure anisotropy reflects the far-from-equilibrium nature of the system immediately after the collision, where $P_L \ll P_T$.

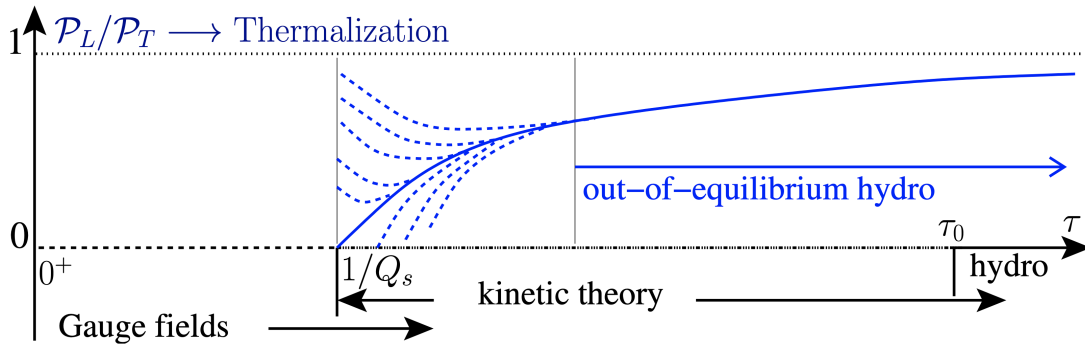


FIGURE 1.18 – Time evolution of the pressure anisotropy P_L/P_T in a heavy-ion collision. Isotropization occurs as the system approaches local equilibrium. Figure taken from [89].

During this early stage, longitudinal expansion is suppressed while transverse expansion dominates [89]. The transition to a hydrodynamic regime (known as

hydrodynamization) corresponds to the restoration of pressure isotropy, typically reached within a time scale $\tau \sim 1 \text{ fm}/c$, as momentum is redistributed through interactions. The evolution of the distribution function toward equilibrium is described in the relaxation-time approximation by the Bjorken equation:

$$\left[\frac{\partial}{\partial \tau} - \frac{p_z}{\tau} \frac{\partial}{\partial p_z} \right] f(p, \tau) = -\frac{f - f_{\text{eq}}}{\tau_R}, \quad (1.52)$$

where f_{eq} is the local equilibrium distribution and τ_R the relaxation time. This formalism describes how a free-streaming distribution evolves under collisions towards local equilibrium, bridging the collisionless initial stage with the hydrodynamic regime.

Pressure gradients and sound waves in the QGP

When pressure becomes isotropic in a heavy-ion collision ($P_L = P_T$), the system can be considered approximately in thermodynamic equilibrium. In this regime, the pressure is related to the energy density via the equation of state, as shown in equation 1.36 (in the ideal inviscid case). More generally, the velocity of sound c_s can be defined as

$$c_s = \left(\frac{\partial P}{\partial \epsilon} \right)^{1/2}, \quad (1.53)$$

which characterizes the response of the medium to compressional disturbances [78]. The square of the sound velocity, c_s^2 , is inversely proportional to the compressibility of the fluid [90]. To study the propagation of small perturbations (sound waves) in a uniform background, one introduces fluctuations around equilibrium values:

$$\epsilon = \epsilon_0 + \delta\epsilon, \quad P = P_0 + \delta P, \quad (1.54)$$

where ϵ_0 and P_0 are the equilibrium energy density and pressure, and $\delta\epsilon$, δP are small perturbations. Linearizing the energy-momentum conservation equations for an ideal (inviscid) fluid to first order in $\delta\epsilon$, δP , and the fluid velocity \mathbf{v} , yields:

$$\frac{\partial \delta\epsilon}{\partial t} + (\epsilon_0 + P_0) \nabla \cdot \mathbf{v} = 0, \quad (\epsilon_0 + P_0) \frac{\partial \mathbf{v}}{\partial t} + \nabla \delta P = 0. \quad (1.55)$$

The first equation expresses local energy conservation: an increase in volume leads to a decrease in energy density. The second equation links fluid acceleration to

pressure gradients²⁸. Using the thermodynamic relation $\delta P = c_s^2 \delta \epsilon$, these equations can be combined into a wave equation for energy density fluctuations:

$$\frac{\partial^2 \delta \epsilon}{\partial t^2} - c_s^2 \Delta \delta \epsilon = 0, \quad (1.56)$$

which governs the propagation of sound waves in a relativistic, non-dissipative medium [78]. Experimentally the speed of sound c_s in the QGP produced in a heavy-ion collision can be determined in the followed way [29]:

$$c_s^2(T_{\text{eff}}) \equiv \frac{dP}{d\epsilon} = \frac{d \ln \langle p_t \rangle}{d \ln \left(\frac{dN_{\text{ch}}}{d\eta} \right)}, \quad (1.57)$$

where, T_{eff} is the effective temperature, $\langle p_t \rangle$ is the average transverse momentum, and $\frac{dN_{\text{ch}}}{d\eta}$ is the charged particle multiplicity. In 2024, $c_s(T_{\text{eff}})$ was measured by the CMS and ALICE collaborations at the LHC [91, 92]. Both measurements were performed by studying the multiplicity dependence of the average transverse momentum of charged particles emitted in head-on Pb-Pb collisions.

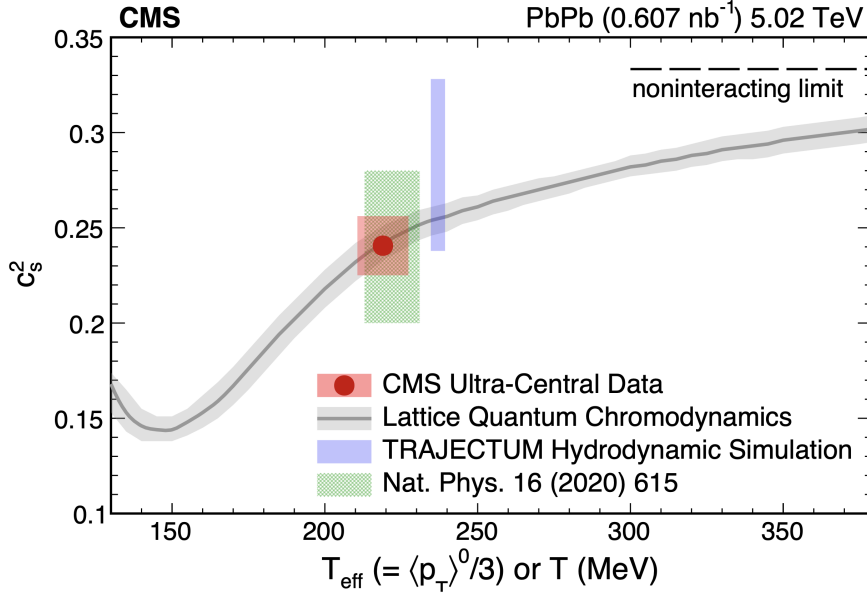


FIGURE 1.19 – c_s^2 as a function of T_{eff} , with the CMS data point obtained from ultra-central Pb-Pb collisions compared with hydrodynamic simulations and lattice QCD predictions [91].

In Figure 1.19, the squared speed of sound c_s^2 is shown as a function of the ef-

28. The covariant expression for the acceleration of a fluid element, analogous to equation 1.55, is $\partial_t u^\mu = \frac{\nabla^\mu P}{\epsilon + P}$, where u^μ is the fluid's four-velocity and ∇^μ is the spatial gradient.

fective temperature T_{eff} . The red point is the first measurement of c_s^2 in ultra-central Pb-Pb collisions at $\sqrt{s_{NN}} = 5.02$ TeV from CMS, indicating that the speed of sound in this matter is nearly half the speed of light (in natural units). Colored boxes give values from the TRAJECTUM hydrodynamic simulation [93] and from earlier work [29], obtained using the same extraction method as for the data. The solid curve shows the lattice QCD prediction [94], while the dashed line at $1/3$ marks the ideal gas limit²⁹ for a noninteracting, massless system (as discussed in section 1.4.1). The CMS measurement lies well below this limit and agrees, within uncertainties, with both lattice QCD and realistic hydrodynamic simulations, consistent with the expected properties of strongly coupled QGP. The CMS collaboration reported the following value for the squared speed of sound:

$$c_s^2 = 0.241 \pm 0.002_{\text{(stat)}} \pm 0.016_{\text{(syst)}}, \quad (\text{natural units}). \quad (1.58)$$

Nevertheless, the ALICE Collaboration has reported that the extracted value of the squared speed of sound, strongly depends on the type of centrality estimator used to select the events [92]. The different measurements of c_s^2 reported by the ALICE collaboration are ranging between the following values:

$$c_s^2 = \begin{cases} 0.113 \pm 0.003_{\text{(stat)}} \pm 0.007_{\text{(syst)}}, \\ 0.438 \pm 0.001_{\text{(stat)}} \pm 0.019_{\text{(syst)}}. \end{cases} \quad (\text{natural units}). \quad (1.59)$$

1.5.2 Radial flow

In ultra-relativistic heavy-ion collisions, the expansion of the medium leads to characteristic patterns in the momentum distribution of emitted particles [95]. Radial flow refers to the collective outward motion of particles from the fireball, characterized by a velocity field that is isotropic (often modeled with spherical symmetry). This type of expansion significantly modifies the particle momentum spectra, particularly at low transverse momentum. Measurements by the ALICE Collaboration of the radial flow of charged particle production have revealed a clear mass ordering spectra for different hadron species [96].

A commonly used phenomenological description is the blast-wave model [97],

²⁹. In the ultrarelativistic limit, using the equation of state in Equation 1.35 together with the definition of the sound speed shown in Equation 1.53, one obtains $c_s^2 = \frac{\partial}{\partial \epsilon} \left(\frac{\epsilon}{3} \right) = \frac{1}{3}$.

which assumes a collective transverse velocity profile at the kinetic freeze-out stage. The resulting transverse momentum distribution takes the form:

$$\frac{1}{p_T} \frac{dN}{dp_T} \propto \exp \left(-\frac{\sqrt{p_T^2 + m^2}}{T_{\text{eff}}} \right), \quad T_{\text{eff}} = T_{\text{fo}} + m \langle \beta_T \rangle^2, \quad (1.60)$$

where, T_{fo} is the freeze-out temperature and $\langle \beta_T \rangle$ denotes the average transverse flow velocity. The mass dependence of the effective temperature T_{eff} provides a clear signature of the collective nature of the expansion.

1.5.3 Eccentricity and anisotropic flow

The QGP is an extremely dense and hot medium that behaves almost as a perfect fluid with the lowest shear-viscosity to entropy density ratio ever estimated [84]. This collective behavior exhibited during the hydrodynamic expansion can be explored through the analysis of azimuthal anisotropies of the emitted particles. In HIC, the anisotropic flow is a response of the medium to the initial spatial coordinate anisotropy [98].

Initial eccentricity

The initial spatial anisotropies of the fireball are quantified with the eccentricity ε_n , which encodes the geometry of the overlap zone of the colliding nuclei (see Figure 1.21). In the transverse plane of the collision, we adopt polar coordinates (r, ϕ) , where r denotes the radial distance ($r^2 = x^2 + y^2$) and ϕ the azimuthal angle. Let $\rho(r, \phi)$ denote the initial energy-density profile in the transverse plane, being 2π -periodic in ϕ , it can be written as a Fourier expansion:

$$\rho(r, \phi) = \rho_0(r) \left[1 + 2 \sum_{n=1}^{\infty} a_n(r) \cos(n[\phi - \Psi_n]) \right], \quad (1.61)$$

where, Ψ_n denotes the symmetry plane angle, different than the reaction plane angle³⁰. The $\rho_0(r)$ coefficient denotes the azimuthally averaged profile, and $a_n(r)$ are the Fourier harmonic coefficients characterizing the anisotropies of the initial

30. The symmetry plane ψ_n is the azimuthal angle that characterizes the orientation of the n -th order eccentricity ε_n . In contrast, the reaction plane ψ_{RP} is defined by the beam axis and the impact parameter vector.

state. The eccentricity vector $\vec{\varepsilon} \equiv \varepsilon_n e^{in\Psi_n}$ can then be written in terms of these Fourier coefficients: [99, 100]:

$$\vec{\varepsilon} = -\frac{\langle r^n e^{in\phi} \rangle}{\langle r^n \rangle}, \quad \text{with} \quad \langle r^n \rangle \equiv \frac{\int r dr d\phi r^n \rho(r, \phi)}{\int r dr d\phi \rho(r, \phi)}. \quad (1.62)$$

Here, the brackets $\langle \cdot \rangle$ denote density-weighted averages over the transverse plane. Decomposing the complex eccentricity into its real (reaction-plane) and imaginary (out-of-plane) parts, we define for the second harmonic the following complex vector:

$$\vec{\varepsilon}_2 = \varepsilon_x + i \varepsilon_y. \quad (1.63)$$

The participant eccentricity (or elliptic eccentricity) $\vec{\varepsilon}_2$ is directly related to the almond-shaped overlap region in non-central collisions.

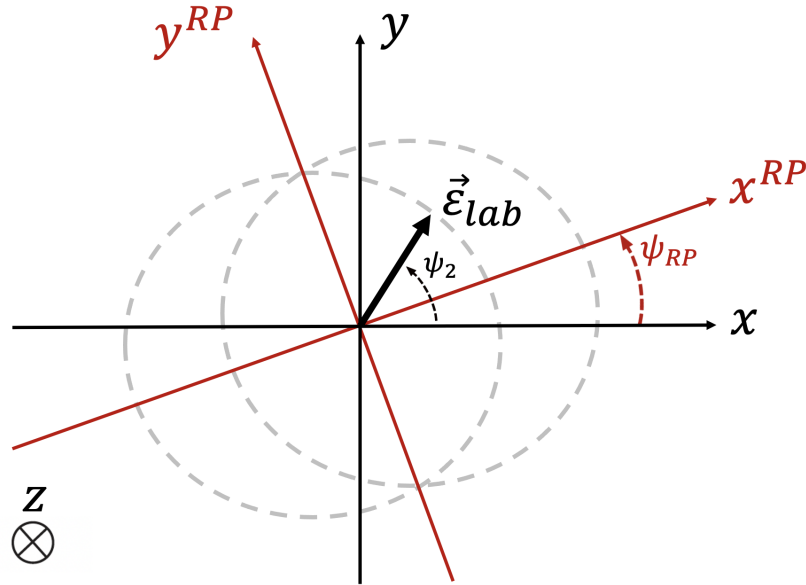


FIGURE 1.20 – Schematic representation of the eccentricity $\vec{\varepsilon}_{Lab} \equiv \varepsilon_2$ in the transverse plane. The black axes denote the laboratory coordinates (x, y) , while the red axes (x^{RP}, y^{RP}) are rotated by the reaction-plane angle ψ_{RP} . The magnitude of ε_2 quantifies the spatial anisotropy of the overlap region. The beam direction z is oriented perpendicular to the transverse plane.

In the (x, y) coordinates of the laboratory, the eccentricity will be denoted $\vec{\varepsilon}_{lab}$ and defined as:

$$\vec{\epsilon}_{lab} \equiv (\epsilon_{RP}, \epsilon_y) \longrightarrow \epsilon_{RP} = \frac{\langle y^2 \rangle - \langle x^2 \rangle}{\langle x^2 \rangle + \langle y^2 \rangle}, \quad \epsilon_y = \frac{2\langle xy \rangle}{\langle x^2 \rangle + \langle y^2 \rangle} \quad (1.64)$$

with the participant angle $\psi_2 = \frac{1}{2}\text{atan2}(\epsilon_y, \epsilon_{RP})$, defining the orientation of eccentricity vector (or participant vector) $\vec{\epsilon}_{lab} \equiv \vec{\epsilon}_2$, as illustrated in Figure 1.20. Note that in the case of a initial symmetric density profile, such that $\rho(r, \phi) = \rho(r, -\phi)$, Equation 1.62 leads to $\epsilon_y = 0$. Consequently, one finds ψ_2 is aligned with the reaction plane $\psi_{RP} = \psi_2 = 0$ or equivalently $(x, y) = (x^{RP}, y^{RP})$. Then, the eccentricity reduces to

$$\epsilon_{lab} = \epsilon_{RP}. \quad (1.65)$$

However, this alignment is broken ($\psi_{RP} \neq \psi_2$) once event-by-event fluctuations are taken into account. In section 1.5.5, we present in detail 1D and 2D Gaussian eccentricity fluctuations.

Anisotropic flow

As the medium undergoes hydrodynamic expansion, the initial spatial anisotropy, quantified by the eccentricity ϵ_n , transforms into momentum space anisotropies, as shown in Figure 1.21.

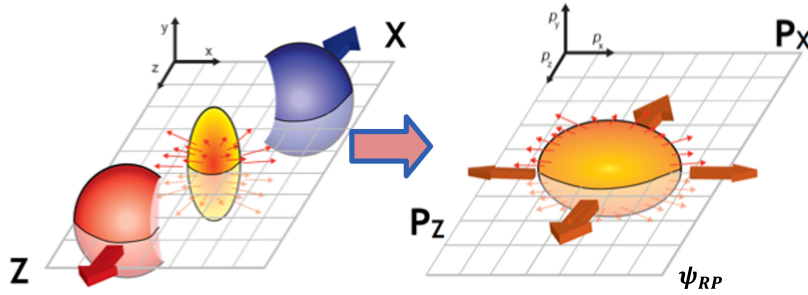


FIGURE 1.21 – Schema of the expansion of the QGP in a heavy-ion collision [101].

This transformation manifests as an azimuthal dependence in the distribution of particles relative to the reaction plane. Anisotropic flow is highly sensitive to the underlying properties of the system during its early stages of evolution. Due to the periodicity in the azimuthal angle ϕ , a Fourier expansion series [98] can be used to

describe the final azimuthal particle distribution:

$$\frac{dN}{d\phi} = 1 + 2 \sum_{n=1}^{\infty} v_n \cos[n(\phi - \psi_n)]. \quad (1.66)$$

Here, anisotropic flow is described by coefficients v_n of the Fourier series, where n is the harmonic number. It is defined as:

$$v_n = \langle \cos[n(\phi - \psi_n)] \rangle. \quad (1.67)$$

where, ψ_n is the symmetry plane (or event plane) [102] defined in Equation 1.62 and the brackets $\langle \dots \rangle$ denote an average over all particles of a given event. The v_1 coefficient is known as directed flow, v_2 as elliptic flow, while higher-order coefficients such as v_3 (triangular flow) and beyond describe more complex azimuthal anisotropies.

Notice that the density profile ρ , given by Equation 1.61, follows the same mathematical structure as $\frac{dN}{d\phi}$, presented in Equation 1.66. Because the measured particle distribution is periodic in the azimuthal angle ϕ , defined relative to the reaction plane ψ_{RP} , it is natural to represent $\frac{dN}{d\phi}$ as a Fourier expansion. Note that the initial eccentricity is converted into the final anisotropic flow v_n , with a nearly linear relation for lower harmonics ($n = 2, 3$), as given by

$$v_n = \kappa_n \epsilon_n, \quad (1.68)$$

where κ_n characterizes the system's response. Figure 1.22 illustrates the different shapes associated with different harmonics of ϵ_n .

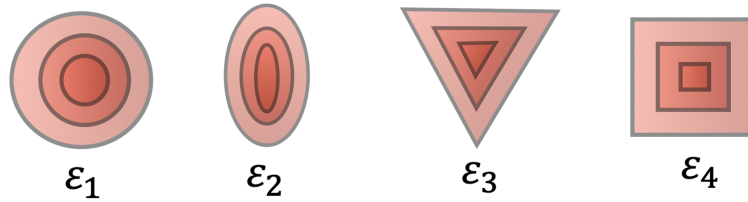


FIGURE 1.22 – Illustration of forces arising from pressure gradients associated with eccentricities ϵ_n across harmonics ($n = 1, 2, 3$ and 4). These patterns are also reflected in the anisotropic flow coefficients v_n .

The v_n coefficients are dependent on p_T and y [95]. Flow coefficients can be measured in AA collisions (like Pb-Pb) but also in smaller collision systems such as pA and pp collisions. Notice that Pb-Pb collisions are particularly advantageous due

to the spherical shape of the lead nuclei³¹, stemming from their unique structure as a doubly magic nucleus ($Z=82$, $N=126$). This sphericity allows for a more accurate parametrization of the initial geometry and facilitates precise modeling of the initial state.

1.5.4 Experimental methods to extract flow

In this section, we outline different experimental methods that can be used to determine flow coefficients. For a given harmonic order n , the Q -vector is constructed by summing over the complex unit vectors of all particles of a given event:

$$Q_n = \sum_{i=1}^N e^{in\phi_i}, \quad (1.69)$$

where ϕ_i is the azimuthal angle of the i -th particle and N represents the total number of charged particles in the event. In general, two different flow vectors are computed, the event flow vector for inclusive charged particles: $Q_n = Q_n^x + iQ_n^y$ and the particle of interest (POI) flow Q -vector: $p_n = p_n^x + ip_n^y$.

Event-plane method

The Event-Plane (EP) method [103] determines the azimuthal symmetry plane by estimating its angle from the Q -vectors. The n -th order event-plane angle is obtained as:

$$\psi_n = \frac{1}{n} \arctan \left(\frac{Q_n^y}{Q_n^x} \right). \quad (1.70)$$

The associated POI flow coefficient is then evaluated via:

$$v_n^{POI}\{\text{EP}\} = \left\langle \frac{\cos [n(\phi^{POI} - \psi_n^A)]}{R_n^{\text{EP}}} \right\rangle, \quad (1.71)$$

where ϕ^{POI} is the azimuthal angle of the POI, ψ_n^A is the plane angle for the detector A, $\langle \dots \rangle$ denotes averaging over all particles in all events and R_n^{EP} denotes the event-plane resolution, given by:

31. At ultra-relativistic energies, Lorentz contraction strongly distorts the nuclei in the beam direction, leading to a pancake-like shape.

$$R_n^{\text{EP}} = \sqrt{\frac{\langle \cos [n(\psi_n^{\text{A}} - \psi_n^{\text{C}})] \rangle \langle \cos [n(\psi_n^{\text{A}} - \psi_n^{\text{B}})] \rangle}{\langle \cos [n(\psi_n^{\text{B}} - \psi_n^{\text{C}})] \rangle}}. \quad (1.72)$$

Here, the symbols B and C correspond to two additional detectors with non-overlapping pseudorapidity coverage. This η -gap requirements ensures the suppression of non-flow effects (correlations produced by jets, di-jets or even resonance decay).

Scalar-product method

The Scalar-Product (SP) method [104, 105] expresses the POI flow coefficients as:

$$v_n^{\text{POI}}\{\text{SP}\} = \left\langle \frac{p_n Q_n^{\text{A}*}}{R_n^{\text{SP}}} \right\rangle, \quad (1.73)$$

this time, the normalization factor R_n^{SP} , which accounts for the event-flow component, is defined as:

$$R_n^{\text{SP}} = \sqrt{\frac{\langle Q_n^{\text{A}} Q_n^{\text{B}*} \rangle \langle Q_n^{\text{A}} Q_n^{\text{C}*} \rangle}{\langle Q_n^{\text{B}} Q_n^{\text{C}*} \rangle}}. \quad (1.74)$$

The notation Q_n^{A} , Q_n^{B} , and Q_n^{C} is consistent with the EP method definitions described above.

Both the EP and SP methods rely on similar underlying computational procedures to extract flow coefficients from the Q-vectors using different detectors, and by consequence suppressing non-flow effects. The EP technique introduce a slight experimental bias due to limitations in determination of the resolution factor R_n^{EP} [106]. In the limit of perfect resolution: $R_n^{\text{EP}} \sim 1$ and the event-plane measurement recovers the mean value of v_n . In contrast, in the limit of poor resolution, $R_n^{\text{EP}} \sim v_n$, the event-plane measurement yields the root-mean-square value of v_n . These two cases can be summarized as

$$\begin{cases} v_n\{\text{EP}\} \xrightarrow{\text{EP high res.}} \langle v_n \rangle, \\ v_n\{\text{EP}\} \xrightarrow{\text{EP low res.}} \sqrt{\langle v_n^2 \rangle}. \end{cases} \quad (1.75)$$

The difference between the two limits ranges from 6% to 13% has shown in Reference [106]. Assuming the absence of flow fluctuations³², the measured elliptic flow

³². This assumption may not hold in practice, as event-by-event fluctuations might not be negligible. Considering Gaussian flow fluctuations, Equation 1.76 is not valid anymore.

coefficient from the SP method is:

$$v_n\{SP\} = \langle v_n \rangle, \quad \text{Without flow fluctuations.} \quad (1.76)$$

Lee-Yang zeroes method

The corresponding estimate of v_n using the Lee-Yang zeroes (LYZ) method [107] can be defined as

$$v_n^{POI}\{LYZ\} \equiv \left\langle W_R \cos \left[n \left(\phi^{POI} - \phi_n^A \right) \right] \right\rangle, \quad (1.77)$$

where ϕ_n^A is the same event-plane angle as in Eq. 1.71, and W_R is an event weight factor that depends on the length of the flow vector Q , defined in [108]. The advantage of the LYZ method, over the standards SP and EP methods is that autocorrelations and non-flow effects are automatically suppressed. This makes the method particularly suitable for precision flow measurements, as it reduces bias from all type of short-range correlations.

Cumulant method

Similarly to the LYZ method, another well-known approach suppressing non-flow effects is the multi-particle cumulant technique [95, 109], which involves azimuthal correlations among observed particles. The simplest approach to compute v_n of inclusive charged particles in this method is through the two-particle correlator, defined as $\langle \cos n(\phi_1 - \phi_2) \rangle$, where ϕ_1 and ϕ_2 are the azimuthal angles of two charged particles in the same event and the brackets denote an average over all particle pairs across all events. Notice that for the cumulant method, even if we assume the absence of flow fluctuations (see Section 1.5.5), a shift δ_2 (representing non-flow effects) arises from correlations unrelated to the initial system's geometry. Therefore, $v_2\{2\}$ can be written as:

$$v_2\{2\}^2 = \langle \cos[n(\phi_1 - \phi_2)] \rangle = \langle v_n^2 + \delta_2 \rangle. \quad (1.78)$$

In two-particle correlations, $\delta_2 \propto \frac{1}{M}$, where M represents the multiplicity. To mitigate non-flow effects, we can employ multi-particle correlations. For example, if we consider 4-particle correlations, the following average needs to be evaluated: $\langle \cos[n(\phi_1 + \phi_2 - \phi_3 - \phi_4)] \rangle$. In the study of collectivity, cumulants are frequently

computed to extract genuine multi-particle correlations, achieved by subtracting internal (lower-order) correlation contributions from the total correlation. The n th cumulant graphically can be represented as a *connected cluster* of n points (as shown in Figure 1.23). The m th moment is then obtained by summing all possible subdivisions of m points into groupings of smaller (connected or disconnected) clusters. The 4-particle cumulant³³ for inclusive charged particles is denoted as $c_2\{4\}$ and it can be written in the following way [102]:

$$\begin{aligned} c_n(4) &= \langle \cos[n(\phi_1 + \phi_2 - \phi_3 - \phi_4)] \rangle \\ &\quad - \langle \cos n(\phi_1 - \phi_3) \rangle \langle \cos n(\phi_2 - \phi_4) \rangle \\ &\quad - \langle \cos n(\phi_1 - \phi_4) \rangle \langle \cos n(\phi_2 - \phi_3) \rangle = -v_2\{4\}^4 \end{aligned} \quad (1.79)$$

Similarly to equation 1.78, this quantity is equivalent to $c_n(4) = \langle v_n^4 + \delta_4 \rangle$, where the non-flow component scales as $\delta_4 \propto \frac{1}{M^3}$ and consequently the non-flow component is more suppressed than in 2-particle correlations.

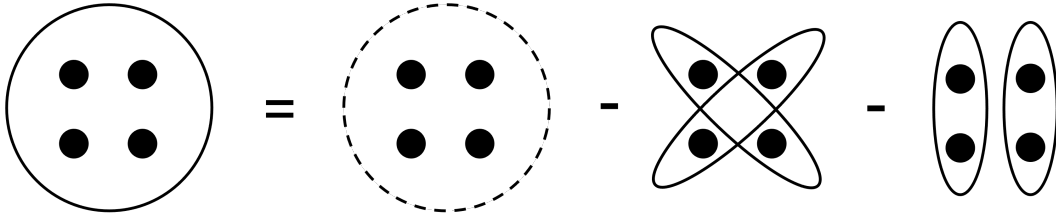


FIGURE 1.23 – Schematic of the 4-particle cumulant construction (defined in Equation 1.79). The leftmost diagram (solid circle) represents the connected 4-particle cumulant, isolating genuine collective behavior. The middle positive term (dashed circle) corresponds to the full 4-particle correlation, which includes both collective and non-collective contributions. The rightmost terms, involving 2-particle correlations, are subtracted to remove contributions from lower-order (pairwise) correlations.

1.5.5 Gaussian models for flow fluctuations

Understanding the role of flow fluctuations is essential for disentangling the different contributions to azimuthal anisotropy measurements in heavy-ion collisions.

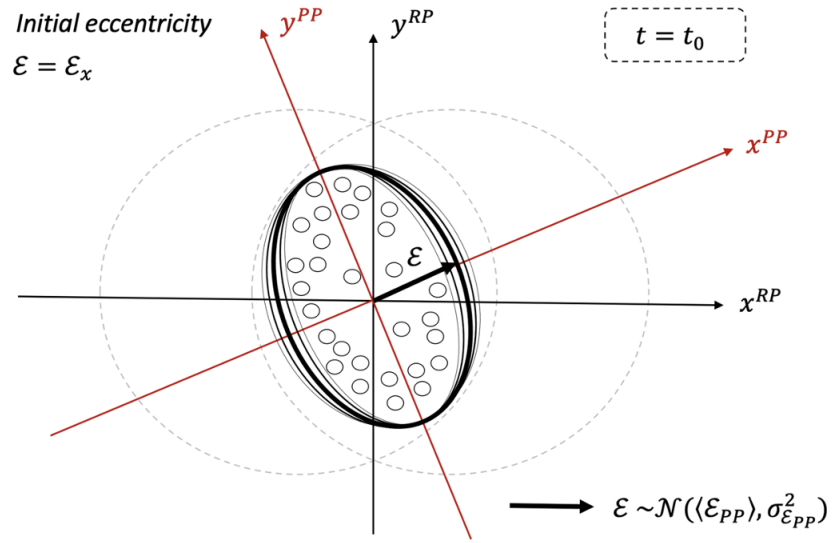
³³ A detailed procedure for calculating cumulants for the particles of interest (POI) is provided in the chapter 4 of this thesis.

In this section, we present in detail two modeling approaches, one-dimensional (1D) and two-dimensional (2D), that address Gaussian eccentricity and flow fluctuations. Within these frameworks, we derive expressions for multi-particle cumulants and the corresponding fluctuation ratios, providing a consistent treatment of event-by-event fluctuations for each observable. Finally, we present fluctuation ratio results for POI strange hadrons measured by CMS and compare them with theoretical model predictions.

1D Gaussian fluctuations in the Participant Plane (PP) coordinate system

In the standard optical Glauber definition, the eccentricity is calculated event-averaged at fixed impact parameter [110], using $\varepsilon = \varepsilon_{RP}$ (defined in Equation 1.65), where all events are assumed to share the same geometry. Miller and Snellins were the first to quantify these fluctuations with Monte Carlo Glauber (MCG) simulations [110]. Similarly, the flow fluctuations can be expressed in terms of $v_2\{2\}$ and $v_2\{4\}$ under the assumption of one-dimensional (1D) Gaussian eccentricity fluctuations [111]. To clarify their connection to the initial geometry, we introduce the concept of the participant zone, which is the overlapping region of the two colliding nuclei, and its geometry fluctuates from event to event. From this region one defines the participant plane (PP) coordinate system, presented in Figure 1.24 as a rotation of the reaction plane (RP) coordinates around the beam (z) axis. In the PP coordinate space, the x_{PP} axis is aligned with the semi-minor axis of the participant zone by definition, as illustrated in Figure 1.24(a). Consequently, in the corresponding PP phase space, v_2 aligns along the p_x^{PP} direction, as shown in Figure 1.24(b). Because of this x-alignment requirements in the PP frame, eccentricity fluctuations in the y^{PP} direction can be neglected³⁴, as no flow component is expected along p_y^{PP} . Therefore, the Gaussian fluctuations can effectively be reduced to a 1D problem in the PP frame.

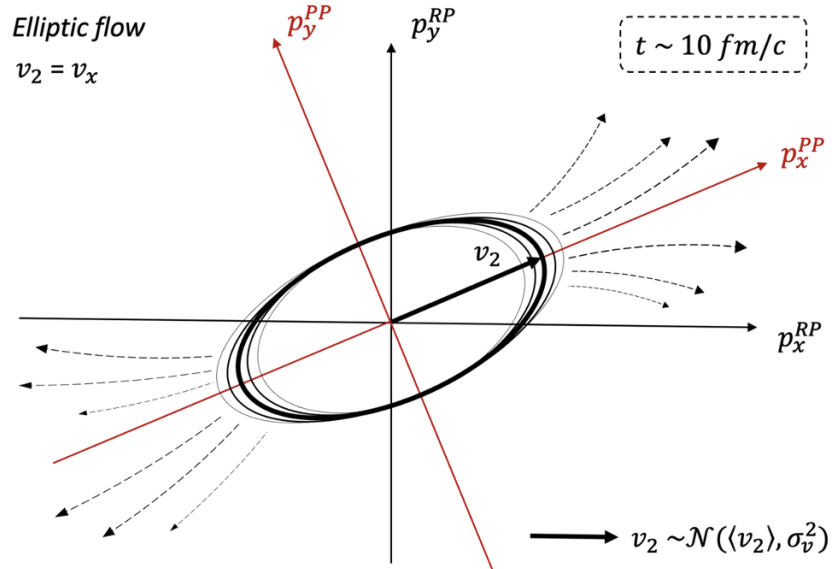
34. This approximation may be too idealistic. Even though v_2 aligns by definition with p_x^{PP} , there is no fundamental reason to exclude eccentricity fluctuations in the y^{PP} direction. Fluctuations arising from the discrete nucleon positions, from nPDF effects, or even from other unknown sources could a priori generate a finite contribution in this direction.



1D eccentricity fluctuations in the PP coordinate system

(A) Initial overlap of two heavy-ions in a peripheral collision (dashed lines). The eccentricity ε vector is aligned with x^{PP} .

1D eccentricity fluctuations in the PP coordinate system



1D flow fluctuations in the PP momentum coordinates

(B) Flow response in final detected particles (dashed arrows). The flow vector v_2 is aligned with p_x^{PP} .

FIGURE 1.24 – Illustration of the initial eccentricity and its anisotropy response in the participant-plane (PP) coordinate system. The ellipses indicate eccentricity (A) and flow (B) fluctuations.

Within this approximation, the eccentricity ε follows a normal distribution, characterized by the mean eccentricity $\langle \varepsilon_{PP} \rangle$ relative to the PP³⁵ and the variance $\sigma_{\varepsilon_{PP}}^2$:

$$\mathcal{N}(\varepsilon; \langle \varepsilon_{PP} \rangle, \sigma_{\varepsilon_{PP}}^2) = \frac{1}{\sqrt{2\pi\sigma_{\varepsilon_{PP}}^2}} \exp \left[-\frac{(\varepsilon - \langle \varepsilon_{PP} \rangle)^2}{2\sigma_{\varepsilon_{PP}}^2} \right]. \quad (1.80)$$

In Figure 1.24, the main idea of the PP frame is illustrated: the flow is aligned with p_x^{PP} , $v_2 = v_x$ and consequently, flow fluctuations occur exclusively along the p_x^{PP} -direction in this model. Similarly to Equation 1.80, in this 1D Gaussian model, the flow coefficient also follows a normal distribution $v_2 \sim \mathcal{N}(\langle v_2 \rangle, \sigma_v^2)$, where $\langle v_2 \rangle$ is the mean elliptic flow with respect to the PP and σ_v represents the flow fluctuation width.

However, MCG results revealed that at fixed impact parameter, the actual eccentricity fluctuates because the number of participants, their transverse positions and their energy deposition per collision fluctuates [112]. It was later recognized that the eccentricity/flow fluctuations not only change the eccentricity/flow magnitude but also rotate the major axis of the overlap ellipse and shift its centroid [113].

2D Bessel-Gaussian fluctuations in the Event Plane (EP) coordinate system

For small systems or small transverse overlap regions, fluctuations in the nucleon positions frequently create a situation where the minor axis of the participant ellipse in the transverse plane formed by the participating nucleons is not along the impact parameter vector [113], as illustrated in Figure 1.25(a). One way to address this issue is to make an axis transformation, rotating the x and y axes used in the eccentricity definition in the transverse plane in such a way that participant width σ_x is minimized (re-centering). We introduce the covariance matrix elements of the nucleon positions in the transverse plane:

$$\sigma_x^2 = \langle x^2 \rangle - \langle x \rangle^2, \quad \sigma_y^2 = \langle y^2 \rangle - \langle y \rangle^2, \quad \sigma_{xy} = \langle xy \rangle - \langle x \rangle \langle y \rangle. \quad (1.81)$$

Here σ_x and σ_y represent the root-mean-square (RMS) widths of the participant distribution projected along the x and y axes, respectively, while σ_{xy} encodes the

35. The true geometric orientation of the collision is RP, defined by the impact parameter vector and the beam axis. In contrast, the PP is determined on an event-by-event basis from the principal axes of the participant zone, and therefore fluctuates around the RP due to the finite number of nucleons.

correlation between the two directions. These quantities form the basis for defining the participant-plane eccentricity and its orientation. Re-centering a given laboratory eccentricity vector $\vec{\varepsilon}_{\text{lab}}$ (defined in Equation ³⁶ 1.64), we can write

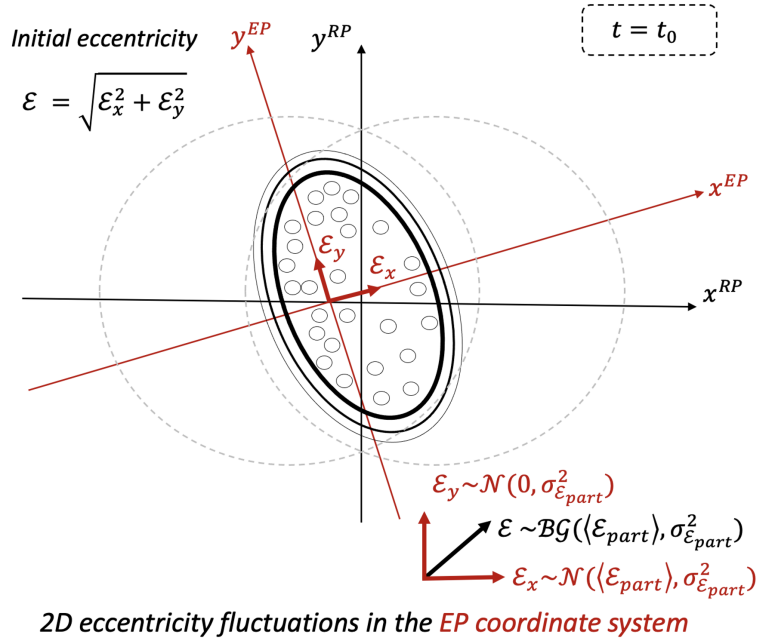
$$\begin{aligned} \vec{\varepsilon}_{\text{lab}} &= \left(\varepsilon_x = \frac{\langle y^2 \rangle - \langle x^2 \rangle}{\langle x^2 \rangle + \langle y^2 \rangle}, \frac{2(\langle xy \rangle - \langle x \rangle \langle y \rangle)}{\langle x^2 \rangle + \langle y^2 \rangle} \right), \\ &\quad \downarrow \text{re-centering} \\ \vec{\varepsilon}_{\text{part}} &= \left(\underbrace{\left\langle \frac{\sigma_y^2 - \sigma_x^2}{\sigma_x^2 + \sigma_y^2} \right\rangle_{\text{part}}}_{\varepsilon_x}, \underbrace{\left\langle \frac{2\sigma_{xy}}{\sigma_x^2 + \sigma_y^2} \right\rangle_{\text{part}}}_{\varepsilon_y} \right). \end{aligned} \quad (1.82)$$

Notice that $\vec{\varepsilon}_{\text{lab}}$ in Equation 1.82 is sensitive to a trivial shift of the participant distribution, meaning that if the system is displaced from the origin, the averages $\langle x \rangle$ and $\langle y \rangle$ are nonzero. By consequence, the eccentricity is artificially inflated. To obtain a better characterization of the intrinsic fluctuations of the geometry, it is therefore better to subtract the mean values (re-center), building $\vec{\varepsilon}_{\text{part}}$. Its orientation defines the participant-plane angle Ψ_{pp} with norm $\varepsilon_{\text{part}}$:

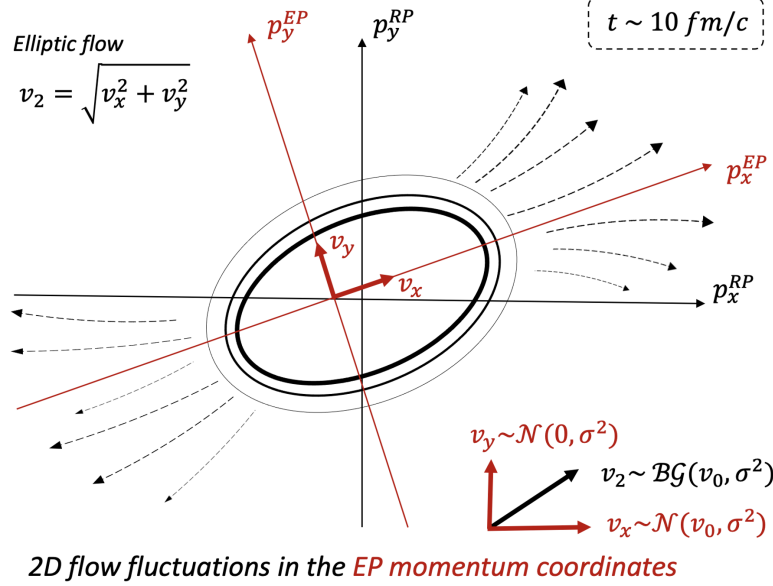
$$\Psi_{pp} = \frac{1}{2} \text{atan2}(\varepsilon_y, \varepsilon_x), \quad \varepsilon_{\text{part}} = \sqrt{\varepsilon_x^2 + \varepsilon_y^2} = \frac{\sqrt{(\sigma_y^2 - \sigma_x^2)^2 + 4\sigma_{xy}^2}}{\sigma_x^2 + \sigma_y^2}. \quad (1.83)$$

Using Equation 1.68, the elliptic flow can be related to the participant eccentricity. Recent calculations [114] have also considered the 2D eccentricity approach (with $\varepsilon_{\text{part}}$) to describe eccentricity and flow fluctuations, leading to new expressions for $v_2\{2\}$ and $v_2\{4\}$. To interpret this type of flow fluctuation, it is necessary to introduce a new event-plane (EP) coordinate system, illustrated in Figure 1.25. Interestingly in the EP frame, the flow vector v_2 has two components, v_x and v_y , with norm $v_2 = \sqrt{v_x^2 + v_y^2}$. This picture motivates the use of a 2D approach to evaluate the flow fluctuations. In addition, MCG simulations have demonstrated that the distributions of ε_x and ε_y are well reproduced by Gaussian functions with nearly equal widths $\sigma_{\varepsilon_x} = \sigma_{\varepsilon_y} = \sigma_{\varepsilon_{\text{part}}}$, reflecting isotropic fluctuations [115, 116].

36. In fact, the vector $\vec{\varepsilon}_{\text{lab}}$ defined in Equation 1.64 was written under the assumption that the participant distribution is already centered at $\langle x \rangle = \langle y \rangle = 0$, which is not always the case. More generally, the definition of $\vec{\varepsilon}_{\text{lab}}$ in Equation 1.82, corresponds to the definition of an eccentricity vector with arbitrary centering at $(\langle x \rangle, \langle y \rangle)$.



(A) Initial eccentricity: $\varepsilon_x, \varepsilon_y$ form the new basis to describe 2D eccentricity fluctuations.



(B) Flow response: v_x and v_y combine to form a radial flow vector v_2 .

FIGURE 1.25 – Illustration of the initial eccentricity and its anisotropy response in the event-plane (EP) coordinate system. The radial ellipses around the thick solid line indicate radial eccentricity (A) and flow (B) fluctuations.

Within this assumption, the 2D Gaussian distribution $\mathcal{N}^2(\varepsilon_x, \varepsilon_y; \langle \varepsilon_{part} \rangle, 0; \sigma_{\varepsilon_{part}}, \sigma_{\varepsilon_{part}})$, can be re-expressed as a Bessel-Gaussian ($\mathcal{BG}(\varepsilon_{part}; \langle \varepsilon_{part} \rangle, \sigma_{\varepsilon_{part}})$) distribution of the radial participant eccentricity ε_{part} :

$$\begin{aligned} \mathcal{N}^2(\varepsilon_x, \varepsilon_y; \langle \varepsilon_x \rangle, 0; \sigma_{\varepsilon_x}, \sigma_{\varepsilon_y}) &= \frac{1}{\sqrt{2\pi} \sigma_{\varepsilon_x}} \exp \left[-\frac{(\varepsilon_x - \langle \varepsilon_x \rangle)^2}{2\sigma_{\varepsilon_x}^2} \right] \frac{1}{\sqrt{2\pi} \sigma_{\varepsilon_y}} \exp \left[-\frac{\varepsilon_y^2}{2\sigma_{\varepsilon_y}^2} \right], \\ \mathcal{BG}(\varepsilon_{part}; \langle \varepsilon_{part} \rangle, \sigma_{\varepsilon_{part}}) &= \frac{\varepsilon_{part}}{\sigma_{\varepsilon_{part}}^2} \exp \left[-\frac{\varepsilon_{part}^2 + \langle \varepsilon_{part} \rangle^2}{2\sigma_{\varepsilon_{part}}^2} \right] I_0 \left(\frac{\langle \varepsilon_{part} \rangle \varepsilon_{part}}{\sigma_{\varepsilon_{part}}^2} \right), \\ \mathcal{N}^2(\varepsilon_x, \varepsilon_y) &\xleftrightarrow[\substack{\langle \varepsilon_x \rangle = \langle \varepsilon_{part} \rangle, \langle \varepsilon_y \rangle = 0 \\ \sigma_{\varepsilon_x} = \sigma_{\varepsilon_y} = \sigma_{\varepsilon_{part}}, \varepsilon_{part} = \sqrt{\varepsilon_x^2 + \varepsilon_y^2}}]{\hspace{1cm}} \mathcal{BG}(\varepsilon_{part}; \langle \varepsilon_{part} \rangle, \sigma_{\varepsilon_{part}}). \end{aligned} \quad (1.84)$$

Here, I_0 denotes a Bessel function of the first kind. The equivalence ($\mathcal{N}^2 \leftrightarrow \mathcal{BG}$) follows from transforming x and y components of the eccentricity vector to polar coordinates. In Figure 1.25, eccentricity and flow fluctuations are represented in a radial form. Similarly to Eq. 1.80, the Gaussian flow fluctuations can be expressed as $\mathcal{N}(\langle v_2 \rangle, \sigma_v^2)$, where $\langle v_2 \rangle$ is the mean elliptic flow with respect to the EP, and σ_v denotes the width of the EP flow fluctuations. Figure 1.26 illustrates the difference between modeling event-by-event fluctuations of the elliptic flow coefficient v_2 with 1D and 2D Gaussian distributions. The three panels are obtained for 10,000 v_2 random values. For the Normal case (in blue) we used $\sigma_v / \langle v_2 \rangle \sim 0.5$, and for the Bessel–Gaussian case (in red) $\sigma / v_0 \sim 0.8$, in order to illustrate large fluctuations.

As shown in the left panel of Figure 1.26, in the PP coordinate system, all events lie along the v_x^{PP} axis, and v_2 is assumed to fluctuate as $v_2 \sim \mathcal{N}(\langle v_2 \rangle, \sigma_v^2)$. This description becomes problematic when the variance σ_v^2 is not small, because the Gaussian distribution naturally extends to negative values, as illustrated in the right panel of Figure 1.26. Since v_2 represents the magnitude of anisotropic flow, it is by definition non-negative, making such outcomes unphysical. In the EP frame, however, 2D Gaussian fluctuations are represented as a cloud of points in the (v_x, v_y) plane, as illustrated in the middle panel of Figure 1.26. The flow magnitude is then defined as the radial distance, $v_2 = \sqrt{(v_x)^2 + (v_y)^2} \sim \mathcal{BG}(v_0, \sigma^2)$, with a distribution whose domain is \mathbb{R}_+ (defined only for non-negative values). The \mathcal{BG} distribution, shown in the right panel of Figure 1.26, is strictly non-negative and thus avoids the unphysical region present in the 1D Gaussian model. Therefore, while the PP

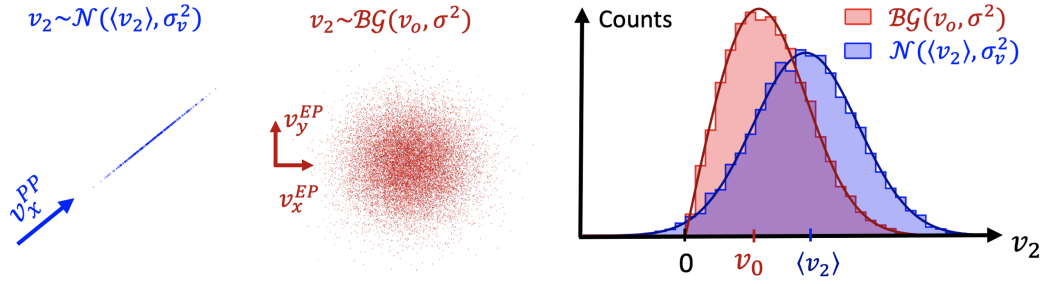


FIGURE 1.26 – Illustration of the event-by-event fluctuations of v_2 , obtained by random sampling of 10000 values. Left: In the PP frame, v_2 values aligns with v_x^{PP} and fluctuates normally around $\langle v_2 \rangle$ with variance σ_v^2 . Middle: In the EP frame, v_2 is the radial magnitude in the (v_x^{EP}, v_y^{EP}) plane, following a Bessel–Gaussian \mathcal{BG} centered at v_0 , with variance σ^2 . Right: Comparison of the distributions $\mathcal{N}(\langle v_2 \rangle, \sigma_v^2)$ and $\mathcal{BG}(v_0, \sigma^2)$. Solid curves represent the analytic functions, while the filled histograms illustrate their distribution, with each bin corresponding to a v_2 interval.

(1D Gaussian) approach is only valid when fluctuations are very small, the EP (2D) framework requires no such approximation. The \mathcal{BG} distribution naturally enforces the positivity of v_2 and provides a more robust and physically consistent description of event-by-event flow fluctuations.

Sensitivity of $v_2\{2\}$, $v_2\{SP\}$ and $v_2\{4\}$ to Gaussian flow fluctuations

As illustrated in Figures 1.24 and 1.25, both Gaussian fluctuations (1D and 2D) can be also used to describe flow fluctuations in PP and EP systems, respectively. The flow moments of $\mathcal{N}(\langle v_2 \rangle, \sigma_v^2)$ and $\mathcal{BG}(v_0, \sigma^2)$ distributions are presented in Table 1.2 and derived in appendix A.

Dimension	Distribution	Moments
1D	$v_2 \sim \mathcal{N}(\langle v_2 \rangle, \sigma_v^2)$	$\langle v_2 \rangle,$
		$\langle v_2^2 \rangle = \langle v_2 \rangle^2 + \sigma_v^2,$
		$\langle v_2^4 \rangle = \langle v_2 \rangle^4 + 6\langle v_2 \rangle^2 \sigma_v^2 + 3\sigma_v^4$
2D	$\left. \begin{array}{l} v_x \sim \mathcal{N}(v_0, \sigma^2) \\ v_y \sim \mathcal{N}(0, \sigma^2) \end{array} \right\} \iff v_2 \sim \mathcal{BG}(v_0, \sigma^2)$	$\langle v_2 \rangle = v_0,$
		$\langle v_2^2 \rangle = v_0^2 + 2\sigma^2,$
		$\langle v_2^4 \rangle = v_0^4 + 8v_0^2 \sigma^2 + 8\sigma^4$

TABLE 1.2 – Exact moments of 1D Gaussian and 2D Bessel–Gaussian distributions.

Assuming negligible non-flow contributions³⁷, the definitions of $v_2\{SP\}$ and $v_2\{4\}$ in terms of flow moments are:

$$v_2\{SP\}^2 = \langle v_2^2 \rangle, \quad (1.85)$$

$$v_2\{4\}^4 = 2\langle v_2^2 \rangle^2 - \langle v_2^4 \rangle. \quad (1.86)$$

With the moments of the 1D Gaussian and 2D Bessel–Gaussian distributions, we obtain the following exact expressions for flow coefficients, reported in Table 1.3.

Model	$v_2\{2\}$	$v_2\{4\}$
1D Gaussian	$v_2\{SP\} = \sqrt{\langle v_2 \rangle^2 + \sigma_v^2}$	$v_2\{4\} = \left(\langle v_2 \rangle^4 - 2\langle v_2 \rangle^2 \sigma_v^2 - \sigma_v^4 \right)^{1/4}$
2D Bessel–Gaussian	$v_2\{SP\} = \sqrt{v_0^2 + 2\sigma^2}$	$v_2\{4\} = v_0 = \langle v_2 \rangle$

TABLE 1.3 – $v_2\{SP\}$ and $v_2\{4\}$ for 1D and 2D models, without approximations.

In the 1D Gaussian case, $v_2\{4\}$ shown in Table 1.3 can be rewritten as

$$v_2\{4\}^2 = \langle v_2 \rangle^2 \sqrt{1 - \frac{2\sigma_v^2}{\langle v_2 \rangle^2} - \frac{\sigma_v^4}{\langle v_2 \rangle^4}}. \quad (1.87)$$

Expanding in a power series for small Gaussian fluctuations ($\sigma_v/\langle v_2 \rangle \ll 1$), we obtain:

$$v_2\{4\}^2 \simeq \langle v_2 \rangle^2 \left(1 - \frac{\sigma_v^2}{\langle v_2 \rangle^2} - \frac{1}{4} \frac{\sigma_v^4}{\langle v_2 \rangle^4} + \dots \right). \quad (1.88)$$

At first order, this reduces to

$$v_2\{4\}^2 \equiv \langle v_2 \rangle^2 - \sigma_v^2, \quad \text{if } v_2 \sim \mathcal{N}(\langle v_2 \rangle, \sigma_v^2). \quad (1.89)$$

Equation 1.89 was originally proposed in Ref. [111] to describe small flow fluctuations. However, in cases where fluctuations are not negligible, this relation no longer holds. In summary, the second-order moment is identical for the 1D Gaussian

37. In the SP method, η -gap requirements are imposed by default, which strongly suppress non-flow contributions ($\delta_{SP} \sim 0$) and thereby justify the validity of Eq. 1.85. However, for $v_2\{2\}^2$, as discussed in Eq. 1.78, an additional δ term may appear that encodes residual non-flow effects. In this case, one has $v_2\{2\}^2 = \langle v_2^2 + \delta_2 \rangle + \sigma_v^2$. For $v_2\{4\}$, the corresponding non-flow contribution is much smaller, scaling as $\delta_4 \sim 1/M^3$. For a high-multiplicity environments with thousands of particle tracks ($M \sim 1000$), this gives $\delta_4 \sim 10^{-9}$, i.e. effectively negligible.

and the 2D Bessel–Gaussian models as shown in Table 1.2. Consequently, $v_2\{SP\}$ or $v_2\{2\}$ yield the same results in both approaches, as reported in Table 1.3. On the other hand, the fourth-order moment differs between the two cases: For the 1D Gaussian distribution, $v_2\{4\}$ contains explicit corrections from flow fluctuations (see Equation 1.89), while in the 2D Bessel–Gaussian model it reduces exactly to the mean value [114]:

$$v_2\{4\} = v_0, \quad \text{if } v_2 \sim \mathcal{BG}(v_0, \sigma^2). \quad (1.90)$$

Thus, while the 1D Gaussian case yields a $v_2\{4\}$ value that depends explicitly on flow fluctuations, the 2D Bessel–Gaussian scenario produces a $v_2\{4\}$ result that is independent of them.

Fluctuation ratio

A convenient way to study flow fluctuations is through the fluctuation ratio observable

$$F \equiv \sqrt{\frac{v_2\{SP\}^2 - v_2\{4\}^2}{v_2\{SP\}^2 + v_2\{4\}^2}} \begin{cases} F \approx \frac{\sigma_v}{\langle v_2 \rangle}, & \text{if } v_2 \sim \mathcal{N}(\langle v_2 \rangle, \sigma_v^2). \\ F = \sqrt{\frac{\sigma^2/v_0^2}{2 + \sigma^2/v_0^2}}, & \text{if } v_2 \sim \mathcal{BG}(v_0, \sigma^2). \end{cases} \quad (1.91)$$

This ratio combines results from the scalar-product method, $v_2\{SP\}$, and the four-particle cumulant, $v_2\{4\}$. By definition, F lies within $0 \leq F \leq 1$. The limit $F = 0$ corresponds to the absence of fluctuations, where $v_2\{SP\} = v_2\{4\}$. At the other extreme, $F = 1$ arises when $v_2\{4\} = 0$, in the case of $v_2\{SP\} > 0$, then the observed flow is entirely driven by flow fluctuations. Consequently, F is only defined when $v_2\{4\} \leq v_2\{SP\}$. Equation 1.91 highlights how the interpretation of F depends on the assumed fluctuation model. For one-dimensional Gaussian fluctuations in the participant plane (PP) system, and in the regime $\sigma \ll \langle v_2 \rangle$, F provides a direct estimate of the relative fluctuation strength, $\sigma_v / \langle v_2 \rangle$. The two-dimensional Gaussian model, by contrast, yields an exact expression, although the dependence of F on σ is non-linear.

1.5.6 Elliptic flow and fluctuation ratio of light hadrons

In heavy-ion collisions, the most pronounced flow signals are observed in the light sector, involving up, down, and strange quarks. Since their masses are small compared to the typical effective temperature of the QGP ($m_{u,d,s} \ll T_{\text{eff}}$), they are expected to reach local thermal equilibrium with the medium. This is supported by experimental measurements from various heavy-ion experiments at RHIC [32, 34] and the LHC [117, 118], which show strong collective behavior among light hadrons.

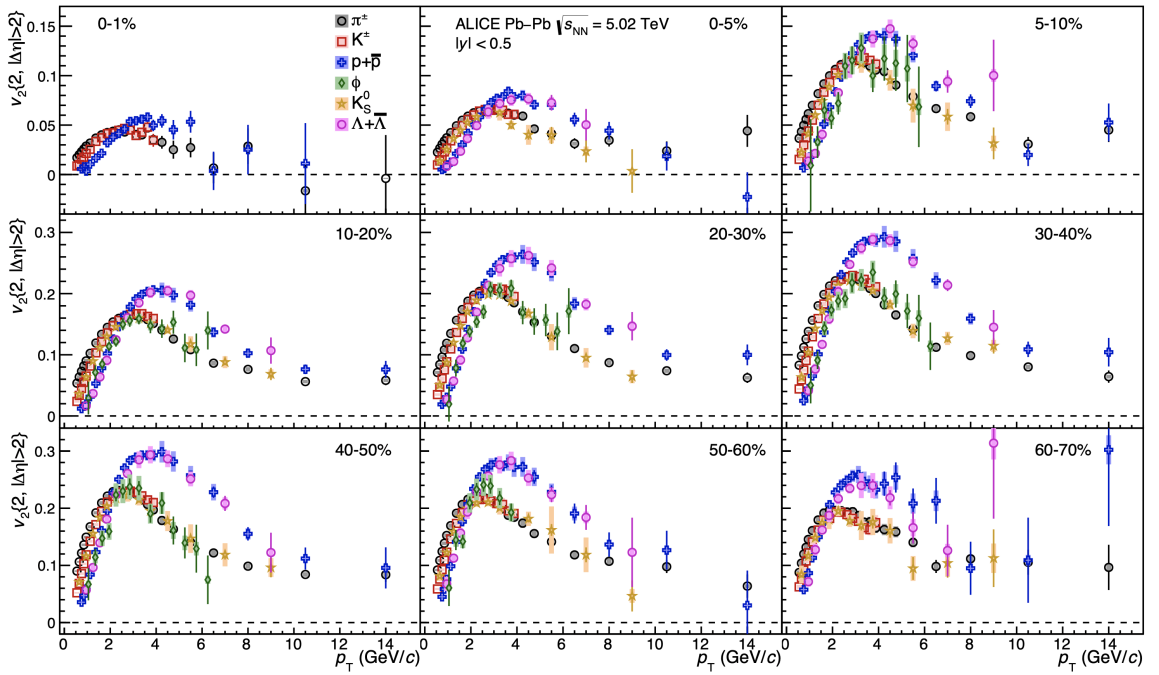


FIGURE 1.27 – The p_T -differential v_2 of π^\pm , K^\pm , $p + \bar{p}$, $\Lambda + \bar{\Lambda}$, K_S^0 , and the ϕ -meson for various centrality classes. Statistical and systematic uncertainties are shown as bars and boxes, respectively [117].

Figure 1.27 presents the elliptic flow coefficient $v_2(p_T)$ for π^\pm , K^\pm , $p + \bar{p}$, $\Lambda + \bar{\Lambda}$, K_S^0 , and the ϕ -meson across different centrality intervals, measured by the ALICE collaboration [117]. The results are shown in separate panels, allowing for a detailed comparison of elliptic and radial flow effects. At low transverse momentum ($p_T < 2 \text{ GeV}/c$), a clear mass ordering of v_2 is observed:

$$v_2^{\pi^\pm} > v_2^{K^\pm} \sim v_2^{K_S^0} > v_2^{p+\bar{p}} \sim v_2^\phi > v_2^{\Lambda+\bar{\Lambda}}. \quad (1.92)$$

Here, lighter particles exhibit larger flow values than heavier ones at the same p_T . This mass hierarchy signals the presence of strong radial flow, which imparts a

common, isotropic velocity boost on top of the anisotropic expansion of the system [119]. In the intermediate range ($3 < p_T < 8 \text{ GeV}/c$), the flow coefficients follow the so-called NCQ scaling, where a baryon-meson splitting emerges. This trend supports the quark coalescence picture of hadron formation. The ϕ -meson provides a particularly sensitive test of these scaling behaviours, as its mass is close to that of the proton.

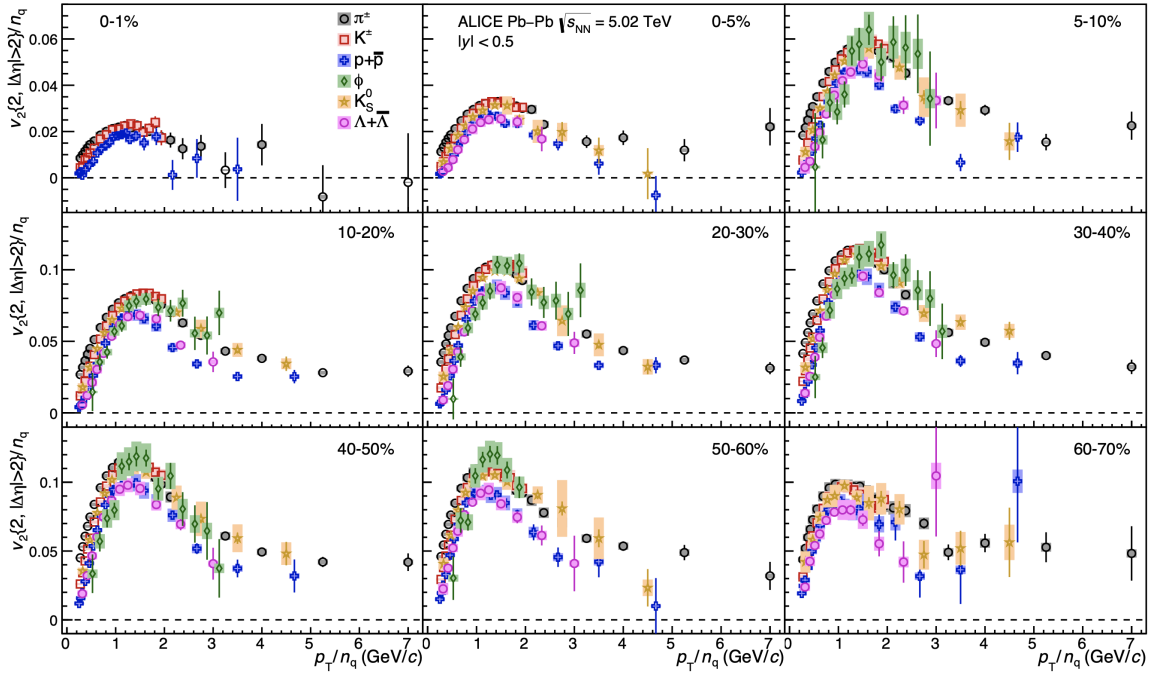


FIGURE 1.28 – Scaled elliptic flow, v_2/n_q , as a function of p_T/n_q for π^\pm , K^\pm , $p + \bar{p}$, $\Lambda + \bar{\Lambda}$, K_S^0 , and the ϕ -meson across centrality classes. Statistical and systematic uncertainties are represented by bars and boxes, respectively [117].

As shown in Figure 1.27, the ϕ -meson follows the proton flow at low p_T , while at intermediate p_T it behaves more like the pion across all centrality classes. The transition point where baryon and meson v_2 curves cross depends on the species and occurs at higher p_T in central than in peripheral collisions, reflecting the stronger radial flow in more central events. Furthermore, baryons exhibit larger elliptic flow values than mesons up to $p_T \approx 10 \text{ GeV}/c$, demonstrating that the particle-type dependence of v_2 extends into the high- p_T region. Beyond $10 \text{ GeV}/c$, the dependence on transverse momentum becomes weak, and the v_2 values of protons and pions are consistent within uncertainties.

To further probe the quark coalescence mechanism [120], which predicts that

mesons and baryons should follow a universal trend at intermediate p_T , both the transverse momentum and the flow harmonics are scaled by the number of constituent quarks (n_q) for each hadron species. The scaled quantity v_2/n_q is shown in Figure 1.28, as functions of p_T/n_q for several centrality intervals. In the interval $1 < p_T/n_q < 3 \text{ GeV}/c$, coalescence is expected to dominate [120, 121], the deviation from perfect scaling is about $\pm 20\%$ in central collisions, reducing to roughly $\pm 15\%$ in peripheral ones.

In addition, flow measurement has been extended to light-ion collisions. In 2025, the ALICE collaboration has measured for the first time, the elliptic flow of charged particles as a function of centrality in Oxygen-Oxygen (O-O) and Neon-Neon (Ne-Ne) at $\sqrt{s_{NN}} = 5.36 \text{ TeV}$ [122], as shown in Figure 1.29. These measurements suggest the formation of a QGP in light-ion collisions.

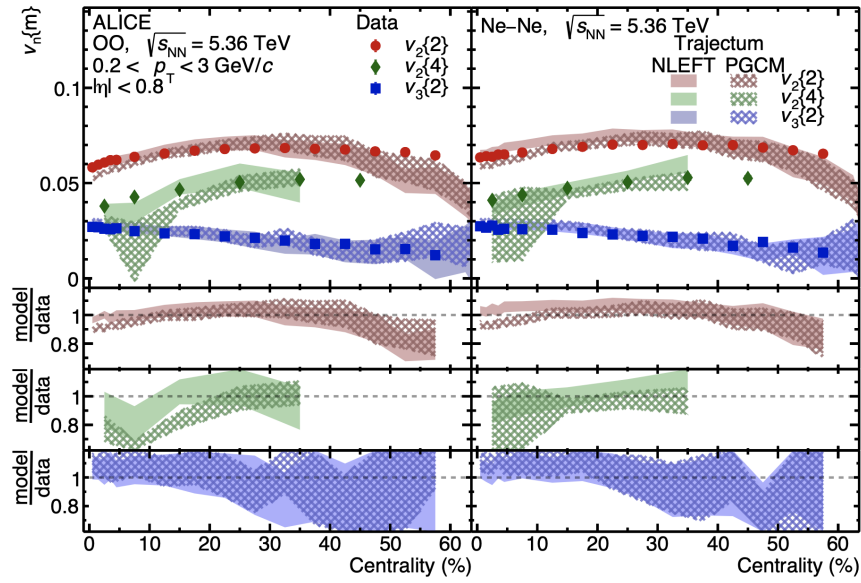


FIGURE 1.29 – Charged-particle $v_2\{2\}$, $v_3\{2\}$, and $v_2\{4\}$ as a function of centrality in O-O (left) and Ne-Ne (right) collisions at $\sqrt{s_{NN}} = 5.36 \text{ TeV}$. The measurements are compared with TRAJECTUM calculations using NLEFT and PGCM inputs [123]. Figure from [122].

The measurements shown in Figure 1.29 are compared with hydrodynamic simulations from the TRAJECTUM framework [93, 123, 124], which incorporate nuclear structure initial conditions for ^{16}O and ^{20}Ne derived from the Nuclear Lattice Effective Field Theory (NLEFT) [125] and the *ab initio* Projected Generator Coordinate Method (PGCM) [126, 127]. In both approaches, ^{20}Ne nuclei display a bowling-pin configuration composed of $^{16}\text{O} + \alpha$, whereas ^{16}O nuclei are characterized by irreg-

ular tetrahedral shapes [123]. NLEFT-based results reproduce both the centrality trend and magnitude of $v_2\{2\}$, $v_3\{2\}$, and $v_2\{4\}$ up to 50% centrality, with a better agreement with the data than PGCM predictions. The centrality dependence of $v_2\{2\}$ and $v_2\{4\}$ reveals a characteristic rise from very central collisions towards mid-central collisions, peaking around 40% centrality. This behaviour also been observed in Pb-Pb collisions at LHC [117] and Au-Au collisions at RHIC [128], reflects the interplay between the geometric anisotropy of the initial nuclear overlap region and the pressure-driven collective expansion of the medium. In mid-central collisions, the initial spatial anisotropy is greatest, resulting in stronger v_2 signals. In addition, the $v_3\{2\}$ values are nontrivial, since their centrality dependence differs from that of the initial triangular eccentricity ϵ_3 , which tends to predict higher values in semicentral collisions. This contrast between initial geometry and final triangular flow highlights the strong medium response, well described by hydrodynamic models.

Fluctuation ratio of POI strange hadrons

The CMS Collaboration has measured the fluctuation ratio F in PbPb collisions at $\sqrt{s_{NN}} = 5.02$ TeV over a wide range of centralities, as well as in pPb collisions at $\sqrt{s} = 8.16$ TeV for events with large multiplicity (number of reconstructed tracks): $185 \leq N^{\text{offline}}_{\text{trk}} < 250$. Results are shown separately for K_S^0 mesons (upper panel) and Λ baryons (lower panel). For comparison, hydrodynamic model predictions of v_2 fluctuations in PbPb collisions, based on AMPT and TRENTo initial conditions [129], are displayed as shaded bands. Statistical uncertainties are represented by vertical bars, while systematic uncertainties are indicated by shaded boxes.

In the intermediate- to high- p_T region, the coalescence mechanism takes place. The light quarks (u, d, s) are expected to achieve chemical thermalization within the QGP, and the collective flow observed for strange hadrons can thus be interpreted as a consequence of their coupling to the bulk medium. This is motivated by the fact that their current quark masses are small compared to the typical QGP temperature: $m_u, m_d, m_s \ll T_{\text{QGP}}$, such that they behave effectively as massless degrees of freedom in the medium.

Comparisons of the pPb and PbPb results of strange hadrons illustrate how event-by-event flow fluctuations depend on the system size. No clear particle-species dependence is observed for either PbPb or pPb collisions in Figure 1.30, suggesting that such fluctuations arise primarily from the fluctuations of the initial-state

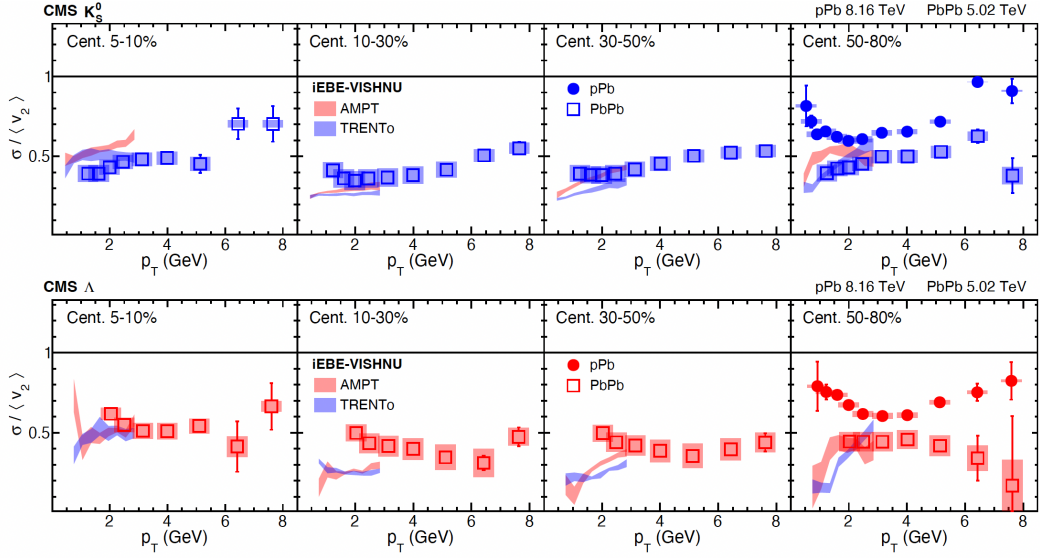


FIGURE 1.30 – Fluctuation ratios of open hadrons: $F_{K_S^0}$ mesons and F_{Λ} baryons, in PbPb collisions for different centrality intervals, and compared to those in pPb collisions with $185 \leq N_{\text{trk}}^{\text{offline}} < 250$. Measured by the CMS Collaboration [130].

geometry [130]. The CMS collaboration analysis interprets these fluctuations as $F \sim \frac{\sigma_v}{\langle v_2 \rangle}$, corresponding to the 1D Gaussian approximation for small flow fluctuations in the PP coordinate system (see Figure 1.24). However, CMS reports values of $F \sim 0.4 - 0.8$, which suggests that the assumption $\sigma_v \ll \langle v_2 \rangle$ may not hold.

Motivated by this, in this thesis we will study the 2D flow fluctuations of J/ψ and compare them, with the CMS Data [130] using a 2D Bessel-Gaussian approach in the EP coordinate system and therefore use the exact expression without small flow fluctuations assumption. This provides a more robust characterization of the event-by-event fluctuation (beyond the $\sigma_v \ll \langle v_2 \rangle$ approximation), to properly evaluate the light - heavy hadron flow fluctuations interplay. Quarkonia, as bound states of heavy quarks, constitute a particularly sensitive probe of the heavy-flavour sector and its degree of collectivity. For charm quarks, partial thermalization in the QGP imply that charmonium states such as the J/ψ carry significant flow. Consequently, the study of flow fluctuations of the J/ψ emerges as a natural extension of the investigation of heavy-flavour collectivity. In chapter 4, we present for the first time new results of J/ψ flow fluctuations, thereby providing new insight about heavy-flavour hadron flow and event-by-event fluctuations in PbPb collisions.

Chapter 2

Charmonium collectivity

While light hadrons in heavy-ion collisions primarily reflect the collective dynamics of the bulk medium, also heavy-flavor hadrons exhibit collective behavior. Measurements of charmonia show pronounced flow signals, consistent with (partial) thermalization¹ of charm quarks.

Motivated by these observations, this chapter lays out a coherent framework for studying charmonium collectivity in heavy-ion collisions. We begin introducing quarkonia, starting with a discussion of their basic properties such as decay channels and lifetimes. We then review the main production mechanisms in hadronic collisions, emphasizing both perturbative and non-perturbative approaches that are commonly employed to model their formation. Particular attention is given to charmonium production, where several competing mechanisms coexist and provide complementary insights into the underlying charm quark dynamics. We also examine the influence of the medium on quarkonium states, distinguishing between cold nuclear matter effects observed in proton–nucleus collisions and the QGP effects. These considerations are followed by a summary of the different modeling strategies developed to interpret the experimental data in these environments. Finally, in Section 2.2.1, we contextualize the discussion by comparing previous J/ψ measurements at the LHC and RHIC, and extend the comparison to include open heavy-flavor observables and flow measurements of other quarkonium species.

1. Here, partial thermalization refers to the fact that charm quarks, due to their large mass, do not reach complete thermal equilibrium with the medium. However, they interact strongly enough to approach kinematic equilibrium and acquire significant collective flow, in contrast to the behavior expected if they were unaffected by the bulk medium.

2.1 Quarkonia as hard probe

Quarkonia are flavor-neutral mesons consisting of a heavy quark bound to its corresponding antiquark. The quantum numbers are labeled as $n^{2S+1}L_J$, where n , L , S , and J represent the energy orbital, spin, and total angular momentum quantum numbers, respectively. Since the influential work by Matsui and Satz [131], which proposed that color screening in a deconfined medium could suppress quarkonium binding, quarkonia have been widely recognized as key hard probes of the QGP formation.

The production of $Q\bar{Q}$ pairs occurs during the initial stages of hadronic collisions via hard partonic scatterings, being sensitive to the full QGP evolution. Their varying binding energies and dissociation thresholds provide insight into the medium's temperature and deconfinement dynamics. Among quarkonia, charmonia (made up of charm-anticharm quark pairs) are of particular interest. The full spectrum of known charmonium states is shown in Figure 2.1.

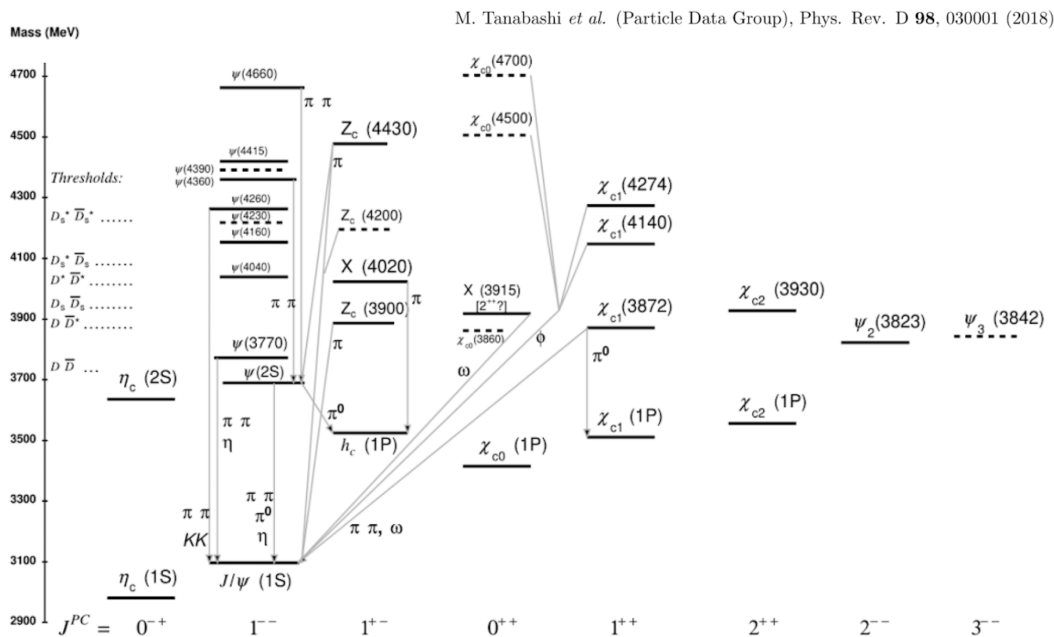


FIGURE 2.1 – Mass spectrum of charmonium states [15].

This section overviews quarkonium properties and decay modes, followed by their production via hard scattering in hadronic collisions. We then discuss the mechanisms that modify charmonium production, beginning with cold nuclear matter effects and subsequently addressing in-medium effects from the QGP.

2.1.1 Decay channels of J/ψ

The second lightest state of charmonia is the $J/\psi(1S)$. This particle has an invariant mass of $3.0969 \text{ GeV}/c^2$ and a mean lifetime of $7.2 \times 10^{-21} \text{ s}$ [1]. The decay occurs via both electromagnetic and strong nuclear channels, which compete with one another (Figure 2.2).

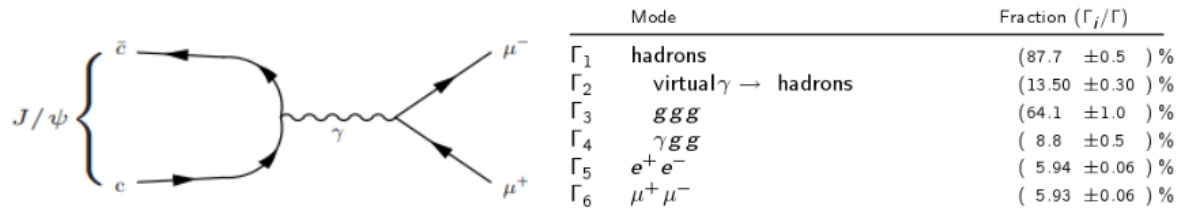


FIGURE 2.2 – Left: The decay diagram of J/ψ into dimuons. Right: The decay modes of J/ψ [1].

The quantum numbers of the J/ψ are the same as the photon: $(J^{PC}) = (1^{--})$, this is because QED and QCD individually conserve charge conjugation, parity, and time-reversal symmetry (C-P-T discrete symmetries)². The branching ratios of J/ψ ($\Gamma_{i=1,5,6}/\Gamma$) associated to real particles satisfy the following relation: $\frac{\Gamma_1}{\Gamma} + \frac{\Gamma_5}{\Gamma} + \frac{\Gamma_6}{\Gamma} \sim 100\%$. All virtuals' branching ratio are linked to the hadronic's branching ratio: $\frac{\Gamma_2}{\Gamma} + \frac{\Gamma_3}{\Gamma} + \frac{\Gamma_4}{\Gamma} \sim \frac{\Gamma_1}{\Gamma}$.

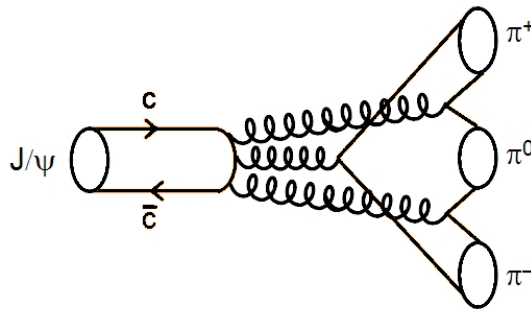


FIGURE 2.3 – J/ψ decays into three pions diagram.

Notice that the decay of the J/ψ into two gluons is forbidden, respecting discrete-symmetry conservation. The gluon carries negative intrinsic charge-conjugation

2. Electromagnetic and strong interactions conserve C , P , and T separately, while the weak interaction violates them individually. The CPT theorem guarantees that any local, Lorentz-invariant quantum field theory preserves the combined CPT symmetry exactly. No experimental evidence of CPT violation has been observed, reinforcing its role as a fundamental principle of QFT.

and parity eigenvalues: $\eta_g^C = \eta_g^P = -1$. For the decay of a J/ψ state into n gluons, conservation of C and P requires:

$$\eta_{J/\psi}^C = (\eta_g^C)^n = (-1)^n, \quad \eta_{J/\psi}^P = (\eta_g^P)^n (-1)^L = (-1)^n (-1)^L, \quad (2.1)$$

with L the orbital angular momentum. Since $\eta_{J/\psi}^P = \eta_{J/\psi}^C = -1$, equation 2.1 imply that only odd values of n are allowed. Therefore, the two-gluon decay channel is forbidden, while the three-gluon decay channel is allowed:

$$J/\psi(1^{--}) \not\rightarrow g + g, \quad J/\psi(1^{--}) \rightarrow g + g + g. \quad (2.2)$$

The hadronic decay mode Γ_3 is strongly suppressed ($\Gamma_3/\Gamma < 100$) because of the OZI rule [132]. This rule applies well in the hadronic channel since internal gluon lines can be removed, and the diagram can be separated into two disconnected diagrams (Figure 2.3).

This effect strongly increases the lifetime of the particle, reducing the decay width. Electromagnetic decays (Γ_2) become non-negligible compared to hadronic decays (Γ_3), allowing a significant branching fraction to leptons ($\Gamma_5 = \Gamma_6$ due to lepton universality). Notice that the lifetime of the J/ψ is long enough that its decay occurs well after the QGP.

2.1.2 Charmonium production in hadronic collisions

In this subsection, we examine the mechanisms underlying the production of charmonium in high-energy hadronic collisions. We aim to provide a comprehensive overview of both perturbative and non-perturbative aspects of heavy-quark dynamics that govern charmonium formation. We begin by describing the initial hard-scattering processes responsible for the creation of heavy quark pairs, followed by a discussion of their subsequent evolution into bound quarkonium states. We introduce key theoretical tools such as the collinear factorization theorem, and present several phenomenological models to describe quarkonium production, including the Color Evaporation Model (CEM), Color Singlet Model (CSM), and Non-Relativistic QCD (NRQCD). We also introduce the prompt and non-prompt J/ψ production, highlighting their respective physical origins and relevance. Finally, we explore charmonium photo-production in AA collisions, where strong electromagnetic fields offer an alternative production mechanism.

2.1.2.1 Hard-scattering

The production mechanisms of quarkonia involve both perturbative and non-perturbative aspects of QCD. The formation of a heavy quark pair $Q\bar{Q}$, requiring at least an energy of $2m_Q$, can be described by perturbative QCD. Given that the charm quark mass is $m_c \sim 1.3 \text{ GeV}/c^2$, it lies well above the QCD scale $\Lambda_{\text{QCD}} \sim 200 \text{ MeV}/c^2$. In contrast, the transition from a $Q\bar{Q}$ pair to a bound quarkonium state is non-perturbative, with a binding energy of the order of Λ_{QCD} .

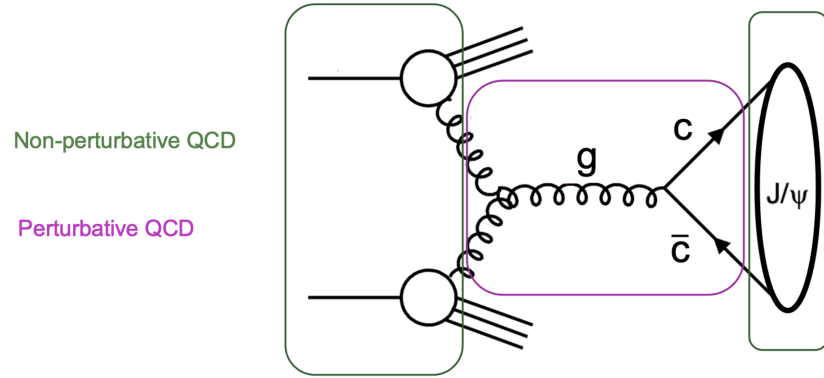


FIGURE 2.4 – Illustration of J/ψ production process (non-perturbative domain in green and perturbative domain in violet), from the initial nPDF, $c\bar{c}$ pair produced via gluon fusion and finally the J/ψ hadronisation process.

Perturbative process and Feynmann diagrams

Since the QCD scale Λ_{QCD} is much smaller than the charm and bottom quark masses (m_c, m_b), perturbative calculations are applicable for the initial production of heavy quark pairs. The characteristic production time for a heavy-quark pair can be estimated as:

$$\tau_p \approx \begin{cases} \frac{E}{p_T^2} \sim \frac{1}{p_T}, & \text{for } p_T \ll m_Q \\ \frac{1}{m_Q}, & \text{for } p_T \gg m_Q \end{cases} \quad (2.3)$$

where p_T is the transverse momentum and m_Q is the heavy-quark mass. For $p_T \sim m_Q$, this yields $\tau_p \approx 0.15 \text{ fm}/c$ for charm ($c\bar{c}$) and $\sim 0.05 \text{ fm}/c$ for bottom ($b\bar{b}$) quark pairs, both significantly shorter than the typical QGP thermalization time ($t \sim 1 \text{ fm}/c$). At high energies produced at LHC, the dominant mechanism

for heavy-quark pair ($Q\bar{Q}$) production is gluon-gluon fusion ($gg \rightarrow Q\bar{Q}$), while other processes such as quark-antiquark annihilation and photoproduction contribute only marginally. Feynman diagrams illustrating the different processes leading to the creation of $c\bar{c}$ pairs at ultra-relativistic energies are shown in 2.5. The first two diagrams on the left depict pair creation through gluon fusion, while the rightmost diagram involves quark-antiquark annihilation.

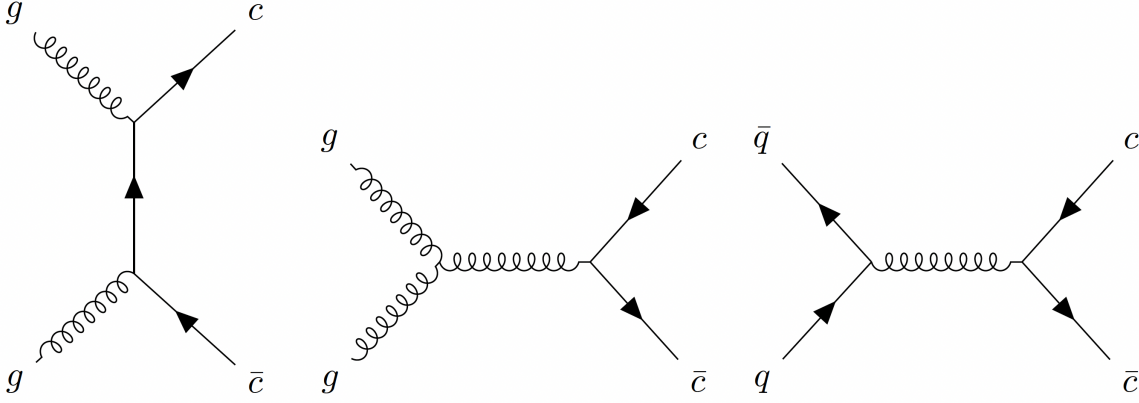


FIGURE 2.5 – Feynman diagrams at Leading Order for $c\bar{c}$ pair production. The two left diagrams represent gluon fusion, namely gluon scattering on the left and gluon annihilation in the middle, while the right diagram corresponds to $q\bar{q}$ annihilation.

Non-perturbative effects and the Cornell potential

The properties of quarkonium bound states are determined by solving the Schrödinger equation with a potential describing the interaction between the heavy quark and antiquark.

$$\left(-\frac{1}{m_Q}\nabla^2 + V_{Q\bar{Q}}(r)\right)\Phi_i(r) = E_i\Phi_i(r), \quad M_i = 2m_Q + E_i. \quad (2.4)$$

The wavefunction $\Phi_i(r)$ is normalized according to:

$$\int d^3r \cdot |\Phi_i(r)|^2 = 1. \quad (2.5)$$

The potential between two heavy quarks in a quarkonium can be modeled using the Cornell potential [133]:

$$V(r, T = 0) = -\frac{\alpha}{r} + \sigma r, \quad (2.6)$$

where $\alpha = \frac{4}{3}\alpha_s$ and σ is the QCD string tension. The first term resembles a Coulomb potential at short distances, while the linear term describes confinement at long distances.

Bound state formation in vacuum

Following their initial production, $Q\bar{Q}$ pairs are created at extremely short distances. To form a $Q\bar{Q}$ resonance, the pair must separate until they reach the typical spatial extent of the bound state. This process can be viewed as the time required for the pair to "choose" which specific quarkonium state with mass m_A or m_B will form. The formation time is commonly estimated by:

$$\tau_f \approx \frac{2E}{m_A^2 - m_B^2}. \quad (2.7)$$

For a pair energy of $E = 10$ GeV, the time required for a $c\bar{c}$ pair to form a J/ψ (ground state) instead of a $\psi(2S)$ is approximately 1 fm/ c . At the same energy, a $b\bar{b}$ pair takes about 0.36 fm/ c to form a $Y(1S)$ (ground state) rather than a $Y(2S)$. Importantly, this formation time τ_f grows significantly with increasing energy E (and with particle momentum). These timescales and the underlying production mechanisms of quarkonium motivates the use of theoretical frameworks such as the collinear factorization theorem, which we discuss in the following section.

Collinear factorization theorem

In pp collisions, the total cross section σ_{pp} for a given process can be computed using the collinear factorization theorem [134]. This framework expresses the cross section as a convolution of the perturbatively calculable partonic cross section with the PDFs:

$$\frac{d\sigma_{pp}}{dydQ} = \sum_{i,j} \int dx_1 f_i^p(x_1, \mu_F) \int dx_2 f_j^p(x_2, \mu_F) \frac{d\hat{\sigma}_{ij}(Q, \mu_R)}{dydQ} + \mathcal{O}\left(\frac{\Lambda_{\text{QCD}}^n}{Q^n}\right). \quad (2.8)$$

Here, $f_i^p(x_1, \mu_F)$ denotes the PDF for finding a parton of type i inside the proton, carrying a longitudinal momentum fraction x_1 at the factorization scale μ_F . Similarly, $f_j^p(x_2, \mu_F)$ refers to a parton of type j in the second proton. The quantity $\frac{d\hat{\sigma}_{ij}}{dydQ}$ is the differential partonic cross section, computed perturbatively at the renormalization

scale μ_R . The variable y is the rapidity of the final state, and Q is the hard scale of the process. The last term in the equation accounts for power-suppressed corrections proportional to $(\Lambda_{\text{QCD}}/Q)^n$, which are negligible when $Q \gg \Lambda_{\text{QCD}}$. The partonic cross section $\hat{\sigma}_{ij}$ can be expressed as a perturbative expansion:

$$\frac{d\hat{\sigma}_{ij}}{dydQ} = \frac{d\hat{\sigma}_{ij}^{\text{LO}}}{dydQ} + \alpha_s(\mu_R^2) \frac{d\hat{\sigma}_{ij}^{\text{NLO}}}{dydQ} + \mathcal{O}(\alpha_s^2), \quad (2.9)$$

where, α_s is the strong coupling constant (at the renormalization scale μ_R), decreasing logarithmically at higher energies due to asymptotic freedom. This scale dependence ensures that the perturbative expansion remains valid at large Q^2 . The factorization theorem holds under the condition $\Lambda_{\text{QCD}}^n \ll Q^n$. In pA collisions, the relevant non-perturbative scale Λ_A is typically of order 1 GeV. While collinear factorization provides a powerful framework for describing hard processes, it does not account for all aspects of quarkonium production, as complex non-perturbative dynamics play a central role. In practice, various phenomenological models are required to describe the hadronisation mechanism of quarkonia. In the following section, we introduce some of the most well-known models in the field.

2.1.2.2 Phenomenological production models

Charmonium production involves a hard perturbative stage for $Q\bar{Q}$ pair creation and a soft non-perturbative stage for bound-state formation. This scale separation justifies factorization models that treat production and hadronization independently. Three main models describe the factorization of $Q\bar{Q}$ pairs in different ways:

Color singlet model (CSM)

The Color Singlet Model (CSM) was the first systematic approach to quarkonium production [135]. Here, the quantum numbers (spin and color) of the initial $Q\bar{Q}$ pair are conserved. The cross-section is expressed as:

$$\frac{d\sigma_{\psi+X}}{dp_T} = \sum_{i,j} f_i f_j \otimes \frac{d\sigma_{i+j \rightarrow Q\bar{Q}+X}}{dp_T} \otimes |\phi_\psi(0)|^2, \quad (2.10)$$

where f_i and f_j are the parton distribution functions and $|\phi_\psi(0)|^2$ is the wave function at the origin.

Color evaporation model (CEM)

The Color Evaporation Model (CEM) provides a phenomenological approach to quarkonium production [136]. In this model, the quarkonium production cross-section σ_ψ is related to the $Q\bar{Q}$ production cross-section by:

$$\sigma_\psi = F_\psi \int_{2m_Q}^{2m_H} \frac{d\sigma_{Q\bar{Q}}}{dm_{Q\bar{Q}}} dm_{Q\bar{Q}}, \quad (2.11)$$

where F_ψ is a phenomenological factor and m_H is the mass of the lightest open heavy-flavor hadron. The integration bounds $2m_Q$ and $2m_H$ represent the kinematic limits: the lower bound $2m_Q$ corresponds to the threshold for $Q\bar{Q}$ pair production, while the upper bound $2m_H$ represents the maximum invariant mass before the pair would hadronize into open heavy-flavor mesons instead of forming a bound quarkonium state.

Non-Relativistic QCD (NRQCD)

The production of heavy quarkonia, such as J/ψ , involves both perturbative and non-perturbative aspects of QCD. The NRQCD framework provides a systematic factorization approach to separate short (distance effects—calculable using perturbative QCD) from long-distance non-perturbative contributions [137]. In this formalism, the heavy quark-antiquark pair $Q\bar{Q}$ can be produced in either a color-singlet or a color-octet state. The transition into a physical quarkonium state involves soft gluon emissions that are encoded in universal, non-perturbative long-distance matrix elements (LDMEs), denoted $\langle \mathcal{O}_n^\psi \rangle$. These matrix elements depend on the specific quarkonium state and must be extracted from experimental data.

The production cross section is written as a sum over intermediate states n , which are characterized by their color (singlet or octet), spin, and angular momentum quantum numbers:

$$\frac{d\sigma_{\psi+X}}{dp_T} = \sum_{i,j,n} f_i f_j \otimes \frac{d\hat{\sigma}_{i+j \rightarrow Q\bar{Q}[n]+X}}{dp_T} \otimes \langle \mathcal{O}_n^\psi \rangle, \quad (2.12)$$

The inclusion of color-octet states, which are forbidden in the older Color Singlet Model (CSM), allows NRQCD to describe a wider range of quarkonium production data, especially at high transverse momentum.

2.1.2.3 Prompt and non-prompt J/ψ

To fully characterize J/ψ production in hadronic collisions, it is crucial to distinguish between prompt and non-prompt sources. This distinction enables the study of different underlying physical mechanisms: prompt J/ψ probes charm quark dynamics and quarkonium production models, while non-prompt J/ψ , originating from B -hadron decays, provides access to beauty production and fragmentation. Understanding both components is essential for accurate phenomenological modeling and for interpreting measurements.

Prompt J/ψ is produced directly in the early stages of the collision or via decays of excited states like $\psi(2S)$. It provides insight into charm quark physics and is described by the models above.

Non-prompt J/ψ originates from the decay of B -hadrons produced via processes like $gg \rightarrow b\bar{b} + X$. The corresponding cross-section is:

$$\frac{d\sigma_\psi}{dp_T} = \frac{d\sigma_b}{dp_T} \otimes D_{b \rightarrow B} \otimes g_{B \rightarrow \psi}, \quad (2.13)$$

where, $D_{b \rightarrow B}$ is the fragmentation function and $g_{B \rightarrow \psi}$ describes the weak decay.

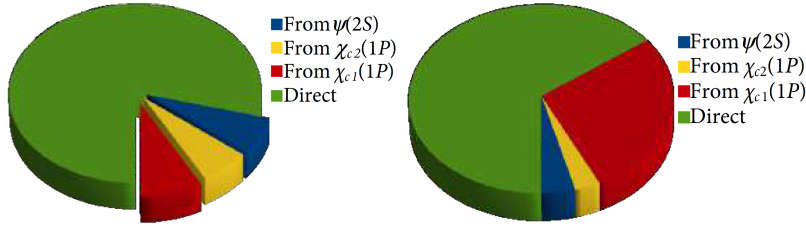


FIGURE 2.6 – Main sources of hadroproduced J/ψ at low and high p_T [138].

The prompt J/ψ cross section has been measured by all LHC experiments in pp collisions at $\sqrt{s} = 2.76, 7, 8$, and 13 TeV, and in Pb–Pb collisions at $\sqrt{s_{NN}} = 5.02$ TeV. The current measurements [139–142] suggest that the fraction of J/ψ from b -hadron decays is $\sim 10\%$ at low p_T and increases with p_T . Additionally, prompt J/ψ receives feed-down contributions from higher resonances: χ_c states contribute 12–30% at high p_T , while $\psi(2S)$ contributes $\sim 10\%$. Figure 2.6 illustrates the various

production channels contributing to prompt J/ψ yields, including direct production and feed-down from higher charmonium states.

2.1.2.4 Photo-production of J/ψ in AA collisions

Charmonia in HIC are not produced exclusively through hadronic mechanisms. Nuclei travelling almost at speed of light are sources of strong electromagnetic fields and by consequence the Pb-Pb collisions can generate gamma-gamma, gamma-nucleon and gamma-lead processes.

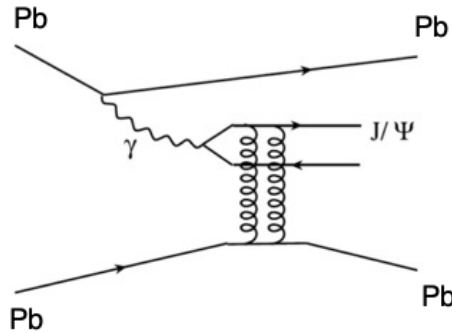


FIGURE 2.7 – Feynman diagram of the coherent photo-production of J/ψ in a Pb-Pb collision [143].

The understanding electromagnetic processes in relativistic heavy-ion collisions lies in the pioneering work of Enrico Fermi, who in 1924 demonstrated that a charged particle moving at relativistic speeds creates an intense electromagnetic [144]. This field manifests as a coherent ensemble of virtual photons surrounding the moving charge, effectively transforming the particle into a source of electromagnetic radiation. The theoretical framework for describing this phenomenon was later formalized through the Weizsäcker-Williams approximation [145]. The use of ultra-relativistic heavy ions thus provides privileged access to photo-induced physics.

Electromagnetic processes at the LHC are well studied in ultra-peripheral collisions (UPC), where there is no nucleon overlap and a large flux of quasi-real photons is produced. However, these processes also occur in peripheral collisions with nuclear overlap, where both photoproduction and hadronic production take place. It will be crucial to properly understand the electromagnetic production to well distinguish it from the hadronic one. Two types of photo-produced J/ψ can be formed:

- Coherent J/ψ : J/ψ can be created from a coherent photo-production process (see Figure 2.7), a virtual photon produced by one nucleus interacts coherently with the gluon field of the whole nucleus (all nucleons together). In this type of interaction, nuclei don't break up and the average transverse momentum is: $\langle p_T \rangle \propto \frac{1}{R_{\text{Lead}}} = 60 \text{ MeV}/c$. The coherent photo-production has a QED part proportional to the electric charge of the heavy ion ($\propto Z^2$) and a QCD part proportional to the square of the gluon density of the target nucleus.
- Incoherent J/ψ : J/ψ can be also generated from an incoherent photo-production; this time the photon interacts with one single nucleon, the whole nucleus breaks up or excites, and the average transverse momentum exchanged is larger than before: $\langle p_T \rangle \propto \frac{1}{R_{\text{Nucleon}}} = 500 \text{ MeV}/c$.

Notice that some J/ψ are formed by the decay of $\psi(2s)$ or other's vector meson from a coherent or an incoherent photo-production process.

2.1.3 Cold nuclear matter (CNM) and QGP in-medium effects on charmonium

Charmonium production in hadronic collisions is subject to significant modifications when the collision system involves nuclear matter, such as in pA or AA collisions. These modifications arise from the interaction of the $c\bar{c}$ pair with the nuclear environment, and they can be broadly categorized into cold nuclear matter (CNM) effects, which reflect nuclear effects unrelated to deconfinement, and QGP effects, which are associated with the presence of a deconfined medium. Understanding in-medium effects is essential for interpreting charmonium suppression or enhancement patterns observed in heavy-ion collisions. In particular, isolating CNM contributions from genuine QGP-induced modifications is critical to reliably probe the deconfined phase of QCD matter. This subsection presents an overview of the key in-medium mechanisms that affect charmonium yields, starting with CNM effects in pA collisions, followed by QGP-induced dissociation, energy loss, and recombination processes relevant in AA systems.

2.1.3.1 Cold nuclear matter effects in pA collisions

In proton-nucleus (pA) collisions, the formation of a QGP is not expected. Nevertheless, quarkonium production is significantly modified compared to proton-

proton (pp) collisions. These modifications, known as **Cold Nuclear Matter** effects, must be carefully considered to disentangle them from genuine hot-matter effects observed in nucleus-nucleus collisions [146]. Several mechanisms contribute to CNM effects:

- **Modification of Nuclear PDFs (Shadowing and Anti-shadowing):**

The parton distribution functions (PDFs) inside a nucleus differ from those in a free proton due to nuclear binding and coherence effects. At small momentum fractions x , gluon densities are suppressed (*shadowing*), leading to reduced quarkonium yields at forward rapidities [147]. Conversely, at intermediate values of x , gluon densities can be enhanced (*anti-shadowing*), which may increase the production rates in certain kinematic regions.

- **Cronin effect and p_T -broadening:**

When comparing hadron yields in pA collisions with those in pp , an enhancement at transverse momenta of a few GeV/ c has been observed. This effect is commonly called the Cronin effect [148]. Its existence has been confirmed in numerous experiments and is usually interpreted as a consequence of multiple scatterings of the incoming partons within the nucleus before the hard scattering takes place (see [149] for a review). Moreover, the same mechanism was suggested to be relevant in the production of the J/ψ [150], since it leads to an increase in the average squared transverse momentum, a phenomenon often termed p_T -broadening.

- **Coherent Energy Loss:**

As an incoming parton traverses the nucleus before the hard scattering, it may lose energy coherently through multiple soft gluon emissions [151]. This effect is enhanced when the quarkonium formation time is long compared to the nuclear size, resulting in coherent suppression, especially at forward rapidities where small- x gluons are probed [152].

- **Nuclear Absorption:**

The pre-resonant $Q\bar{Q}$ pair can be broken up as it passes through the nuclear medium before forming a bound quarkonium state. This process depends on the nuclear path length and the hadronization time of the quarkonium. While less relevant at LHC energies due to smaller crossing time (shorter path) of the nuclei, it is a significant suppression mechanism at lower energies (e.g., at SPS) [153].

- **Interaction with Comovers:**

After formation, a quarkonium state may be dissociated by interactions with comoving particles—secondary hadrons produced in the collision [154]. The probability of such dissociation depends on the local density of comovers and the interaction cross-section, and this mechanism helps to describe the suppression patterns observed in both pA and AA systems [155].

The combined impact of CNM effects is quantified by the nuclear modification factor:

$$R_{pA}(y) = \frac{1}{A} \cdot \frac{d\sigma_{pA}/dy}{d\sigma_{pp}/dy} \quad (2.14)$$

Here, $R_{pA} < 1$ indicates suppression (e.g., due to shadowing or energy loss), while $R_{pA} > 1$ may signal enhancement (e.g., anti-shadowing).

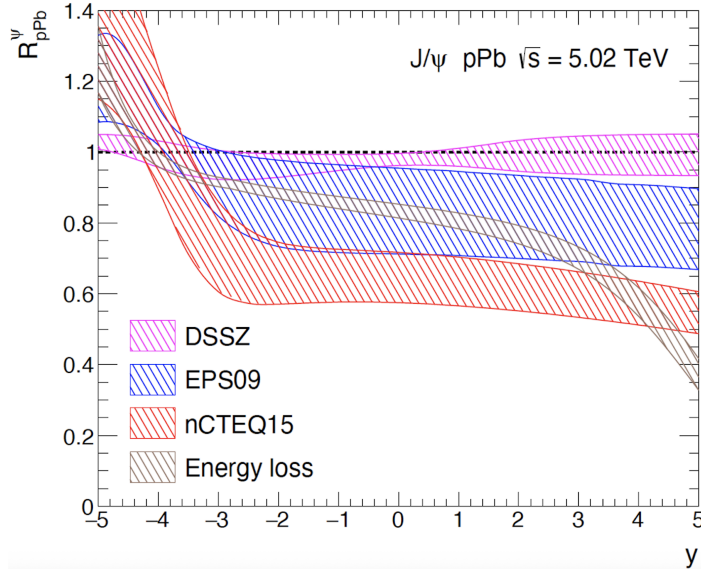


FIGURE 2.8 – J/ψ suppression in p – Pb collisions at $\sqrt{s} = 5.02$ TeV for the various nPDF sets. The prediction for J/ψ suppression from the effect of coherent energy loss alone is also shown [156].

The rapidity dependence of R_{pA} provides insight into the dominant CNM mechanisms at play. The suppression of J/ψ due to nuclear shadowing can be approximated by

$$R_{pPb}^\psi \sim R_g^{\text{Pb}}(x_2, Q = M_\psi), \quad (2.15)$$

where $R_g^{\text{Pb}}(x_2, Q)$ denotes the ratio between the gluon parton distribution function (PDF) in a lead nucleus and in a free proton, evaluated at momentum fraction $x_2 = \frac{M_\psi}{\sqrt{s}} e^{-y}$ (equation derived in detail in appendix A) and scale $Q = M_\psi$. This quantity

reflects the depletion (or enhancement) of gluon densities in nuclei. At LHC energies, J/ψ production is dominated by gluon-gluon fusion, making it highly sensitive to the gluon distributions at small Bjorken- x . In this regime, nuclear effects such as shadowing become pronounced, and the onset of gluon saturation (where the growth of gluon densities is tamed due to non-linear QCD dynamics) may also play a role. These effects modify the initial parton flux and, consequently, the observed quarkonium yields. Figure 2.8 illustrates the predicted shadowing effects on J/ψ suppression in p-Pb collisions at the LHC, emphasizing the substantial uncertainties at forward rapidity, where small- x gluons dominate. Predictions based solely on coherent energy loss are also shown, highlighting the challenge of disentangling competing mechanisms responsible for the observed suppression pattern. A clear understanding of these cold nuclear matter effects is essential for interpreting quarkonium production in AA collisions, where both cold and hot nuclear matter effects are present.

2.1.3.2 QGP effects in AA collisions

2.1.3.3 Characteristic timescales of charm thermalisation

Two distinct notions of thermalization are relevant for quarks in the QGP: chemical and kinetic. Chemical thermalization concerns number-changing processes that drive a given flavour quark abundance toward its equilibrium value. Because the charm mass satisfies $M_c \gg T_{QGP}$, thermal pair creation/annihilation is suppressed ($\propto \exp(-2M_c/T_{QGP})$). By consequence, the charm yield remains essentially fixed by initial hard production and chemical equilibrium is not achieved. By contrast, kinetic thermalization refers to the relaxation of the quark momentum distribution with conserved quantum numbers. This proceeds via elastic scatterings with partons and is controlled by the relaxation time τ_{therm} .

At the LHC, the lifetime of the QGP produced in heavy-ion collisions is about $\tau_{QGP} \sim 10, \text{ fm}/c$, which sets the characteristic scale for the system's evolution. The nuclear crossing time, $\tau_{crossing} \sim 0.1, \text{ fm}/c$, is extremely short. After the collision, the system requires a finite period to reach local equilibrium. Hydrodynamic models rely on assuming thermalisation within about $\tau_{therm} \sim 0.1 - 1 \text{ fm}/c$. The J/ψ hadronization time $\tau_{J/\psi}$ is typically estimated at $\tau_{J/\psi} \sim 0.3-1.0 \text{ fm}/c$ depending on the chosen approach [157–159]. The color-neutralisation time of a $c\bar{c}$ pair depends on the production mechanism: in the color-singlet model it occurs promptly, while

in the color-octet scenario it is delayed until hadronisation.

A rough estimate of the charm thermalization time $\tau_{c,\text{therm}}$, which characterizes how quickly heavy quarks approach thermal equilibrium with the medium, can be obtained by comparing the relevant scales of the system. In a simple scaling picture one may write

$$\tau_{c,\text{therm}} \sim \frac{M_c}{T} \tau_{\text{therm}}, \quad (2.16)$$

where M_c is the charm mass and T the medium temperature. We evaluate this estimate for representative low/high temperatures and slow/fast bulk thermalization.

Case	T [GeV]	τ_{therm} [fm/ c]	$\tau_{c,\text{therm}}$ [fm/ c]
Low T , long thermalization	0.25	1.0	5.1
Low T , fast thermalization	0.25	0.1	0.5
High T , long thermalization	0.50	1.0	2.5
High T , fast thermalization	0.50	0.1	0.2

TABLE 2.1 – Estimate of $\tau_{c,\text{therm}}$ with the $M_c = 1.27$ GeV [1] in low/high temperatures and slow/fast bulk thermalization cases.

The values of $\tau_{c,\text{therm}}$ in Table 2.1 range from 0.2 to 5.1 fm/ c and they are smaller than the typical QGP lifetime at LHC ($\tau_{\text{QGP}} \sim 10$ fm/ c), suggesting that charm can at least partially thermalize in QGP as originally proposed in Refs [160, 161]. Charmonium states are not expected to form before QGP creation. Instead, their formation may occur inside the QGP (if in-medium bound states survive) or during hadronisation, particularly for low- p_T $c\bar{c}$ pairs. The expected hierarchy of timescales is

$$\tau_{\text{crossing}} \ll \tau_{\text{therm}} < \tau_{c,\text{therm}} < \tau_{\text{QGP}}, \quad (2.17)$$

$$\tau_{\text{therm}} \ll \tau_{J/\psi} \ll \tau_{\text{QGP}}. \quad (2.18)$$

This ordering highlights that while charm quarks thermalize more slowly than the bulk QGP constituents, their relaxation time still fits within the QGP's finite lifetime. Therefore, partial or even full thermalization of charm quarks in the QGP appears feasible in LHC heavy-ion collisions.

Energy loss of heavy quarks

After the QGP thermalization, heavy quarks interact with the medium through both collisional (elastic) and radiative (inelastic) processes. The momentum transferred from the thermal bath is typically of order T , much smaller than the heavy-quark thermal momentum³ $p_Q \sim \sqrt{2m_Q T}$. Accordingly, the heavy quark's interaction with the medium can be well approximated as a sequence of independent, uncorrelated momentum transfers. Their momentum diffusion in the plasma can be described by the Langevin equation or, equivalently, approximated using the Fokker-Planck equation [162]:

$$\frac{\partial f_Q}{\partial t} = \frac{\partial}{\partial p} \left[A(p)f_Q + \frac{\partial}{\partial p} (B(p)f_Q) \right] \quad (2.19)$$

Here, $A(p)$ and $B(p)$ are the drag and momentum diffusion coefficients, respectively. Within this approach, the relaxation time $\tau_{c,therm}$ can be expressed as:

$$\tau_{c,therm} \sim \frac{m_Q}{T} \frac{\eta}{e + P} = \frac{m_Q}{T} D_s, \quad (2.20)$$

where m_Q is the heavy-quark mass, T the temperature, η the shear viscosity, $e + P$ the enthalpy density, and D_s the spatial diffusion coefficient. Identifying terms in Equations 2.16 and 2.20, one sees that the relaxation time τ_{therm} can be understood as a diffusion coefficient $\tau_{therm} \sim D_s$.

Heavy quarks lose energy in the QGP through both elastic scatterings and gluon radiation [67]. The average collisional energy loss can be estimated as

$$\langle \Delta E_{coll} \rangle \approx \frac{1}{\sigma T} \int t \frac{d\sigma}{dt} dt, \quad \frac{d\sigma}{dt} \propto \frac{1}{t^2} \quad (2.21)$$

The average radiative energy loss is given by

$$\langle \Delta E_{rad} \rangle \propto \alpha_s C_R \hat{q} L^2, \quad \omega_c = \frac{1}{2} \hat{q} L^2 \quad (2.22)$$

where \hat{q} is the transport coefficient and C_R is the Casimir factor. As the QGP cools, heavy quarks hadronize into D or B mesons. At low transverse momentum (p_T), hadronization predominantly occurs via coalescence with a light quark from the

3. From the nonrelativistic kinetic energy and the equipartition principle, $p^2/(2m) \sim k_B T$. In natural units $k_B = 1$, so $p \sim \sqrt{2mT}$.

medium, while at high p_T , fragmentation becomes the dominant mechanism. Additionally, final state interactions near the critical temperature T_c can further influence the yields and spectra of the resulting hadrons.

Charmonium dissociation in the medium

The use of quarkonia to probe the QGP was proposed by Matsui and Satz in 1986 [131]. The formation time of a $c\bar{c}$ pair is $\tau_f \sim 1/2m_c \approx 0.1 \text{ fm}/c$, while the QGP lifetime is $\sim 10 \text{ fm}/c$. This allows interaction between the pair and the medium. At high temperatures, color screening (Debye screening) leads to quarkonium dissociation [163]. The in-medium potential becomes:

$$V(r, T) = -\frac{\alpha}{r} e^{-r/r_D(T)} + \sigma r_D(T) \left(1 - e^{-r/r_D(T)}\right), \quad (2.23)$$

where $r_D(T)$ is the Debye screening radius. States with smaller binding energies dissociate at lower temperatures, leading to sequential suppression (e.g., $\psi(2S)$ dissociates before J/ψ) [164]. At high T , the potential becomes screened:

$$V_{Q\bar{Q}}(r) = \sigma r - \frac{\alpha_{\text{eff}}}{r}, \quad (T \ll T_c) \quad V_{Q\bar{Q}}(r, T) = -\frac{\alpha_{\text{eff}}}{r} e^{-r/r_D(T)}, \quad (T > T_c) \quad (2.24)$$

with Debye radius $r_D(T)$ shrinking with increasing T . Dissociation occurs when $r_D < r_i$.

Suppression and regeneration mechanisms

Above the critical temperature T_c , charmonium states like the J/ψ are expected to melt. However, at LHC energies, the large number of produced charm quarks opens the possibility of an additional mechanism: regeneration. Thus, both suppression and regeneration must be considered to fully characterize charmonium production in a deconfined medium:

— Suppression of charmonia:

At high temperatures, a significant number of color charges in a small volume generates a color screening effect. This mechanism reduces the range of the quark - antiquark interaction by increasing the color density. When the range of the interaction (screening radius) becomes smaller than the size of charmonia (calculated in theoretical models), the strong interaction can not form heavy bound states anymore. In this case, quark-antiquark binding is

well prevented in the deconfined regions, leading them a dissociation from each other. Quarkonia suppression is an important QGP observable that is well studied with the nuclear modification factor R_{AA} [165].

— **Recombination of charmonia:**

The surprising results obtained at LHC energies in Pb–Pb collisions, particularly the behavior of R_{AA} as a function of p_T and N_{part} compared to those measured at RHIC, have brought renewed attention to the regeneration mechanism for charmonia, which had been predicted well before the LHC era (see Figure 2.9).

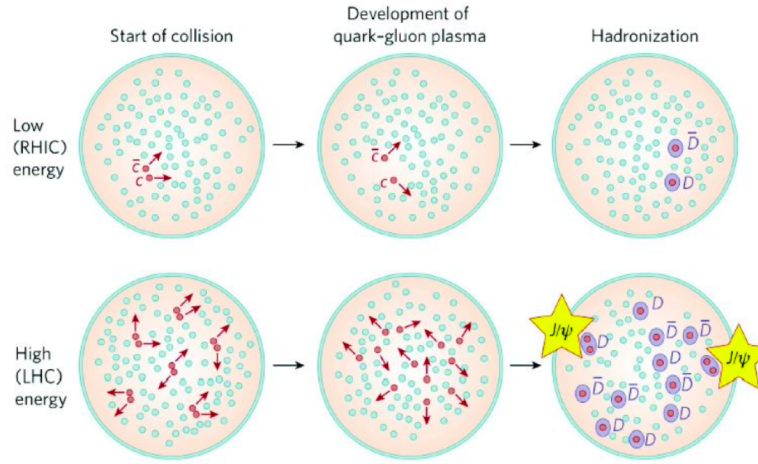


FIGURE 2.9 – Schematic illustration showing that recombination is negligible at RHIC energies but becomes a significant contribution at LHC energies. Figure from [166].

This regeneration mechanism can take place due to the abundance of charm and anti-charm pairs (compared to RHIC) [166]. This means that two charm pairs that were firstly suppressed can be lately recombined into a charmonia state (at the freeze-out or during the QGP evolution). Notice that charmonia suppression is not necessarily always stronger than recombination, since in principle charmonia can also form from (c) and \bar{c} originating from distinct initial-state scatterings.

Similarly than equation 2.14, a key observable used to quantify the suppression in AA collisions is the nuclear modification factor R_{AA} :

$$R_{AA}^{J/\psi} = \frac{Y_{AA}^{J/\psi}}{\langle T_{AA} \rangle \cdot \sigma_{pp}^{J/\psi}} \quad (2.25)$$

where $\langle T_{AA} \rangle$ is the nuclear overlap function, typically estimated using the Glauber model. The quantity $Y_{AA}^{J/\psi}$ denotes the measured J/ψ yield in heavy-ion collisions, while $\sigma_{pp}^{J/\psi}$ is the production cross-section in proton-proton collisions used as a baseline.

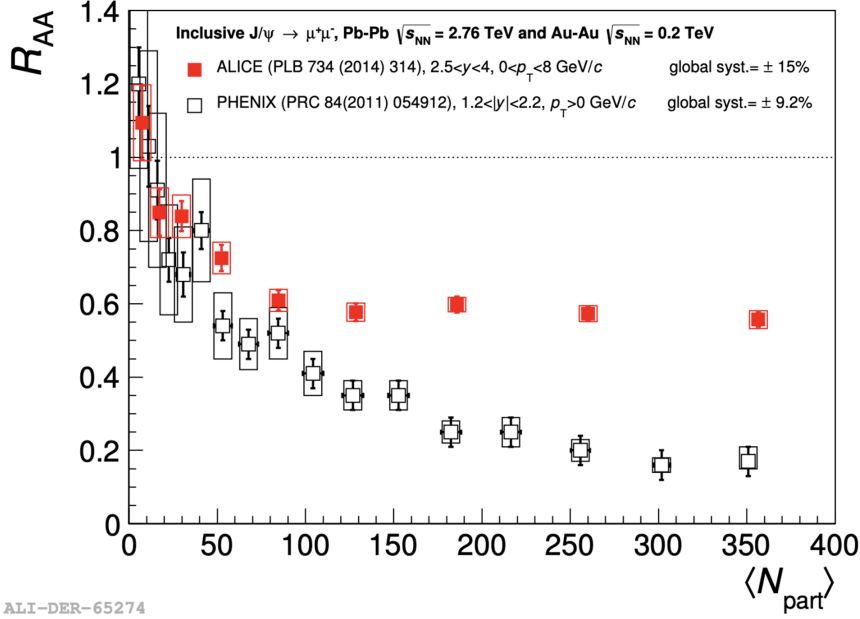


FIGURE 2.10 – Nuclear modification factor R_{AA} versus N_{part} comparing RHIC and ALICE data. Figure from [167].

Figure 2.10 shows the nuclear modification factor R_{AA} as a function of the number of participating nucleons N_{part} , comparing RHIC results [168] (PHENIX, black points) with LHC results [169] from ALICE (red points). The ALICE measurements lie systematically above the PHENIX values across the entire N_{part} range. The difference becomes particularly pronounced in the most central collisions (large N_{part}), where R_{AA} at the LHC is significantly higher than at RHIC. This striking behavior was interpreted as evidence for an additional contribution to J/ψ production at LHC energies. Due to the much larger number of $c\bar{c}$ pairs produced in Pb-Pb collisions at the LHC, charmonium regeneration during plays a substantial role, partially compensating the suppression observed at lower energies.

In Figure 2.11, the p_T dependence of R_{AA} is shown, providing valuable insights into the interplay between suppression and regeneration mechanisms. The enhancement of R_{AA} at low p_T is consistent with the presence of a regeneration component. A strong hint of higher R_{AA} values is observed at $\sqrt{s_{NN}} = 5.02$ TeV (red points) compared to $\sqrt{s_{NN}} = 2.76$ TeV (blue points), reflecting the increased contribution

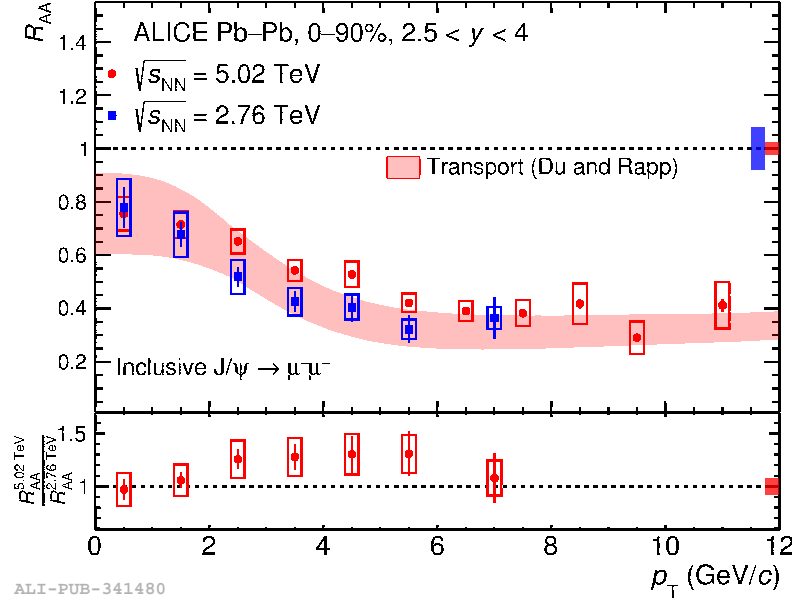


FIGURE 2.11 – The p_T dependence of the inclusive J/ψ (R_{AA}) at $\sqrt{s_{NN}} = 5.02$ TeV [170] (red points) is presented, together with the corresponding results at $\sqrt{s_{NN}} = 2.76$ TeV [171] (blue points) and the prediction from the transport model (TAMU) [172] for the centrality range 0-90%. The ratio $r = R_{AA}^{5.02} / R_{AA}^{2.76}$ is also shown as a function of p_T . Statistical uncertainties are represented by vertical error bars, uncorrelated systematic uncertainties by open boxes, and global p_T -correlated systematic uncertainties by a filled box around $R_{AA} = 1$ [170].

of regeneration at higher collision energies due to the larger abundance of charm-anti-charm pairs. This trend is also visible in the ratio $r = R_{AA}^{5.36} / R_{AA}^{5.02}$, which is greater than one (in the range $2 < p_T < 4$ GeV/c). Theoretical predictions from the TAMU model [172] reproduce the overall p_T shape of the data. A detailed overview of TAMU and other models is provided in the following section.

2.1.4 In-Medium quarkonium models in the QGP

The theoretical description of quarkonium production and suppression in heavy-ion collisions is a challenging problem, owing to the complex interplay between initial hard production, in-medium dissociation, and regeneration mechanisms. Several phenomenological and microscopic models have been developed to account for the observed yields of charmonia and bottomonia at RHIC and LHC energies.

These models differ in the treatment of quarkonium formation, medium effects, and hadronization, reflecting diverse theoretical assumptions and approximations. In the following, we present a not exhaustive list of models that have been proven to be effective in describing quarkonium observables in the QGP.

Statistical hadronization model

Another scenario proposed to explain charmonium production in AA collisions is the Statistical Hadronization Model (SHM) [173]. In this framework, charm quarks are assumed to be produced exclusively in initial hard scatterings and to thermalize in the QGP. No bound charmonium states survive inside the deconfined medium. All charmonia are formed only at the phase boundary during hadronization. Consequently, all hadron species (open and hidden charm included) are assumed to share a common chemical freeze-out temperature.

The total number of charm quarks must be conserved between their initial production and the hadronization stage. This constraint is implemented through the charm fugacity g_c , which adjusts the thermal equilibrium densities such that the final hadron yields reproduce the fixed total charm content. The balance equation relating open- and hidden-charm hadrons then reads:

$$N_{c\bar{c}} = \frac{1}{2}g_c V \left[\sum_i n_{D_i} + n_{\Lambda_i} + \dots \right] + g_c^2 V \left[\sum_i n_{\Psi_i} + n_{\chi_i} + \dots \right]. \quad (2.26)$$

Here, V is the fireball volume at chemical freeze-out, and n denotes the thermal densities of the various open- and hidden-charm states. The terms proportional to g_c and g_c^2 correspond to open- and hidden-charm hadron contributions, respectively.

Tsinghua model

The Tsinghua model is a transport approach that describes the evolution of heavy quarks in the QGP, including both collisional and radiative energy loss, as well as hadronization via coalescence [174]. Tsinghua model employs the non-relativistic Schrödinger equation to describe charmonium wave functions, justified by the large charm-quark mass:

$$\left(\frac{\mathbf{p}_1^2}{2m_1} + \frac{\mathbf{p}_2^2}{2m_2} + V(\mathbf{r}_1, \mathbf{r}_2) \right) \Psi = E\Psi. \quad (2.27)$$

Here $m_{1,2}$ and $\mathbf{p}_{1,2}$ are the masses and momenta of the charm (anti-charm) quarks, and $V(\mathbf{r}_1, \mathbf{r}_2)$ is the heavy-quark potential. Within the coalescence picture, J/ψ mesons are regenerated at $T = T_c$ similarly to light hadrons. On the hadronization hypersurface, color-screening effects on the heavy-quark potential are neglected in this model. The interaction between the $c\bar{c}$ pair is described by the Cornell potential, defined in Equation 2.6.

TAMU model

The TAMU model describes quarkonium suppression and regeneration within a hydrodynamically evolving QGP using rate equations [175]. It incorporates statistical approaches that account for medium-modified binding energies obtained from lattice QCD calculations. This model employs the integration of a Boltzmann kinetic equation to obtain the yield evolution of charmonia as function of time:

$$\frac{dN_\psi(t)}{dt} = -\Gamma_\psi(t)[N_\psi(t) - N_\psi^{eq}(t)]. \quad (2.28)$$

where $N_\psi(t)$ and $N_\psi^{eq}(t)$ is the number of suppressed and regenerated J/ψ and Γ_ψ is the reaction rate.

Open quantum systems

A complementary and dynamic description is provided by the open quantum systems framework, where the heavy $Q\bar{Q}$ pair is treated as a subsystem interacting with a thermal environment (the QGP) [176]. The state of an open quantum system is described not by a wavefunction but by a density operator:

$$\rho = \sum_i p_i |\psi_i\rangle\langle\psi_i|, \quad (2.29)$$

where p_i is the probability for the system to be in the pure state $|\psi_i\rangle$, with $\sum_i p_i = 1$. The density operator evolves non-unitarily due to interactions with the environment, and its trace is conserved: $\text{Tr}[\rho] = 1$. The time evolution of the reduced density matrix ρ_S is governed by a master equation of Lindblad form [177]:

$$\frac{d}{dt}\rho_S = -i[H, \rho_S] + \sum_k \left(L_k \rho_S L_k^\dagger - \frac{1}{2} \{L_k^\dagger L_k, \rho_S\} \right), \quad (2.30)$$

where L_k are Lindblad operators encoding decoherence and dissipation due to the medium. This approach naturally incorporates both screening and stochastic effects such as in-medium dissociation and regeneration.

2.2 Flow in the heavy-sector

The study of flow in the heavy-flavor sector, including both quarkonia and open heavy-flavor hadrons, provides unique insights into the QGP. Heavy quarks are produced early in the collision and traverse the entire medium evolution. They interact strongly enough with the medium to acquire collective motion. Significant flow coefficients indicate that heavy quarks can kinematically thermalize within the QGP.

In this chapter, we present an overview of quarkonia flow measurements. We begin with results for the elliptic flow coefficient v_2 of J/ψ at different collision energies at RHIC ($\sqrt{s_{\text{NN}}} = 200$ GeV) and the LHC ($\sqrt{s_{\text{NN}}} = 5.02$ TeV). Next, we compare $v_2^{J/\psi}$ results at $\sqrt{s_{\text{NN}}} = 5.02$ TeV with transport model predictions. Finally, we report Run 3 v_2 heavy-flavor measurements at $\sqrt{s_{\text{NN}}} = 5.36$ TeV, highlighting comparisons between quarkonia (J/ψ and Υ) and open charm-flavor hadrons (prompt and non-prompt D^0 , prompt D_s^+ , and Λ_c^+).

2.2.1 Flow of J/ψ at LHC and RHIC

At the LHC, $v_2^{J/\psi}$ at forward rapidity in Pb–Pb collisions at $\sqrt{s_{\text{NN}}} = 5.02$ TeV was measured by the ALICE collaboration [178]. At RHIC, $v_2^{J/\psi}$ has been also measured at mid-rapidity in Au–Au collisions at $\sqrt{s_{\text{NN}}} = 200$ GeV by the STAR collaboration [179].

In Figure 2.12, we show the preliminary result of $v_2^{J/\psi}$ at $\sqrt{s_{\text{NN}}} = 200$ GeV from the PHENIX collaboration, comparing them with STAR and ALICE results. The RHIC $v_2^{J/\psi}$ measurements at $\sqrt{s_{\text{NN}}} = 200$ GeV are shown in red (PHENIX) and black (STAR). Within uncertainties, both are consistent with zero, suggesting the absence of the positive v_2 expected from a sizable regeneration contribution. In contrast, the ALICE measurement at forward rapidity (blue) at $\sqrt{s_{\text{NN}}} = 5.02$ TeV clearly shows a positive inclusive J/ψ v_2 . This behavior indicates that regeneration is negligible at RHIC energies, where J/ψ production is dominantly primordial and suppressed, while at the LHC regeneration becomes relevant and leads to a

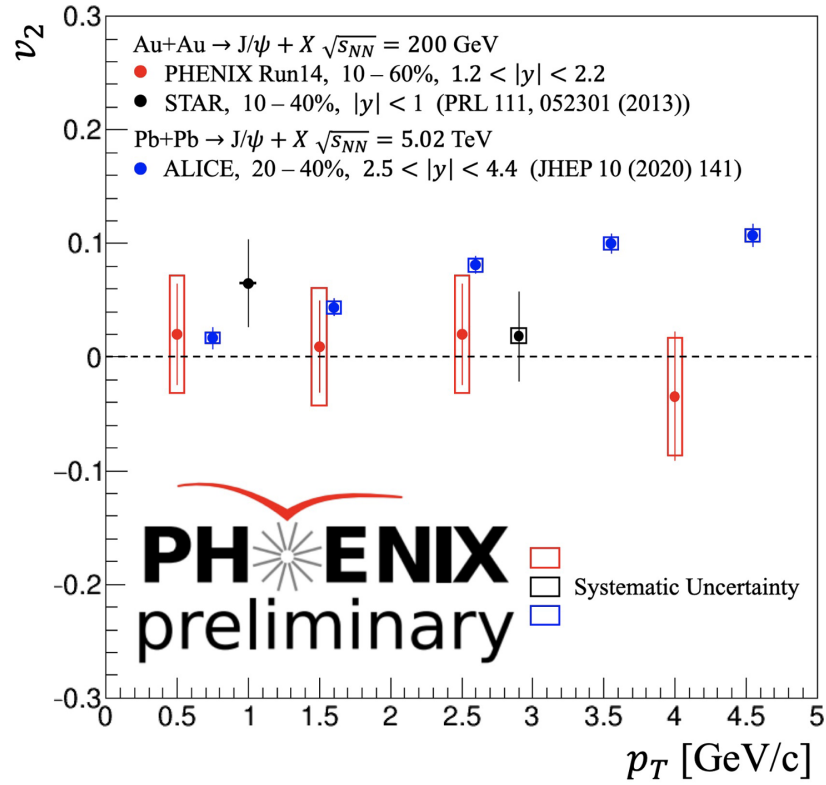


FIGURE 2.12 – Summary of inclusive J/ψ v_2 measurements from ALICE [178], STAR [179] and PHENIX. Figure from [180].

measurable collective flow.

In left panel of Figure 2.13, the $v_2^{J/\psi}$ measurements from ALICE, already shown in Figure 2.12, are reported over an extended p_T range and compared with predictions from the Resonance Recombination Model (RRM) [182]. The positive $v_2^{J/\psi}$ coefficient at low p_T supports the regeneration mechanism. At high p_T , it is not clear if the v_2 of J/ψ could be explained by charm energy loss. The new transport model RRM implements new charm distributions transported through the QGP using Langevin simulations. The model also accounts for charm space-momentum correlations (SMCs) coming from the expanding medium (see the figure 2.13). It also uses a new path-dependence for J/ψ suppression, increasing the elliptical flow value with respect to previous predictions. As shown in figure 2.13, the new RRM model enhances recombination processes at higher momenta compared to earlier predictions and provides a better description of the ALICE data. In the right panel of Fig. 2.13, the J/ψ elliptic flow v_2 from RRM model with 15% shadowing is shown for the inclusive, regenerated, primordial, and bottom-feeddown components (colored curves). Solid lines represent results including SMCs, while dashed lines correspond

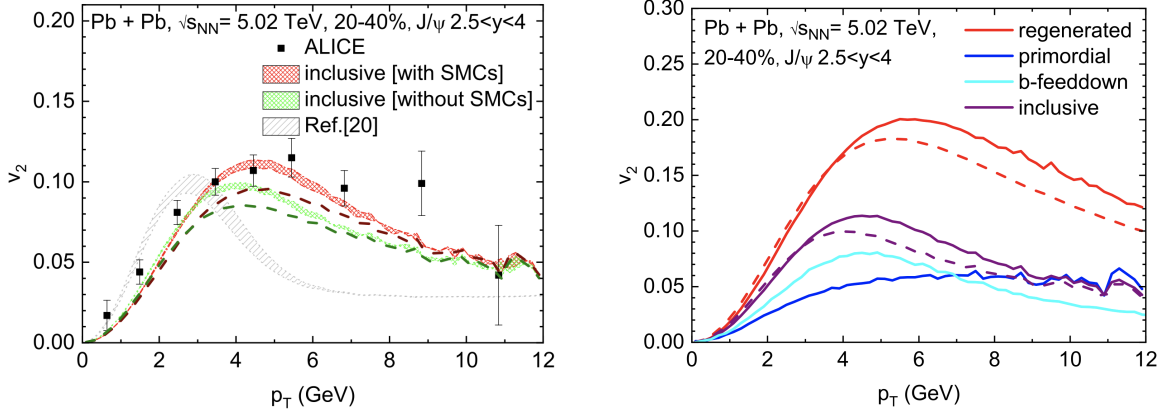


FIGURE 2.13 – Left: Elliptic flow $v_2(p_T)$ of inclusive J/ψ in Pb-Pb collisions at $\sqrt{s_{NN}} = 5.02$ TeV measured by the ALICE collaboration [178], data points are compared with the RRM models [181]. Red/green bands show RRM c -quark spectra at $\tau = 5.2$ fm/ c ; dashed lines at $\tau = 4.2$ fm/ c . Grey band: previous predictions [172]. Right: v_2 of J/ψ with 15% shadowing for inclusive (purple), regenerated (red), primordial (blue), and bottom feeddown (cyan); solid/dashed lines indicate inclusion/exclusion of SMCs.

Figures from [181].

to calculations without SMCs.

Nevertheless, it is important to note that none of these models include event-by-event fluctuations. In Chapter 4 of this thesis, we will investigate the effect of event-by-event fluctuations on the $v_2^{J/\psi}$ measurement, showing that at least for inclusive J/ψ , the effect is not negligible.

Physics interpretation of $v_2^{J/\psi}$ at LHC

In non-central collisions, a positive v_2 is expected from the initial eccentricity ($v_2 \sim \kappa_2 \epsilon_2$). The elliptic flow directly reflects the momentum field of individual charm quarks within the medium [183].

- **At low p_T :** The flow of charmonia such as the J/ψ is significantly influenced by the regeneration mechanism. The uncorrelated c and \bar{c} quarks can recombine to form charmonium states. This coalescence-like process becomes more probable in central collisions, where the charm quark density is highest. The yield of regenerated J/ψ can be approximately described by:

$$N_{J/\psi}^{\text{reg}} \sim \frac{N_{c\bar{c}}^2}{N_h} \quad (2.31)$$

where N_h is the number of light hadrons. In the coalescence approach, the elliptic flow of J/ψ is given by the sum of the charm quark flows, assuming equal flow and collinear recombination of uncorrelated charm-anticharm quarks:

$$v_n^{J/\psi}(p_T) \sim 2 \cdot v_n^c(p_T/2). \quad (2.32)$$

The derivation of Equation 2.32 is given in the annexe.

- **At high p_T :** The suppression mechanism (where $R_{AA} < 1$) is primarily driven by path-length dependent parton energy loss in the QGP. In non-central collisions, the spatial geometry of the overlapping nuclei is anisotropic: the in-plane direction ($\varphi = 0$) corresponds to a shorter medium path length, while the out-of-plane direction ($\varphi = \pi/2$) corresponds to a longer one. It has been shown that, for High- p_T partons traversing the medium therefore lose more energy when emitted out-of-plane, leading to stronger suppression in that direction. This results in an azimuthal dependence of $R_{AA}(\varphi)$ at high p_T , which is closely related to the elliptic flow coefficient v_2 . For high- p_T probes (like jets), this anisotropy has been approximated by [184]:

$$2v_2 \sim \frac{R_{AA}(\varphi = 0) - R_{AA}(\varphi = \pi/2)}{R_{AA}(0) + R_{AA}(\pi/2)} \quad (2.33)$$

what about path-length dependent dissociation

However, the path-length dependent dissociation adds an additional layer of complexity to the interpretation of charmonium production: the observed suppression at high p_T is not solely dictated by partonic energy loss but also depends on the interplay between color-singlet and color-octet production channels. The relative contribution of these states, and their distinct interactions with the medium, can modify both the magnitude and the angular dependence of R_{AA} , adding further complexity to the extraction of the underlying mechanisms.

2.2.2 Flow of open heavy flavor and quarkonia in Run 3

Comparing the flow coefficients (v_2) of different heavy-flavor hadrons (such as D mesons and Λ_c baryons) with Quarkonia (like J/ψ and Υ) is crucial for disentangling the mechanisms of heavy-quark thermalization in the QGP [185].

D mesons and Λ_c baryons, as open-charm hadrons, each contain not only a

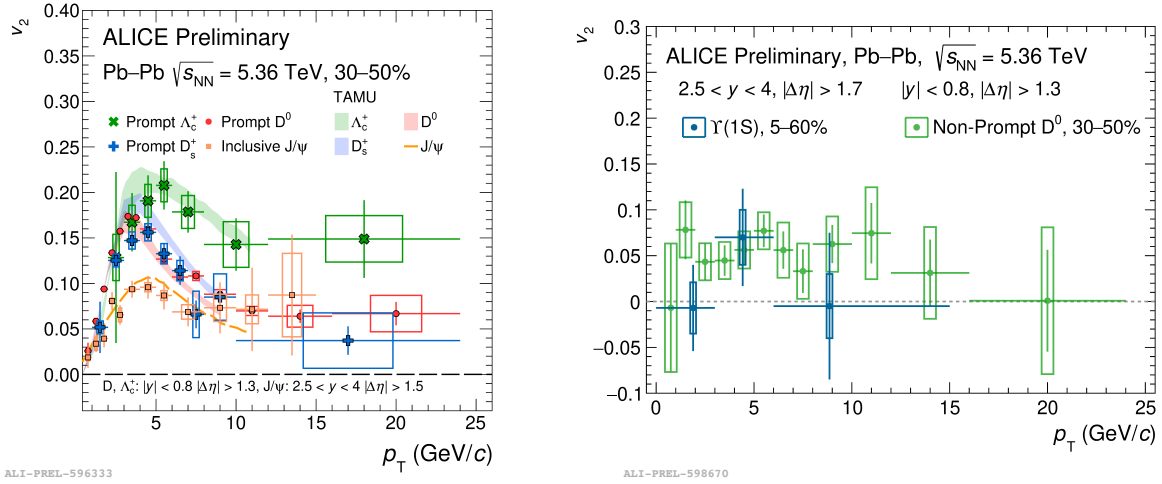


FIGURE 2.14 – Left panel: v_2 of prompt Λ_c^+ , D_s^+ and D^0 at midrapidity vs. J/ψ v_2 at forward rapidity. Right panel: v_2 of non-prompt D^0 at midrapidity vs $Y(1S)$ v_2 at forward rapidity.

charm quark but also a light quark (up, down, or strange quarks). This light component allows these hadrons to more efficiently inherit the collective flow of the medium, as light quarks are expected to thermalize in the QGP.

In contrast, Quarkonia J/ψ and Y mesons are composed solely of heavy-quarks, making their flow a more direct probe of charm quark thermalization.

Figure 2.14 presents a comparison of v_2 for various heavy-flavor hadrons using Run 3 data. The left panel shows a hierarchy of v_2 for hadrons containing a c quark at intermediate p_T : $v_2^{J/\psi} < v_2^{\text{prompt } D^0} \sim v_2^{\text{prompt } D_s^+} < v_2^{\text{prompt } \Lambda_c^+}$. This ordering supports the thermalization process of charm quark in QGP. The TAMU model reproduces the data qualitatively. Alternatively, other theoretical frameworks based on initial-state models, like CGC, predict that correlations among final-state particles could produce flow-like effects. The right panel of Fig. 2.14 shows a hierarchy of v_2 for $Y(1S)$ and non-prompt D^0 : $v_2^{Y(1S)} < v_2^{\text{non-prompt } D^0}$. These data add new constraints on the thermalization of beauty quarks.

Motivation and scope of this thesis

Measuring the J/ψ flow is crucial for understanding the J/ψ production mechanism, particularly the contribution of charm and anti-charm quark recombination, which appears to play a significant role at the LHC. This is suggested by R_{AA} measurements of J/ψ at low- p_T in central collisions. If recombination is indeed

at the heart of J/ψ production in the QGP formed at the LHC, a non-zero elliptic flow (v_2) of the J/ψ is expected. In Run 2, employing the scalar product method, a non-zero v_2 of J/ψ was confirmed by ALICE [178]. These results strongly constrain theoretical models that describe open-charm and quarkonium production, as well as the interactions of charm quarks with light quarks and the QGP. They also constrain models that describe the possible recombination of charm quarks to form quarkonia at later stages of the collision, thus enabling accurate predictions of both the nuclear modification factor (R_{AA}) and v_2 . Currently, experimental v_2 measurements are limited to inclusive J/ψ , without accounting for possible extraction of event-by-event fluctuations. In future, it will be crucial to measure v_2 separately for prompt and non-prompt J/ψ particles, extend v_2 measurements to other quarkonium species such as the $\psi(2S)$ and χ_c particles, and quantify flow fluctuations contributions to the J/ψ azimuthal anisotropy. This thesis addresses this final aspect by applying the cumulant method to measure the inclusive J/ψ $v_2\{2\}$ and $v_2\{4\}$ for the first time. Beyond presenting these novel results, the analysis also provides access to flow fluctuations, which prove to be significant as discussed in Chapter 4.

In parallel, the thesis will also investigate cold nuclear matter effects via Drell-Yan production in proton-nucleus collisions. DY processes provide a sensitive probe of nuclear parton distribution functions (nPDFs) at low Bjorken- x , where gluon saturation and shadowing remain poorly constrained. Using reweighting techniques and DY pseudo-data in the LHCb kinematic range, the Chapter 5 evaluates how future DY measurements could reduce nPDF uncertainties, improving the separation of cold nuclear matter effects from QGP signatures in heavy-ion studies.

Chapter 3

Experimental setup

This chapter provides the foundation for understanding the experimental context of this thesis. It provides a detailed overview of the apparatus used for the measurements discussed in this work. We begin by introducing CERN, the Large Hadron Collider (LHC), and its principal experiments, before focusing on the ALICE experiment. A thorough understanding of the ALICE detector's design, new data acquisition systems, and analysis frameworks is essential for interpreting the results and evaluating systematic uncertainties in the measurements of quarkonia production and flow observables, which constitute the central theme of this thesis. By outlining this experimental context, the chapter lays the groundwork for the robustness and reliability of the results discussed in the analysis chapter.

3.1 The Large Hadron Collider

The Large Hadron Collider (LHC) at CERN consists of two concentric beam pipes arranged in a 26.7-kilometre ring buried approximately 100 metres underground beneath the Franco-Swiss border near Geneva [186]. It was constructed within the tunnel that previously hosted the Large Electron-Positron Collider (LEP) [187], which operated from 1989 until it was decommissioned in 2000. Following the shutdown of the LEP, the tunnel was repurposed for the LHC, a next-generation accelerator approved by the CERN Council in 1994. The LHC was designed to investigate the fundamental nature of matter by studying hadronic interactions, particularly proton-proton and heavy-ion collisions, at the highest centre-of-mass energies ever attained, reaching the tera-electronvolt (TeV) scale [188].

As shown in Figure 3.1, the LHC employs a sequence of pre-existing accelerators as injectors to supply high-energy beams to the main ring. For proton beams, the

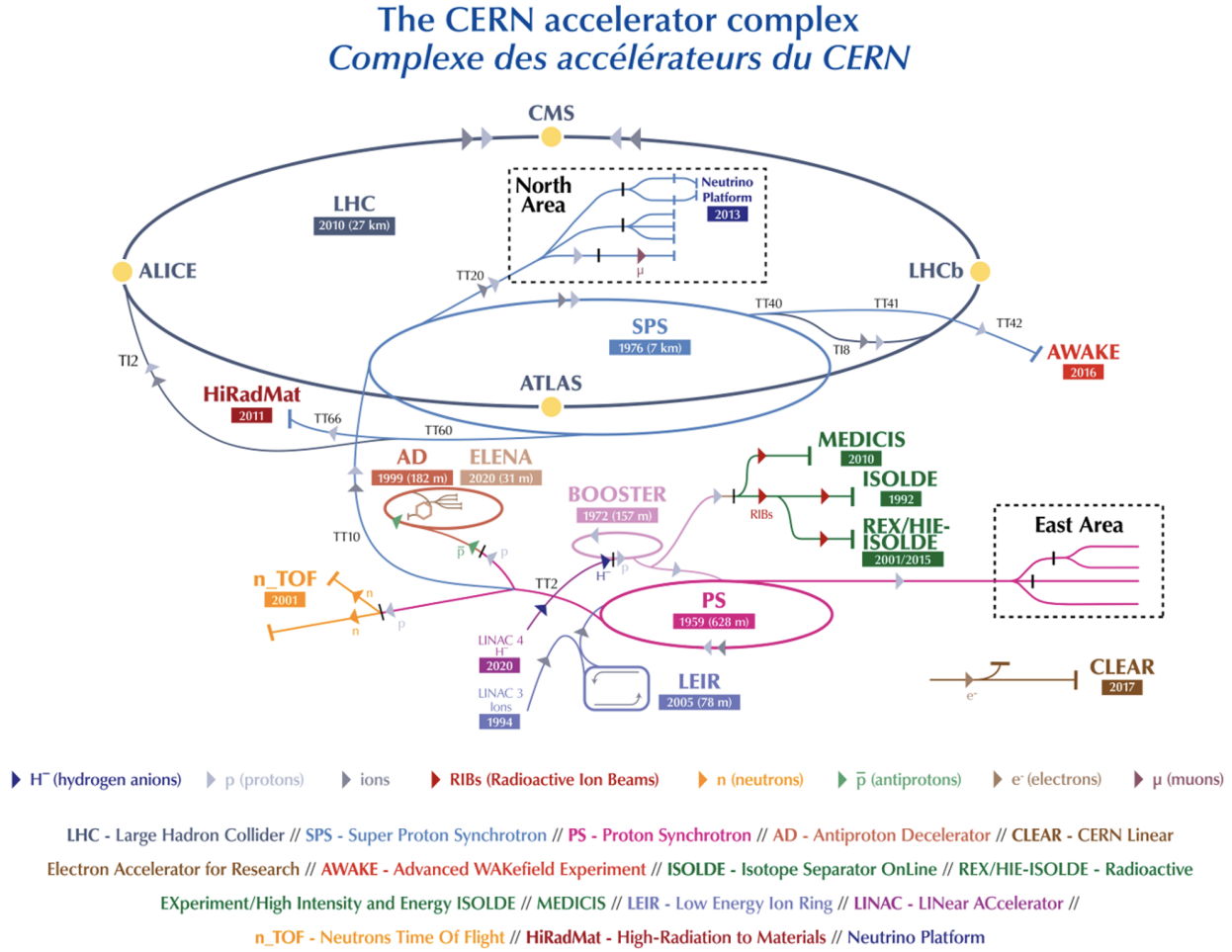


FIGURE 3.1 – The CERN accelerator complex. Figure taken from [189].

injection chain begins with H^- ions generated by LINAC4 [190], where 400 MHz radiofrequency (RF) cavities accelerate them to 160 MeV. These ions pass through a stripping foil, which removes their electrons, yielding protons that are transferred to the Proton Synchrotron Booster (PSB) [191]. There, they are accelerated to 1.4 GeV and bunched before being injected into the Proton Synchrotron (PS), which boosts their energy to 25 GeV. The protons are then transferred to the Super Proton Synchrotron (SPS), where they are accelerated to 450 GeV before being injected into the LHC ring, where their energy is increased to nearly the target value of 7 TeV (the maximum achieved is 6.8 TeV). A comparable acceleration chain is used for lead ions, originating from isotopically pure ^{208}Pb in an Electron Cyclotron Resonance (ECR) source [192]. These ions are accelerated and progressively stripped of electrons through LINAC3, the Low Energy Ion Ring (LEIR), the PS, and the SPS,

reaching about 177.4 GeV per nucleon at the SPS, before being injected into the LHC where they are finally accelerated to approximately 2.68 TeV per nucleon. In addition to symmetric systems (pp and Pb-Pb), the LHC can also perform asymmetric collisions such as proton–lead (p–Pb) and proton–oxygen (p–O).

Within the twin beam pipes of the LHC, two counter-rotating beams (beam 1 clockwise and beam 2 anti-clockwise) circulate simultaneously. Each beam may consist of up to 2800 bunches, with roughly 10^{11} particles per bunch and a nominal bunch spacing of 25 ns. Beam steering are accomplished by 1232 superconducting dipole magnets made of Nb-Ti, cooled with superfluid helium to 1.9 K, generating magnetic fields of 8.33 T. Additional quadrupole and higher-order multipole magnets provide beam focusing and correction. These elements are organized across eight sectors of the ring, which also house critical systems such as collimation (sectors 3 and 7) and beam dumping (sector 6). The interaction point (IP) is where the two beams cross and collide within the LHC. The four main interaction points (1, 2, 5, and 8, shown in Figure 3.1) host the principal LHC experiments:

- **ATLAS** (A Toroidal LHC ApparatuS) [193] is a general-purpose detector and the largest at the LHC. It addresses a broad spectrum of physics topics, from Higgs boson measurements to searches for Beyond the Standard Model (BSM) phenomena such as dark matter. ATLAS is built around a toroidal magnetic system producing a 2 T field and covers a pseudorapidity range of $|\eta| < 2.5$.
- **ALICE** (A Large Ion Collider Experiment) [194] is dedicated to studying heavy-ion collisions and the formation of the QGP, discussed in more detail in the following section.
- **CMS** (Compact Muon Solenoid) [195] is a general-purpose detector designed to investigate a wide range of physics phenomena (similar topics than ATLAS). It is structured around a large solenoid magnet producing a 4 T magnetic field and provides tracking coverage up to $|\eta| < 2.5$.
- **LHCb** detector [196] is a single-arm forward spectrometer designed for precision studies of heavy-flavor physics, in particular processes involving b - and c -quarks, as well as CP violation and rare decays. Covering the pseudorapidity range $2 < \eta < 5$, it exploits the strong forward production of heavy quarks at the LHC¹. The detector provides excellent vertexing, tracking, and

1. The LHCb offers ideal conditions for investigating the Drell–Yan process in the forward region, owing to its wide rapidity coverage, high-precision tracking, efficient muon identification, and the large datasets recorded in both pp and pA collisions. These features motivated the choice of the LHCb kinematic region for the phenomenological Drell–Yan analysis presented in this thesis.

particle-identification (PID) performance. The Vertex Locator (VELO) achieves an impact-parameter resolution of $\sim 20\mu\text{m}$ and decay-time resolution of $\sim 45\text{ fs}$, enabling precise reconstruction of displaced vertices from heavy-flavor hadrons. Momentum measurements are performed by a high-precision tracking system located upstream and downstream of the 4 T·m dipole magnet, reaching a relative momentum resolution of $\Delta p/p \simeq 0.5\text{--}1.0\%$ for tracks in the 5–100 GeV/ c range. Particle identification is provided by two RICH detectors, offering efficient $K/\pi/p$ separation over a wide momentum range, while ECAL and HCAL calorimeters measure photon, electron, and hadron energies. A dedicated muon system enables robust muon identification, essential for many key b -physics channels. LHCb also operates as a charm and beauty factory, benefiting from high luminosity ($\sim 4 \times 10^{32}\text{ cm}^{-2}\text{s}^{-1}$ in Run 2) and producing $c\bar{c}$ pairs at a rate close to 1 MHz. The detector further enhances its physics reach through SMOG, an internal gas-injection system that introduces noble gases (He, Ne, Ar) into the interaction region, enabling fixed-target (p -Gas) operation simultaneously with standard pp running.

ALICE was initially dedicated to heavy-ion physics, and CMS soon became interested in this area too. With its high- p_T measurement capabilities, CMS provides a complementary programme for hard probes, such as bottomonium, jets, and electroweak bosons. ATLAS has also participated in heavy-ion data taking since the start of the LHC. More recently, LHCb has also developed a robust heavy-ion programme, focusing on reference measurements in proton–proton and proton–nucleus collisions, photon–nucleus interactions, and a fixed-target programme with SMOG [197].

Additional specialized experiments (TOTEM [198], LHCf [199], MoEDAL [200], and FASER [201]) are positioned near the main detectors and are dedicated to probing forward physics, cosmic-ray analogues, exotic particles, and BSM signatures.

During the data taking, all LHC experiments follow the LHC operational cycle, that encompasses different phases as shown in Figure 3.2.

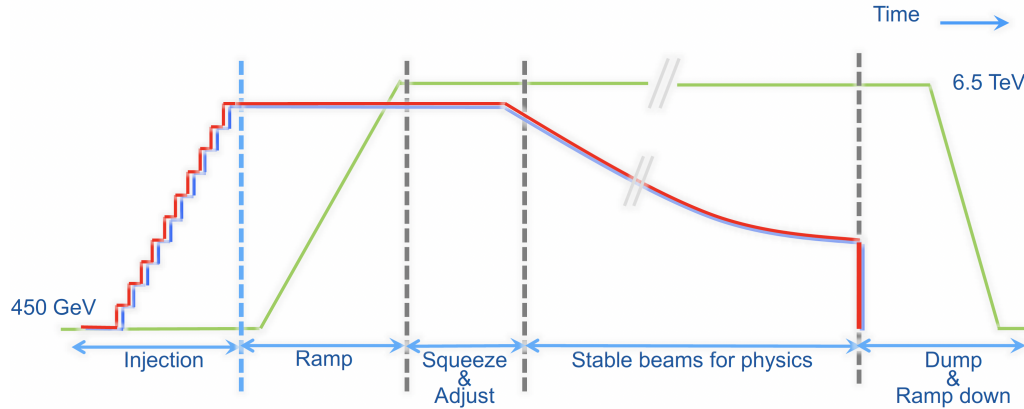


FIGURE 3.2 – The main stages involved in an LHC cycle. The blue and red curves indicate the intensity of the two colliding beams, whereas the green curve shows the beam energy.

It begins with the injection phase, where protons or ion beams are introduced into the LHC.

Once inside, the ramp-up phase starts, gradually powering up the dipole and increasing the energy of the beams by accelerating protons or ions in the radiofrequency cavities. This process leads to a huge stored energy in various components of the machine, such as radiofrequency cavities and dipole magnets. Following this, the squeeze and adjust phase fine-tunes the beam parameters. Here, the intensity, focus, and alignment of the beams are optimized to achieve the desired conditions for collisions at each interaction point. Once these adjustments are complete, the stable beam phase is initiated. At this time, the beams collide in the interaction points of the LHC experiments at full energy and optimal luminosity. The interaction points extend along several centimeters along the beam axis and less than millimeter in the transverse plane. Over time, the number of particles in the beams naturally decreases due to ongoing collisions and beam losses. When the beam intensity drops below a useful level, the beam dump phase begins. The remaining particles are safely directed into dedicated absorption areas. Finally, during the ramp-down phase, the magnetic systems are gradually powered down, releasing the stored energy and resetting the machine for the next cycle.

At the LHC, interaction processes are inherently probabilistic. The likelihood of a specific process occurring in a collision is characterized by its cross section σ , a fundamental quantity with units of area. For rare processes, the cross-section can be calculated theoretically, mainly perturbatively and can be used as a candle for the luminosity monitoring. Investigations of rare processes necessitate large event

samples due to their small cross sections. To reach the required statistical sensitivity, high interaction rates are essential. The event rate $\frac{dR}{dt}$ of a particular process with a cross-section σ (nuclear interaction, Z -boson production...) is given by:

$$\frac{dR}{dt} = L \cdot \sigma, \quad (3.1)$$

where L is the instantaneous luminosity [202], a measure of the collider's performance in terms of interaction potential. Luminosity carries units of $\text{cm}^{-2}\text{s}^{-1}$ and is a crucial metric for any high-energy physics experiment. The integrated luminosity L_{int} represents the accumulated potential for interactions over time and is defined by:

$$L_{\text{int}} = \int L dt = \int \frac{1}{\sigma} \cdot \frac{dR}{dt} dt = \frac{N_{\text{events}}}{\sigma} \quad (3.2)$$

It is commonly expressed in inverse femtobarns (fb^{-1}), where 1 fb^{-1} corresponds to approximately 10^{14} pp collisions at nominal luminosity. An approximate expression for the instantaneous luminosity in circular colliders is given by:

$$L = f_{\text{coll}} \cdot \frac{N_1 N_2}{4\pi\sigma_x^* \sigma_y^*} \cdot F, \quad (3.3)$$

where N_1 and N_2 denote the number of particles per bunch in each beam, σ_x^* and σ_y^* are the transverse Gaussian beam sizes at the interaction point, and F is a geometric factor (typically ~ 1) accounting for effects like the crossing angle and bunch geometry. The collision frequency f_{coll} is determined by the revolution frequency f_0 about 11.2 kHz and the number of bunches per beam n_b , such that $f_{\text{coll}} = n_b f_0$ [203].

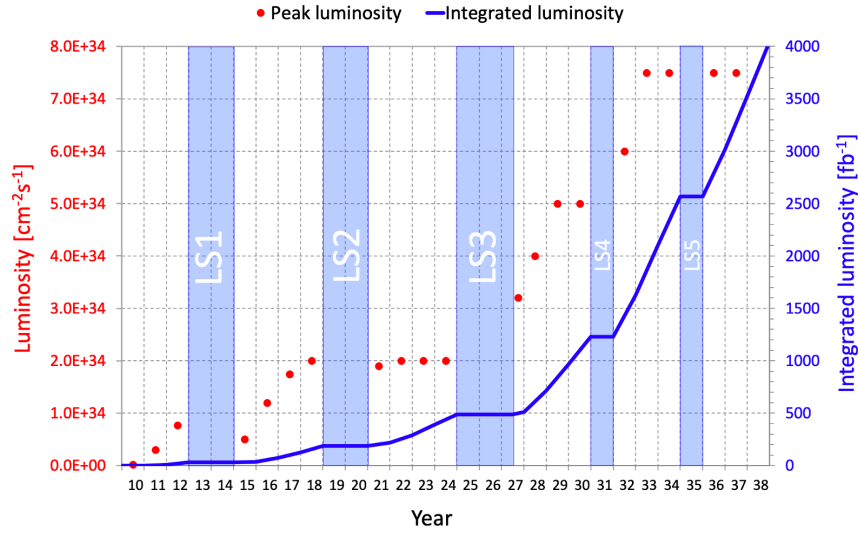


FIGURE 3.3 – Integrated and instantaneous luminosities expected in proton-proton as function of years, including LHC run and long shutdown schedule, taken from [204].

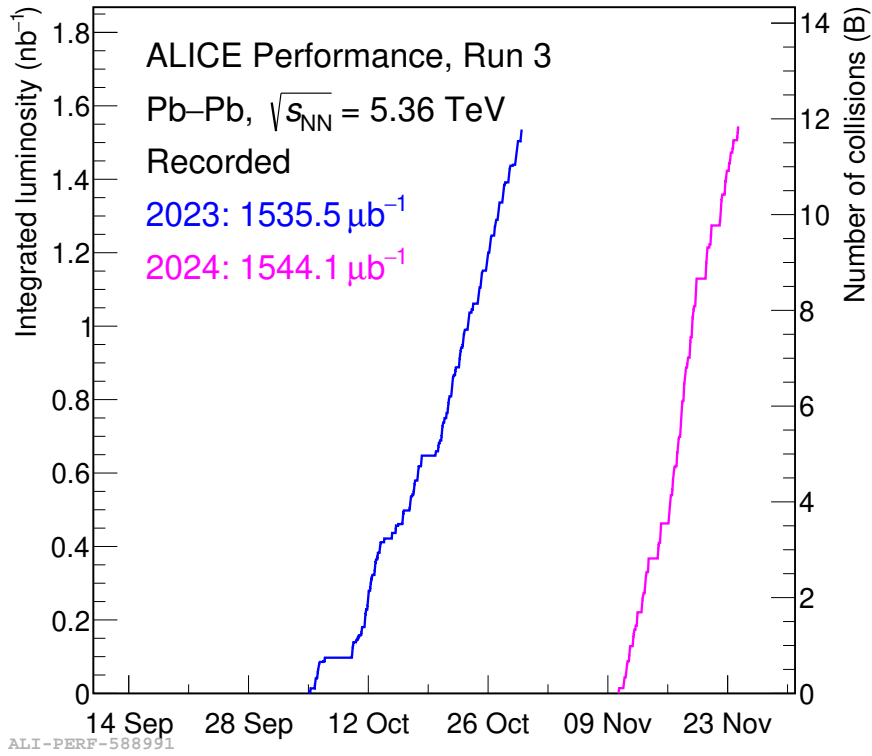
The LHC has been delivering collisions since 2010, and that the operating periods (lasting a few years) are called "Runs", followed by long shutdowns (LS), during which the machine's performance is improved. Figure 3.3 summarizes both the current and projected luminosities (instantaneous and integrated) for pp collisions, together with the long-term schedule of LHC operation. This includes Runs 3 and 4 as well as the major long shutdowns (LS2 and LS3), which define the broader framework for future data-taking opportunities.

The heavy-ion luminosity is limited to $6.4 \times 10^{27} \text{ cm}^{-2}\text{s}^{-1}$ (due to the large electromagnetic cross-sections in such systems), reaching collision rates of 50 kHz for Pb–Pb interactions. The center-of-mass energy and the maximum instantaneous luminosity reached at LHC for pp and Pb–Pb collision modes are summarized in Table 3.1.

Figure 3.4 shows the integrated luminosity and the corresponding number of Pb–Pb events recorded in Run 3 by ALICE. The curves illustrate the accumulation of statistics in October 2023 and November 2024, with the final integrated luminosities reaching $1535.5 \mu\text{b}^{-1}$ and $1544.1 \mu\text{b}^{-1}$ for 2023 and 2024, respectively. However, throughout this thesis, only the 2023 dataset is used, as it was the dataset available at the time of the analysis.

System	\mathcal{L} ($\text{cm}^{-2}\text{s}^{-1}$)	E (TeV)
Run 1 pp	7.7×10^{33}	8
Run 1 Pb–Pb	0.5×10^{27}	2.76
Run 2 pp	2.1×10^{34}	13
Run 2 Pb–Pb	7.4×10^{27}	5.02
Run 3 pp	2.3×10^{34}	13.6
Run 3 Pb–Pb	6.4×10^{27}	5.36

TABLE 3.1 – Maximum energy and luminosity values at the LHC.

FIGURE 3.4 – Integrated luminosity and number of recorded Pb–Pb collisions as a function of time, showing the ALICE Run 3 performance in 2023 and 2024 at $\sqrt{s_{NN}} = 5.36$ TeV.

Note that the LHC has featured extra collision systems in Run 3: proton–oxygen (p–O) at $\sqrt{s_{NN}} = 9.62$, TeV, as well as oxygen–oxygen (O–O) and neon–neon (Ne–Ne) at $\sqrt{s_{NN}} = 5.36$, TeV.

3.2 A Large Ion Collider Experiment (ALICE)

The ALICE collaboration comprises nearly 2000 scientists from 174 institutes across 40 countries. The detector is specifically designed to study the properties of matter under extreme conditions, particularly through Pb–Pb collisions at the LHC, where the Quark–Gluon Plasma (QGP) is formed.

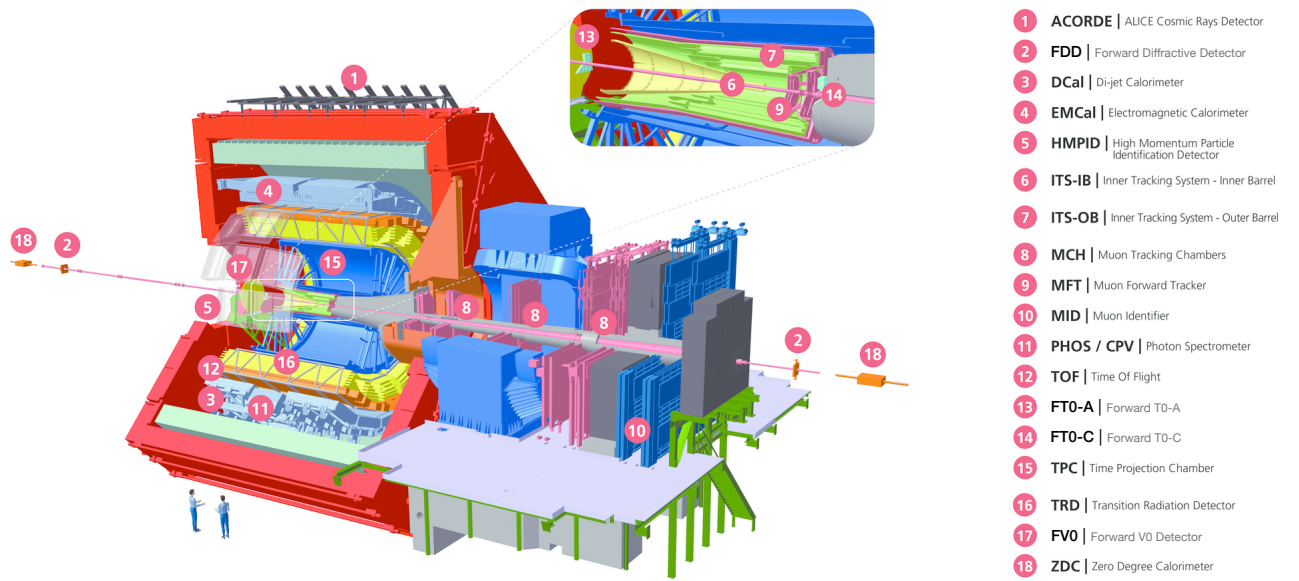


FIGURE 3.5 – Schematic view of ALICE during Run 3.

ALICE is a 10,000-tonne detector, measuring 26 meters in length, 16 meters in height, and 16 meters in width. It is optimized for high-multiplicity events and can reconstruct particles down to very low transverse momenta.

The ALICE detector is organized into the following sections:

- **The central barrel**, covers the mid-rapidity region (left side in Figure 3.5) and it is described in detail in section Section 3.2.1.
- **The forward and backward detectors**, aligned collinearly with the beam pipe and positioned on each side of the interaction point (IP), described in Section 3.2.2.
- **The forward muon spectrometer**, located at forward-rapidity (right side in Figure 3.5), is discussed separately in Section 3.2.3.

The results presented in this thesis concerns data taken during Run 3, the experiment in Run 3 will be described in the following section.

3.2.1 Central barrel

The central barrel of ALICE detector hosts various tracking and particle identification detectors [205], as illustrated in Figure 3.6.

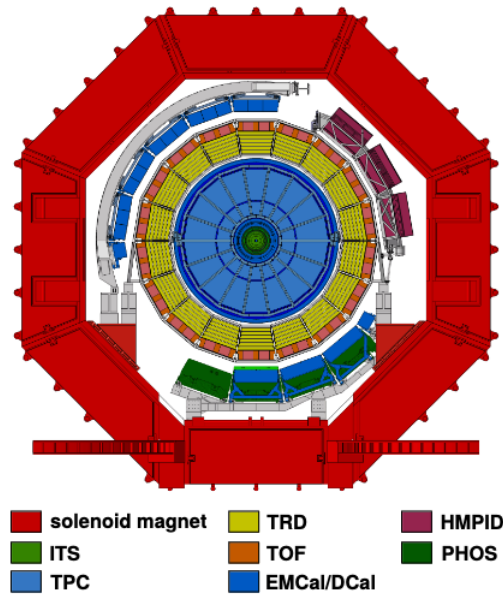


FIGURE 3.6 – Central barrel of ALICE. Figure taken from [205].

Each of these detectors is described in detail in the following subsections.

Inner Tracking System (ITS2)

The Inner Tracking System 2 (ITS2) [206, 207] is the detector closest to the interaction point and plays a vital role in vertex reconstruction, tracking, and particle identification, particularly at low transverse momentum. This detector was completely redesigned and rebuilt for Run 3. The upgraded version, referred to as ITS2, is entirely based on Monolithic Active Pixel Sensors (MAPS). It is composed of 7 concentric cylindrical layers of silicon detectors surrounding the beam pipe, covering a pseudorapidity range of $|\eta| < 1.22$. The left panel of Figure 3.7 shows a schematic representation of the ITS2, highlighting the distinct arrangement of layers separated into two parts. The inner part (Inner Barrel) consists of three 27 cm-long

layers, located between 2.3 and 3.8 cm from the interaction point. The outer part (Outer Barrel) contains four layers with radii ranging from 20 to 40 cm. Each layer is made of ALPIDE (ALice PIdel DEtector) chips, ensuring high spatial granularity.

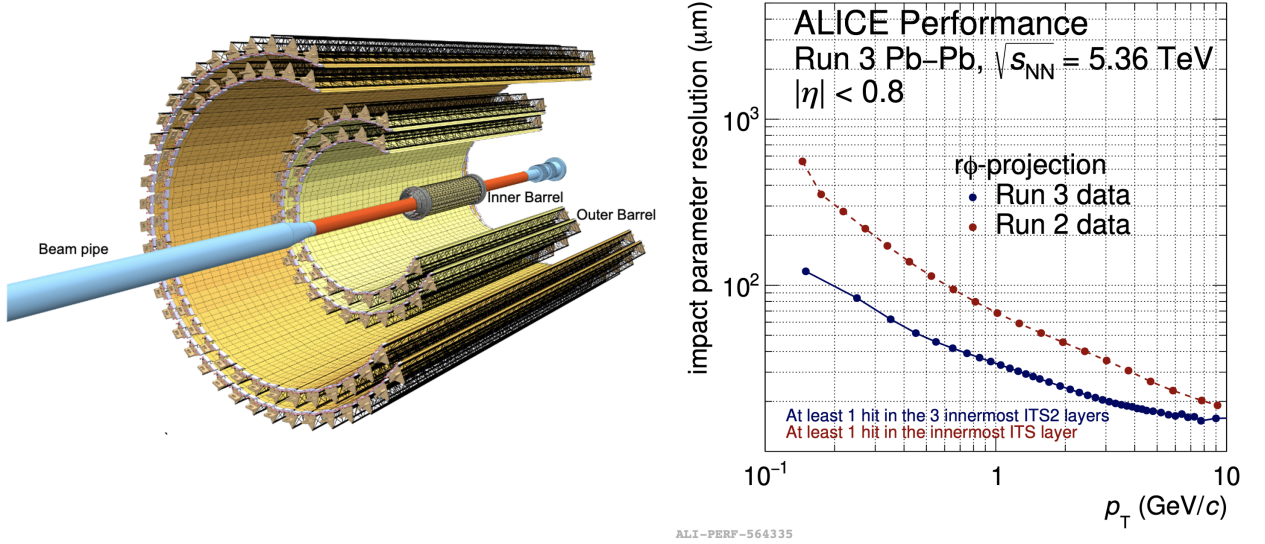


FIGURE 3.7 – Left panel: 3D representation of the ITS2 in Run 3 [206]. Right panel: ITS2 performance with Run 3 Pb-Pb data, showing the impact-parameter resolution as a function of p_T , compared with Run 2 (ITS) [208].

This technology, combined with optimized mechanical support design and materials, results in a silicon pixel detector with a material budget below 0.35% of radiation length (X_0) for the inner part and 0.8% X_0 for the outer part. Minimizing X_0 is crucial in the innermost layers crossed by particles to improve tracking performance and vertex resolution at low momentum. The ITS2 is designed to locate the primary vertex with a spatial resolution on the order of 10 μm and to reconstruct secondary vertices in the central rapidity region with a resolution around 100 μm . The right panel of Figure 3.7 shows the ITS2 performance of the impact-parameter resolution in the transverse plane [208], compared with the corresponding ITS results from Run 2. At $p_T = 1$ GeV/c, the resolution is improved by a factor of two relative to Run 2.

Time Projection Chamber (TPC)

The Time Projection Chamber (TPC) [209] is the main tracking detector of ALICE's central barrel. As shown in Figure 3.8, it is a cylindrical detector around the

ITS2 with a full azimuthal coverage and a pseudorapidity range of $|\eta| < 0.9$. The TPC contains an inner radius of 85 cm, an outer radius of 250 cm, and a length of nearly 500 cm. The TPC is divided into 18 sectors, each with a 20° azimuthal coverage, and has two new readout chambers on each endplate. These chambers use multi-gap Gas Electron Multiplier (GEM) technology [210]. The cylinder is filled with a gas mixture (Ne, CO₂, and N₂) with total volume of 90 m³. Charged particles ionize the gas as they pass through, and the freed electrons drift toward the endplates under an electric field. Based on the charge positions, and electrical signal strengths, it is possible to reconstruct particle tracks and, using the L3 magnetic field, determine their momenta.

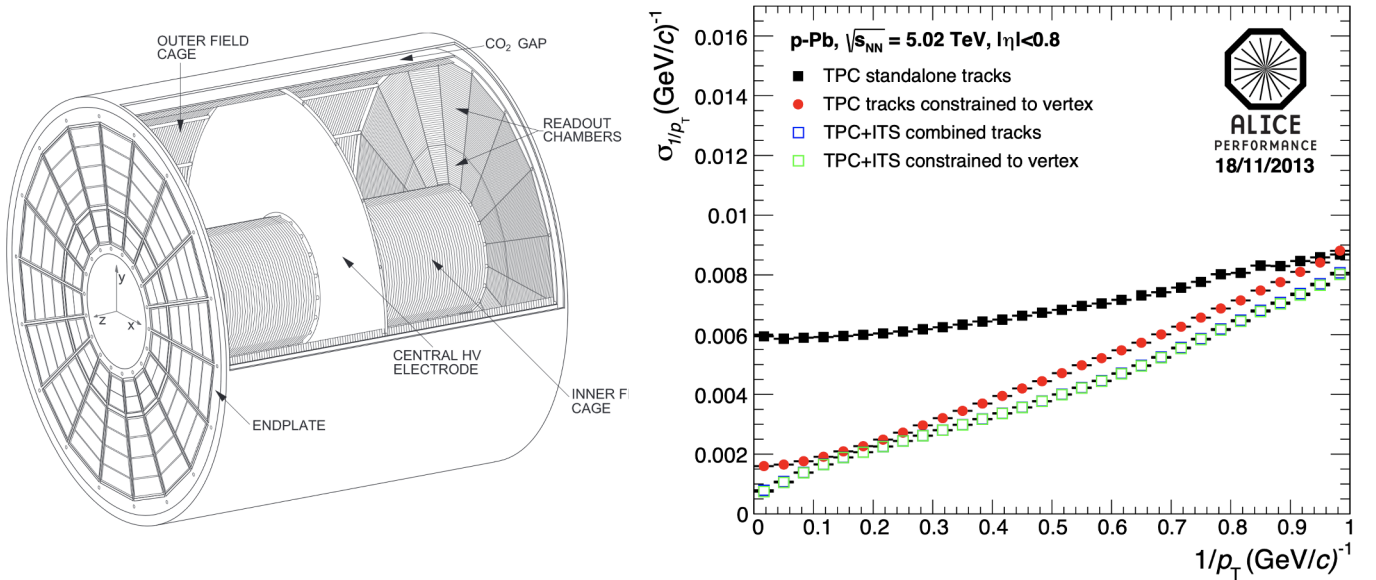


FIGURE 3.8 – Left: Illustration of the TPC layout [209]. Right: Resolution in $1/p_T$ as a function of $1/p_T$ for the ALICE central barrel. The plot compares TPC-only tracking with global tracking (ITS+TPC), both with and without a vertex constraint. Results are based on p-Pb collisions at $\sqrt{s_{NN}} = 5.02$ TeV [211].

The energy loss (dE/dx) of charged particles traversing the TPC gas volume is measured and exploited for particle identification (PID). The right panel of Figure 3.8 illustrates the achievable resolution in the inverse transverse momentum $1/p_T$ [211]. Including the primary vertex in the track fit already yields a significant improvement compared to the TPC standalone tracks case, while the combination of TPC with ITS hits provides the best resolution across the entire momentum range. This enhanced momentum resolution, strengthens the PID capabilities of the TPC,

especially at low momenta where a reliable separation of electrons, pions, kaons, and protons is achieved.

Time-Of-Flight (TOF)

The Time-Of-Flight (TOF) detector [212] is a cylindrical system positioned at a radial distance of 3.7 m from the interaction point, covering the full azimuth ($\Delta\varphi = 2\pi$) in the pseudorapidity range $|\eta| < 0.9$. It is composed of approximately 1600 Multigap Resistive Plate Chambers (MRPCs), providing a total active area of about 140 m^2 . The primary function of the TOF is particle identification through precise measurement of the time taken by particles to travel from the interaction point to the detector. With a time resolution better than 50 ps, the system enables an accurate determination of particle velocity. This allows for the identification of charged hadrons, in particular pions and kaons up to momenta of approximately $2.5\text{ GeV}/c$.

Transition Radiation Detector (TRD)

The Transition Radiation Detector (TRD) [213] is a cylindrical subsystem measuring approximately 7 m in both length and diameter, surrounding the Time Projection Chamber (TPC). It provides full azimuthal coverage and spans the pseudorapidity range $|\eta| < 0.9$. The TRD consists of more than 500 Multi-Wire Proportional Chambers (MWPCs), arranged in 18 sectors, each covering 20° in azimuth. These chambers are filled with a xenon and carbon dioxide gas mixture and feature both amplification and drift regions. The primary role of the TRD is the identification of electrons with transverse momentum $p_T \geq 1\text{ GeV}/c$, a momentum range where pion rejection by the TPC alone becomes insufficient. In addition to electron identification, the TRD contributes significantly to the overall tracking performance by enhancing the momentum resolution for high- p_T tracks and by correcting space charge distortions in the TPC caused by high interaction rates.

ElectroMagnetic Calorimeter (EMCal) and Di-jet Calorimeter (DCal)

The Electromagnetic Calorimeter (EMCal) [214] is located between the TOF detector and the L3 solenoid magnet. It covers an azimuthal angle of $\Delta\varphi = 110^\circ$ and a pseudorapidity range of $|\eta| < 0.7$. The EMCal is complemented by an additional detector, the Di-jet Calorimeter (DCal) [215], which extends the azimuthal coverage by

an additional 70° . Together, the EMCal and DCal comprise 4416 modules organized into twenty supermodules. Each module is a layered sampling calorimeter, made of alternating layers of lead and polystyrene scintillator in a tower geometry. Since photons don't produce a signal in the TPC, electrons and photons are distinguished from one another by matching the EMCal clusters to the TPC tracks. For electrons with energies larger than 10 GeV, the ALICE EMCal's energy resolution is lower than 5%. The detectors enable the measurement of high-energy photons, neutral mesons, and electrons from heavy-flavor decays in jets over a p_T range from 100 MeV/ c to over 100 GeV/ c [216].

High Momentum Particle IDentification (HMPID)

The HMPID [217] is located above the TOF and covers the pseudorapidity region $|\eta| < 0.5$ and the azimuthal range $\Delta\phi = 58^\circ$. It consists of seven modules based on Cherenkov imaging technology [218], with a total detection surface of about 10 m². This detector provides additional identification of high-momentum particles, enabling pion/kaon separation up to 3 GeV/ c and kaon/proton separation up to 5 GeV/ c [219].

PHOton Spectrometer (PHOS) and Charged Particle Veto (CPV)

The PHOS [220] is an electromagnetic calorimeter made of four lead tungstate scintillator modules. It covers $|\eta| < 0.12$ and 70° in azimuth. PHOS is optimized for studying direct photons with a high energy resolution. To reduce background from charged particles, the CPV [221], based on MWPCs, is installed on the PHOS modules. PHOS and CPV measures photons, π^0 and η mesons in the low transverse momentum region up to 10 GeV/ c .

3.2.2 Forward and backward detectors

Two detection systems cover the forward and backward rapidity regions, complementing the central barrel. These systems are characterized by being split into two distinct parts placed on either side of the interaction point.

Sides A and C are defined with respect to the clockwise direction when looking at the LHC from above: side A faces ATLAS and side C faces CMS, corresponding to the right and left directions in Figure 3.5, respectively.

Fast Interaction Trigger (FIT)

The (FIT) [222, 223] is the principal detector system responsible for providing precise measurements of the collision time in ALICE detector in Run 3. Designed as the upgrade and replacement of the V0 and T0 trigger detectors from Run 2. As shown in Figure 3.9, FIT is composed of three subsystems: FT0, FV0, and FDD, strategically positioned along the beam pipe. The FDD consists of two detectors located in the far-backward and far-forward regions at $z = -19.5$ m and $z = +17$ m relative to the interaction point (IP), respectively.

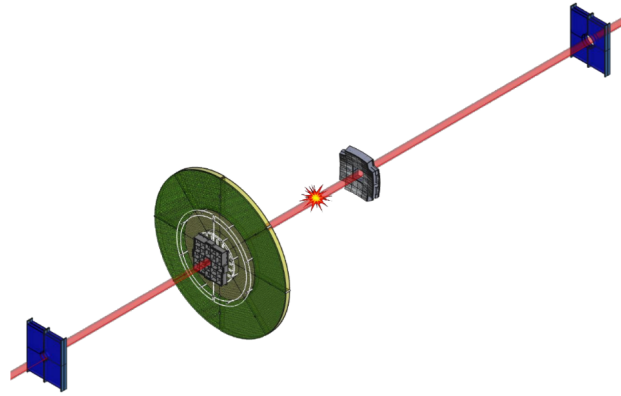


FIGURE 3.9 – 3D view of FIT (not to scale), illustrating the relative positions of the detectors. From bottom left to top right: FDD-A, FT0-A, FV0, FT0-C, and FDD-C [223].

- **FT0:** Composed of two arrays of 12 Cherenkov counters, FT0A and FT0C, placed on opposite sides of the IP. This subsystem delivers precise timing information with a resolution of approximately 25 ps, allowing the determination of the collision time and serving as the start-timer for the TOF detector. FT0 also contributes to the determination of the vertex position.
- **FV0:** A segmented scintillator disk divided into five concentric rings, each covering an equal range in pseudorapidity. With an outer diameter of 144 cm and an inner diameter of 8 cm, FV0 provides detailed multiplicity information across the forward region. In conjunction with FT0, it enables efficient triggering on minimum-bias and high-multiplicity events, as well as the determination of centrality and the event plane orientation.
- **FDD:** This forward detector consists of two arrays of eight rectangular scintillator tiles, symmetrically located on either side of the IP. The FDD contributes

to the identification of diffractive events, the rejection of background from beam-gas interactions, and the measurement of centrality through charged-particle multiplicity. It also aids in selecting ultra-peripheral collisions.

The FIT serves as the fastest and most immediate interaction trigger in the ALICE detector. Beyond triggering, it provides vital input for event characterization, including luminosity monitoring, multiplicity measurements, and precise timing for time-of-flight-based particle identification.

Zero Degree Calorimeter (ZDC)

The ZDC [224, 225] consists of two hadronic calorimeter assemblies located symmetrically on either side of the interaction point, along the beam line (sides A and C), at $z = \pm 112.5$ m from the nominal interaction point. In addition, an electromagnetic calorimeter is installed only on side A, at $z = +7.35$ m. All ZDC subsystems are based on Cherenkov imaging techniques, using quartz fibers that produce Cherenkov light when traversed by charged particles moving faster than the speed of light in quartz. This light is collected and amplified using photomultiplier tubes. The hadronic calorimeters are segmented to allow separate measurement of energy deposited by spectator protons and neutrons emerging from the collisions at zero degrees. The electromagnetic calorimeter, located in the forward region on side A, is dedicated to measuring the energy of photons at large rapidity. The ZDC is primarily used for rejecting beam–gas background events and for determining the collision centrality by measuring the energy deposited by spectator nucleons. It also contributes to luminosity measurements in heavy-ion collisions.

3.2.3 The muon spectrometer

Among the ALICE detectors, the Muon Spectrometer plays a particularly central role in this thesis, since the J/ψ mesons are measured in the muon decay channel at forward rapidity. For this reason, a more detailed description is provided compared to the other detectors discussed in this chapter.

The muon spectrometer [226, 227] (shown in figure 3.10) studies heavy-flavor production via the muonic decay channel, down to $p_T = 0$ for quarkonia, in the large rapidity range $2.5 < y < 4$. Measuring muons in the muon spectrometer will give precious information about open heavy flavor (B mesons and D mesons via semileptonic decays), charmonium production (such as the J/ψ and its excited

state $\psi(2S)$, as well as heavier bottomonia $Y(1S)$, $Y(2S)$, and $Y(3S)$). It also enables studies of low-mass vector mesons like ρ , ω , and ϕ , as well as the gauge bosons W^\pm and Z^0 . The forward spectrometer consists of two primary detector systems: the Muon Chambers (MCH) and the Muon Identifier (MID). As illustrated in Figure 3.10, the spectrometer includes five tracking stations (denoted TRK 1 to TRK 5), each equipped with two tracking chambers that collectively form the MCH. In addition, two trigger stations (denoted TRG 1 and TRG 2), each comprising two trigger chambers, constitute the MID. The diagram also shows the absorbers and the dipole magnet located around the third MCH station.

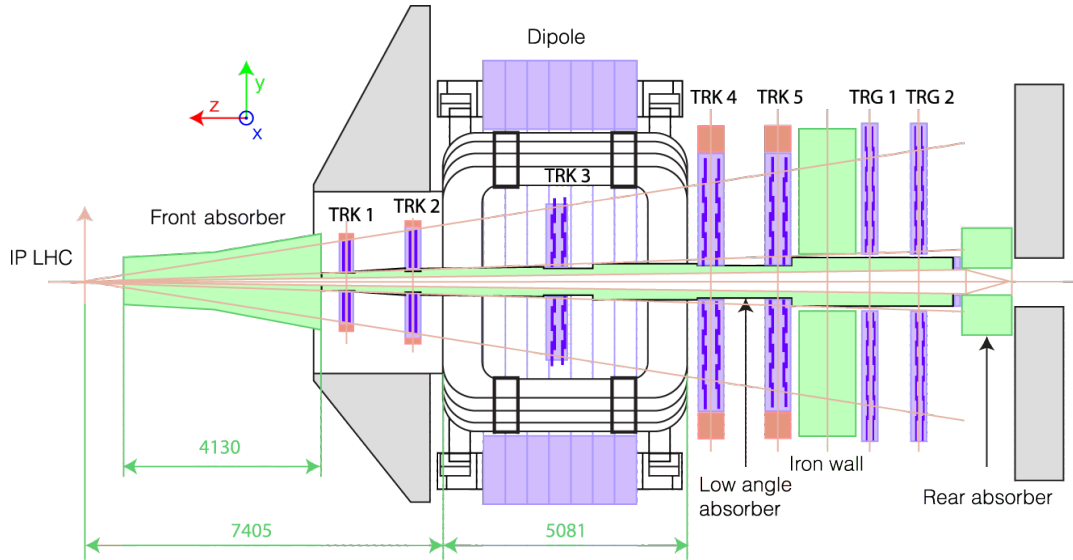


FIGURE 3.10 – Diagram of the muon spectrometer. Figure taken from [228].

The Dipole Magnet

The dipole magnet, situated approximately 7 meters from the interaction point, is among the largest warm dipoles ever built. It spans 5 meters along the beam axis, stands about 9 meters tall, and weighs roughly 900 tons. With a free gap of around 3 meters between its poles, the magnet generates a central magnetic field of approximately 0.67–0.7 tesla (T), yielding an integrated field of 3 T·m perpendicular to the beam axis. This field configuration is essential for bending the paths of charged particles as they pass through MCH, allowing precise determination of their momentum and charge.

The Absorbers

The muon spectrometer employs absorbers to filter out particles other than high-energy muons².

- A small-angle absorber is placed along the beam line to reject beam-gas interactions producing tracks nearly parallel to the beam axis.
- A very thick front absorber is located between the interaction point and MCH. Its purpose is to reduce the flux of initial hadrons by a factor of 100 and stops most of the particles from secondary interactions with small p_T (principally electrons).

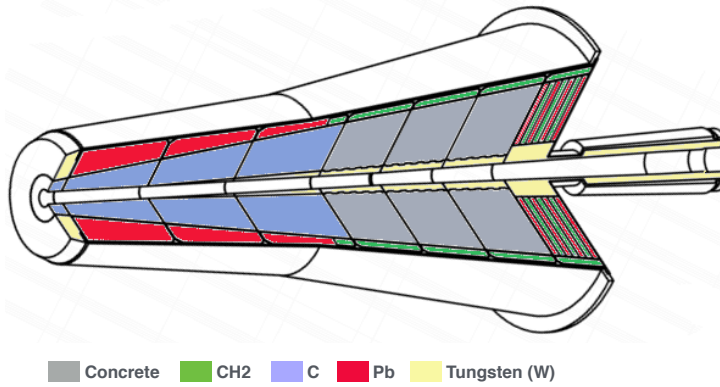


FIGURE 3.11 – Internal structure of the front absorber. Figure taken from [229].

One of the design requirements of the absorber is to minimise the invariant mass resolution deterioration caused by interacting processes like multiple scattering and straggling energy loss ($10 \lambda_{int}, 60X_0$). The absorber consists of low-Z materials at its core and high-Z materials at its outer ends. The material arrangement has been carefully optimised to minimise the impact on the deterioration of the momentum resolution of the muon spectrometer tracking system. A schematic detailing its internal composition is presented in Figure 3.11.

- A muon filter is located between the MCH and MID. Its purpose is to reduce the background from low momentum muon originating from decays within the front absorber and MCH (most of them coming from the decay of kaons

2. Muons, which interact with matter approximately as minimum-ionizing particles (MIPs), can traverse the absorbers and reach the detectors.

and pions).

- Finally, an extra absorber is placed behind the MID to protect the muon spectrometer for particles coming from beam.

Muon Tracking Chambers(MCH)

The Muon Tracking Chambers (MCH) [226, 227] is a muon tracking system consisting of 156 multi-wire proportional chambers distributed over five stations. Stations 1 and 2 are located 5.4 m and 6.8 m from the interaction point upstream of the dipole, while stations 3 (within the dipole), 4, and 5 are at 9.7 m, 12.6 m, and 14.2 m, respectively. Each station contains two chambers. As shown in Figure 3.12, the chambers employ two different *Cathode Pad Readout* (CPR) designs: chambers 1–4 are segmented into four quadrants, while chambers 5–10 are built from several slats³.

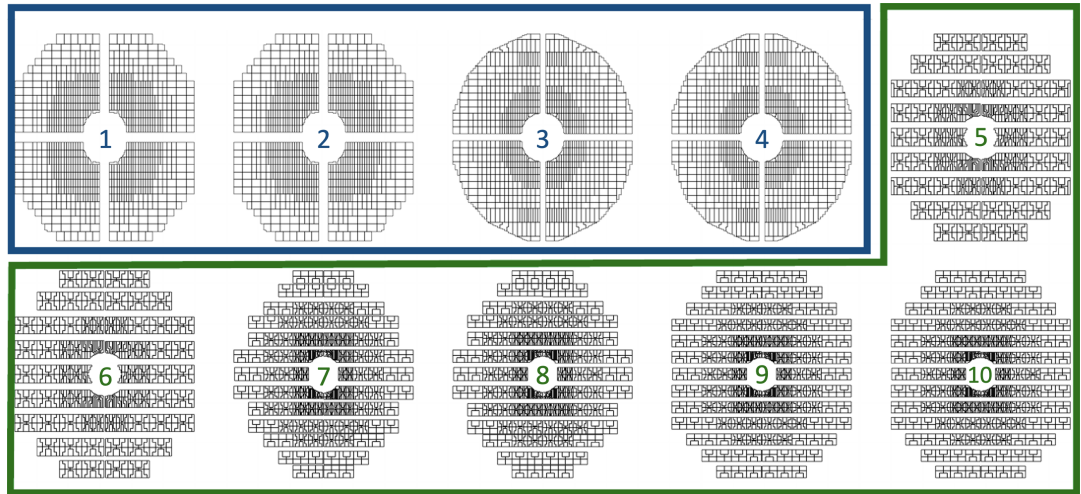


FIGURE 3.12 – Geometry of MCH chambers. In blue: Stations 1 and 2 using quadrants. In green: Stations 3, 4, and 5 using slats. The different contours inside each quadrant/slat represent the Dual Sampas (DS).

Image performed with the cluster map tool (see Section 3.4).

Each quadrant/slat is made of two cathode planes with an anode wire plane in between, immersed in a gas mixture of 80% argon and 20% carbon dioxide. A high voltage electric field is applied between the anode and cathode. When a muon passes through a chamber, the gas is ionized along its path, and the freed electrons

3. The choice of segmentation into quadrants/slats reflects the need to efficiently cover the full azimuthal ($0-2\pi$) detector surface while maintaining acceptable occupancy per readout element.

drift to the nearest cathode. A charge deposit, called a *cluster*, forms and generates an electrical signal. The particle trajectory can be reconstructed in MCH, only if a charged deposit is measured in several chambers. At least one cluster must be present in stations 1, 2, and 3, and one per chamber in either station 4 or 5. In Run 3, the MCH readout electronics were accommodated due to the increased interaction rate in Pb–Pb collisions. The new Dual Sampa (DS) readout cards contain two SAMPA chips [222]. Data are collected on a SOLAR board from several DS cards and then transmitted to the *Common Readout Unit* (CRU), which centralizes data from all detectors. A slight degradation in spatial resolution is expected compared to Run 2 due to the higher readout frequency, which results in a narrower time window for integrating the cluster charge.

In Section 3.4, we present more details about MCH, introducing the cluster map which is a powerful diagnostic and analysis tool developed for the ALICE experiment to visualize and evaluate the response of MCH.

Muon identification system (MID)

The MID is a muon identification system based on *Resistive Plate Chamber* (RPC) technology [226]. It is designed to identify muon tracks, crucial for enhancing the signal of the quarkonium production and to access the muon heavy flavor decay signal of open heavy quarks mesons. The selection is made on the p_T of the two individual muons. MID consists of 72 RPCs across two stations located at 16.1 m and 17.1 m from the interaction point, positioned behind the muon filter. The spatial resolution should be better than 1 cm. Special front-end electronics have been designed to obtain the time resolution of 25 ns necessary for the identification of the bunch crossing. A track is reconstructed in the MID only if three out of four chambers have a signal. In this case, the MID track can be matched with an MCH track.

The Muon Forward Tracker (MFT)

The Muon Forward Tracker (MFT) [230] is a silicon pixel detector introduced in Run 3 to enhance the performance of the ALICE muon spectrometer. With a spatial resolution of $\sim 5 \mu\text{m}$, it allows separation of prompt and non-prompt J/ψ , as the B meson decay length $\sim 500 \mu\text{m}$ exceeds the $\sim 50 \mu\text{m}$ secondary vertex resolution. The MFT comprises 5 disks with 2 detection planes each, housed in

two half-cones around the beam pipe, spanning from $z = -46$ cm to $z = -77$ cm. Each plane holds ladders fitted with 1-5 ALPIDE chips—Monolithic Active Pixel Sensors (MAPS) also used in the ITS2. The MFT includes 936 ALPIDE chips in total (with 512×1024 pixels), delivering the fine granularity needed for high-resolution tracking. The design ensures pseudorapidity coverage of $-3.6 < \eta < -2.5$ with full azimuthal acceptance. The low material budget (0.6% X_0 per disk) preserves tracking precision.

The MFT significantly improves the mass resolution for light vector mesons (ρ , ω et ϕ), and for the J/ψ (by helping, through the removal of accidental tracks from pion and kaon decays).

3.3 Continuous readout and data Processing

During the Long Shutdown 2 (2018-2021), ahead of Run 3, significant upgrades were made to the detector electronics to enable a new operational mode known as continuous readout [231]. In this mode, the detectors record data continuously throughout the entire physics fill, unlike the previous system used during Run 1 and Run 2. Previously, data acquisition was triggered by specific hardware signals (triggers) that responded to detected events of interest. On the software's side, the continuous readout is made possible by the newly developed Online-Offline (O2) framework [232], which is built on the ROOT data analysis framework [233] and incorporates Apache Arrow [234], using a language-independent columnar memory format for flat and nested data, enabling efficient operations on CPUs and GPUs.

In Run 3, to maintain synchronization across the system in continuous mode, all detectors receive a clock signal derived from the LHC's radio-frequency cavities, commonly referred to as the "beam clock". This allows each data point to be timestamped with a precision of approximately 25 nanoseconds, matching the LHC bunch crossing rate. The duration of a Time Frame (TF) is defined as 32 LHC orbits, to enhance synchronous processing efficiency. Each LHC orbit lasts approximately 89 microseconds and includes approximately 2800 bunch crossings (BC). During the synchronous reconstruction phase, the signals collected by each detector are transmitted from the front-end electronics to the First Layer Processors (FLPs).

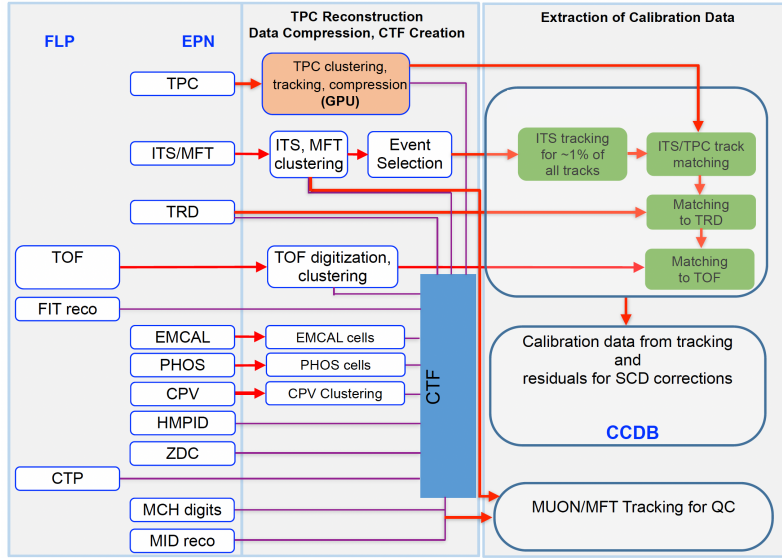


FIGURE 3.13 – Data flow diagram in O² for different detectors. Figure from [231].

At this stage (see Figure 3.13), the raw data are grouped and partially compressed into Sub-Time Frames (STFs) by each FLP. Next, the STFs are aggregated into TFs by the Event Processing Nodes EPNs. In this form, an initial reconstruction and calibration step is performed. The data are then compressed and stored as Compressed Time Frames (CTFs). Each TF can be reconstructed independently and processed in parallel (one TF per EPN) which greatly enhances processing efficiency. The front-end electronics produce raw data at a rate of about 3.4 TB/s. The FLPs compress this to 900 GB/s, and after synchronous (online) processing by the EPNs, the output is reduced further to approximately 130 GB/s [134]. After the synchronous stage, as shown in Figure 3.14, the workflow transitions into the asynchronous phase. In this stage, data reconstruction and final calibrations are carried out using objects retrieved from the Conditions and Calibration Database (CCDB), which stores time-dependent parameters. These operations take place on the EPNs and within the GRID computing infrastructure. The outcome is a set of Analysis Object Data (AOD), which are permanently stored on disk. These AODs contain detailed information about the reconstructed tracks.

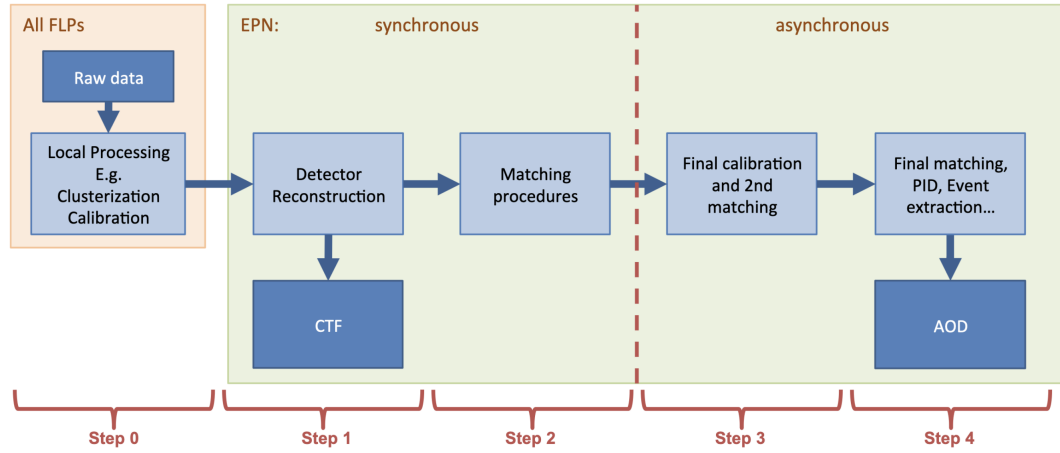


FIGURE 3.14 – Data flow diagram detailing the primary steps involved in the synchronous and asynchronous phases of O². Figure from [232].

In addition, the physics analysis is conducted using the O2Physics framework [235]. Parameters related to collisions and tracks are stored separately in dedicated tables, facilitating flexible and efficient data access. O2physics includes a wide range of specialized tasks developed by the ALICE Collaboration. Analyses across multiple data-taking periods can be carried out using a specialized web-based platform called Hyperloop [236].

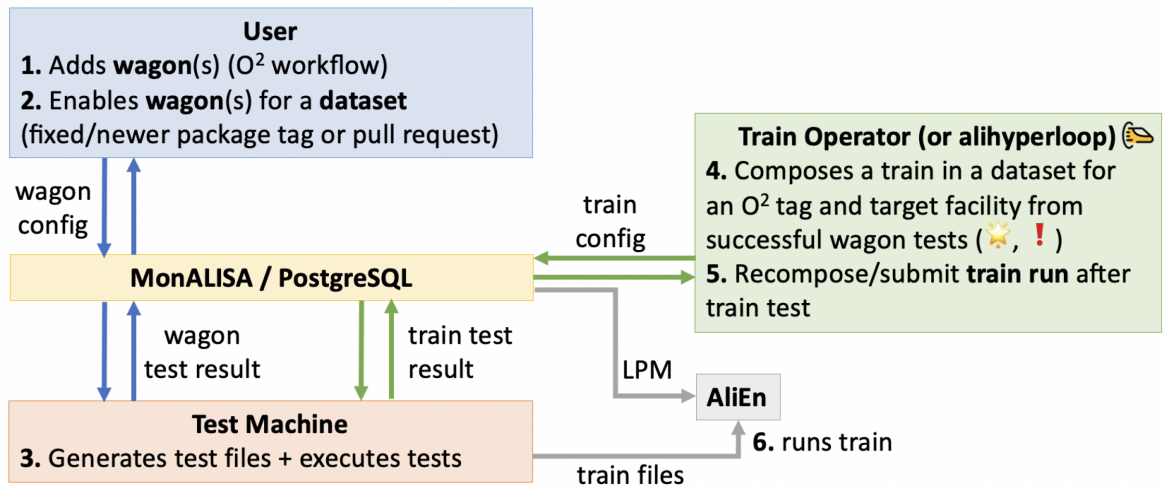


FIGURE 3.15 – Detailed process to submit a Hyperloop train run. Figure taken from [237].

ALICE developed a system known as "LEGO trains" (Lightweight Environment for Grid Operators), which enables users to configure and run multiple analysis

tasks (referred to as wagons) on the same dataset. Figure 3.15 illustrates the complete workflow for submitting a Hyperloop train run. Hyperloop integrates components of the O2 analysis framework to streamline and coordinate the entire analysis process. The final execution is carried out on the AliEn infrastructure [238]. The shift to continuous readout, together with the accompanying new framework and data analysis techniques, is essential for efficiently managing the increased luminosity expected in Run 3.

Although this new working framework has brought considerable advances, its implementation has also posed a number of challenges. Shifting from a trigger-based acquisition paradigm to a continuous data stream needed profound changes in the logic of data acquisition, processing, and analysis. Although the O² framework is powerful and flexible, it demands a significant learning effort from users, particularly with regard to managing parallelised processing tasks, configuring workflows, and optimising performance on heterogeneous architectures (CPU/GPU). Furthermore, transitioning to O2Physics necessitated the partial rewriting of codes, as well as the harmonisation of tools used across the collaboration. Finally, integrating with distributed infrastructures such as GRID and Hyperloop introduced further challenges, particularly in defining efficient data skimming procedures and handling time-dependent conditions.

3.4 Muon reconstruction and quality assurance

Having introduced the global data processing framework in Run 3, we now turn to the muon track reconstruction process and data flow in MCH detector. In this context, diagnostic and monitoring tools are essential to ensure data quality and to identify potential inefficiencies. One such tool is the muon cluster map, developed for the ALICE experiment to visualize and evaluate the response of MCH. Rather than focusing solely on the reconstruction of individual muon tracks, the cluster map provides a comprehensive spatial overview of where clusters are detected across the MCH system. This visualization is essential for identifying dead zones, noisy regions, and inhomogeneities in the detector response, which can arise from hardware issues or electronic failures. The cluster map also plays a crucial role in the development of realistic Monte Carlo simulations, as it allows for the accurate modeling of detector inefficiencies and dead regions. A key component of this process is the implementation of a muon reject list, which identifies all problematic

readout channels that must be masked during reconstruction for both real data and simulations.

In Subsection 3.4.1, we describe the reconstruction process of muon tracks in MCH. Subsequently, in Subsection 3.4.2, we introduce the muon cluster map, providing a data-driven approach to the evaluation of the tracking chamber efficiency. Here we show the final visualization of all chambers and discusses the implementation of a muon reject list, ensuring that the simulated detector response remains consistent with real data conditions.

3.4.1 Data taking and track reconstruction in MCH

The process of data taking in Run 3 of MCH [239, 240] follows a well-defined electronic and data flow chain, as shown in figure 3.16, ensuring that the signals produced by traversing muons are efficiently recorded for subsequent analysis. At the most granular level, the detector is composed of pads (the smallest readout units) across the system. A total of 1,063,528 pads are read with the help of 16,820 Dual Sampa (DS), which collect the analog signals from the pads.

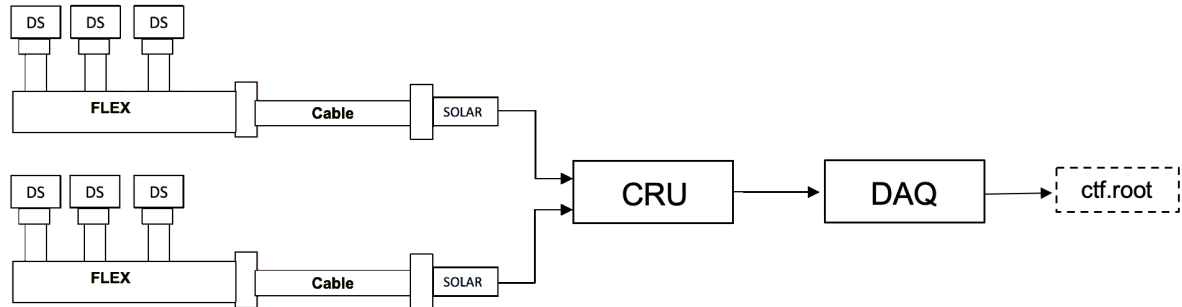


FIGURE 3.16 – Schematic representation of the data taking process of MCH.

These signals are transmitted via FLEX cables to the main readout cables, which carry the data to the SOLARS boards (624 Solars). These boards aggregate and forward the data to the Common Readout Units (CRUs) (30 CRUs), which digitize and format the information before sending it to the Data Acquisition (DAQ) system. Finally, the DAQ system writes the event data to disk in the form of compressed time frame root files (ctf.root), which serve as the starting point for offline analysis [241]. Once the data is stored in the ctf.root files, the reconstruction process takes place as shown in figure 3.17.

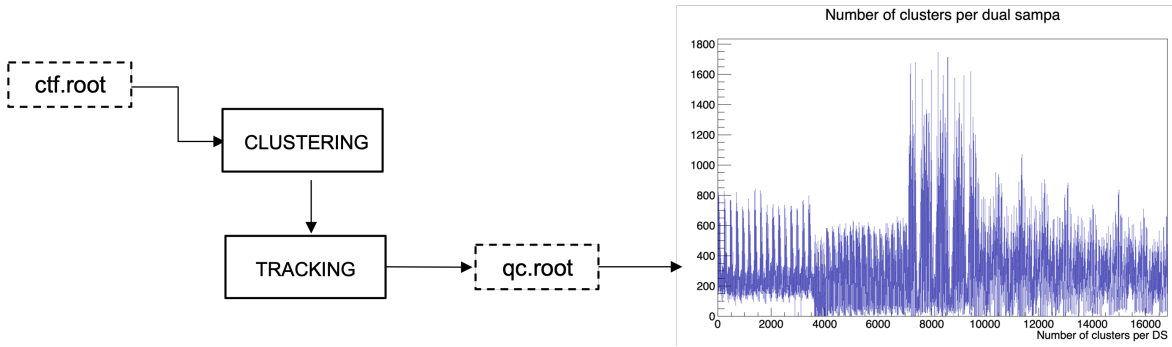


FIGURE 3.17 – Overview of the reconstruction procedure in MCH. The number of clusters per Dual Sampa for 1000 Time-frames of data (2023 pp data) is also shown.

The first step in the reconstruction process is the clustering, where raw detector signals are analyzed to identify clusters (groups of adjacent hits that correspond to the passage of a muon). Hits represent the signals collected in individual pads when a muon traverses the detector. To accurately characterize the charge distribution within each cluster, a Mathieson fit is applied, modeling the expected charge deposition profile and improving position resolution. These clusters are then passed as input to the tracking algorithms, which reconstruct the muon trajectories through the detector. The results of the tracking stage, including detailed information about the reconstructed tracks and the associated clusters, are stored in ‘qc.root’ files for further analysis. Among the various outputs, a key quantity for detector diagnostics is the number of clusters per Dual Sampa, used to construct both the muon cluster map and the muon reject list. Ideally, this list would be determined at the pad level, but the large data volume and computational constraints make this impractical. Instead, the DS granularity is adopted as the fundamental unit for defining detector dead zones. The number of clusters per DS thus serves as the primary metric for identifying inactive regions. In the next section, we present the muon cluster map, the central diagnostic tool for building the reject list and establishing the correct detector acceptance.

3.4.2 Cluster map display

The process of constructing and displaying the muon cluster map begins with a detailed examination of the detector’s segmentation. In this context, each quadrant and slat (as defined in Section 3.2.3) is referred to as a Detection Element (DE). Each

DE is assigned an identification number.

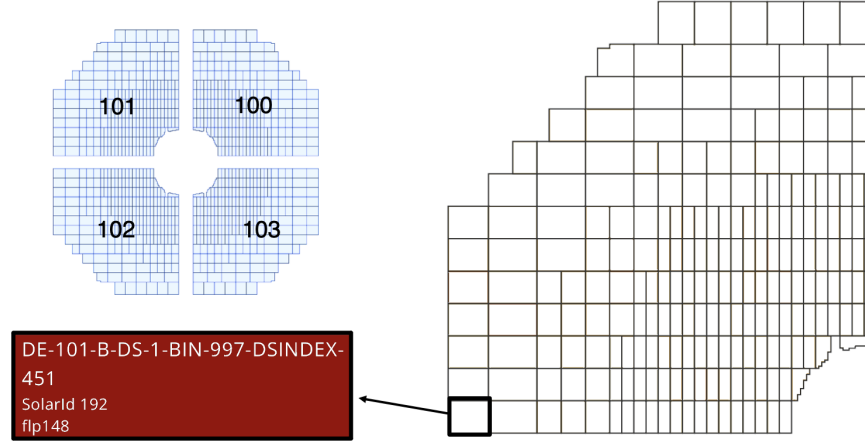


FIGURE 3.18 – Illustration of detection elements (DE) 101, 102, 103 and 104 of the first MCH chamber. The zoom on DE-101 shows all DS with different granularities. The information of the first DS in DE-101 is provided.

In Figure 3.18, we show the geometry of the first four DE (101, 102, 103, and 104) produced with the cluster map code. The DE-101 of the first MCH chamber is shown in a zoomed view, displaying all Dual Sampa (DS) chips at various levels of granularity to illustrate the electronic segmentation. Special attention is given to the first DS chip, highlighting its global identification number (DSINDEX 451) and its associated SOLAR ID.

A normalized color map will be used to display the number of clusters per cm^2 . Once the color mapping is established for all MCH chambers, the final step involves reading the input file that contains the number of clusters per Dual Sampa. Using this information, it is possible to generate the display for all chambers. This comprehensive visualization enables the assessment of detector performance across the entire system.

Figure 3.19 shows the final display of the muon tracking chambers. This mapping is used to identify and mask dead regions during data analysis. The density of clusters is higher near the beam pipe, where particle flux is greater due to the collision kinematics and detector geometry. In chamber 3, we can clearly see a rectangular dead zone in the top-right detection element. The full solar was not working during the data taking, resulting in several DS being masked. Accurate mapping is essential for ensuring that the simulation reflects the true status of the detector. In order to extract the acceptance and efficiency of MCH, realistic simulations are needed.

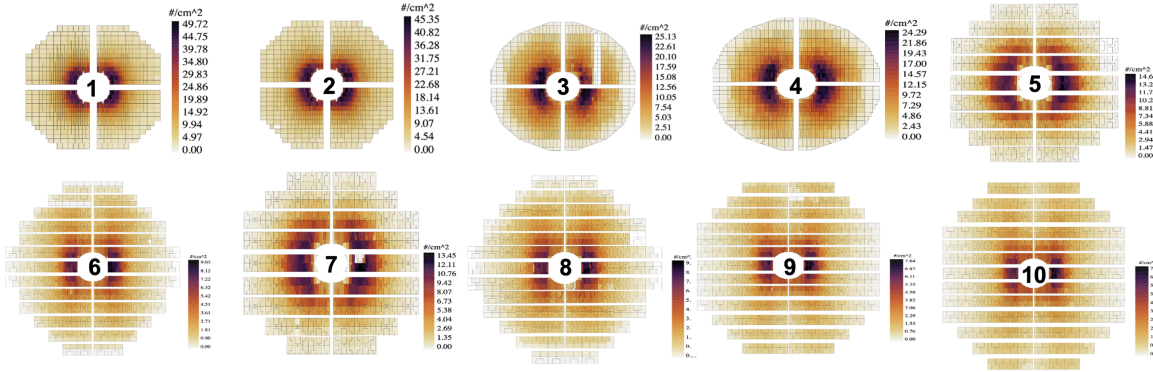


FIGURE 3.19 – All MCH chambers containing a total of 156 detection elements (DE).

By distinguishing systematically the dead regions in the data, we can reproduce a realistic status of the detector in MC simulations.

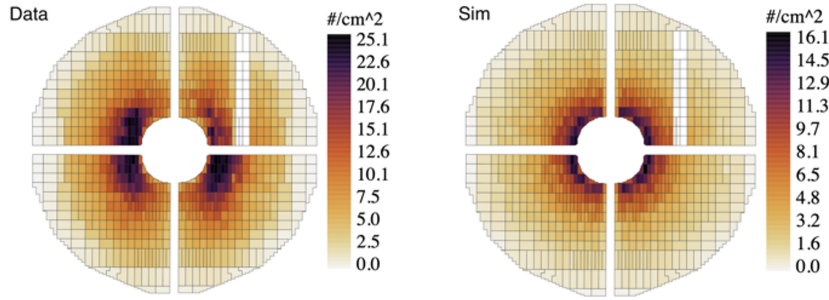


FIGURE 3.20 – Display of the MCH chambers. Left: 1000 TF of MCH data. Right: MC Simulation of 10000 J/ψ decaying to dimuon pairs.

In Figure 3.20, a comparison between experimental data and Monte Carlo (MC) simulation is presented. A realistic acceptance in simulations was achieved through the implementation of a muon rejection list, which identifies all problematic DS. Then a realistic acceptance \times efficiency ($A \times \epsilon$) can be calculated in the following way:

$$A \times \epsilon = \frac{N^{rec}}{N^{gen}}. \quad (3.4)$$

where N^{gen} and N^{rec} are the number of generated and reconstructed J/ψ . The generated J/ψ candidates are obtained by combining all pairs of opposed sign (OS) muon tracks in the spectrometer's acceptance. Future analysers will use the cluster map code to compute the $A \times \epsilon$ factor for different data-taking periods, enabling new Run 3 analyses such as cross-section measurements.

The development of the algorithm for generating cluster maps constituted the service work that every ALICE collaboration member must provide, contributing to the overall detector understanding and analysis capabilities of the experiment.

Chapter 4

Multi-particle cumulant J/ψ analysis

This chapter presents the methodology and results of the elliptic flow and flow fluctuation measurements of the J/ψ meson in Pb–Pb collisions, obtained using the multi-particle cumulant technique with ALICE 2023 Run 3 data.

4.1 Data sample and event selection

4.1.1 Data sample

In this analysis, we used Pb-Pb collisions data collected in November 2023. The data sample consists of 90 runs¹ from various data-taking periods, with the complete list of periods and corresponding run numbers reported in Table 4.1. The following quality control conditions are checked:

- FT0, ITS, MCH, MID detectors are verified to have good data quality, with any missing parts reproduced by simulation to allow further corrections.
- TPC shows Good or Limited Acceptance, while MC is reproducible or indicates Bad PID².

The latest reconstruction pass (pass4) is adopted for this analysis, which includes the most recent calibrations and detector alignments. To optimize resources, a streaming procedure is applied using the **O2Physics framework**, which records only selected collision and track-level data for analysis. This significantly reduces the dataset size from 2.3 PB of raw data to 7.1 TB of the streamed dataset.

1. A run is a continuous period of stable data acquisition during which the LHC’s detectors record signals from particles produced in collisions (or other processes, such as cosmic rays).

2. The term bad PID refers to tracks for which the particle identification is unreliable or inconsistent with expectations. This may arise from detector malfunctions, misassociated clusters, insufficient signal-to-noise ratio, or discrepancies in the reconstructed kinematic variables. Such tracks are excluded from physics analyses.

Period	Runlist
LHC23zzf	544013
LHC23zzg	544028, 544032
LHC23zzh	544091, 544095, 544098, 544116, 544121, 544122, 544123, 544124
LHC23zzi	544184, 544185, 544389, 544390, 544391, 544392
LHC23zzk	544454, 544474, 544475, 544476, 544477, 544490, 544491, 544492, 544508, 544510, 544511, 544512
LHC23zzl	544548, 544549, 544550, 544551, 544564, 544565, 544567, 544568, 544580, 544582, 544583, 544585
LHC23zzm	544614, 544652, 544653, 544672, 544674, 544692, 544693, 544694, 544696, 544739, 544742, 544754, 544767
LHC23zzn	544795, 544813
LHC23zzo	544868, 544887, 544917, 544931, 544961, 544963, 544964, 544968, 545004, 545008, 545009, 545041, 545044, 545047, 545060, 545062, 545063, 545086, 545103, 545117, 545184, 545185, 545210, 545222, 545223, 545246, 545249, 545262, 545289, 545291, 545295, 545311, 545312, 545345

TABLE 4.1 – Run numbers corresponding to each data-taking period (october 2023) in the LHC23 dataset.

4.1.2 Event Selection

Events are selected based on several physics-motivated criteria to ensure data quality and minimize systematic biases. The selection process focuses on identifying clean collision events while preserving the physics of interest. The following conditions are applied:

- **Primary vertex selection:** Requires the primary vertex to be within ± 10 cm of the nominal interaction point along the z -axis ($|z_{vtx}| < 10$ cm).
- **Trigger selection:** The TVX (T0 Vertex) trigger is required to be active, ensuring that events have a valid collision signal. This trigger uses timing information from the FT0 detector to identify Pb-Pb collisions, as explained in chapter 3.
- **Time frame border rejection:** Events located at time frame borders are excluded to avoid reconstruction issues that could affect the flow measurements.
- **Same bunch crossing rejection:** Events involving collisions within the same bunch crossing are removed.
- **Vertex consistency:** Events with a discrepancy greater than 1 cm between the vertex position reconstructed from tracks (z_{PV}^{tracks}) and from FT0A-C timing

coincidence (z_{pV}^{FT0A-C}) are discarded.

- **TPC occupancy control:** Events with extremely high TPC occupancy³ can cause ambiguities, overlapping signals, and are rejected to avoid tracking inefficiencies that could bias the flow measurements.
- **ITS dead zone rejection:** Events affected by known ITS dead zones are excluded to ensure uniform detector acceptance, which is essential for accurate flow measurements.

4.1.2.1 Centrality determination

In heavy-ion collisions, centrality characterises the impact parameter of the collision, which determines the initial geometry of the system. The centrality classes of Pb–Pb collisions are determined by fitting the measured FT0 amplitude on the C side ($-3.3 < \eta < -2.1$) to a Glauber Monte Carlo (MC) model coupled to a negative binomial distribution (NBD), in accordance with the procedure established in previous analyses [242]. The average number of participating nucleons, $\langle N_{\text{part}} \rangle$, which characterises the collision geometry, is obtained from the Glauber calculation by classifying events according to the FT0C amplitude.

Figure 4.1 shows the measured distribution of the FT0C amplitude in Pb–Pb collisions at $\sqrt{s_{NN}} = 5.36$ TeV. The data are fitted with the Glauber MC model coupled to an NBD (red curve). The vertical lines indicate the boundaries of the centrality classes, ranging from the most central to the most peripheral events. In this analysis, we focus on the semi-central centrality class⁴ 10–30% in order to ensure sufficient statistics for reliable flow measurements, using the multi-particle cumulant method.

3. Occupancy refers to the average probability that a given readout channel registers at least one hit in a defined time window.

4. We will typically refer to centrality class as a disjoint partition of events. This means one event can only be in a given centrality class.

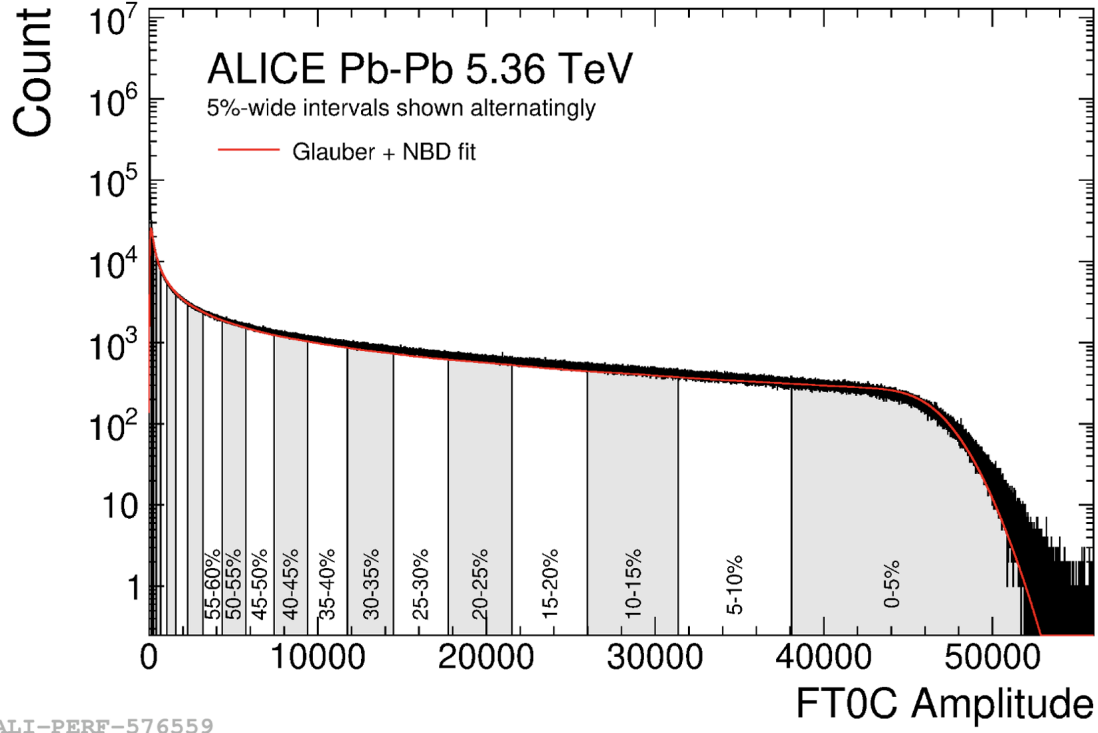


FIGURE 4.1 – Distribution of the FT0C amplitude measured in Pb-Pb collisions at $\sqrt{s_{NN}} = 5.36$ TeV. The distribution is fitted with the Glauber MC combined with a NBD, shown as a red line. Centrality classes are also indicated by vertical lines.

4.2 Track and muon selections

The general tracking procedure followed in the ALICE experiment has already been presented in Chapter 3. In this section, we focus on the specific selection criteria applied to barrel tracks, single muons, and dimuons, as described in the following subsections.

4.2.1 Barrel track selections

To ensure the quality of the central barrel reconstructed tracks, the following set of selections is applied:

- Central barrel matched tracks between ITS and TPC detectors.
- Pseudorapidity selection: $-0.8 < \eta < 0.8$ to ensure the correct acceptance of the TPC detector.

A dedicated transverse momentum p_T range is applied to the analysis: $0.2 < p_T < 3.0$ GeV/c. This interval is chosen to align with the standard selection used in other ALICE charged-particle cumulant studies and allows us to focus on tracks predominantly originating from bulk physics processes. The lower limit of 0.2 GeV/c ensures we capture the maximum number of particles while maintaining good tracking efficiency, while the upper limit of 3.0 GeV/c helps suppress contributions from jets and high- p_T processes that could introduce non-flow correlations. This p_T range provides optimal sensitivity to collective behavior.

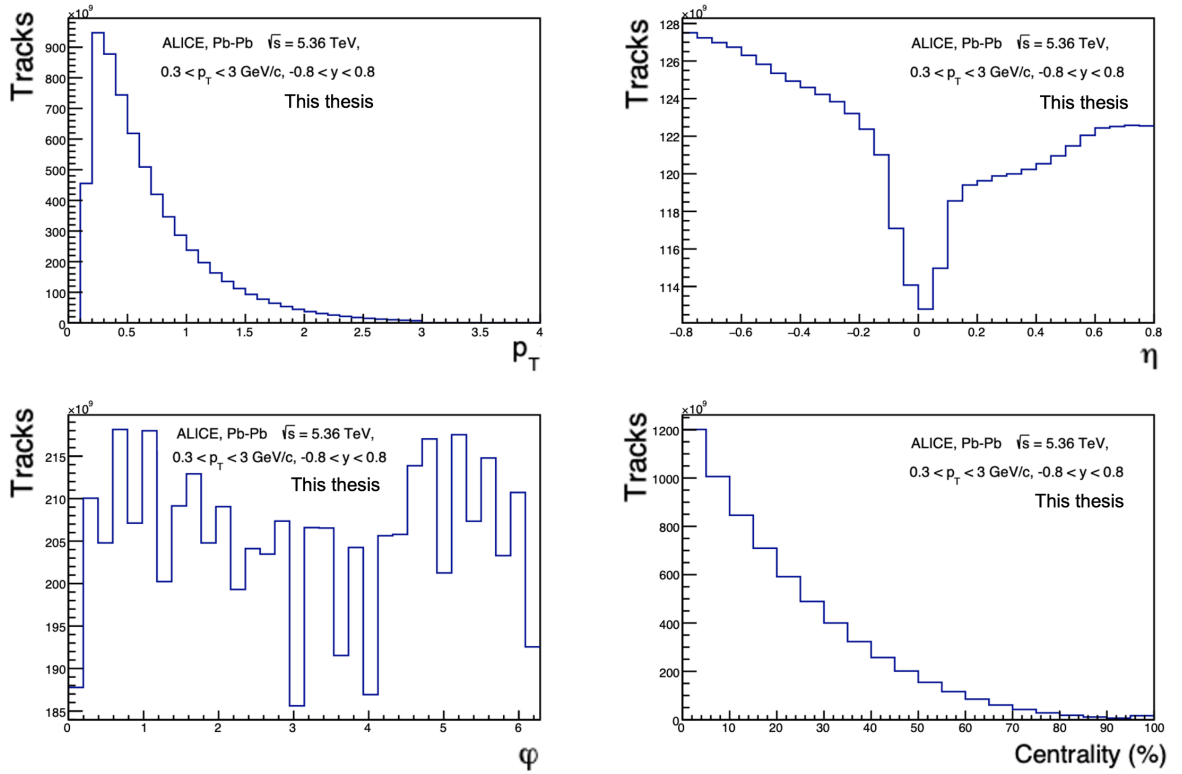


FIGURE 4.2 – Distributions of charged particle tracks at mid-rapidity as functions of transverse momentum (p_T), pseudorapidity (η), azimuthal angle (ϕ), and centrality.

Figure 4.2 shows the distributions of charged particle tracks at mid-rapidity as functions of transverse momentum (p_T), pseudorapidity (η), azimuthal angle (ϕ), and centrality. Already at this stage, with only track selection criteria applied (before any event cut), the expected physical distributions are clearly observed: The p_T spectrum (top left panel) exhibits the characteristic steeply falling shape. Most produced charged particles carry low transverse momentum, while high- p_T tracks are comparatively rare. The spectrum decreases smoothly across several orders of mag-

nitude. The η distribution (top right panel) is nearly flat over the measured interval, considering the large range of the y-axis. A small dip appears at $\eta = 0$, originating from detector acceptance limitations and track reconstruction inefficiencies in the central region. The azimuthal distribution φ (bottom left panel) is approximately uniform. Minor deviations arising from detector inhomogeneities or acceptance effects may still be present (corrections for these effects are in principle required). However, to first order, these do not impact the analysis because cumulant-based techniques are intrinsically insensitive to such distortions⁵. The centrality distribution (bottom right panel) decreases steeply toward more peripheral collisions. This trend is expected, as central collisions (low centrality percentiles) produce a much larger number of charged particle tracks, while peripheral events (high centrality percentiles) yield significantly fewer tracks.

4.2.2 Muon and dimuon selection criteria

To obtain a high-purity muon sample, several selection criteria are applied to individual muon tracks. The cuts are defined as follows:

- Only tracks matched between the MCH and MID detectors are considered, ensuring complete muon identification through the entire spectrometer.
- The pseudorapidity of each muon track must satisfy $-4 < \eta < -2.5$, corresponding to the acceptance of the muon spectrometer.
- The transverse momentum (p_T) of single muon track is required to be $p_T > 1$ GeV/c. This selection is crucial for suppressing low-momentum muons, which significantly contribute to the combinatorial background in the dimuon spectrum.
- The track radius at the end of the absorber must lie between 17.6 cm and 89.5 cm to exclude muons passing through the high-Z absorber region, where multiple scatterings takes place.
- The product of the track momentum and its distance of closest approach (DCA) must be less than 6σ to suppress background from beam-gas interactions.

Opposite-sign dimuon track pairs (referred to as dimuons) that fulfill the above

5. When extracting the flow of J/ψ using dimuons with the cumulant method (see Section 4.5), the results are not affected by this effects, since the method does not rely on the reference flow shape (see Equation 4.59). Likewise, the scalar product method employs three sub-events requirements with an imposed η -gap, ensuring insensitivity to artificial anisotropies (see Section 1.5.4 in Chapter 1).

requirements are combined to form J/ψ candidates. Only candidates falling inside the spectrometer's rapidity coverage ($2.5 < y < 4.0$) are considered in the analysis.

4.3 Multi-particle cumulant method

This section describes in detail the multi-particle cumulant technique used to extract the flow coefficient v_n [243], focusing in the second harmonic flow coefficient v_2 . This approach is based on analyzing azimuthal correlations among charged particles within each event. The multi-particle cumulant method offers several advantages over traditional flow measurement techniques such as the Event Plane (EP) and Scalar Product (SP) methods. While EP and SP methods can provide precise measurements, they are sensitive to non-flow effects (contributions from jets, di-jets, resonance decays, and other short-range correlations) that can enhance the measured flow signal. The cumulant method addresses this limitation by constructing higher-order correlations that naturally suppress these non-flow contributions. Multi-particle cumulants have been successfully applied to measure v_2 for charged particles in the central barrel [244, 245], demonstrating their effectiveness in suppressing non-flow effects. In this analysis, we extend this technique to measure J/ψ flow at forward rapidity, where the separation between the central barrel and muon spectrometer provides a natural pseudo-rapidity gap that further minimizes non-flow contributions. Moreover, detector-related artifacts (such as inhomogeneous acceptance or track splitting) can artificially enhance two-particle correlations. Multi-particle cumulants provide a more robust measurement by mitigating the impact of such experimental effects, including fake tracks more generally. This robustness has been discussed in detail in Ref [246].

4.3.1 Q-vectors

The Q-vector for harmonic n is constructed as the complex sum over all charged particle tracks in an event:

$$Q_n = \sum_{i=1}^N e^{in\phi_i}, \quad (4.1)$$

where ϕ_i is the azimuthal angle of the i -th particle, and N denotes the total number of charged particles in the event. To minimize non-flow effects, the analysis exploits

the natural pseudo-rapidity gap between the ALICE central barrel and the muon spectrometer. Two flow vectors are defined: the event flow vector, $Q_n = Q_n^x + iQ_n^y$, constructed from soft charged particles, and the dimuon flow vector, $p_n = p_n^x + ip_n^y$.

4.3.2 Multi-particle correlation

As already introduced in section 1.5.3, the coefficients $v_n = \langle \cos[n(\phi - \Psi_n)] \rangle$ characterize the anisotropic flow of particles produced in heavy-ion collisions respect to the symmetry plane Ψ_n and generally exhibit dependence on transverse momentum (p_T) and rapidity (y). When studied as functions of these kinematic variables, they are referred to as differential flow. The average $\langle \dots \rangle$ is taken over all particles of an event within a given kinematic interval. Since Ψ_n is not directly accessible in experiments, anisotropic flow is typically calculated through azimuthal correlations among detected particles.

The natural pseudo-rapidity gap of approximately 1.7 units between the ALICE central barrel and the muon spectrometer provides an effective separation that drastically limits non-flow effects. Since short-range correlations from jets typically occur at $\Delta\eta \lesssim 1$, this large gap ensures that the particles used to construct the flow vectors are sufficiently separated in rapidity, thereby minimizing jet-related and other non-flow contributions.

4.3.2.1 2-particle correlations

The simplest approach to compute v_n without estimation of Ψ_n , involves two-particle azimuthal correlations [243]:

$$\langle 2 \rangle = \left\langle e^{in(\varphi_i - \varphi_j)} \right\rangle \quad (4.2)$$

where i is the imaginary unit⁶, φ_i and φ_j are the azimuthal angles of two different charged tracks ($\varphi_i \neq \varphi_j$) in the same event. The brackets $\langle \rangle$ indicate an average taken over all track combinations within a given event. To relate this to v_n , we take the real part of equation 4.2 and decompose the angles relative to the reaction plane Ψ_n :

6. In this thesis, the symbol i may appear in two distinct contexts: as the imaginary unit ($i^2 = -1$) in complex numbers, and as an index label in summations or subscripts (e.g. x_i). The intended meaning should be clear from the context, but readers are advised to pay attention to avoid confusion.

$$\begin{aligned}
\langle \cos(n(\varphi_i - \varphi_j)) \rangle &= \langle \cos(n[(\varphi_i - \psi_n) - (\varphi_j - \psi_n)]) \rangle \\
&= \left\langle \cos(n(\varphi_i - \psi_n)) \cos(n(\varphi_j - \psi_n)) \right. \\
&\quad \left. + \sin(n(\varphi_i - \psi_n)) \sin(n(\varphi_j - \psi_n)) \right\rangle.
\end{aligned} \tag{4.3}$$

Due to the symmetry of the system in heavy-ion collisions⁷, such as in Pb–Pb, the sinus terms average to zero:

$$\langle \sin(n(\varphi_i - \psi_n)) \sin(n(\varphi_j - \psi_n)) \rangle = 0, \tag{4.4}$$

The corresponding two-particle correlation becomes:

$$\langle 2 \rangle = \langle \cos(n(\varphi_i - \psi_n)) \cdot \cos(n(\varphi_j - \psi_n)) \rangle = \langle v_n^2 \rangle. \tag{4.5}$$

As shown in Equation 4.2, the two-particle correlator $\langle 2 \rangle$ is computed on an event-by-event basis by summing over all distinct pairs of charged tracks ($i \neq j$) in the event, so it can be written as:

$$\langle 2 \rangle = \frac{\sum_{i \neq j}^M e^{in(\phi_i - \phi_j)}}{\sum_{i \neq j}^M 1}. \tag{4.6}$$

where M is the number of charged tracks in the event (multiplicity). The denominator counts the number of distinct particle pairs, which is simply: $\sum_{i \neq j}^M 1 = \sum_i^M \sum_j^{M-1} 1 = M(M-1)$. Substituting this relation into Equation 4.6, we have:

$$\langle 2 \rangle = \frac{1}{M(M-1)} \sum_{i \neq j} e^{in(\phi_i - \phi_j)}. \tag{4.7}$$

This result provides a direct method for computing two-particle correlations using measured particle azimuthal angles. Furthermore, this summation can be expressed compactly using the Q-vector defined earlier. Specifically, by evaluating the squared module of Q_n :

7. In symmetric collisions (e.g. Pb–Pb), the particle distribution is mirror-symmetric about the event-plane angle ψ_n . Since $\sin(n(\varphi - \psi_n))$ is odd under this reflection, its event-averaged contribution cancels, while $\cos(n(\varphi - \psi_n))$ survives.

$$|Q_n|^2 = Q_n Q_n^* = \sum_{i=1}^M \sum_{j=1}^M e^{in(\phi_i - \phi_j)} = M + \sum_{i \neq j} e^{in(\phi_i - \phi_j)}, \quad (4.8)$$

we isolate the contribution from particle pairs, yielding the equivalent expression:

$$\langle 2 \rangle = \frac{|Q_n|^2 - M}{M(M-1)}. \quad (4.9)$$

This Q-vector formulation offers a computationally efficient way to evaluate two-particle correlations.

4.3.2.2 4-particle correlations

In the high-multiplicity environment characteristic of Pb–Pb collisions, relying solely on two-particle correlations can be insufficient because they remain sensitive to non-flow effects (even applying pseudorapidity gaps) [243]. To achieve a more accurate characterization of collective behavior, it is essential to explore higher-order correlations. However, this comes at the cost of reduced statistical precision, as higher-order cumulants require more particle combinations. The four-particle correlator is defined as [247]:

$$\langle 4 \rangle = \left\langle e^{in(\phi_1 + \phi_2 - \phi_3 - \phi_4)} \right\rangle, \quad (4.10)$$

where $\phi_1, \phi_2, \phi_3, \phi_4$ are the azimuthal angles of four different particles in the same event. $\langle 4 \rangle$ is calculated by averaging over all distinct quadruplets of particles. The number of such combinations in a given event is:

$$P_{M,4} = M(M-1)(M-2)(M-3). \quad (4.11)$$

Thus, the estimator for the four-particle correlation becomes⁸:

$$\langle 4 \rangle = \frac{1}{P_{M,4}} \sum_{i \neq j \neq k \neq l} e^{in(\phi_i + \phi_j - \phi_k - \phi_l)}. \quad (4.12)$$

8. Note that an expression for m -particle correlations could be derived, but they are not addressed in this thesis.

4.3.3 Event-averaged correlators

After computing the per-event particle correlators, the next step is to average these values over all events within a given centrality class. Centrality classes partition the data sample into subsets of events with similar collision geometry, typically characterized by comparable impact parameters. We denote these final, event-averaged correlators using double angle brackets. This notation implies two levels of averaging: first over particle combinations within a single event, and then over all events in the selected centrality class [109].

$$\langle\langle 2 \rangle\rangle = \left\langle \left\langle e^{in(\phi_1 - \phi_2)} \right\rangle \right\rangle, \quad (4.13)$$

$$\langle\langle 4 \rangle\rangle = \left\langle \left\langle e^{in(\phi_1 + \phi_2 - \phi_3 - \phi_4)} \right\rangle \right\rangle \quad (4.14)$$

The event-averaged 2-particle and 4-particle correlators are computed as weighted averages over events:

$$\langle\langle 2 \rangle\rangle \equiv \frac{\sum_{\text{events}} (W_{\langle 2 \rangle})_i \langle 2 \rangle_i}{\sum_{\text{events}} (W_{\langle 2 \rangle})_i}, \quad (4.15)$$

$$\langle\langle 4 \rangle\rangle \equiv \frac{\sum_{\text{events}} (W_{\langle 4 \rangle})_i \langle 4 \rangle_i}{\sum_{\text{events}} (W_{\langle 4 \rangle})_i}. \quad (4.16)$$

Here, $\langle 2 \rangle_i$ and $\langle 4 \rangle_i$ represent the per-event correlators calculated for the i -th event, while $W_{\langle 2 \rangle}$ and $W_{\langle 4 \rangle}$ are corresponding event weights.

If we consider that v_n is approximately constant within a given centrality class (i.e., independent of multiplicity variations within that class):

$$W_{\langle 2 \rangle} = P_{M,2} = M(M-1), \quad (4.17)$$

$$W_{\langle 4 \rangle} = P_{M,4} = M(M-1)(M-2)(M-3), \quad (4.18)$$

The weights represent the total number of distinct particle combinations, as defined in Equation 4.11. In these expressions, M denotes the multiplicity of a given event. These weights are used to suppress the influence of event-by-event multiplicity fluctuations on the final results, leading to a more robust estimation of the underlying particle correlations across the full dataset.

4.3.4 Cumulants

Although equation 4.9 can provide a useful estimate of v_n when short-range correlations are minimal, contributions such as non-flow effects are often significant and must be mitigated. To address this, one can leverage the collective behavior inherent to flow phenomena through multi-particle cumulant methods [247]. As explained in Chapter 1, higher-order cumulants are not sensitive to flow fluctuations. Cumulants are obtained by combining correlators, the cumulants for 2-particle and 4-particle correlations, can be expressed in the following way:

$$c_n\{2\} = \langle\langle 2 \rangle\rangle, \quad (4.19)$$

$$c_n\{4\} = \langle\langle 4 \rangle\rangle - 2 \cdot \langle\langle 2 \rangle\rangle^2, \quad (4.20)$$

where, $c_n\{2\}$ and $c_n\{4\}$ represent the cumulant coefficients for the n -th harmonic. Note that, even in an idealized scenario without event-by-event fluctuations, multi-particle cumulants are still affected by nonflow contributions. The general expression for the m -particle ($m = 2, 4$) cumulant is given by [109]:

$$c_n\{m\} \equiv (-1)^{\frac{m}{2}-1} v_n\{m\}^m = (-1)^{\frac{m}{2}-1} \langle v_n^m + \delta_m \rangle. \quad (4.21)$$

Here, $c_n\{m\}$ denotes the m -particle cumulant of the n -th harmonic and the factor $(-1)^{\frac{m}{2}-1}$ fixes the sign convention of the cumulant expansion, ensuring that the extracted flow coefficients are real and positive. The quantity $v_n\{m\}$ is the flow coefficient obtained from m -particle correlations. On the right-hand side, $\langle v_n^m \rangle$ represents the genuine collective flow contribution, averaged over many events. The term δ_m , accounts for non-flow effects. Note that it scales differently with multiplicity M , depending on the m -particle correlation:

$$\delta_m = \frac{1}{M^{m-1}}. \quad (4.22)$$

Equation 4.22 shows that the 4-particle cumulant mitigates non-flow contributions ($\delta_4 < \delta_2$). Note that, as discussed in Section 1.5.5, the flow coefficient $v_n\{2\}$ is also influenced by event-by-event fluctuations. Neglecting non-flow contributions and assuming two-dimensional Gaussian fluctuations of the flow vector, such that $v_n \sim \mathcal{BG}(\langle\langle v_n \rangle\rangle, \sigma)$, the corresponding flow coefficients can be expressed as:

$$v_n\{2\}^2 = \langle\langle v_n^2 \rangle\rangle + 2\sigma^2, \quad (4.23)$$

$$v_n\{4\} = \langle\langle v_n \rangle\rangle, \quad (4.24)$$

Surprisingly, Equation 4.24 shows that the 4th order cumulant does not depend on the gaussian flow fluctuation. Notice for small multiplicity environments (events with low number of particles), non-flow contributions might become significant and therefore Equation 4.21 will need to be taken into account.

4.4 Elliptic flow coefficients with ALICE detector

The study of low-order harmonics is especially insightful to study collectivity because, for small n ($n=2,3$), the coefficients follows $v_n = k\varepsilon_n$ (see Section 1.5.3). This relation implies that elliptic flow v_2 coefficient, serve as direct probes of how the medium converts initial spatial anisotropies into final-state momentum anisotropy. In particular, measurements of v_2 for heavy-flavor hadrons are especially valuable, as they provide unique sensitivity to the degree of thermalization of heavy quarks within the medium. In this chapter, we show the calculations needed to compute the dimuon elliptic flow coefficients $v_2^{\mu\mu}\{m\}$ for m -particle correlations ($m = 2$ and $m = 4$).

As illustrated in Figure 4.3, correlations between three charged particles and one dimuon pair are required to compute $v_2^{\mu\mu}\{4\}$. The multi-particle cumulants technique for differential measurements relies on calculations between the unit flow vector of particle of interest (POI) and the reference (REF) flow vector in a sub-detector A. In our case, POI particles refers to dimuons at forward-rapidity and REF particles to all type of inclusive charged particles at mid-rapidity. We show that REF and POI flow coefficients can be expressed in terms of the following correlators:

$$\langle\langle 2^{REF} \rangle\rangle, \quad \langle\langle 4^{REF} \rangle\rangle, \quad \langle\langle 2^{\mu\mu} \rangle\rangle, \quad \langle\langle 4^{\mu\mu} \rangle\rangle. \quad (4.25)$$

The definition of this correlators and how to obtain them is explained in the next section.

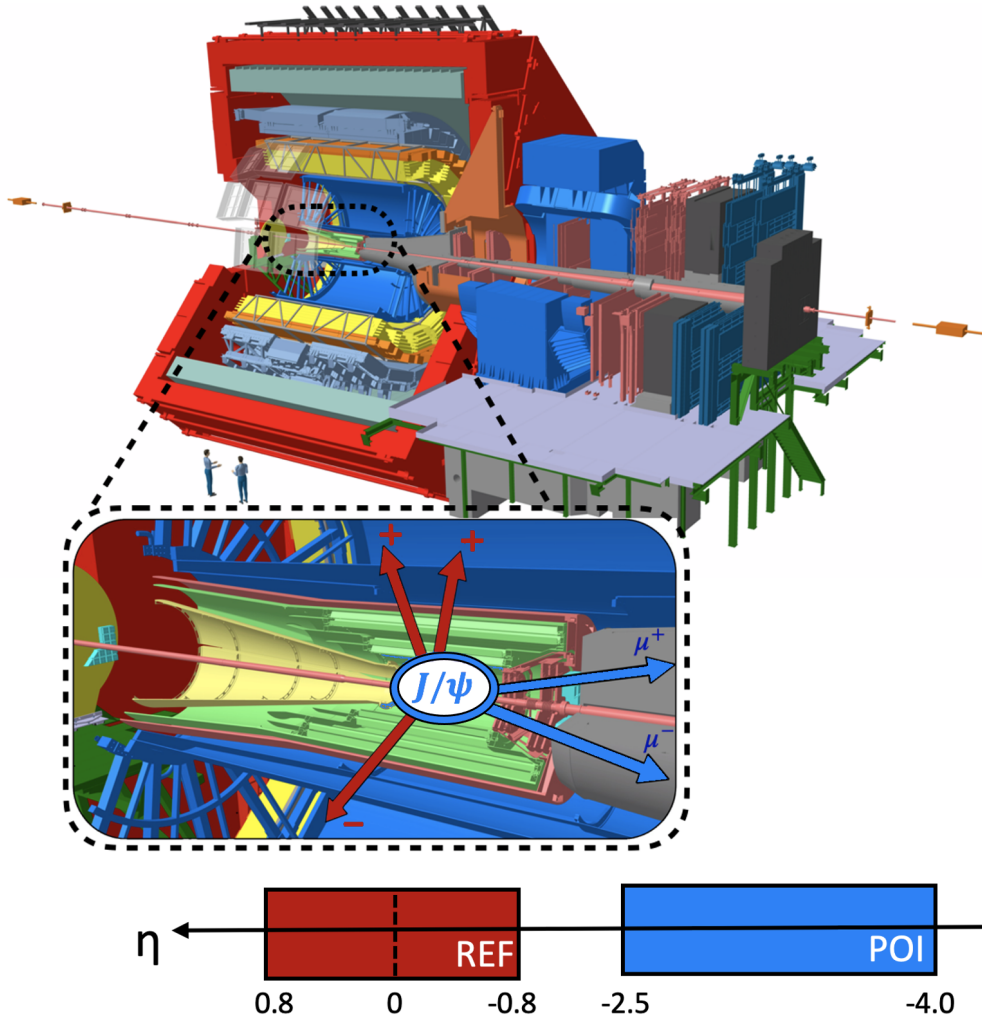


FIGURE 4.3 – Schematic view of the ALICE detector, illustrating inclusive charged particles at mid-rapidity (red tracks) and the decay of a J/ψ meson into a dimuon pair at forward rapidity (blue tracks).

4.4.0.1 Flow vectors using Non-Uniform Acceptance (NUA) weights

From equation 4.1 defined at the beginning of the section, we introduce the weighed flow vector for the n th harmonic as:

$$Q_{n;k} = \sum_{i=1}^M w_i^k e^{(in\phi_i)}, \quad (4.26)$$

where, w_i^k represents the non-uniform acceptance weight (NUA) for the i th charged track and k is an exponent allowing to compute flow vectors with all powers up to the order of multi-particle correlations. The cumulant analysis uses NUA weights

to correct for non-uniform detector acceptance and efficiency. These weights are obtained through a fully data-driven procedure, as described in Ref. [243]. Based on these weights, we introduce the following quantities:

$$S_{p;k} = \left[\sum_{i=1}^M w_i^k \right]^p, \quad (4.27)$$

$$M_{abcd} = \sum_{i,j,k,l=1}^M w_i^a w_j^b w_k^c w_l^d, \quad (4.28)$$

$$M'_{abcd} = \sum_{i=1}^{m_p} \sum_{j,k,l=1}^M w_i^a w_j^b w_k^c w_l^d, \quad (4.29)$$

where, a, b, c and d are exponents similar to k in Equation 4.39. These quantities will be used in the next steps of the calculations.

4.4.0.2 Reference correlators (REF) with NUA weights

The weighted average of 2-particle correlations $\langle 2^{REF} \rangle$ is proportional to the norm of the REF flow vector of charged particles Q_2 . The event-by-event correlator is an average over all tracks in a given event as denoted by the single brackets $\langle \dots \rangle$. This correlator is defined as:

$$\langle 2^{REF} \rangle = \frac{|Q_{2,1}|^2 - S_{1,2}}{S_{2,1} - S_{1,2}}. \quad (4.30)$$

The final 2-particle correlator $\langle \langle 2^{REF} \rangle \rangle$ is an average over all events as denoted by the double brackets $\langle \langle \dots \rangle \rangle$. It is defined as:

$$\langle \langle 2^{REF} \rangle \rangle = \frac{\sum_{i=1}^N (M_{11})_i \langle 2^{REF} \rangle_i}{\sum_{i=1}^N (M_{11})_i}, \quad (4.31)$$

$$M_{11} = \sum_{i,j=1}^n w_i w_j = S_{2,1} - S_{1,2}. \quad (4.32)$$

where, N represents the total number of events, n the total number of charged particle tracks within a given event, and M_{11} is the 2-particle event's weight for a given 2-particle correlator ($M_{11} \propto W_{\langle 2 \rangle}$) when all NUA weight's are set to 1, see Equation 4.17).

These calculation are usually performed in correlation analysis in the ALICE central barrel using ITS-TPC tracks and running over all Minimum Bias (MB) events. In the case of this analysis, we are also using the ITS-TPC tracks to compute de reference correlator. Nevertheless, in our case we are only selecting events containing at least a dimuon (or a muon pair) and the final averaging of the correlator is done over all dimuon pairs. The equation are therefore slightly modified as shown below:

$$\langle\langle 2^{REF} \rangle\rangle = \frac{\sum_{i=1}^N \frac{1}{m_p} \sum_{j=1}^{m_p} (M_{11})_i \langle 2^{REF} \rangle_i}{\sum_{i=1}^N \frac{1}{m_p} \sum_{j=1}^{m_p} (M_{11})_i} = \frac{\sum_{k=1}^{N'} (M_{11}/m_p)_k \langle 2^{REF} \rangle_k}{\sum_{k=1}^{N'} (M_{11}/m_p)_k}, \quad (4.33)$$

where, m_p represents the multiplicity of dimuons in a given event. Summing over j dimuons across all i events is equivalent to summing over all N' dimuons. We can notice that averaging over all minimum bias events or over all dimuon pairs could have an impact on the results, but we discuss later this hypothesis. Similarly, the weighted average of 4-particle correlations depend on the orientation of the flow vectors Q_2 and Q_4 . The average over all tracks is given by:

$$\begin{aligned} \langle 4^{REF} \rangle = & \frac{|Q_{2,1}|^4 + |Q_{4,2}|^2 - 2 \operatorname{Re}(Q_{4,2} Q_{2,1} Q_{2,1}^*)}{M_{1111}} \\ & + \frac{8 \operatorname{Re}(Q_{2,3} Q_{2,1}^*) - 4 S_{1,2} |Q_{2,1}|^2 - 6 S_{1,4} + 2 S_{2,2}}{M_{1111}}, \end{aligned} \quad (4.34)$$

and average over all dimuon pairs is given by:

$$\langle\langle 4^{REF} \rangle\rangle = \frac{\sum_{i=1}^N (M_{1111}/m_p)_i \langle 4^{REF} \rangle_i}{\sum_{i=1}^N (M_{1111}/m_p)_i}, \quad (4.35)$$

$$M_{1111} = \sum_{i,j,k,l=1}^M w_i w_j w_k w_l = S_{4,1} - 6 S_{1,2} S_{2,1} + 8 S_{1,3} S_{1,1} + 3 S_{2,2} - 6 S_{1,4}. \quad (4.36)$$

where, M_{1111} is the 4-particle event's weight for a given 4-particle correlator ($M_{1111} \propto W_{\langle 4 \rangle}$ when all NUA weight's are set to 1), N represents the total number of events, n the total number of tracks charged particle within a given event, and M_{11} is the 2-particle event's weight for a given 2-particle correlator.

4.4.0.3 Particle of interest (POI) correlators with NUA weights

In order to construct Particle Of Interest (POI) correlators involving dimuons, it is important to clarify how the azimuthal angle $\varphi_{\mu\mu}$ is computed. In contrast to single-particle flow analyses where the angle φ is taken directly from the trajectory of individual particles, here the dimuon system is treated as a composite object. The azimuthal angle of the dimuon pair is calculated from its total four-momentum:

$$p_{\mu\mu}^\nu = p_{\mu^+}^\nu + p_{\mu^-}^\nu. \quad (4.37)$$

From this total four-vector $p_{\mu\mu}^\nu$, the components p_x and p_y of the dimuon are extracted, and the azimuthal angle is computed as:

$$\varphi_{\mu\mu} = \tan^{-1} \left(\frac{p_y}{p_x} \right). \quad (4.38)$$

This ensures that $\varphi_{\mu\mu}$ reflects the actual kinematics of the dimuon system, and not simply the average or difference of the two individual muons' angles ($\varphi_{\mu\mu} \neq \varphi_{\mu^+} - \varphi_{\mu^-}$). We define the following n' harmonic POI Q-vector for dimuons:

$$p_{n'}^{\mu\mu} = \sum_{i=1}^{m_p} e^{in'\varphi_{\mu\mu}}, \quad (4.39)$$

Having already applied muon and dimuon track quality criteria outlined in [248, 249], the remaining data sample is restricted to well-reconstructed dimuon candidates. This selection ensures that residual detector effects are minimized, removing artificial anisotropies. Consequently, all POI weights are set to unity ($w_i = 1$). In other words, each dimuon contributes equally to the POI flow vector of a given event. The weighted average of 2-particle correlations $\langle 2'^{\mu\mu} \rangle$ is proportional to POI and REF flow vectors ($p_2^{\mu\mu}$ and Q_2 respectively), as shown in equation 4.40. In this analysis, the REF flow vector is taken from the central barrel and the POI flow vector from the muon spectrometer. As both flow vectors are fed with totally different tracks, the equations 4.30, 4.33 and 4.32 can be adapted and simplified as followed:

$$\langle 2'^{\mu\mu} \rangle = \left\langle e^{i2(\varphi_{\mu\mu} - \varphi_{\text{ref}})} \right\rangle = \frac{p_2^{\mu\mu} Q_{2,1}^*}{m_p S_{1,1}}, \quad (4.40)$$

$$\langle \langle 2'^{\mu\mu} \rangle \rangle = \frac{\sum_{i=1}^N (M'_{01}/m_p)_i \langle 2'^{\mu\mu} \rangle_i}{\sum_{i=1}^N (M'_{01}/m_p)_i}, \quad (4.41)$$

$$M'_{01} = \sum_{i=1}^{m_p} \sum_{j=1}^M w_j = m_p S_{1,1}. \quad (4.42)$$

Similarly, the weighted average of 4-particle correlations $\langle 4' \rangle$ depends on the orientation of POI and REF flow vectors $p_2^{\mu\mu}$, Q_2 and Q_4 and can be expressed as:

$$\begin{aligned} \langle 4'^{\mu\mu} \rangle &= \left\langle e^{i2(\varphi_{\mu\mu} + \varphi_1 - \varphi_2 - \varphi_3)} \right\rangle = \\ &+ \frac{p_2^{\mu\mu} Q_{2,1}^3 - p_2^{\mu\mu} Q_{2,1} Q_{4,2}}{M'_{0111}} \\ &+ \frac{-2S_{1,2} p_2^{\mu\mu} Q_{2,1} - 2s_{1,1} |Q_{2,1}|^2}{M'_{0111}} \\ &+ \frac{2p_2^{\mu\mu} Q_{2,3} + 2s_{1,1} S_{1,1} S_{1,2} - 6s_{1,3}}{M'_{0111}}, \end{aligned} \quad (4.43)$$

$$\langle \langle 4'^{\mu\mu} \rangle \rangle = \frac{\sum_{i=1}^N (M'_{0111}/m_p)_i \langle 4'^{\mu\mu} \rangle_i}{\sum_{i=1}^N (M'_{0111}/m_p)_i}, \quad (4.44)$$

$$M'_{0111} = \sum_{i=1}^{m_p} \sum_{j,k,l=1}^{M_{0jkl}} w_j w_k w_l = m_p [S_{3,1} - 3S_{1,1} S_{1,2} + 2S_{1,3}]. \quad (4.45)$$

4.4.0.4 REF and POI cumulants

REF cumulants are obtained by combining REF correlators. The REF flow cumulant of the 2-particle and 4-particle correlation can be expressed in the following way:

$$c_2^{REF}\{2\} = \langle \langle 2^{REF} \rangle \rangle, \quad (4.46)$$

$$c_2^{REF}\{4\} = \langle \langle 4^{REF} \rangle \rangle - 2 \cdot \langle \langle 2^{REF} \rangle \rangle^2, \quad (4.47)$$

where, $c_2^{REF}\{2\}$ and $c_2^{REF}\{4\}$ represent the REF flow cumulants of charged particles at mid-rapidity for events containing a pair of dimuons. Using a similar logic, one can defined POI cumulant combining POI and REF correlators as:

$$d_2^{\mu\mu}\{2\} = \langle \langle 2'^{\mu\mu} \rangle \rangle, \quad (4.48)$$

$$d_2^{\mu\mu}\{4\} = \langle \langle 4'^{\mu\mu} \rangle \rangle - 2 \cdot \langle \langle 2^{REF} \rangle \rangle \cdot \langle \langle 2'^{\mu\mu} \rangle \rangle, \quad (4.49)$$

where, $d_2^{\mu\mu}\{2\}$ and $d_2^{\mu\mu}\{4\}$ denote the POI flow cumulants of dimuons. The brackets $\langle\langle\cdot\rangle\rangle$ indicate an average over all dimuon pairs for a given centrality class. In Section 4.5, we combine the REF and POI cumulants to compute the flow coefficients v_2^{REF} and v_2^{POI} .

4.5 v_2^{REF} and $v_2^{\mu\mu}$ using cumulants with Run 3 data

4.5.1 REF flow at mid-rapidity

As shown before in Equation 4.21, the elliptic flow coefficient denoted as v_2^{REF} for all inclusive charged tracks (known as reference flow) can be computed in the following way:

$$v_2^{REF}\{2\} \equiv \sqrt{c_2^{REF}\{2\}}, \quad (4.50)$$

$$v_2^{REF}\{2, |\Delta\eta| > 1\} \equiv \sqrt{c_2^{REF}\{2, |\Delta\eta| > 1\}}, \quad (4.51)$$

$$v_2^{REF}\{4\} \equiv (-c_2^{REF}\{4\})^{1/4}. \quad (4.52)$$

Here, $v_2^{REF}\{2\}$ is obtained from two-particle correlations, $v_2^{REF}\{2, |\Delta\eta| > 1\}$ from two-particle correlations with a pseudorapidity gap, and $v_2^{REF}\{4\}$ from four-particle correlations. The first step of the analysis consists in extracting the reference flow v_2^{REF} of charged tracks as a function of centrality at mid-rapidity, using the method described at the beginning of Section 4.4.

Figure 4.4 shows the run-by-run comparison of $v_2^{\text{REF}}\{2\}$ for all minimum-bias events collected in the 2023 Pb–Pb dataset.

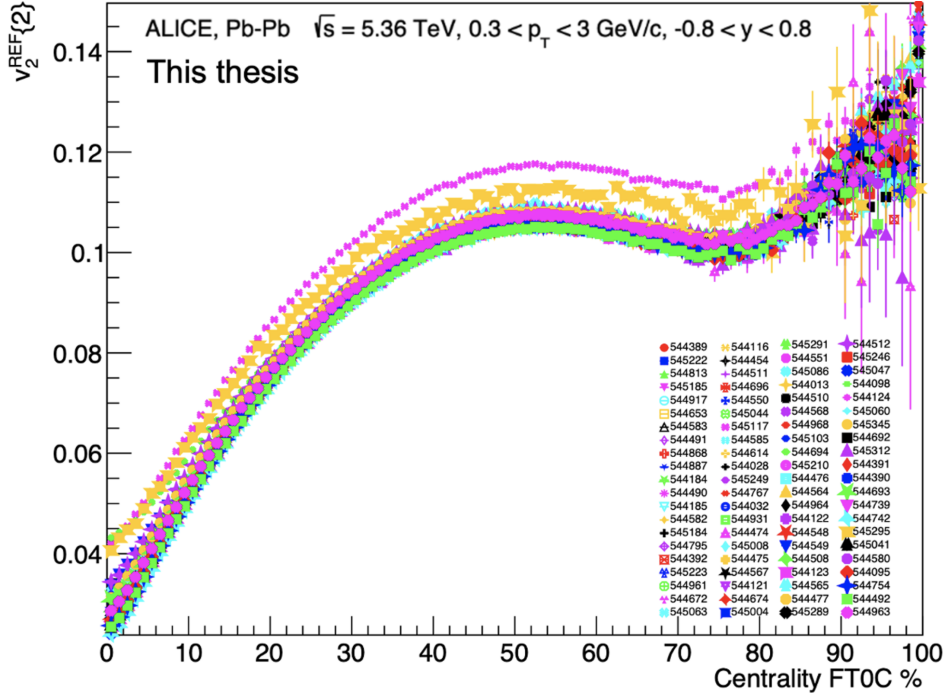


FIGURE 4.4 – Run-by-run comparison of Run 3 data. $v_2^{\text{REF}}\{2\}$ as a function of centrality.

Each run is represented with different colored icons. Note that two particular runs, 545117 (pink) and 545124 (yellow), clearly stand out above the others. Since their statistics are negligible, they were excluded from the analysis to ensure reliability.

Similarly, Figure 4.5 presents the run-by-run comparison of $v_2^{\text{REF}}\{2, |\Delta\eta| > 1\}$. The ordering of runs is consistent with that in Figure 4.4. The good stability observed over the different running periods confirms the robustness of the measurement and the quality of the data sample. A similar comparison for $v_2^{\text{REF}}\{4\}$ can be found in Annexe B.

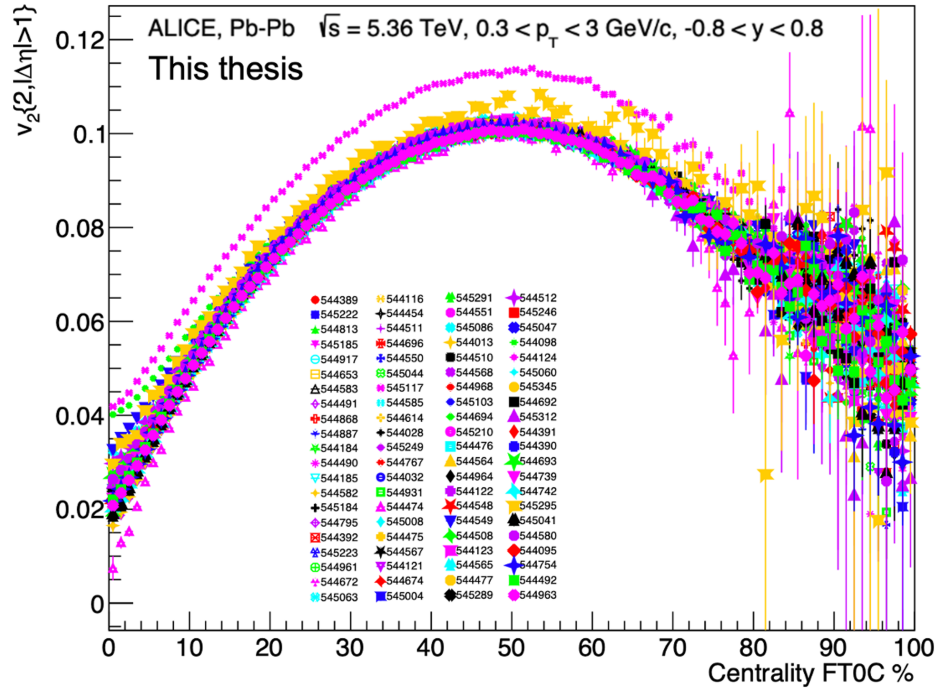


FIGURE 4.5 – Run-by-run comparison of Run 3 data. $v_2^{\text{REF}}\{2, |\Delta\eta| > 1\}$ as a function of centrality.

In addition, Figure 4.6 compares $v_2^{\text{REF}}\{2\}$ measured in minimum-bias events with that extracted from events containing at least one dimuon pair.

The excellent agreement (red and blue points) demonstrates that events with a dimuon are representative of the inclusive minimum-bias sample, thereby validating the event-averaging procedure defined in equation 4.33. A comparison with Run 2 results is included. We notice that $v_2^{\text{REF}}\{2, |\Delta\eta| > 1\}$ is systematically smaller than $v_2^{\text{REF}}\{2\}$ due to the suppression of non-flow effects by the η -gap requirement, with the difference being most pronounced in peripheral collisions.

It should be noted that the center-of-mass energy is not exactly the same in Run 3 ($\sqrt{s_{NN}} = 5.36$ TeV) and Run 2 ($\sqrt{s_{NN}} = 5.02$ TeV), so the comparison is not straightforward, although one does not expect a big change on the flow factors with the increase of less than 10% of the available energy in the center of mass of the collision.

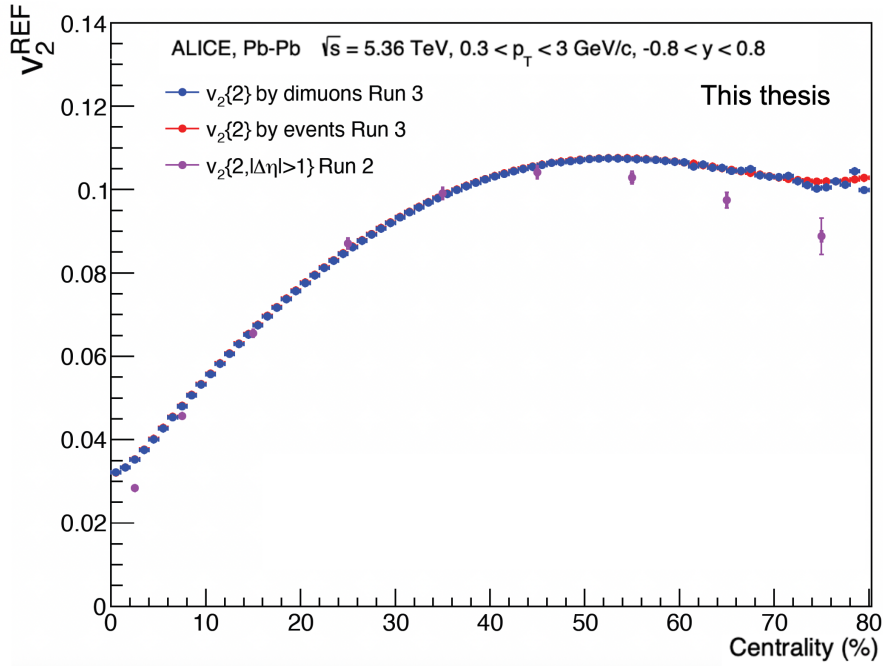


FIGURE 4.6 – $v_2^{\text{REF}}\{2\}$ from minimum-bias events compared to events containing a dimuon pair, $v_2^{\text{REF}}\{2, |\Delta\eta| > 1\}$ from Run 2 is also reported.

In addition, in Figure 4.7, $v_2^{\text{REF}}\{2\}$ is compared to $v_2^{\text{REF}}\{2, |\Delta\eta| > 1\}$. As expected, applying an η -gap reduces short-range non-flow correlations, resulting in the observed hierarchy. The comparison with Run 2 further confirms the stability of this suppression. This demonstrates that non-flow effects remain well under control in the Run 3 dataset.

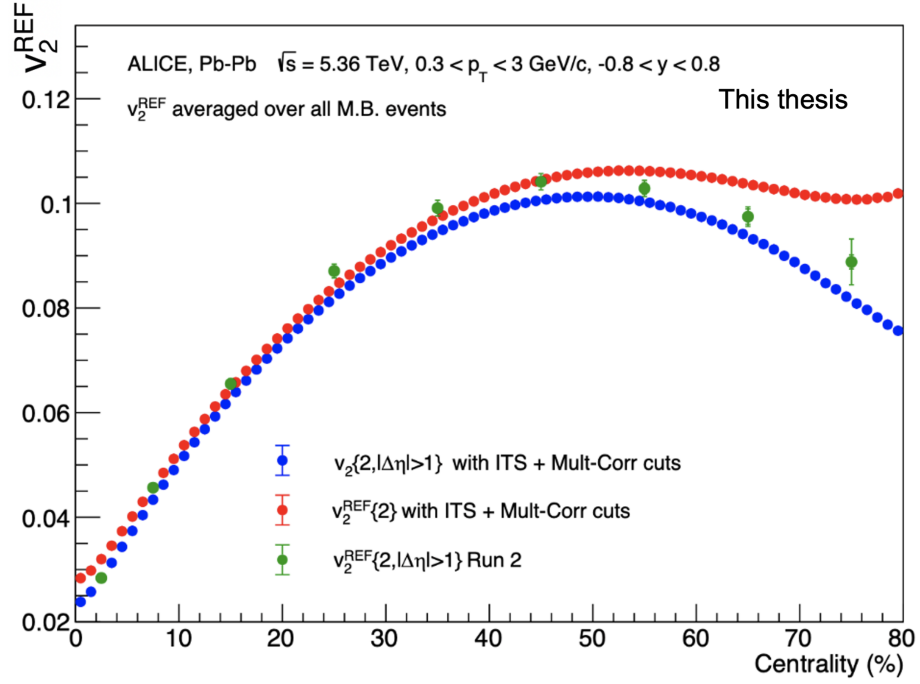


FIGURE 4.7 – Comparison of $v_2^{\text{REF}}\{2\}$ with $v_2^{\text{REF}}\{2, |\Delta\eta| > 1\}$ in Run 3 and Run 2. The expected hierarchy reflects the suppression of non-flow effects.

Finally, Figure 4.8 shows the centrality dependence of $v_2^{\text{REF}}\{2\}$ and $v_2^{\text{REF}}\{4\}$. The difference between the two reflects the presence of flow fluctuations in addition to residual non-flow effects (encoded in $v_2^{\text{REF}}\{2\}$), consistent with Run 2 observations.

The agreement in overall trends between Run 2 and Run 3 underlines both the stability of the measurement and the reliability of the multi-particle cumulant method within the Run 3 framework.

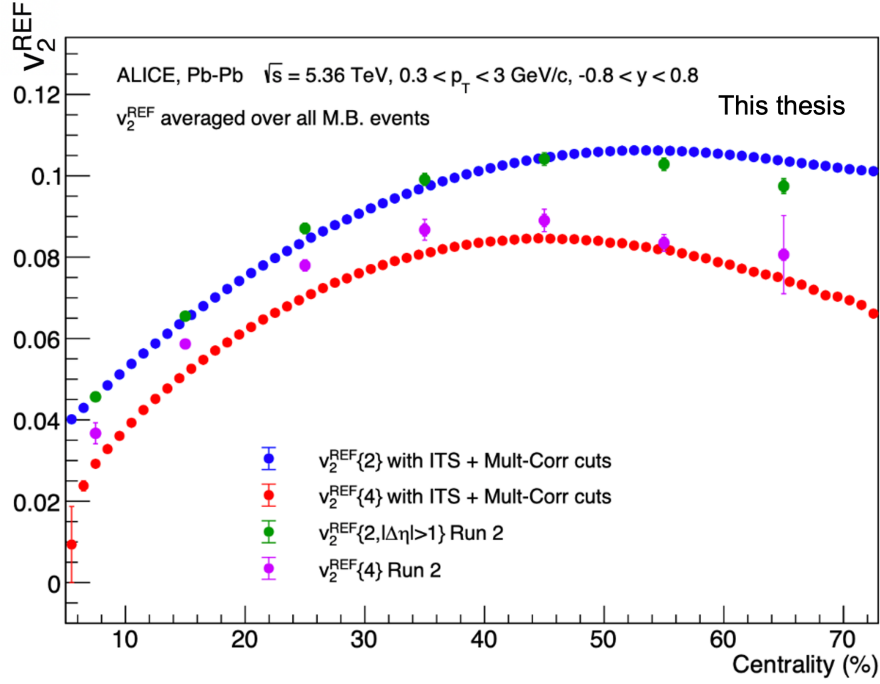


FIGURE 4.8 – Centrality dependence of $v_2^{\text{REF}}\{2, |\Delta\eta| > 1\}$ and $v_2^{\text{REF}}\{4\}$ in Run 3, compared to Run 2.

In all Figures shown in 4.6, 4.7, and 4.8, the Run 2 and Run 3 reference flow results are not a direct comparison, as they correspond to different collision energies. All presented measurements are obtained from datasets in which the individual runs were merged by taking the mean value over all runs, such that longer runs naturally carry a larger statistical weight than shorter ones. The improved agreement observed for Run 3 is expected with ongoing refinements in event and track selection criteria.

4.5.2 POI flow at forward rapidity

4.5.2.1 Invariant mass of dimuons

The invariant mass of one or more particles is a conserved quantity that is independent of the overall motion of the system (lorentz invariant), making it a powerful tool in particle physics. It allows the identification of parent particles by reconstructing the mass from the energy and momentum of the decay products. Because it remains unchanged across reference frames, the invariant mass is especially useful

in high-energy experiments for detecting resonances associated with unstable, decaying states. The J/ψ lifetime is too short to be detected directly, and its daughter tracks are reconstructed as coming from the J/ψ production point. At the same time, the J/ψ lifetime is long enough to probe the full evolution of the QGP formed in the collisions.

In the case of a simple two-body decay ($J/\psi \rightarrow \mu^+ \mu^-$), the invariant mass can be easily obtained:

$$M^2 = (P_1 + P_2)^2 = P_1^2 + P_2^2 + 2P_1 P_2 \quad (4.53)$$

$$P_1^\mu P_{2\mu} = P_1^0 P_{20} + P_1^i P_{2i} = P_1^0 P_2^0 - \vec{P}_1 \vec{P}_2 = E_1 E_2 - \vec{P}_1 \vec{P}_2 \quad (4.54)$$

$$M^2 = P_1^2 + P_2^2 + 2P_1 P_2 = m_1^2 + m_2^2 + 2(E_1 E_2 - \vec{P}_1 \vec{P}_2) \quad (4.55)$$

$$M = \sqrt{m_1^2 + m_2^2 + 2(E_1 E_2 - P_1 P_2 \cos \theta)} \quad (4.56)$$

where:

- m_1 and m_2 denote the masses of the muon and anti-muon, with $m_1 = m_2 = m_\mu$.
- E_1 and E_2 are their energies and \vec{P}_1, \vec{P}_2 are their momenta.
- θ is the angle between their momenta.

Figure 4.9 shows the same-event opposite sign pairs (SEPM) invariant mass spectra for different dimuon pair transverse momentum.

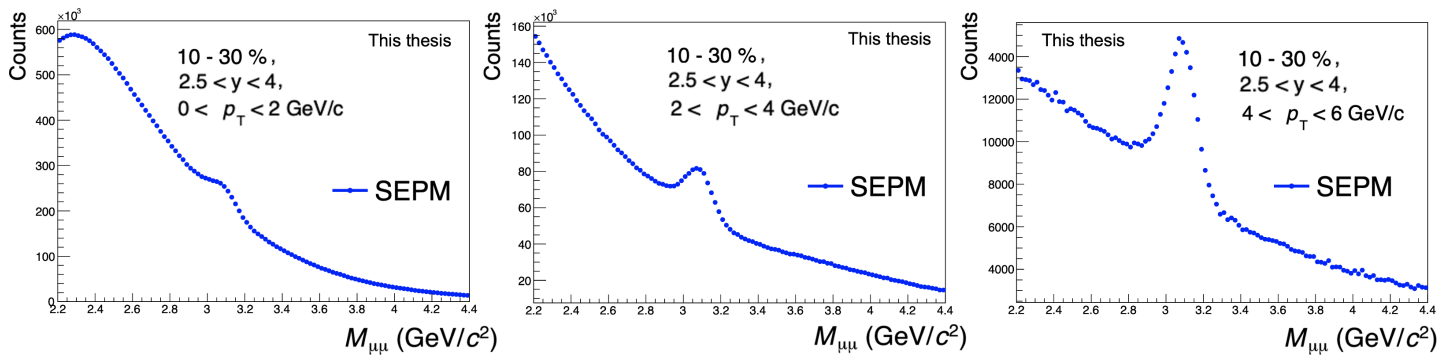


FIGURE 4.9 – Example of dimuon invariant mass spectra $M_{\mu\mu}$ for the p_T bins: 0-2, 2-4, and 4-6 GeV/c (from left to right, respectively) within the centrality class 10-30%.

The signal-to-background ratio increases with the transverse momentum (p_T) of the dimuon pairs, as shown in the highest p_T bin 4–6 GeV/c in the right panel, where

the signal becomes more pronounced relative to the background. A clear J/ψ peak is visible near $3.1 \text{ GeV}/c^2$, superimposed on a sizable combinatorial background. Beyond this component, non-combinatorial background sources may also contribute, especially in the more peripheral collision classes. The peak width is determined by the detector resolution, which improves at higher p_T ⁹. Meanwhile, the background contribution decreases with increasing p_T , as the probability of forming random high p_T muon pair becomes increasingly limited.

4.5.2.2 Elliptic flow of dimuons

To evaluate the flow coefficient of dimuons (POI) with respect to the reference (REF) particles, the mixed two-particle correlator defined in Equation 4.48 is used. To disentangle flow fluctuations from non-flow effects, we first consider the simplified case where the participant plane ψ_2 is fixed in all events and therefore no event-by-event fluctuations occur (see Section 1.5.5). In this limit, the following flow factorization relation holds

$$d_2^{\mu\mu}\{2\} \equiv \left\langle \left\langle e^{i2(\varphi_{\mu\mu} - \varphi_{\text{REF}})} \right\rangle \right\rangle_{M_{\mu\mu}} \sim \langle v_2^{\mu\mu} \rangle \cdot \langle v_2^{\text{REF}} \rangle, \quad (4.57)$$

where, the first bracket $\langle \dots \rangle$ represents the average over all possible pairwise muon combinations (1 for two muons, 2 for three muons, etc.). The second $\langle \langle \dots \rangle \rangle_{M_{\mu\mu}}$ denotes the average over all events that contain at least one dimuon, within a given invariant mass interval $M_{\mu\mu}$. Here, we use the notation $\langle v_2^A \rangle \equiv \langle e^{i2(\varphi_A - \Psi_2^A)} \rangle$, with Ψ_2^A the participant plane angle, where A denotes either the reference REF or POI contribution. Equation 4.57 represents the flow factorization hypothesis (assuming absence of flow fluctuations), where the two-particle correlator factorizes into the product of single-particle flow coefficients [106], meaning $\Psi_2^{\text{REF}} = \Psi_2^{\mu\mu}$. Similarly, using Equation 4.46, for the reference flow we have

$$c_2^{\text{REF}}\{2\} \equiv \langle (v_2^{\text{REF}})^2 \rangle \sim \langle v_2^{\text{REF}} \rangle^2. \quad (4.58)$$

The dimuon flow coefficient is defined as the following POI/REF ratio:

9. This behavior is not universal. For the J/ψ , with a mass of $3096.900 \pm 0.006 \text{ MeV}/c^2$ and an intrinsic width of $\Gamma \sim 92.9 \pm 2.8 \text{ keV}$ [1], the resonance is extremely narrow compared to the experimental resolution. As a result, the J/ψ resonance always appears as a sharp peak. In contrast, for broader states, the natural decay width dominates over detector effects.

$$v_2^{\mu\mu}\{2\} \equiv \frac{d_2^{\mu\mu}\{2\}}{\sqrt{c_2^{\text{REF}}\{2\}}} \sim \frac{\langle v_2^{\mu\mu} \rangle \langle v_2^{\text{REF}} \rangle}{\sqrt{\langle v_2^{\text{REF}} \rangle^2}} \sim \langle v_2^{\mu\mu} \rangle, \quad (4.59)$$

which demonstrates that, in the absence of flow fluctuations, both $v_2^{\mu\mu}\{2\}$ and $v_2^{\text{REF}}\{2\}$ reduce to their respective mean flow values. However, when performing two-particle correlations, non-flow effects may become non-negligible, as no η -gap is applied in the method. In such cases, Equation 4.59 should be modified as

$$v_2^{\mu\mu}\{2\} \sim \langle v_2^{\mu\mu} + \delta_2 \rangle, \quad (4.60)$$

where the non-flow contribution δ_2 scale inversely with the multiplicity $\delta_2 \sim 1/M$.

Figure 4.10 presents $v_2^{\mu\mu}\{2\}$ (defined in Equation 4.59) as a function of the dimuon invariant mass for two p_T intervals: 0–2 and 2–4 GeV/c (shown in the left and right panels, respectively), within the 10–30% centrality class. The signal is relatively small and difficult to extract due to the large combinatorial background. In addition, the shape of the background varies strongly between the two kinematic ranges: in the left panel it increases monotonically with mass, while in the right panel it first decreases and then rises again. This pronounced change in shape further motivates the need for event mixing to model and subtract the background reliably.

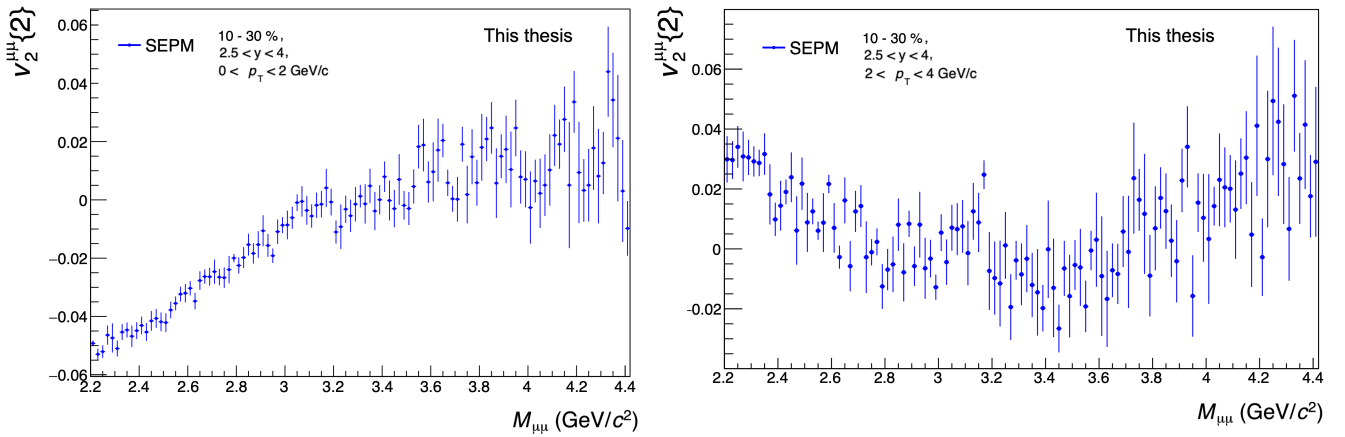


FIGURE 4.10 – Example of $v_2^{\mu\mu}\{2\}$ as function of the dimuon invariant mass for the p_T bins: 0-2 and 2-4 GeV/c (left and right, respectively) within the centrality class 10-30%.

To further reduce the influence of non-flow correlations, one need to consider the mixed four-particle correlator involving one dimuon and three reference particles

(see Equation 4.49). We continue under the assumption of factorization, so we can write the following 4-particle POI cumulant:

$$\begin{aligned}
 d_2^{\mu\mu}\{4\} &\equiv \left\langle \left\langle e^{i2(\varphi_{\mu\mu} + \varphi_1 - \varphi_2 - \varphi_3)} \right\rangle \right\rangle_{M_{\mu\mu}} \\
 &\quad - 2 \left\langle \left\langle e^{i2(\varphi_{\mu\mu} - \varphi_1)} \right\rangle \right\rangle_{M_{\mu\mu}} \cdot \left\langle \left\langle e^{i2(\varphi_2 - \varphi_3)} \right\rangle \right\rangle_{M_{\mu\mu}} \\
 &= \langle v_2^{\mu\mu} (v_2^{\text{ref}})^3 \rangle - 2 \langle v_2^{\mu\mu} v_2^{\text{ref}} \rangle \cdot \langle (v_2^{\text{ref}})^2 \rangle \\
 &\sim - \langle v_2^{\mu\mu} \rangle \langle v_2^{\text{ref}} \rangle^3.
 \end{aligned} \tag{4.61}$$

Similarly, the corresponding four-particle REF cumulant can be also expressed in terms of the fourth-order flow moment:

$$c_2^{\text{REF}}\{4\} \equiv \langle (v_2^{\text{REF}})^4 \rangle - 2 \langle (v_2^{\text{REF}})^2 \rangle^2 \sim - \langle v_2^{\text{REF}} \rangle^4. \tag{4.62}$$

The dimuon flow coefficient is then obtained from the POI/REF ratio, in analogy with the two-particle case:

$$v_2^{\mu\mu}\{4\} \equiv - \frac{d_2^{\mu\mu}\{4\}}{(-c_2^{\text{REF}}\{4\})^{3/4}} \sim - \frac{- \langle v_2^{\mu\mu} \rangle \langle v_2^{\text{REF}} \rangle^3}{(\langle v_2^{\text{REF}} \rangle^4)^{3/4}} = \langle v_2^{\mu\mu} \rangle. \tag{4.63}$$

An illustration of $v_2^{\mu\mu}\{4\}$ as a function of the dimuon invariant mass is presented in Figure 4.11.

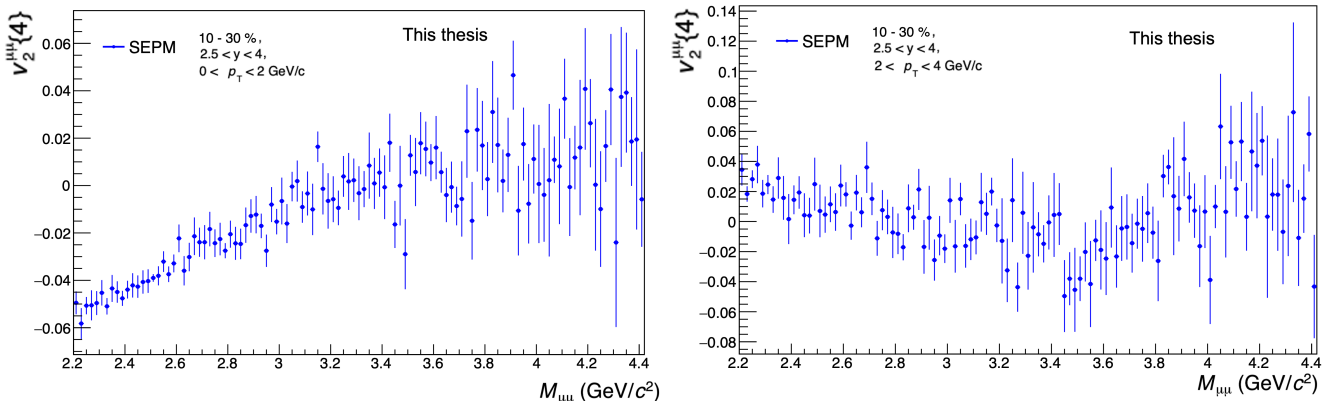


FIGURE 4.11 – Example of $v_2^{\mu\mu}\{4\}$ as function of the dimuon invariant mass for the p_T bins: 0-2 and 2-4 GeV/c (left and right, respectively) within the centrality class 10-30%.

The $v_2\{4\}$ distribution shows similar behavior to the $v_2\{2\}$ results shown pre-

viously in Figure 4.10, with the background contribution exhibiting a comparable structure in both p_T ranges. This similarity is expected to first order, since both observables probe the same underlying physics processes. As shown in Figures 4.10 and 4.11, the statistical uncertainties associated with $v_2^{\mu\mu}\{2\}$ are noticeably smaller than those of $v_2^{\mu\mu}\{4\}$, as expected given the lower statistical precision of the four-particle cumulant method.

Notice that Equation 4.59 shows that, in the absence of flow fluctuations, the coefficient $v_2^{\mu\mu}\{2\}$ also reduces to the mean dimuon flow coefficient. However, as discussed previously in Section 1.5.5 of Chapter 1, when 2D Gaussian fluctuations of the initial eccentricity are considered, the second-order moment of the Bessel-Gaussian distribution $\mathcal{BG}(v_2^{\mu\mu}; \langle v_2^{\mu\mu} \rangle, \sigma^2)$, depends explicitly on the fluctuation width σ and therefore $v_2^{\mu\mu}\{2\}$ and $v_2^{\mu\mu}\{SP\}$ are sensitive to flow fluctuations. The sensitivity of dimuon elliptic flow coefficients, associated with different flow methods, to Gaussian fluctuations and non-flow effects is summarized in Table 4.2.

Flow method	No δ -dependence	No σ -dependence
$v_2^{\mu\mu}\{2\}^2 = \langle v_2^{\mu\mu} + \delta_2 \rangle^2 + \sigma^2$	$\times \delta_2 \sim M^{-1} \neq 0$	\times
$v_2^{\mu\mu}\{SP\}^2 = \langle v_2^{\mu\mu} \rangle^2 + \sigma^2$	$\checkmark \delta \sim 0$	\times
$v_2^{\mu\mu}\{4\}^2 = \langle v_2^{\mu\mu} \rangle^2$	$\checkmark \delta_4 \sim M^{-3} \sim 0$	\checkmark

TABLE 4.2 – Summary of $v_2\{2\}^2$, $v_2\{SP\}^2$, and $v_2\{4\}^2$ depending on non-flow contributions and flow fluctuations (within 2D Bessel-Gaussian approach).

From Table 4.2, we see that $v_2\{4\}^2$ is the only observable that is insensitive to both non-flow and flow fluctuations. In contrast, $v_2\{SP\}^2$ is insensitive to non-flow but remains sensitive to flow fluctuations. Therefore, by combining measurements of $v_2\{SP\}$ and $v_2\{4\}$, one can directly access to event-by-event flow fluctuations.

4.5.2.3 Statistical error estimation of $v_2^{\mu\mu}$

The statistical uncertainties of $v_2^{\mu\mu}\{2\}$ and $v_2^{\mu\mu}\{4\}$ are evaluated using a sub-sampling technique, also commonly referred to as a shuffling method. This method provides a data-driven estimate of statistical fluctuations by resampling the original dataset multiple times, preserving the global event structure [250]. In practice, the full event sample is divided into N_{sub} statistically independent subsamples, each containing approximately the same number of events. For each subsample

k , the elliptic flow coefficient v_2 is computed independently using the same analysis procedure as applied to the full dataset. The mean value of the observable v_2 is computed as:

$$\bar{v}_2 = \frac{1}{N_{\text{sub}}} \sum_{k=1}^{N_{\text{sub}}} v_2^k, \quad (4.64)$$

and the corresponding statistical variance is estimated using the unbiased sample variance formula:

$$\text{Var}(v_2) = \frac{1}{N_{\text{sub}} - 1} \sum_{k=1}^{N_{\text{sub}}} \left(v_2^k - \bar{v}_2 \right)^2. \quad (4.65)$$

The statistical uncertainty on v_2 is then given by:

$$\delta v_2 = \sqrt{\text{Var}(v_2) / N_{\text{sub}}}. \quad (4.66)$$

This sub-sampling method accounts for statistical fluctuations, with the choice of N_{sub} reflecting a balance between statistical stability and the granularity of the p_T binning. While values around $N_{\text{sub}} \sim 5$ tended to yield smaller statistical error estimates, a more conservative choice of $N_{\text{sub}} \sim 10$ was adopted, possibly leading to an overestimation of the statistical uncertainties but ensuring robustness (a stable v_2 was obtained across the 10 different subsamples).

4.6 Event mixing procedure

When studying resonance decays, the resulting invariant mass distribution typically features a pronounced peak at the resonance mass, accompanied by a background mainly arising from random combinations of muon tracks. Accurately extracting the resonance signal requires a reliable estimation of this underlying background. If the background exhibits a smooth, monotonic decline, it can often be described analytically using a simple fitting function. However, the variable $v_2^{\mu\mu}$ can vary significantly across different kinematic ranges, complicating the fitting modeling process.

To address these challenges, a technique known as event mixing is employed to construct a combinatorial background. This method involves combining particles from different events, effectively removing the signal contribution while preserv-

ing the statistical properties of the background. In the O2Physics framework, this approach is implemented using event pools provided by the [O2 mixing library](#).

The **event pool** is a collection of events grouped together for the purpose of estimating the background. A pool is characterized by two parameters:

- **Track depth** refers to the maximum number of muon tracks allowed per pool.
- **Pool size** denotes the maximum number of events within a pool.

Pools are categorized based on centrality and primary z-vertex (V_z) position:

- **Centrality bins (%)**: 0–5, 5–10, 10–20, 20–30, 30–40, 40–50, 50–60, 60–70, 70–80 and 80–90.
- **Primary vertex range**: $-10.0 < V_z < 10.0$ cm.

The same sign ($\mu^+\mu^+$ and $\mu^-\mu^-$) and opposite sign ($\mu^+\mu^-$) dimuon spectra are constructed using two muons from same or different events, respectively. The F-factor defined below is used to normalize the mixed spectrum.

$$F = \frac{\int 2R \sqrt{N_{same}^{++} N_{same}^{--}} dm}{\int N_{mix}^{+-} dm}$$

The integration limit is in a large mass region around the signal peak. N_{same}^{++} and N_{same}^{--} are the number of like-sign same-event dimuon pairs from raw spectra and N_{mix}^{+-} are opposite-sign mixed dimuons. R is defined as $R = \frac{N_{mix}^{+-}}{2\sqrt{N_{mix}^{++} N_{mix}^{--}}}$ and it is close to unity in the mass range covered by this analysis. The R factor is used to take into account the different acceptance of the like-sign and same-sign dimuon pairs. The resulting F factor used in this analysis is summarized in the below Table 4.3 for all p_T bins.

Normalization factors (pool size = 5), 10–30% centrality								
p_T (GeV/c)	0–2	2–4	4–5	5–6	6–8	8–10	10–12	12–15
F	0.104	0.102	0.103	0.104	0.104	0.104	0.106	0.101

TABLE 4.3 – Normalization factors F for background estimation in different p_T intervals for the 10–30% centrality class.

To normalize mixed-event invariant mass spectra, one should only need to rescale the original mixed-event spectra by the F factor found in the corresponding p_T bin.

In Figure 4.12, the blue distribution corresponds to opposite-sign muon pairs containing the signal, referred to in the following as SEPM. The combinatorial background estimated using mixed-event opposite-sign pairs (MEPM) shows excellent

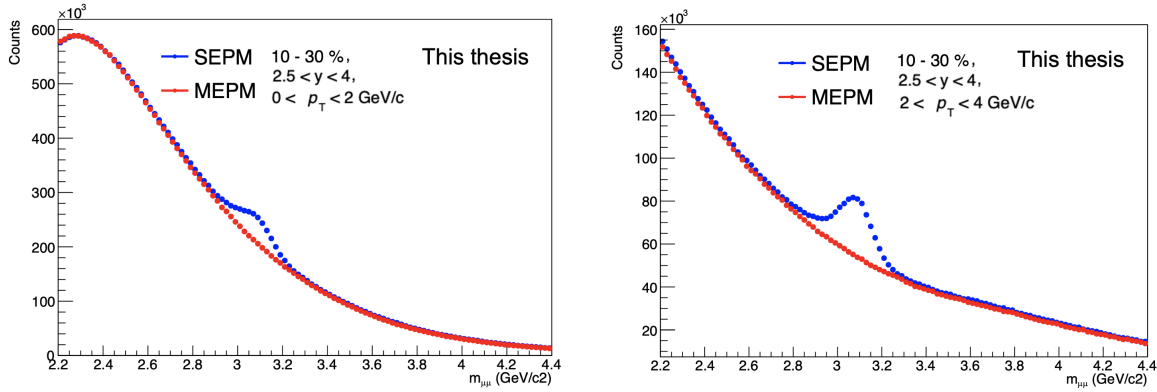


FIGURE 4.12 – Dimuon invariant mass distributions for the 10–30% centrality class: the same-event distribution (SEPM, in blue) compared with the mixed-event distribution normalized with the MEPM procedure (in red). Results are shown for p_T ranges of 0–2 and 2–4 GeV/ c .

agreement with the SEPM background in the sideband regions, confirming the reliability of the normalization procedure. This agreement also validates the use of the F-factor approach for background subtraction and the full implementation of the event mixing technique. The consistency (between SEPM and MEPM) distributions demonstrates that the mixed-event background accurately reproduces the combinatorial background structure, providing confidence in the event mixing technique.

4.6.1 Application of event mixing to flow methods

Flow coefficients of mixed dimuons

The integrated elliptic flow coefficient of the background dimuon distribution, weighted by its invariant yield, is defined as:

$$v_2^B = \langle \cos[2(\phi - \Psi_2)] \rangle = \frac{\int_0^{2\pi} \frac{dN_{\mu\mu}}{d\phi} \cos[2(\phi - \Psi_2)] d\phi}{\int_0^{2\pi} \frac{dN_{\mu\mu}}{d\phi} d\phi}, \quad (4.67)$$

where the B in v_2^B denotes the background contribution. The numerator of equation 4.67 can be developed by calculating the azimuthal distribution of the dimuon combinatorial background $\frac{dN_{\mu\mu}}{d\phi}$ as a product of the independent azimuthal distributions of the single muons from which the background dimuons are formed.

$$\frac{dN_{\mu\mu}}{d\phi} \propto \frac{dN_{\mu}}{d\phi_1} \frac{dN_{\mu}}{d\phi_2} \quad (4.68)$$

The following relationship can be obtained:

$$\int_0^{2\pi} \frac{dN_{\mu\mu}}{d\phi} \cos[2(\phi - \Psi_2)] d\phi = v_2^{(1)} \cos[2(\phi_1 - \phi)] + v_2^{(2)} \cos[2(\phi_2 - \phi)] \quad (4.69)$$

where $v_2^{(1)}(p_T^{(1)})$ and $v_2^{(2)}(p_T^{(2)})$ are the elliptic flow coefficients of two single muons from different events, ϕ_1 and ϕ_2 are their corresponding azimuthal angles, ϕ is the azimuthal angle of mixed dimuon pair.

Surprisingly, the right-hand side of equation 4.69 is not dependent on the participant plane Ψ_2 . This is because the azimuthal distribution of the dimuon combinatorial background is a product of the independent azimuthal distributions of the single muons from which the background dimuons are formed (see Equation 4.69). In order to normalize the mixed flow contribution, the denominator of equation 4.67 must account for the modification of the dimuon yield. If we assume that there is no correlated flow from mixed dimuon pairs, the following equation can be calculated:

$$\int_0^{2\pi} \frac{dN_{\mu\mu}}{d\phi} d\phi = N_{+-}^B / N_{+-}^{\text{mix}} \quad (4.70)$$

where N_{+-}^B is the background yield of opposite-sign dimuon pairs, and N_{+-}^{mix} is the normalized mixed-event opposite-sign yield. Both quantities are extracted from fits of the invariant mass distribution. Note that the assumption used in equation 4.70 that there is no correlated flow from mixed dimuon pairs is based on the fact that the background under the J/ψ peak is predominantly combinatorial noise from random muon combinations. While this assumption is not strictly true due to contributions from open charm decays, it works well in practice because the combinatorial background dominates the spectrum in the mass regions of interest. Combining equations 4.69 and 4.70, equation 4.67 becomes:

$$v_2^B = \frac{v_n^{(1)}(p_T^{(1)}) \cos[2(\phi_1 - \phi)] + v_n^{(2)}(p_T^{(2)}) \cos[2(\phi_2 - \phi)]}{N_{+-}^B / N_{+-}^{\text{mix}}}. \quad (4.71)$$

Finally, the flow combinatorial background of dimuons (v_2^B) as a function of $M_{\mu\mu}$ is obtained by averaging over all dimuons belonging to a given $M_{\mu\mu}$ interval:

$$v_2^B(M_{\mu\mu}) = \frac{\langle v_2^{(1)} \cos[2(\phi_1 - \phi)] + v_2^{(2)} \cos[2(\phi_2 - \phi)] \rangle_{M_{\mu\mu}}}{N_{+-}^B / N_{+-}^{\text{mix}}}. \quad (4.72)$$

The detailed derivation of equation 4.72 can be found in the Appendix of the reference [251].

Cumulants and flow coefficients of single muons

To extract the single muon elliptic flow coefficients $v_2^{\mu\pm}\{2\}$ and $v_2^{\mu\pm}\{4\}$ needed in Equation 4.72, the following correlators are required: $\langle\langle 2^{\text{REF}} \rangle\rangle$, $\langle\langle 4^{\text{REF}} \rangle\rangle$, $\langle\langle 2'^{\mu\pm} \rangle\rangle$, and $\langle\langle 4'^{\mu\pm} \rangle\rangle$ (see appendix B for full details of the calculation). These elliptic flow coefficients contribute to the construction of the combinatorial background $v_2^B(M_{\mu\mu})$, as defined in Equation 4.72. The associated cumulants $c_2\{m\}$ and $d_2^{\mu\pm}\{m\}$ are computed using the correlators as functions of $p_T^{\mu-}$ and $p_T^{\mu+}$, respectively. The reference flow remains unchanged, all events considered in this analysis now contain at least one single muon.

$$c_2\{2\} = \langle\langle 2^{\text{REF}} \rangle\rangle_{p_T^{\mu\pm}}, \quad (4.73)$$

$$c_2\{4\} = \langle\langle 4^{\text{REF}} \rangle\rangle_{p_T^{\mu\pm}} - 2 \cdot \langle\langle 2^{\text{REF}} \rangle\rangle_{p_T^{\mu\pm}}^2 \quad (4.74)$$

POI cumulants of single muons:

$$d_2^{\mu\pm}\{2\} = \langle\langle 2'^{\mu\pm} \rangle\rangle_{p_T^{\mu\pm}}, \quad (4.75)$$

$$d_2^{\mu\pm}\{4\} = \langle\langle 4'^{\mu\pm} \rangle\rangle_{p_T^{\mu\pm}} - 2 \cdot \langle\langle 2^{\text{REF}} \rangle\rangle_{p_T^{\mu\pm}} \cdot \langle\langle 2'^{\mu\pm} \rangle\rangle_{p_T^{\mu\pm}} \quad (4.76)$$

The final elliptic flow coefficient of single muons (from Same-Event) are computed in the following way:

$$v_2^{\mu\pm}\{2\} = -\frac{d_2^{\mu\pm}\{2\}}{\sqrt{c_2^{\text{REF}}\{2\}}}, \quad v_2^{\mu\pm}\{4\} = -\frac{d_2^{\mu\pm}\{4\}}{(-c_2^{\text{REF}}\{4\})^{3/4}}. \quad (4.77)$$

Figure 4.13 shows the elliptic flow coefficients $v_2\{2\}$ and $v_2\{4\}$ of inclusive muons as a function of transverse momentum p_T in the 10–30% centrality class. At low p_T , the signal is dominated by contributions from light hadrons, mostly muons from pion and kaon decays, while for $p_T > 2$ GeV it is increasingly driven by muons from open heavy-flavor decays. The current procedure uses a variable binning strategy,

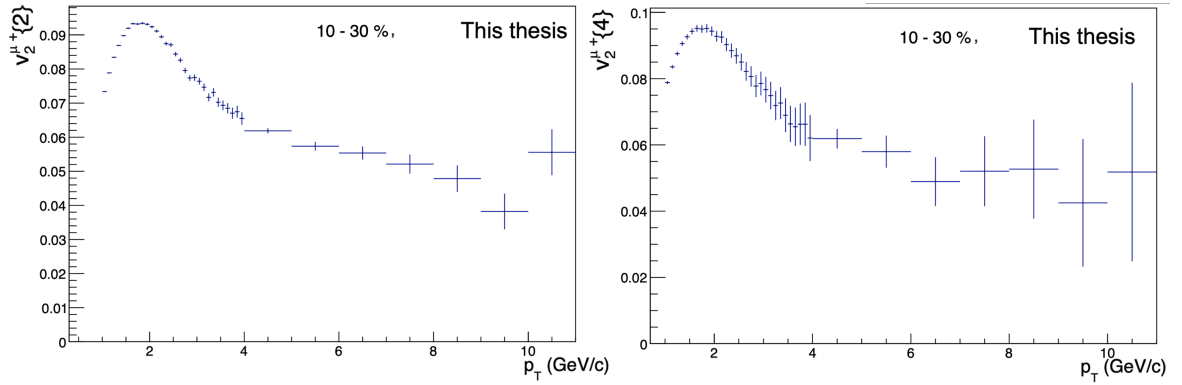


FIGURE 4.13 – v_2 of inclusive muons as a function of p_T within the centrality class 10-30% (left: $v_2\{2\}$, right: $v_2\{4\}$).

with finer granularity at low p_T to capture the detailed shape of the distribution and wider bins at high p_T to optimize the statistical precision. Another possible, but not yet tested, approach could be to parametrize the shape of the distribution (for instance by fitting), thereby reducing the residual impact of statistical fluctuations.

Notice that the extracted values of the single muon flow coefficients are first uploaded to the ALICE Condition and Calibration Database (CCDB), from where it can be retrieved and initialized in Equation 4.72 to accurately reproduce the combinatorial background of dimuons using $v_2^{\mu\pm}\{2\}$ and $v_2^{\mu\pm}\{4\}$.

Validation of the mixed-event background flow method

We compare the distribution of v_2 of the dimuon pairs (SEPM) and the v_2 distribution of the background estimated via the Mixed Event Method (MEPM) in the 10–30% centrality class. The consistency of the background flow estimation can be assessed by examining the agreement between the SEPM and MEPM results.

Figure 4.14 shows such a comparison for the elliptic flow coefficient v_2 in the 10–30% centrality class, for two different p_T ranges. A good agreement is observed in the sideband regions, where the flow contribution is dominated by combinatorial background. This agreement confirms that the procedure implemented in Equation 4.72 correctly reproduces the shape of the flow background.

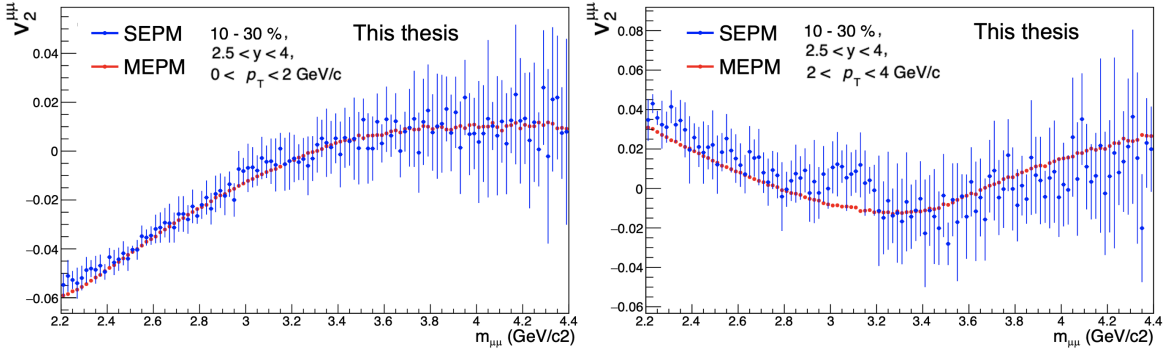


FIGURE 4.14 – Distribution of v_2 of the dimuon pairs (SEPM) in blue in the 10–30% centrality class. The red points represent the v_2 distribution of the background estimated via the Mixed Event Method (MEPM). Results are shown for two transverse momentum (p_T) intervals: 0–2 and 2–4 GeV/c (left and right, respectively).

4.7 J/ψ v_2 Signal Extraction

The extraction of the v_2 coefficient for the J/ψ is performed through a two-step fitting procedure applied to the dimuon invariant mass distribution, $m_{\mu\mu}$, and the corresponding $v_2^{\mu\mu}$ as a function of $m_{\mu\mu}$. Both distributions contain contributions from signal and background processes. As discussed in Section 4.6.1, event mixing plays a crucial role in providing an accurate description of the background. In the first step, the invariant mass spectrum is fitted to determine the signal-to-background ratio. The signal is modeled using either a double-sided Crystal Ball function (CB2) or the NA60 function, while the background is described by a Chebyshev polynomial. The mathematical definition of these functions can be found in appendix B, following the prescription outlined in [252]. The signal-to-background fraction as a function of the invariant mass is then expressed as

$$\alpha(m_{\mu^+\mu^-}) = \frac{S(m_{\mu^+\mu^-})}{S(m_{\mu^+\mu^-}) + B(m_{\mu^+\mu^-})}, \quad (4.78)$$

where, S and B denote the signal and background contributions, respectively. This ratio is then used to fit the $v_2^{\mu^+\mu^-}$ as a function of the invariant mass $m_{\mu^+\mu^-}$:

$$v_2^{\mu^+\mu^-}(m_{\mu^+\mu^-}) = \alpha(m_{\mu^+\mu^-}) v_2^{J/\psi} + [1 - \alpha(m_{\mu^+\mu^-})] v_2^{\text{bkg}}, \quad (4.79)$$

where $v_2^{J/\psi}$ represents the elliptic flow J/ψ signal, and v_2^{bkg} corresponds to the elliptic flow of the combinatorial background. An example of the fit results is presented

in Figure 4.15, which illustrates the extraction of the J/ψ yield and the $v_2^{J/\psi\{4\}}$ signal in three representative p_T intervals: 0–2, 1–2, and 2–4 GeV/ c . Note that the bin 1–2 GeV/ c is of course included in 0–2 GeV/ c . In the v_2 final results, we will use the bin 0–2 GeV/ c . But we computed also the bin 1–2 GeV/ c to study flow fluctuations that will be discussed later. The panels of Figure 4.15 demonstrate how both the signal-to-background ratio and the behavior of the background v_2 vary with p_T .

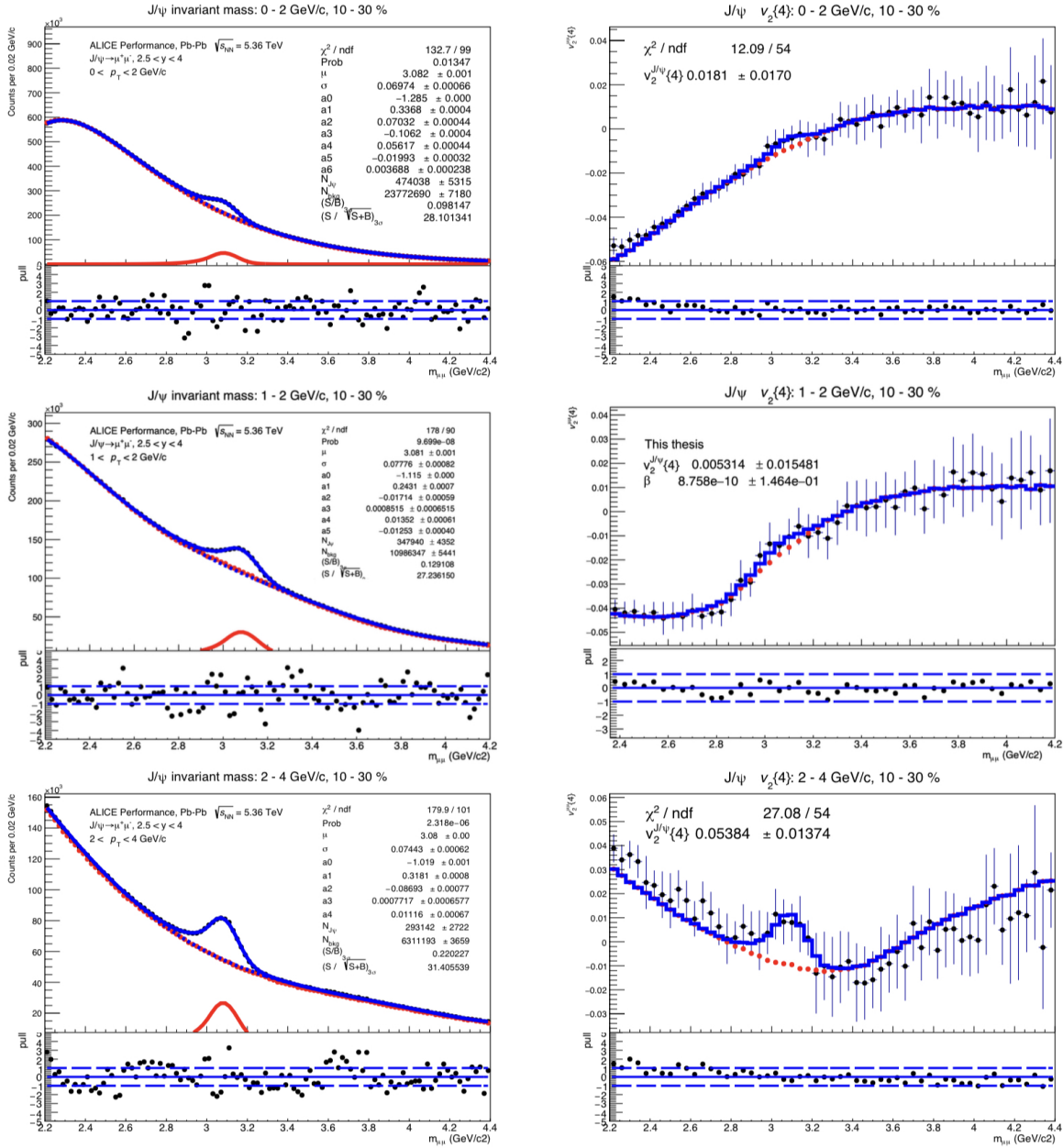


FIGURE 4.15 – Example of fitting results for dimuon invariant mass spectra (left panels) and $v_2\{4\}$ as a function of the invariant mass (right panels) for the p_T bins: 0-2, 1-2, and 2-4. (from top to bottom, respectively) within the centrality class 10-30%. The fit results use CB2 as the signal and event mixing as background for the mass fit, and event mixing for the v_2 background with one free parameter β modeling the correlated background flow contribution for v_2 background.

- **Top panel** ($p_T = 0\text{--}2$ GeV/c): The signal-to-background ratio is relatively low, and the background v_2 exhibits a steadily increasing trend as a function of $m_{\mu\mu}$. This rise appears approximately linear at lower masses, suggesting a smooth combinatorial background contribution that increases with invariant mass.
- **Central panel** ($p_T = 1\text{--}2$ GeV/c): The background v_2 shows a more complex structure. The linear trend observed at lower p_T breaks down, particularly at low invariant masses, where the background deviates from a straight-line behavior. This indicates the presence of nontrivial mass-dependent effects in the v_2 background.
- **Bottom panel** ($p_T = 2\text{--}4$ GeV/c): The background v_2 displays a clear "U" shaped dependence on $m_{\mu\mu}$ with decreasing values below the J/ψ peak, followed by a rise at higher masses.

Note that in all p_T ranges, a significant v_2 value is observed at high invariant mass. At the LHC, these pairs originate mainly from semi-leptonic decays of heavy-flavor hadrons, with open charm hadrons providing the dominant contribution. Additional, smaller contributions arise from charm/bottom quark decays and Drell–Yan processes [253]. Both of these are preferentially produced in the in-plane direction, thereby enhancing the observed flow signal. This explains the increased v_2 values at large $m_{\mu\mu}$.

To assess the quality of the fits, the reduced chi-squared value χ^2/ndf is reported in each plot. Here, χ^2 quantifies the overall deviation between the data points and the fit function, while ndf (number of degrees of freedom) corresponds to the number of data points minus the number of fitted parameters. Each panel of Figure 4.15 includes a pull distribution, defined as

$$\text{Pull} = \frac{x^{\text{Data}} - x^{\text{Fit}}}{\sigma_{\text{Data}}} \quad (4.80)$$

where σ_{Data} represents the statistical uncertainty of the measured data point. Pull distributions centered around zero ($x^{\text{Data}} = x^{\text{Fit}}$) with a width close to one further support the quality and reliability of the fitting procedure. The complete set of fitting extraction plots, corresponding to all p_T intervals considered in this analysis, is provided in the appendix A.

To ensure the reliability of the fits, different binning choices were tested to verify that the outcome is robust and not tied to a specific configuration.

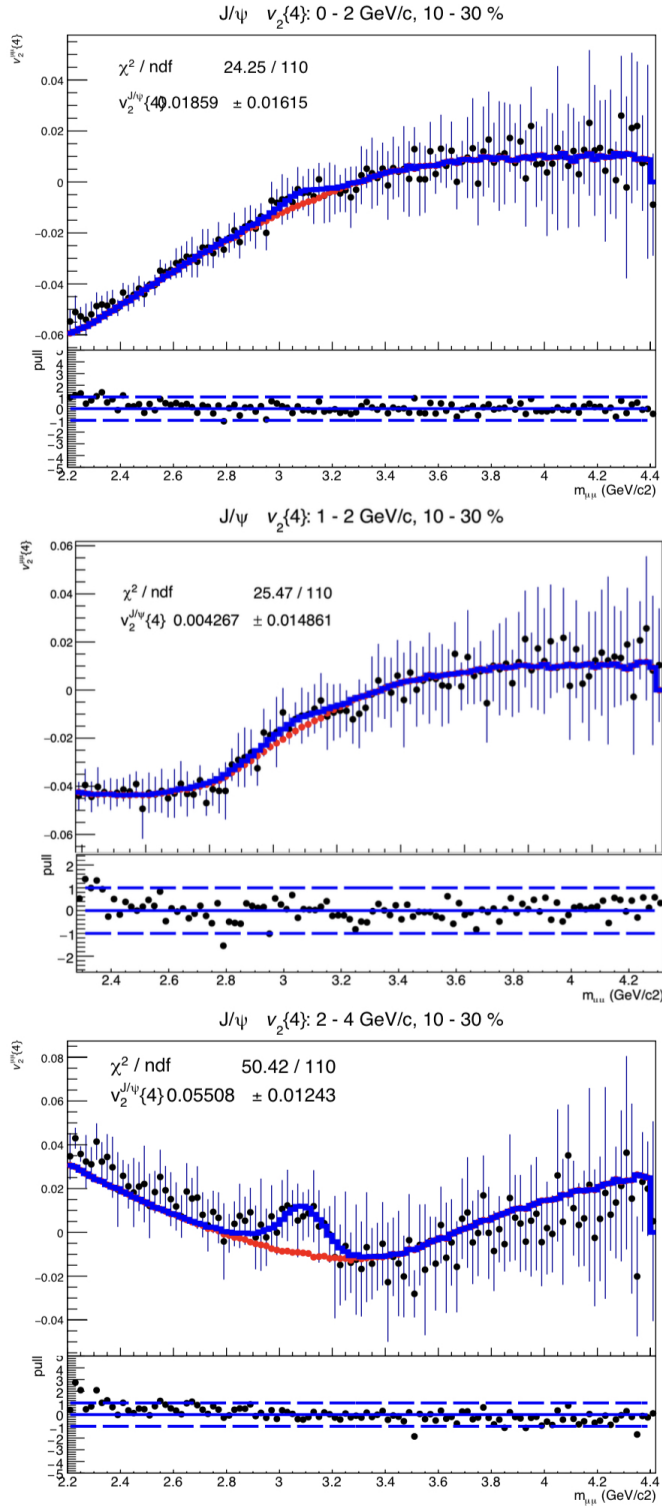


FIGURE 4.16 – $v_2\{4\}$ with a finer mass binning for the p_T bins: 0–2, and 2–4 GeV/c.

Accordingly, the same fits were repeated with a finer mass binning, as shown in Figure 4.16. The results are consistent with those shown in Figure 4.15. The complete set of fit results used to extract the J/ψ yield, as well as the $v_2^{J/\psi}\{2\}$ and $v_2^{J/\psi}\{4\}$ coefficients across all p_T intervals, is presented in appendix A.

4.7.1 Systematic uncertainties study

About the signal extraction, two main sources of uncertainty must be considered:

1. The uncertainty in the J/ψ yield extracted from the dimuon invariant mass distribution, obtained from the first fit used in the determination of α (see Section 4.7.1.1).
2. The uncertainty on $v_2^{J/\psi}$, derived from a second fit to the v_2 distribution as a function of the invariant mass. This uncertainty originates from the assumptions on the shape of v_2^{bkg} , which depends on the specific configuration of the v_2 fit (see Section 4.7.1.2).

In addition, a systematic uncertainty σ_{rebin} is introduced to account for the choice of invariant-mass binning. Finally, we note that further sources of systematic uncertainties will need to be evaluated in future studies.

4.7.1.1 Uncertainties of J/ψ yield

As explained in the beginning of this section, the errors from α are subject to the fitting procedure i.e. the setup of fitting. For J/ψ invariant mass fitting, here we summarise different options that could be possibly used in this analysis:

- Signal shapes: **double-sided Crystal Ball (CB2) with tail parameters fixed by data or MC, NA60 function.**
- Background shapes with event-mixing: **Chebyshev function.**
- Mass fit range: [2.2 - 4.2], [2.3 - 4.3], [2.4 - 4.4] GeV/c².

All the detailed fitting functions used in this analysis are provided in appendix A. Note that the $\psi(2S)$ resonance, which could in principle contribute to the measured spectra, was not included in the fitting model. This omission is justified in Pb–Pb collisions, where there is a large combinatorial background and the tails of the $\psi(2S)$ resonance make a negligible contribution to the mass range of interest. The fit stability was investigated by varying the fitting setup, the fitting procedure have been repeated with different combinations from available options listed above, this leads to a pool of trials for J/ψ yields. The average values of the J/ψ yields and their

corresponding statistical uncertainties obtained from all trials are taken as final values of the J/ψ yields and their corresponding statistical uncertainties, respectively. Finally an estimation of systematic uncertainty is evaluated as the root mean square (RMS) of all estimations. The p_T -differential J/ψ yields within 10-30% centrality is also shown below in Fig.4.17.

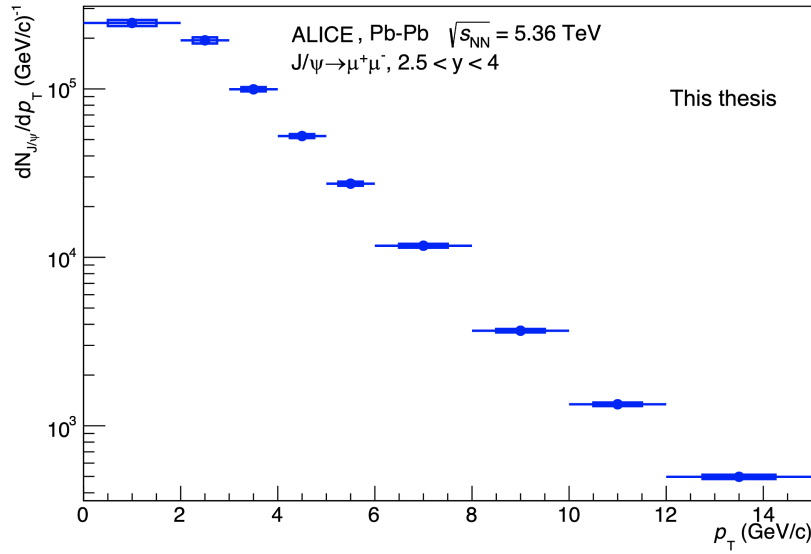


FIGURE 4.17 – J/ψ yields as function p_T within 10-30% centrality.

In Figure 4.17, the p_T -differential yield of J/ψ mesons at forward rapidity is shown for Pb–Pb collisions at $\sqrt{s_{NN}} = 5.36$ TeV in the 10–30% centrality class. Note that this spectrum has not been corrected for acceptance or efficiency. The x-axis represents the J/ψ transverse momentum, ranging from 0 to 15 GeV/c, while the y-axis (in logarithmic scale) shows the invariant differential yield, $dN_{J/\psi}/dp_T$, in units of (GeV/c) $^{-1}$. The distribution exhibits a steeply decreasing trend with increasing p_T . The yield is largest at very low p_T (< 2 GeV/c), where recombination of charm quarks contributes significantly in addition to primordial production. For $p_T \geq 2$ GeV/c, the yield decreases rapidly but remains statistically significant up to 15 GeV/c.

With the previously defined trials for yield extraction¹⁰, the Figure 4.18 shows an example of the systematic results for different fit configurations, corresponding to the transverse-momentum interval $12 < p_T < 15$ GeV/c in the 10–30% centrality

10. For the CB2 function, two types of initialization were employed: one using parameters obtained from Run 2 MC simulations, denoted as CB2(MC), and another based on data-driven parameters, denoted as CB2(data).

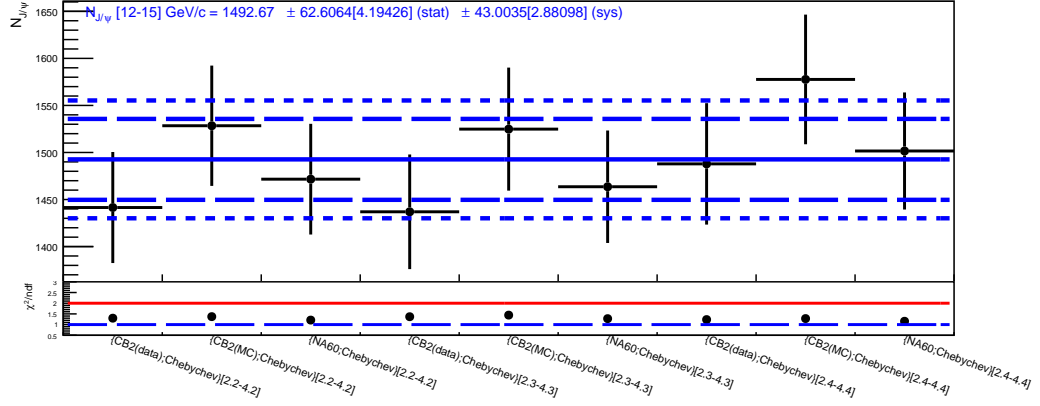


FIGURE 4.18 – Systematic result of $N^{J/\psi}$ for the p_T bin 12-15 GeV/c within the centrality class 10-30%.

class. The complete set of systematic uncertainties on the J/ψ raw yield, covering all p_T intervals, is reported in Appendix B. The final values of J/ψ yield with the estimated errors are shown in Table 4.4. These yield results are consistent with other Run 3 physics analyses performed by the ALICE collaboration.

p_T (GeV/c)	$N^{J/\psi}$ [10–30%]
0 – 2	492565 ± 5550 (1.1%) ± 20290 (4.1%)
1 – 2	336386 ± 4750 (1.4%) ± 12080 (3.6%)
2 – 3	194220 ± 2420 (1.2%) ± 8070 (4.2%)
3 – 4	99436 ± 1160 (1.2%) ± 2940 (3.0%)
4 – 5	52476 ± 607 (1.2%) ± 1390 (2.7%)
5 – 6	27363 ± 377 (1.4%) ± 779 (2.9%)
6 – 8	23433 ± 296 (1.3%) ± 600 (2.6%)
8 – 10	7332 ± 150 (2.0%) ± 174 (2.4%)
10 – 12	2682 ± 88 (3.3%) ± 66 (2.4%)
12 – 15	1493 ± 63 (4.2%) ± 43 (2.9%)

TABLE 4.4 – J/ψ raw yield as a function of p_T in 10–30% centrality. The first uncertainty is statistical, the second is systematic. The bin 1–2 GeV/c is shown in grey, this particular bin will be used to study flow fluctuations.

4.7.1.2 Uncertainties from $v_2^{J/\psi}$ extraction

In this section, we will discuss the systematic uncertainties from the $v_2^{J/\psi}$ extraction. We adopted event mixing technique to fix the combinatoric background of v_2 , and in the standard fitting procedure with event mixing, we made hypothesis that there is no correlated flow from mixed dimuon pair. Let's first introduce a generalised denominator expression for eq. 4.71:

$$\frac{N_{+-}^B}{N_{+-}^{\text{mix}} + \beta(N_{+-}^B - N_{+-}^{\text{mix}})} \quad (4.81)$$

where β is a free fit parameter that regulates the contribution of the correlated residual background, effectively weighting the difference $N_{+-}^B - N_{+-}^{\text{mix}}$. From the above defined expression, we classify two setups:

1. **No correlated flow contribution:** the β value will be fixed to 0.
2. **Undetermined correlated flow contribution:** in this case, we assume that the correlated flow contributes in the resulting mixed event shape, but we don't have a prior knowledge about how much it amounts. So β will be left as a free parameter that can vary from 0 to 1.

By performing multiple fit variations used to extract the yield, we collect a set of results. The variation among these results is taken as the systematic uncertainty of the fit, denoted as σ_{fit} . Here below in Figure 4.19 we show an example of systematic uncertainty estimation for the p_T range 0 – 2 GeV/c within centrality 10-30%. Complete systematic plots for all p_T and centrality bins used in this analysis can be found in appendix A.

At the bottom of the Figure 4.19, the χ^2/ndf of each fit is reported, providing a quantitative evaluation of the fit quality for the different configurations¹¹. This information ensures that the observed systematic spread is not driven by poorly constrained fits but rather reflects genuine sensitivity to the chosen fit settings. The points are grouped into three distinct blocks, each block containing 6 points, correspond to a different choice of fit mass range: [2.2, 4.2] (left), [2.3, 4.3] (middle), and [2.4, 4.4] (right) GeV/ c^2 . The clear separation between these three groups directly demonstrates that the dominant source of systematic uncertainty arises from the choice of fit mass range. This reflects the sensitivity of the measurement to the description

11. Unfortunately, in Figures 4.19 and 4.20, the end of the trial's name is cut off, so the fit mass range of each trial is not visible.

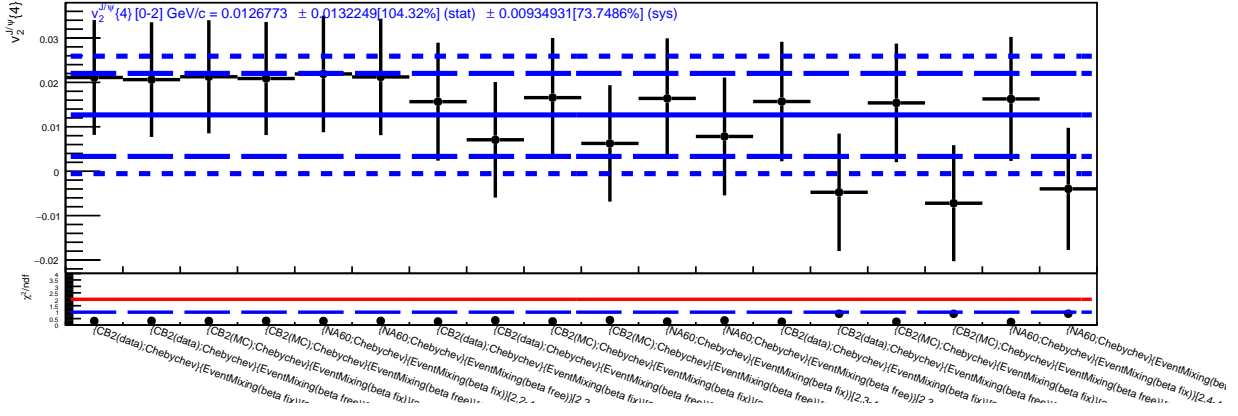


FIGURE 4.19 – Systematic uncertainty of J/ψ $v_2\{4\}$ from $v_2^{\mu\mu}\{4\}$ distributions (with larger mass binning) for the p_T bin 0-2 GeV/c in 10-30% centrality.

of the combinatorial background, which changes significantly when the fit range is modified. Within each block, different variations are tested, namely the treatment of the β parameters (either fixed or left free in the event-mixing background) and the choice of signal line shape (CB2 or NA60, with parameters taken from data or from simulation). These variations produce fluctuations inside each block, but the spread between blocks is larger. The figure therefore makes it evident that the leading contribution to the systematic uncertainty is driven by the fit mass range (related to the modeling of the combinatorial background). Notice that the second and third blocks, corresponding to the higher-mass fit ranges ($[2.3, 4.3]$ and $[2.4, 4.4]$ GeV/ c^2), a residual separation between the β -fixed and β -free configurations becomes visible. This effect represents the second-largest source of systematic uncertainty considered in the analysis. In addition, in Figure 4.20, we show the same type of study for distributions with finer mass binning as shown in figure 4.16.

A comparison of Figures 4.19 and 4.20 shows that the choice of binning has only a minor impact on the extracted v_2 within the statistical precision of Run3. In Run2, varying the binning had no visible effect, and thus no additional systematic uncertainty was assigned [178]. To remain conservative, however, a binning-related contribution is included in Run 3 by quantifying the spread of results obtained under rebinning. For each p_T range, we define

$$\sigma_{\text{rebin}} \equiv \sqrt{\frac{1}{N_{\text{rebin}} - 1} \sum_{i=1}^{N_{\text{rebin}}} \left(v_2^{(i)} - \bar{v}_2 \right)^2}, \quad (4.82)$$

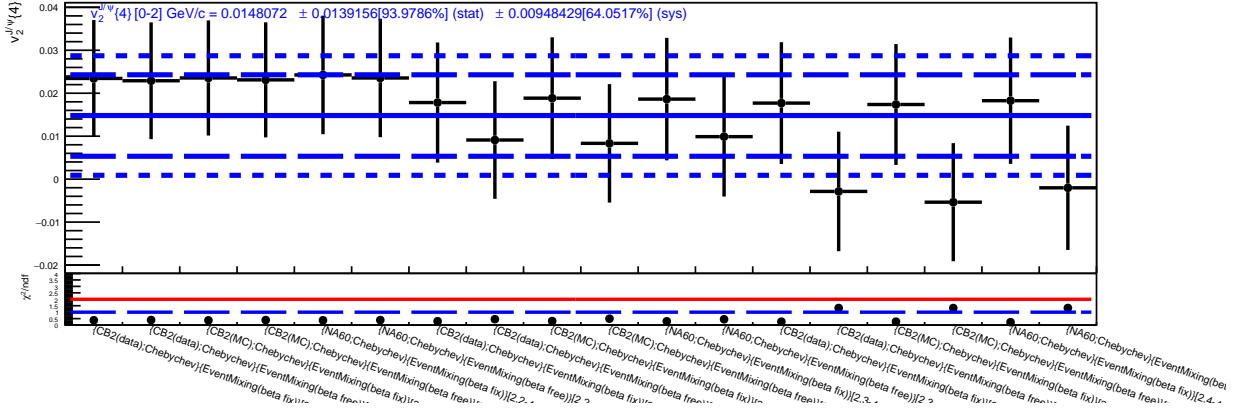


FIGURE 4.20 – Systematic uncertainty of J/ψ $v_2\{4\}$ from $v_2^{\mu\mu}\{4\}$ distributions with finer mass binning for the p_T bin 0-2 GeV/c in 10-30% centrality.

where, $v_2^{(i)}$ is the result for the i -th rebinning configuration and \bar{v}_2 is the mean value. In order to be conservative, we have used the following expression to define the total systematic uncertainty:

$$\sigma_{\text{sys}} = \sqrt{(\sigma_{\text{fits}})^2 + (\sigma_{\text{rebin}})^2}. \quad (4.83)$$

Nevertheless, it is important to note that the systematic uncertainties discussed here represent only a subset of all possible sources of uncertainty in our analysis. Other sources have been identified but not quantitatively evaluated in this work, including the following:

- Uncertainties in centrality estimation.
- Variations in event and track selection criteria.

In addition, several aspects that can be improved in future work are:

- Muon tracking efficiency and MID identification efficiency.
- Acceptance and efficiency corrections.
- Improvement of the initialization of the flow of single muons, to optimize the event-mixing setup.

In summary, in the context of this thesis, the analysis focused on the main sources of uncertainty identified in Run 2, particularly those associated with signal extraction. In conclusion, the robustness of the results was further ensured by systematically testing different fit functions, introducing the β parameter to account for correlated flow contributions, and variations of the mass fit ranges (the latter yielding

the largest systematic uncertainty).

4.8 J/ψ flow results

The Figure 4.21 presents, for the first time, the measurements of $v_2^{J/\psi}\{2\}$ and $v_2^{J/\psi}\{4\}$ as a function of p_T in Pb-Pb collisions at $\sqrt{s_{NN}} = 5.36$ TeV in the 10-30% centrality class.

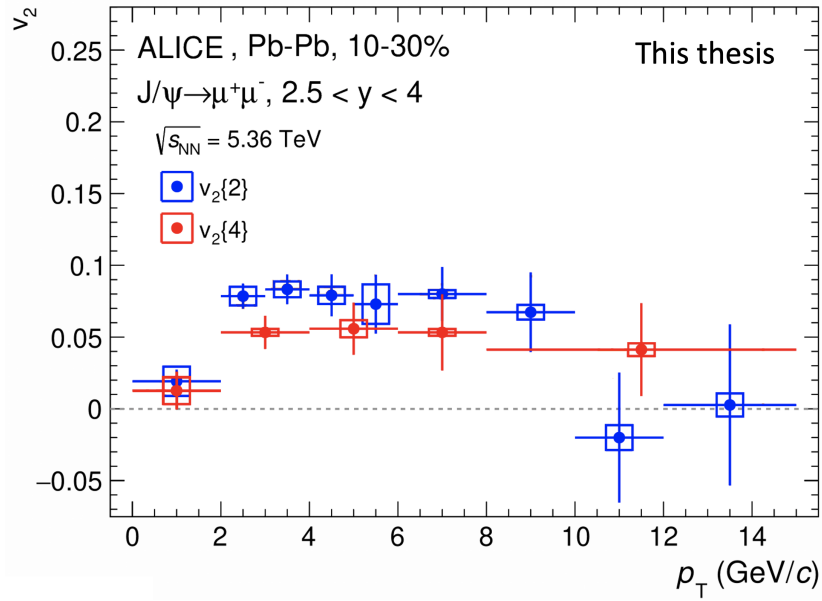


FIGURE 4.21 – First measurements of $v_2^{J/\psi}\{2\}$ and $v_2^{J/\psi}\{4\}$ in Pb-Pb collisions at $\sqrt{s_{NN}} = 5.36$ TeV in the 10-30% centrality class.

All J/ψ v_2 values with statistical and systematic uncertainties from the cumulant method are reported in the appendix A. A positive v_2 is observed over a broad p_T range (from 0 up to 10 GeV/c). In non-central collisions, a significant v_2 is expected due to the initial eccentricity (ϵ_2) [254], following the relation $v_2 \sim \kappa_2 \epsilon_2$, where κ_n characterizes the system's response. In the 10–30% centrality class, a significant v_2 at low p_T is attributed to the regeneration mechanism [255]. At higher p_T , v_2 appears to be relatively flat with slightly positive values. However, due to large statistical uncertainties above 10 GeV/c, no definitive conclusions can be drawn in this region.

In Figure 4.22, these results are compared to those obtained using the scalar product (SP) and event plane (EP) methods [256], offering a broader perspective on the consistency and differences among the various v_2 extraction techniques. We see an agreement between $v_2\{\text{EP}\}$, $v_2\{\text{SP}\}$ and $v_2\{2\}$ validating the robustness of the

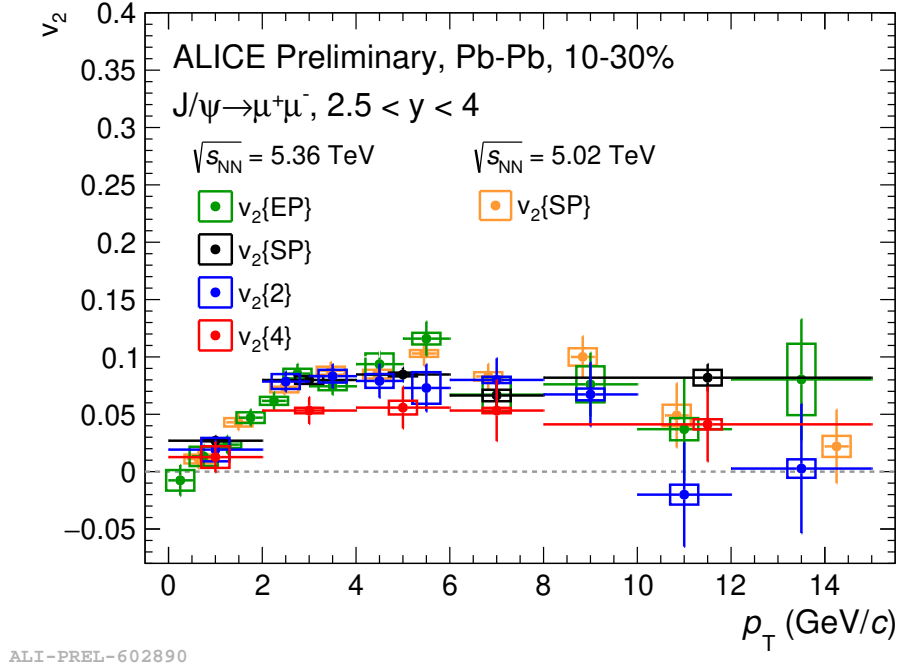


FIGURE 4.22 – Comparison of all Run 3 flow methods: cumulants, EP and SP [256] with the $v_2\{SP\}$ result from Run 2 [178].

observed J/ψ anisotropy. The Event Plane (EP) method estimates the reaction plane using the flow vector of all particles, while the Scalar Product (SP) method correlates the J/ψ flow vector with the reference flow vector. Both methods provide complementary approaches to measuring anisotropic flow, and their agreement with the cumulant method demonstrates the consistency of our results. In addition, in Figure 4.22, the Run 3 results at $\sqrt{s_{NN}} = 5.36$ TeV are compared with the Run 2 results at $\sqrt{s_{NN}} = 5.02$ TeV, obtained with the scalar product method [178]. The observed consistency can be attributed to the fact that the two collision energies are very similar.

Comparison to phenomenological models

We compare the measured $v_2\{SP\}$ and $v_2\{4\}$ with finer p_T binning (0-2, 2-3, 3-4, 4-5, 5-6 and 6-8 GeV/c) to theoretical predictions from the Tsinghua model [257] and the TAMU model [181], in order to assess the degree of consistency between the data and their predicted trends. The Tsinghua model is a transport-based framework that accounts for both initial-state fluctuations and medium-induced suppression. Heavy-quark evolution is described within a Langevin approach embedded in a hy-

hydrodynamically expanding QGP medium. The model incorporates color screening, dissociation, recombination dynamics, and regeneration from uncorrelated $c\bar{c}$ pairs. The TAMU model, based on the Recombination plus Resonance Model (RRM), provides an alternative description. Heavy quarks diffuse in the QGP and may recombine at hadronization to form bound states. Both primordial production and regeneration are included, with explicit treatment of medium effects on charmonium survival. A distinctive feature of the model is the inclusion of space momentum correlations (SMCs), which substantially modify the recombination probability and strongly influence the resulting v_2 .

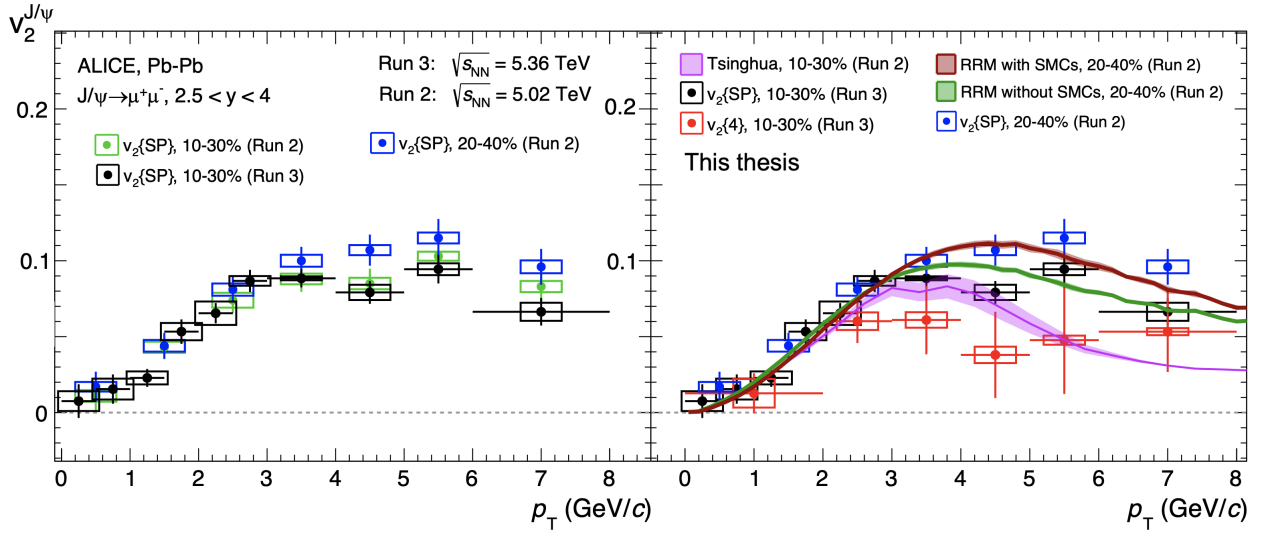


FIGURE 4.23 – $v_2^{J/\psi}$ as a function of p_T . The left panel shows $v_2\{SP\}$ for centrality intervals 20–40% and 10–30% from Run 2 data [178], together with the 10–30% measurement from Run 3. The right panel shows a comparison of $v_2\{SP\}$ and $v_2\{4\}$ with the Tsinghua transport model [257] and the TAMU Recombination Resonance Model (RRM), with and without soft medium correlations (SMCs) [181].

The left panel of Figure 4.23 shows $v_2\{SP\}$ for two centrality intervals from Run 2 data [178] (20–40% and 10–30%), together with 10–30% result from Run 3. The measurements exhibit comparable trends, consistent with expectations, since these centrality classes share similar initial eccentricities, where reduced regeneration is compensated by enhanced geometry-driven anisotropy. The right panel of Figure 4.23 reveals a systematic ordering $v_2\{4\} < v_2\{SP\}$ across all p_T bins. The Tsinghua model provides a reasonable description at low p_T but underestimates $v_2\{SP\}$ at intermediate and high p_T , consistent with earlier findings [257].

By contrast, the TAMU RRM with SMCs reproduces the Run 2 $v_2\{SP\}$ data with remarkable accuracy, as also reported in [181]. Interestingly, the measured $v_2^{J/\psi}\{4\}$ exhibits closer agreement with the Tsinghua predictions than with those of TAMU. Since none of the models account for event-by-event fluctuations (see Section 1.5.5 in Chapter 1), their predictions are expected to follow $v_2\{4\}$.

Although current uncertainties prevent firm quantitative conclusions, these comparisons underscore the importance of further model developments, particularly the explicit treatment of fluctuations and their role in quarkonium anisotropy.

Flow fluctuations measurements

A significance of 2.7σ is observed for $v_2\{4\} < v_2\{SP\}$, indicating a sensitivity of multi-particle cumulant v_2 of J/ψ to flow fluctuations. As detailed in section 4.2, the $v_2^{\mu\mu}$ coefficients are influenced by event-by-event fluctuations and non-flow contributions. Naturally, the same applies to the $v_2^{J/\psi}$ coefficients. Table 4.5 summarizes how the J/ψ coefficients $v_2\{2\}$, $v_2\{SP\}$, and $v_2\{4\}$ depend on the mean flow $\langle v_2^{J/\psi} \rangle$, flow fluctuations σ , and non-flow contributions δ , under the assumption of 2D Gaussian eccentricity fluctuations [247].

Flow method	δ -independence?	σ -independence?
$v_2^{J/\psi}\{2\}^2 = \langle v_2^{J/\psi} + \delta_2 \rangle^2 + \sigma^2$ $v_2^{J/\psi}\{SP\}^2 = \langle v_2^{J/\psi} \rangle^2 + \sigma^2$ $v_2^{J/\psi}\{4\}^2 = \langle v_2^{J/\psi} \rangle^2$	$\delta_2 \sim M^{-1} \neq 0$ $\delta_{SP} \sim 0$ $\delta_4 \sim M^{-3} \sim 0$	\times \times \checkmark
$\left. \begin{array}{l} \times \\ \times \\ \checkmark \end{array} \right\} \mathcal{BG}(\langle v_2^{J/\psi} \rangle, \sigma^2)$		

TABLE 4.5 – Summary of the dependence of $v_2^{J/\psi}\{2\}$, $v_2^{J/\psi}\{SP\}$, and $v_2^{J/\psi}\{4\}$ on non-flow contributions and flow fluctuations.

Note that in Table 4.5, $v_2\{SP\}$ depends on flow fluctuations and is considered unaffected by the non-flow contribution δ_{SP} , since an η -gap is applied by default in this method (see Section 1.5.4 in Chapter 1). The $v_2^{J/\psi}\{4\}$ coefficient corresponds to the mean value $\langle v_2^{J/\psi} \rangle$, denoting the average elliptic flow of J/ψ relative to the participant plane. Importantly, $v_2^{J/\psi}\{4\}$ is not influenced by non-flow effects or flow fluctuations¹². The derivation of the equations presented in Table 4.5 is provided in

12. Here, we consider 2D flow fluctuations rather than 1D, since the 1D approximation breaks down when the fluctuations are of the same order as the mean, $v_2^{J/\psi} \sim \sigma^{J/\psi}$, which seems to be the

appendix A. The difference between $v_2\{SP\}$ and $v_2\{4\}$ has been already estimated by CMS collaboration [130] in the sector of light hadrons, with the quantity F called fluctuation ratio, defined in the following way:

$$F = \sqrt{\frac{v_2\{2\}^2 - v_2\{4\}^2}{v_2\{2\}^2 + v_2\{4\}^2}}. \quad (4.84)$$

Using equations defined in Table 4.5, we can rewrite the above expression¹³ as:

$$F\left(\frac{\sigma_v}{\langle v_2 \rangle}\right) \sim \sqrt{\frac{\frac{\sigma_v^2}{\langle v_2 \rangle^2}}{2 + \frac{\sigma_v^2}{\langle v_2 \rangle^2}}}, \quad (4.85)$$

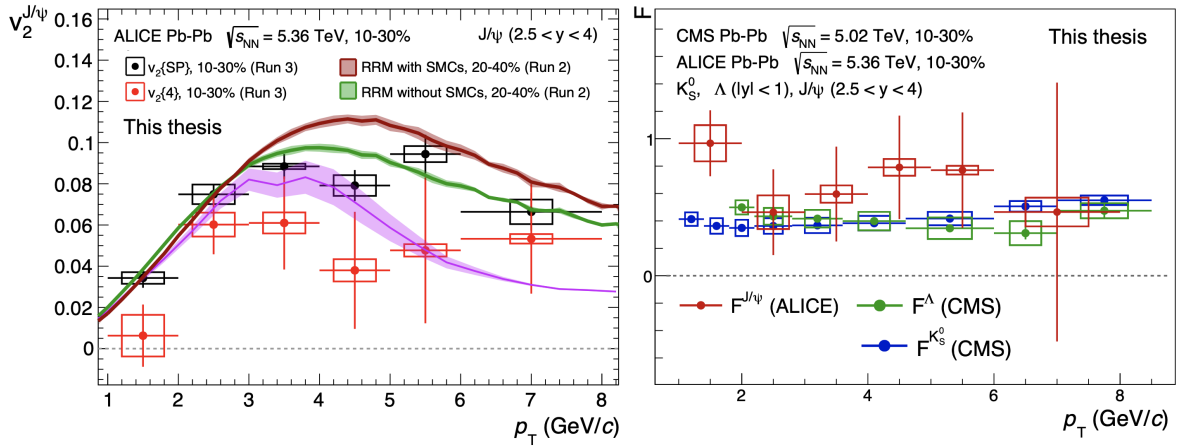


FIGURE 4.24 – Left panel: Results of $v_2\{SP\}$ and $v_2\{4\}$ as a function of p_T within the centrality class 10-30%. Right panel: Fluctuation ratio $F^{J/\psi}$ as function of p_T (Run 3 data) and compared to previous Run 2 CMS results [130].

The propagated uncertainties using second order corrections¹⁴ of $F^{J/\psi}$ employed in this analysis are presented in the appendix A. In order to properly estimate the fluctuation ratio, optimizing the statistics, we have used a larger binning at high p_T . In addition, we observed that the v_2^B background estimation via event mixing was not optimal at low p_T in the 0-2 GeV/c bin for low masses, as shown in top case for J/ψ in the 10-30% centrality class.

13. Before adopting equations shown in Table 4.5, it was assumed that $v_2\{2\}^2 = \langle v_2 \rangle^2 + \sigma_v^2$ and $v_2\{4\}^2 \approx \langle v_2 \rangle^2 - \sigma_v^2$, which leads to $F \approx \sigma_v / \langle v_2 \rangle$ [130].

14. Since F depends nonlinearly on $\langle v_2 \rangle$, the standard linear error propagation fails when $\langle v_2 \rangle \rightarrow 0$. In particular, near the first p_T bin, where $\langle v_2 \rangle$ is close to zero, the propagated error cannot be defined linearly and a second-order correction becomes mandatory.

panel of Figure 4.15. This underestimation of the background can be attributed to the lowest p_T of the bin as seen by comparing bin 0.2 GeV (Top panel) to bin 1-2 GeV (middle panel). For that reason we decided to exclude the bin 0-1 GeV. In left panel of Figure 4.24, the $v_2^{J/\psi}\{SP\}$ and $v_2^{J/\psi}\{4\}$ have then been studied with the following binning: 1-2, 2-3, 3-4, 4-5, 5-6 and 6-8 GeV/c. The same models shown in Figure 4.23 are again compared with the new binning. In addition, in the right panel of Figure 4.24, $F^{J/\psi}$ measured by ALICE is compared to F^Λ and $F^{K_S^0}$ ¹⁵ measured by CMS [130]. It has been claimed that if F shows a significant dependence on p_T , the observed fluctuations are predominantly driven by variations in the initial-state geometry and final-state dynamical effects. Notice that $F^{J/\psi}$ is relatively flat at high p_T , similar to the F^Λ and $F^{K_S^0}$ values. The $F^{J/\psi}$ ratio of the first p_T bin is near 1, meaning flow fluctuations are quite significant. Nevertheless, within the present uncertainties, $F^{J/\psi}$ appears consistent with a roughly flat behavior (~ 0.6) across the entire p_T range. The reported values of $v_2^{J/\psi}\{SP\}$, $v_2^{J/\psi}\{4\}$ and $F^{J/\psi}$ are reported in table 4.6.

$J/\psi \rightarrow \mu^+ \mu^-, 2.5 < y < 4$				Pb-Pb, $\sqrt{s_{NN}} = 5.36$ TeV, 10-30%					
p_T [GeV/c]	$v_2\{SP\}$	Stat	Sys	$v_2\{4\}$	Stat	Sys	F	Stat	Sys
1 - 2	0.0343	0.0047	0.0028	0.0063	0.0151	0.0101	0.9666	0.1570	0.1055
2 - 3	0.0749	0.0049	0.0048	0.0571	0.0157	0.0052	0.5153	0.2551	0.1000
3 - 5	0.0855	0.0047	0.0013	0.0598	0.0161	0.0070	0.5859	0.2067	0.0886
5 - 15	0.0814	0.0058	0.0035	0.0551	0.0209	0.0027	0.6091	0.2728	0.0460

TABLE 4.6 – $v_2^{J/\psi}\{SP\}$, $v_2^{J/\psi}\{4\}$, and $F^{J/\psi}$ with their corresponding statistical and systematic uncertainties.

In this thesis, to properly evaluate the magnitude of flow fluctuations, we have evaluated the p_T dependence of the following difference:

$$\sigma = \sqrt{v_2\{SP\}^2 - v_2\{4\}^2}. \quad (4.86)$$

The propagated errors of σ is detailed in the appendix A. Figure 4.25 allows to distinguish two different contributions to the elliptic flow of particles measured

¹⁵ The quark composition of Λ is uds . The short-lived neutral kaon is not a pure flavor state but a superposition of $K^0 = d\bar{s}$ and $\bar{K}^0 = \bar{d}s$. Including CP violation, the physical states is $|K_S^0\rangle = \frac{1}{\sqrt{1+|\epsilon|^2}}(|K^0\rangle + (1+\epsilon)|\bar{K}^0\rangle)$, where $\epsilon \sim 2 \times 10^{-3}$ quantifies indirect CP violation in the neutral kaon system.

with the scalar product method: The mean elliptic flow $\langle v_2 \rangle$ and the event-by-event fluctuations σ .

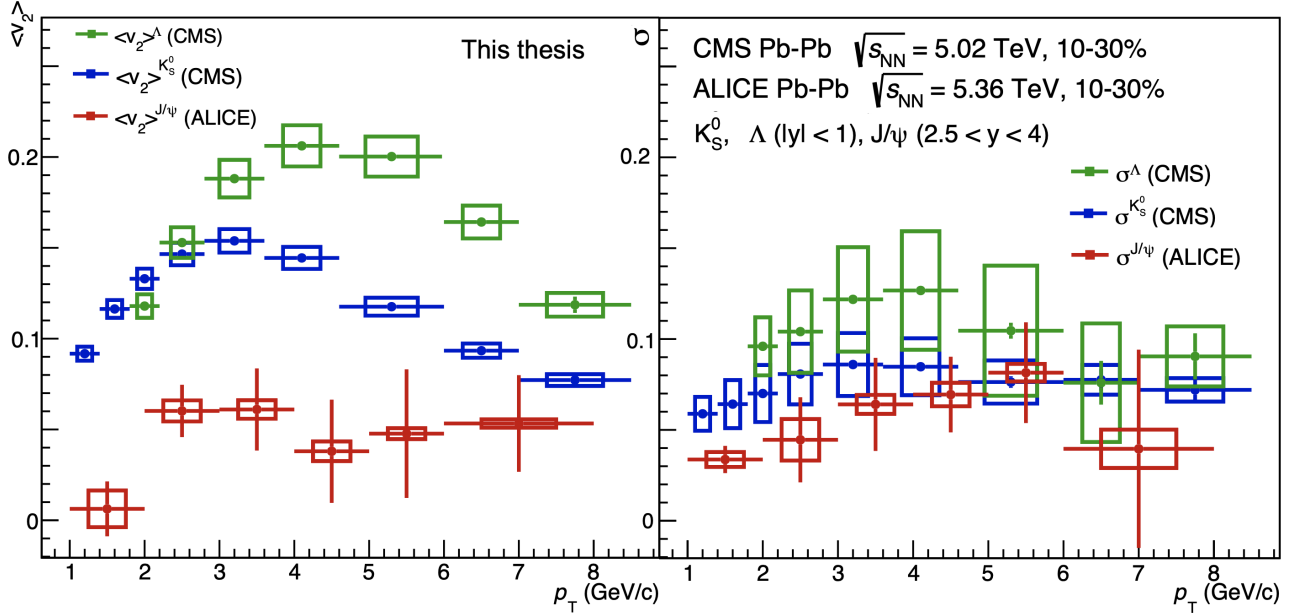


FIGURE 4.25 – Comparison of $\langle v_2 \rangle$ (left) and $\sigma_{v_2}/\langle v_2 \rangle$ (right) as a function of p_T for J/ψ from ALICE and K_S^0 , Λ from CMS in Pb–Pb collisions [130].

While the mean elliptic flow is expected to be produced by collective effects in the medium, the event-by-event fluctuations could arise from initial eccentricity fluctuations or system dynamic evolution, or even later stages in the medium evolution such as coalescence (at intermediate p_T) or fragmentation (at high p_T) [258]. While the contributions to the elliptic flow from initial eccentricity fluctuations is expected to be independent of p_T and particle species [259], fluctuations from later-stage processes are expected to depend on the kinematics of the considered particles, as well as on the particle species. The left panel of Figure 4.25 presents the transverse momentum dependence of $\langle v_2 \rangle$ (which is in fact the measured $v_2\{4\}$) for J/ψ , Λ , and K_S^0 .

At very low p_T : The mean flow of J/ψ is driven by the regeneration mechanism. When comparing it to K_S^0 and Λ , the mean elliptic flow shows a hint of a characteristic mass dependence that could be understood from an m_T -scaling approximation¹⁶.

16. Such a scaling behavior is expected to emerge if the constituent quarks fully thermalize in QGP medium.

A simple parametrization of the elliptic flow is

$$v_2 = \frac{\alpha}{T} (p_T - v m_T), \quad (4.87)$$

where α is a proportionality constant, T a characteristic scale, p_T the transverse momentum, $m_T = \sqrt{p_T^2 + m^2}$ the transverse mass, and v an average collective velocity [78]. In principle, Equation 4.87 works in the light-sector of hadrons, it shows that the buildup of elliptic flow depends on the competition between the particle's momentum and its mass. For light mesons such as kaons, one has $m_T \simeq p_T$ at low momentum, so the mass term has little effect and v_2 rises nearly linearly with p_T . For heavier hadrons such as the Λ baryon, the larger m_T suppresses the elliptic flow in the first p_T bin, giving rise to the expected mass ordering. The observed hierarchy is in alignment with the mass scaling of light hadrons and recombination of charm quarks picture:

$$v_2^K > v_2^\Lambda > v_2^{J/\psi}, \quad (4.88)$$

which is observed below about 2 GeV/ c .

At mid-high p_T :

The J/ψ is produced predominantly in the earliest stages of the collision. In this regime, no significant coalescence (J/ψ regeneration) contribution is expected, in contrast to light hadrons. In this p_T region, a phenomenon often referred to as baryon–meson splitting is observed for light hadrons. Interestingly, when comparing ALICE and CMS results, a clear hierarchy in the elliptic flow v_2 emerges:

$$v_2^{J/\psi} < v_2^{K_S^0} < v_2^\Lambda. \quad (4.89)$$

For K_S^0 and Λ , the ordering in Eq. 4.89 can be qualitatively understood in terms of number-of-constituent-quark (NCQ) scaling,¹⁷ [260] which is consistent with expectations from quark coalescence models. Since the light quark masses $m_u, m_d, m_s \ll T_{\text{eff}}^{\text{QGP}}$, they can be considered fully thermalized in the QGP. This implies that their elliptic flows are approximately the same: $v_2^u \sim v_2^d \sim v_2^s$. For the charm quark, its much larger mass compared to $T_{\text{eff}}^{\text{QGP}}$ prevents full chemical thermalization (the thermal production of charm quarks can be neglected). Theoretical considerations suggest that it undergoes only partial kinematic thermalization [160, 161]. The

17. NCQ scaling refers to the empirical observation that when v_2 is scaled by the number of constituent quarks n , i.e. v_2/n , as a function of p_T/n , particles of different species approximately fall onto a common curve, indicating that collective flow is established at the partonic level.

behavior of the J/ψ flow at mid-to-high p_T , therefore, remains poorly understood. If regeneration (coalescence of charm quarks) were to extend to higher p_T values, then the hierarchy in Eq. 4.89 would be naturally accommodated. Assuming coalescence, the flow of hadrons can be understood as the sum of the contributions from their constituent quarks:

$$v_2^\Lambda \sim v_2^u + v_2^d + v_2^s, \quad v_2^{K_S^0} \sim v_2^d + v_2^s. \quad (4.90)$$

In Eq. 4.90, the Λ baryon, composed of three light quarks (uds), inherits the flow generated by the strongly interacting bulk medium, where light quarks are believed to thermalize efficiently. The K_S^0 meson, containing two light quarks (d and s), carries the combined flow of two thermalized constituents.

The Right panel of Figure 4.25 presents σ as function of p_T for J/ψ , Λ and K_S^0 . It shows a mid-high p_T a hint of a similar hierarchy (shown in equation 4.89), emerging in the fluctuation observable σ , with

$$\sigma^{J/\psi} < \sigma^{K_S^0} < \sigma^\Lambda. \quad (4.91)$$

Nevertheless, with the current uncertainties, it is not possible to have a strong conclusion. While Figure 4.25 clearly shows, based on CMS measurements, that the event-by-event fluctuations are smaller than $\langle v_2 \rangle$ in the light sector, in particular at intermediate p_T , in the case of J/ψ both are found to be of similar order over the whole p_T range: $\sigma^{J/\psi} \sim \langle v_2^{J/\psi} \rangle$. In addition a striking observation arrives when comparing the first p_T bin of J/ψ presented in the left panel to the one of the right panel of Figure 4.25. One finds a hint of $\langle v_2^{J/\psi} \rangle < \sigma^{J/\psi}$, which is a consequence of $v_2\{4\} \sim 0$ and $v_2\{SP\} > 0$ in this p_T bin. This shows for the first time a hint that at low p_T flow fluctuations may be even larger than the flow expected from regeneration mechanisms. Finally, we emphasize that the fact that their flow fluctuations $\sigma^{J/\psi}$ are quite large in the entire p_T region, comparable to the $\langle v_2^{J/\psi} \rangle$, suggests that event-by-event fluctuations may play an important role in the observed $v_2\{SP\}$. Better statistical precision on this measurement would enable a more quantitative understanding of the shape of the event-by-event fluctuations distributions with p_T , and thus would shed light on the dominant mechanism at play behind these fluctuations. The extracted values of $\sigma^{J/\psi}$ are reported in table 4.7.

In Figures 4.25 and 4.24, a weak p_T dependence of $\sigma^{J/\psi}$ cannot be excluded. In particular, the first p_T bin (1–2 GeV/c) yields a significantly smaller value, $\sigma^{J/\psi} \sim 0.03$, compared to the higher- p_T intervals. Similarly, the fluctuation ratio in the same

$J/\psi \rightarrow \mu^+\mu^-, 2.5 < y < 4$		Pb-Pb, $\sqrt{s_{NN}} = 5.36$ TeV, 10-30%	
p_T [GeV/c]	σ	Stat	Sys
1 - 2	0.0337	0.0056	0.0034
2 - 3	0.0485	0.0200	0.0095
3 - 5	0.0611	0.0170	0.0071
5 - 15	0.0598	0.0208	0.0053

TABLE 4.7 – Flow fluctuation measurements $\sigma^{J/\psi} \equiv \sqrt{v_2^{J/\psi} \{SP\}^2 - v_2^{J/\psi} \{4\}^2}$ with statistical and systematic uncertainties.

bin amounts to $F^{J/\psi} \sim 0.97$, i.e. close to unity. Although the limited statistical precision at higher p_T prevents a firm conclusion, the relatively large value of $F^{J/\psi}$ in the first bin suggests a possible p_T dependence, accompanied by an increase of $\sigma^{J/\psi}$ in the low and mid p_T regions.

4.9 2D representation of flow fluctuations

To illustrate the event-by-event flow fluctuations results presented in Figure 4.25, we use a 2D representation in the EP plane to interpret the fluctuations of different species (See Figure 4.26).

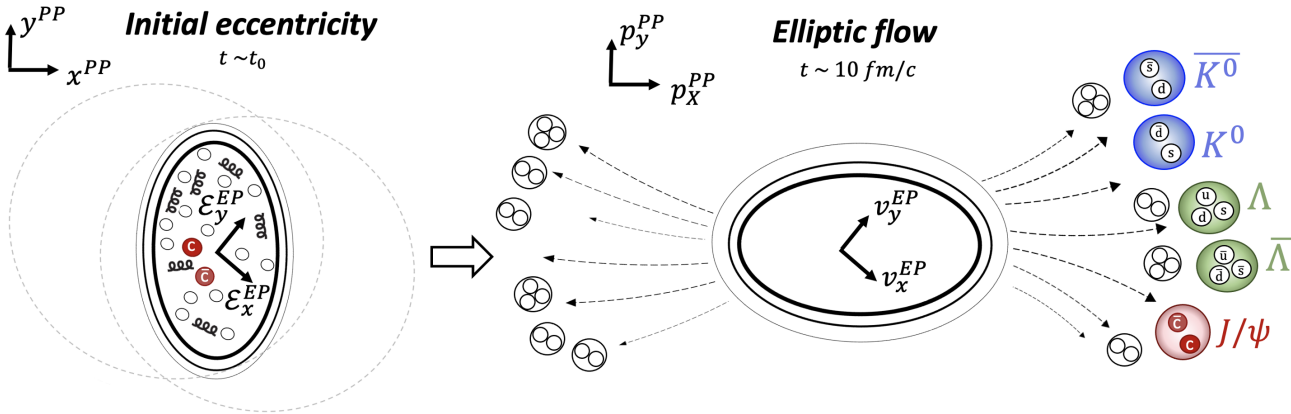


FIGURE 4.26 – Illustration of the initial eccentricity and its anisotropic response for Λ , $\bar{\Lambda}$, K^0 , \bar{K}^0 , and J/ψ with respect to the event plane.

We employ a 2D random sampling modeling, using Bessel-Gaussian \mathcal{BG} distributions, described in Section 1.5.5 of Chapter 1. In this representation, the v_2 values are displayed as a cloud of points, while the spread of the cloud illustrates the dispersion associated with the size of the flow fluctuations. The comparison

of event-by-event fluctuations is obtained for J/ψ , K_S^0 , and Λ , as illustrated in Figure 4.27.

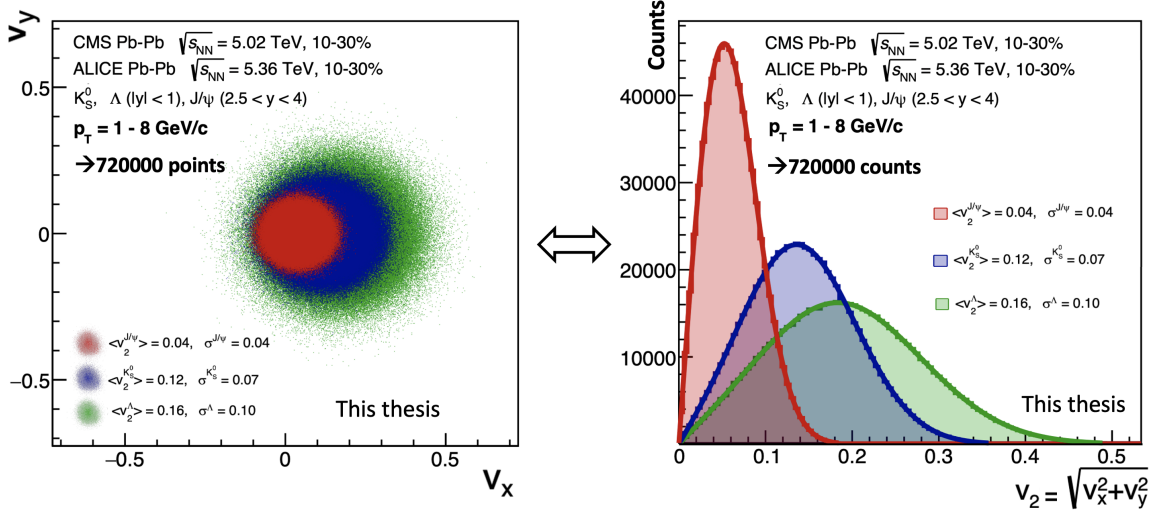


FIGURE 4.27 – Event-by-event flow fluctuations of J/ψ , K_S^0 , and Λ , obtained from random sampling of 720000 values, corresponding to the number of J/ψ in the 10–30% centrality class integrated over the interval $p_T = 1\text{--}8$ GeV/c. The left panel shows clouds of $v_2^{J/\psi}$, $v_2^{K_S^0}$, and v_2^{Λ} , where $v_2 = \sqrt{v_x^2 + v_y^2}$ represents the radial magnitude in the (v_x, v_y) plane, following a \mathcal{BG} distribution centered at $\langle v_2 \rangle$ with variance σ^2 . The right panel shows the distribution of counts as a function of v_2 . Solid curves denote the analytic \mathcal{BG} functions, while the filled histograms show the sampled distributions, with bin width $\Delta v_2 = 0.005$.

In the left panel of Figure 4.27, we show the 2D distributions in the (v_x, v_y) plane, referred to as the clouds. Each point of a cloud corresponds to a realization of the flow vector, whose Cartesian components are sampled as $v_x \sim \mathcal{N}(\langle v_2 \rangle, \sigma^2)$ and $v_y \sim \mathcal{N}(0, \sigma^2)$, with fluctuations taken as isotropic. Then, the corresponding flow magnitude $v_2 = \sqrt{v_x^2 + v_y^2}$, is distributed according to a Bessel–Gaussian \mathcal{BG} distribution $v_2 \sim \mathcal{BG}(\langle v_2 \rangle, \sigma^2)$. Note that the chosen values of $\langle v_2 \rangle$ and σ were obtained by taking a simple (unweighted) average over all p_T bins within the interval $p_T = 1\text{--}8$ GeV/c, and should therefore be regarded only as estimates.

The approximated values¹⁸. We can see that the red (J/ψ) cloud is not centered with the blue (K_S^0) and green (Λ) clouds. This directly visualizes Equation 4.89 (also reflected in the left Panel of Figure 4.25). The dispersion of the green points is the largest, the blue points intermediate, and the red points the narrowest, reflecting the hierarchy of Equation 4.91 (also hinted in the right Panel of Figure 4.25). One can clearly see that the centers of the green and blue clouds are noticeably larger than their respective radii, $\langle v_2^{K_S^0} \rangle > \sigma^{K_S^0}$ and $\langle v_2^\Lambda \rangle > \sigma^\Lambda$. In contrast, the position of the red cloud is of the same order of magnitude as the cloud's radius, $\langle v_2^{J/\psi} \rangle \sim \sigma^{J/\psi}$.

In addition, the right panel of Figure 4.27 can be understood as the radial projection of the v_2 clouds shown in the left panel, illustrating the corresponding flow-magnitude distributions. The solid curves in the right panel indicate the analytical \mathcal{BG} functions determined from the $\langle v_2 \rangle$ and σ parameters, providing the expected probability distributions of v_2 for each particle species. By construction, v_2 is a positive-definite quantity, which explains the absence of entries below zero. The red distribution is the narrowest and most asymmetric, reflecting the quadratic nature of the underlying \mathcal{BG} distribution. In contrast, the green distribution is the broadest, while the blue distribution exhibits an intermediate shape between the narrow red and the broad green distributions. Because of these features, one can see that the flow distribution shape of J/ψ is more similar to that of K_S^0 than to Λ .

The same type of display was applied across three different p_T intervals, as shown in Figure 4.28. The number of random samplings in each interval was determined from the raw J/ψ yields reported in Table 4.4. By summing the corresponding bins, we obtained the total yields in the three p_T intervals of interest. The values of $\langle v_2 \rangle$ and σ in each interval were then computed as unweighted averages of the v_2 measurements within the respective ranges. The green and blue clouds (corresponding to strange hadrons) display nearly identical radii in the low- and intermediate- p_T ranges, as shown in left and middle panels of Figure 4.28. However, in the high- p_T range, both distributions shrink in size, as illustrated in the right panel of Figure 4.28. In contrast, the red cloud, representing J/ψ flow fluctuations, remains approximately constant across all three p_T intervals. At high p_T , its radius becomes comparable to that of the blue and green clouds, indicating that the magnitude of J/ψ flow fluctuations is of the same order as that of light hadrons. Overall, Figure 4.28 is visually consistent with the trends reported in Figure 4.25.

18. Notice that here we do not display the uncertainties on $\langle v_2 \rangle$ and σ . The purpose is purely illustrative, to convey the idea of the associated event-by-event fluctuations.

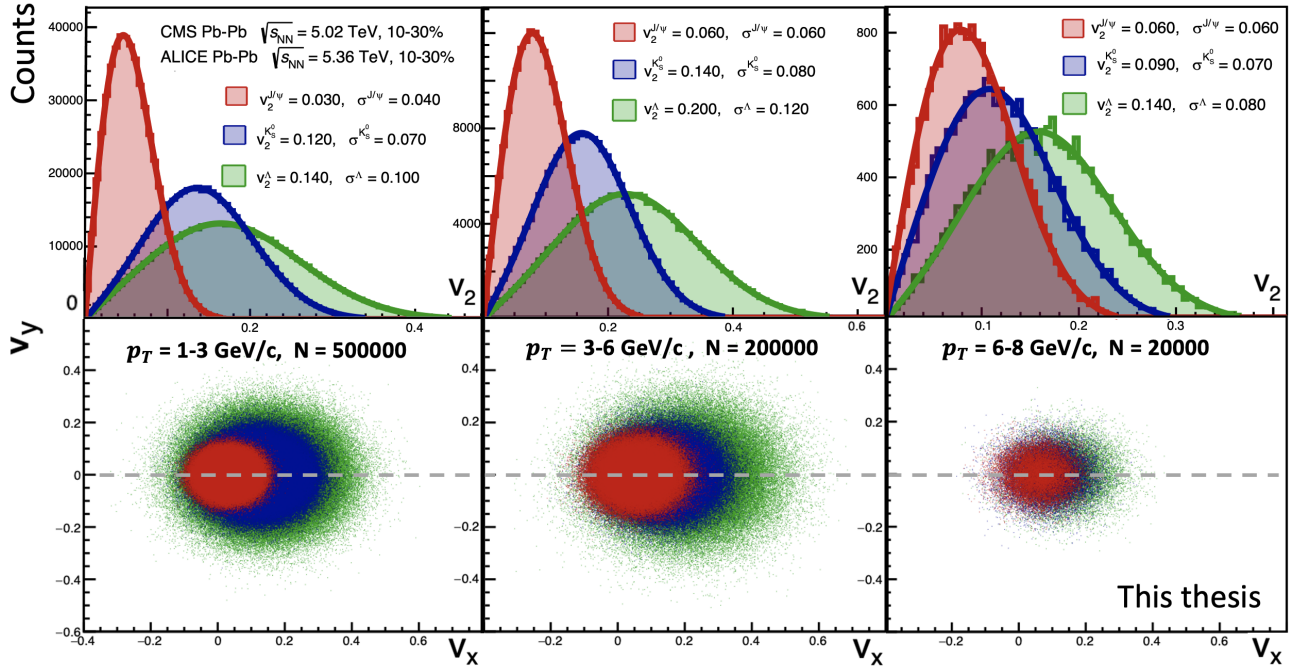


FIGURE 4.28 – Event-by-event flow fluctuations of J/ψ , K_S^0 , and Λ in the 10–30% centrality class, obtained via random sampling of N entries. Left panel: $N = 500,000$ for low p_T (1–3 GeV/c). Middle panel: $N = 200,000$ for intermediate p_T (3–6 GeV/c). Right panel: $N = 20,000$ for high p_T (6–8 GeV/c).

In summary, this BG-based representation, rather than providing a direct derivation of $v_2\{2\}$ and $v_2\{4\}$ in terms of fluctuations, offers an intuitive framework to visualize their dispersion and to evaluate the impact of event-by-event fluctuations.

Chapter 5

Study of cold nuclear matter effects with Drell-Yan production

In the previous chapter, we saw that the non-zero elliptic flow of the J/ψ can be used to probe both their production mechanisms and the properties of the QGP. In the introduction chapter, we also mentioned the importance of parametrizing the nuclear parton distribution functions (nPDF) in order to properly study particle production in heavy-ion collisions. We will now present a phenomenological study which aims at predicting the distribution of nuclear partons (nPDF) at low Bjorken- x in lead nuclei, where cold nuclear matter effects (such as gluon saturation or shadowing) remain poorly understood. Usually, nPDF are determined from global fits. The potential impact from Drell-Yan (DY) data for p-Pb collisions is shown using reweighting techniques applied to pseudo-data. In section 5.1, we introduce the Drell-Yan process in hadronic collisions. In section 5.2, we present a detailed analysis of the predicted DY pseudo-data (at LHCb kinematic region), explaining the nPDF reweighting procedure. Preliminary results are also provided in section 5.2.4.

5.1 Drell-Yan in high-energy collisions

The DY process at leading-order (LO) happens when a quark from one hadron and an antiquark from another hadron annihilate, giving rise to a virtual photon (γ^*) or Z boson, this intermediate state decays into a pair of oppositely-charged leptons. The next-to-leading order (NLO) corrections for the DY process involves real corrections, e.g. annihilation ($q\bar{q} \rightarrow \gamma^*g$), Compton scattering ($qg \rightarrow \gamma^*q$), as well as virtual diagrams, e.g. self-energy and vertex corrections to the Born rate

$(q\bar{q} \rightarrow \gamma^*)$.

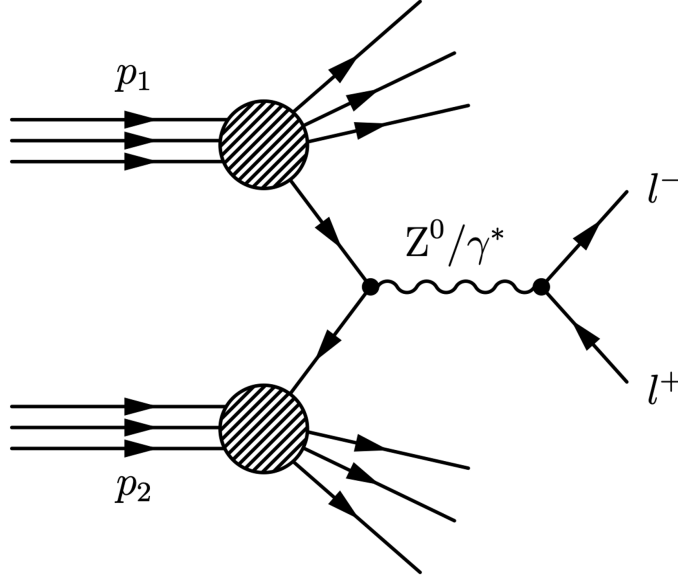


FIGURE 5.1 – Illustration of the DY process at LO.

The LO Drell–Yan process, illustrated in Figure 5.1, occurs when a quark from nucleus A annihilates with an antiquark from nucleus B . Each nucleus contributes a parton carrying longitudinal momentum fractions x_1 and x_2 , respectively. Their annihilation produces either a virtual photon (γ^*) or a Z boson, which subsequently decays into a lepton pair. The corresponding LO differential cross section is given by:

$$\frac{d\sigma_{AB \rightarrow \ell^+ \ell^-}^{LO}}{dM^2 dy} = \sum_{i,j} \frac{e^4 Q_i Q_j}{36\pi M^2 s} f_{i/A}(x_1) f_{j/B}(x_2), \quad (5.1)$$

where, the cross-section describes the LO DY process for producing a lepton pair with invariant mass M and rapidity y in a hadronic collision. The sum runs over quark flavors i, j , with Q_i and Q_j denoting their electric charges in units of the electron charge e ¹ and s is the square of the center-of-mass energy of the collision. The functions $f_{i/A}(x_1)$ and $f_{j/B}(x_2)$ represent the parton distribution functions (PDFs). In addition, equation 5.1 shows that the DY cross section is more sensitive to up quarks than to down quarks, because up quarks have a larger electric charge ($Q_u = +\frac{2}{3}$) than down quarks ($Q_d = -\frac{1}{3}$). As a result, the contribution from

1. e is the elementary electric charge, with a value of approximately $e \approx 1.602 \times 10^{-19}$ C.

up–anti-up annihilation to the cross section is about four times larger than that from down–anti-down annihilation.

Notice that at LO, the longitudinal momentum fractions of partons x_1 and x_2 are directly related to the rapidity y of the dilepton system in the following way

$$x_{1,2} = \frac{M}{\sqrt{s}} e^{\pm y}. \quad (5.2)$$

5.1.1 Isospin effects in pA

Proton–nucleus (pA) collisions are useful for constraining nPDFs because they are simpler than nucleus–nucleus (AA) collisions and benefit from well-understood proton PDFs. However, electron–ion collisions would offer cleaner access to nPDFs². While the LHC is primarily known for its symmetric pp and AA collision programs, it can also perform asymmetric pA collisions. A particular advantage of pA at the LHC lies in the broad kinematic coverage provided by the high beam energy, which enables simultaneous access to both very small and very large parton momentum fractions in nuclei³, as reflected in equation 5.2. At backward rapidity where $x_2 \gg x_1$ the DY cross section is dominated by the valence quarks of nucleus A ($\sigma^{DY} \propto \bar{q}^P q^A$). In this region, isospin effects coming from the type of nucleons (neutron or proton) in nucleus takes place. These effects are due to the difference between protons and neutrons (consisting of different valence quarks). If we ignore nuclear matter effects, the parton distribution function f_i^A can be expressed by the following average of f_i^p and f_i^n :

$$f_i^A = Z f_i^p + (A - Z) f_i^n, \quad (5.3)$$

where, Z is the atomic number and A the mass number. The neutron PDF f_i^n is obtained with isospin symmetry hypothesis:

2. This is a key motivation behind the proposed Electron-Ion Collider (EIC).

3. In symmetric systems (pp, AA), the physics at forward and backward rapidities are equivalent by construction. In asymmetric pA collisions, however, forward rapidities probe exclusively the low- x partons of the nucleus, whereas backward rapidities provide sensitivity to its high- x components.

$$\begin{aligned}
f_d^n(x) &\equiv f_u^p(x), \\
f_u^n(x) &\equiv f_d^p(x), \\
f_{\bar{d}}^n(x) &\equiv f_{\bar{u}}^p(x), \\
f_{\bar{u}}^n(x) &\equiv f_{\bar{d}}^p(x).
\end{aligned} \tag{5.4}$$

Using the collinear factorization theorem, the R_{pA} factor can be expressed as:

$$R_{pA} = \frac{\sigma_{pA}}{A\sigma_{pp}} = \frac{f_i^p [Zf_i^p + (A-Z)f_i^n] \otimes \hat{\sigma}}{Af_i^p f_i^p \otimes \hat{\sigma}}, \tag{5.5}$$

where, $\hat{\sigma}$ is the perturbatively calculable partonic cross section, and \otimes denotes the convolution of PDFs with the partonic cross section. By cancelling $\hat{\sigma}$ in the numerator and denominator, one isolates the isospin-dependent structure of the nuclear modification factor. This approximation reflects the universality of the hard scattering process in collinear factorization and leads to:

$$R_{pA} \sim \frac{f_i^p [Zf_i^p + (A-Z)f_i^n]}{Af_i^p f_i^p}. \tag{5.6}$$

At backward rapidity, the DY process probes large- x partons in the nucleus, where valence quarks dominate. Because DY couples most strongly to up quarks, it is particularly sensitive to the relative abundance of valence u -quarks. A proton carries two valence up quarks, while a neutron carries only one. Consequently, the effective partonic flux is reduced by roughly a factor of two when scattering on neutrons compared to protons. Motivated by this argument, one can approximate at backward rapidity, the neutron PDF as being about half that of the proton: $f_i^n \sim \frac{1}{2}f_i^p$. Then the nuclear modification factor R_{pA} can be expressed as:

$$R_{pA} \sim \frac{(Z + \frac{A-Z}{2})f_i^p}{Af_i^p}. \tag{5.7}$$

This leads to the simplified expression:

$$R_{pA} \sim \frac{Z}{A} + \frac{1}{2} - \frac{Z}{2A} = \frac{A+Z}{2A} < 1. \tag{5.8}$$

Equation 5.8 predicts a suppression of R_{pA} at backward rapidity ($x_2 \gg x_1$) due to the isospin effects. For lead ($Z = 82$, $A = 208$), this gives $R_{pA}^{\text{Pb}} \sim 0.697$. We notice if $A = Z$ then $R_{pA} = 1$.

5.1.2 Antiquark flavor asymmetry in the nucleon sea

In proton–deuteron collisions, another effect known as antiquark flavour asymmetry becomes relevant. This asymmetry arises from the difference in the parton distribution functions (PDFs) of \bar{u} and \bar{d} quarks in the nucleon sea. The perturbative cross section of DY in $p - p$ collision system can be approximated as:

$$\sigma_{pp} \propto \frac{4}{9}f_u^p(x_1)f_{\bar{u}}^p(x_2) + \frac{1}{9}f_d^p(x_1)f_{\bar{d}}^p(x_2). \quad (5.9)$$

Similarly, the asymmetric $p-n$ collision system can be written as:

$$\sigma_{pn} \propto \frac{4}{9}f_u^p(x_1)f_{\bar{d}}^n(x_2) + \frac{1}{9}f_d^p(x_1)f_{\bar{u}}^n(x_2). \quad (5.10)$$

Combining equations 5.9 and 5.10, we can build the deuteron-proton nuclear factor R_{DY}^{pd} , directly linked to the antiquark flavor asymmetry:

$$R_{pd}^{DY} = \frac{\sigma_{pd}}{2\sigma_{pp}} = \frac{\sigma_{pp} + \sigma_{pn}}{2\sigma_{pp}} \quad (5.11)$$

$$= \frac{1}{2} \left[\frac{\frac{4}{9}f_u^p(x_1)f_{\bar{u}}^p(x_2) + \frac{1}{9}f_d^p(x_1)f_{\bar{d}}^p(x_2) + \frac{4}{9}f_u^p(x_1)f_{\bar{d}}^n(x_2) + \frac{1}{9}f_d^p(x_1)f_{\bar{u}}^n(x_2)}{\frac{4}{9}f_u^p(x_1)f_{\bar{u}}^p(x_2) + \frac{1}{9}f_d^p(x_1)f_{\bar{d}}^p(x_2)} \right] \quad (5.12)$$

$$= \frac{1}{2} \left[1 + \frac{4f_u^p(x_1)f_{\bar{d}}^n(x_2) + f_d^p(x_1)f_{\bar{u}}^n(x_2)}{4f_u^p(x_1)f_{\bar{u}}^p(x_2) + f_d^p(x_1)f_{\bar{d}}^p(x_2)} \right]. \quad (5.13)$$

At forward rapidity where $x_1 \gg x_2$, there are more quarks up than down in a proton, the following approximation can be done:

$$R_{pd}^{DY} \approx \frac{1}{2} \left[1 + \frac{f_{\bar{d}}^n(x_2)}{f_{\bar{u}}^p(x_2)} \right]. \quad (5.14)$$

This equation shows that it is possible to extract the $f_{\bar{d}}^n(x_2)/f_{\bar{u}}^p(x_2)$ ratio from the proton-deuteron proton-proton cross sections ratio. In Figure 5.2, we can see the ratio $f_{\bar{d}}^n(x_2)/f_{\bar{u}}^p(x_2)$ as a function of x_2 from the E866 experiment, the curve is from the CTEQ4M parton distributions and the isolated data point is from NA51 experiment [261]. The E866 points are not in agreement with the NA51 measurement. Both results, however, clearly indicate that the anti-flavour asymmetry ratio is different from unity. The CTEQ4M distribution follows the general trend at small values of

x , but at larger x a significant disagreement with the experimental data is observed.

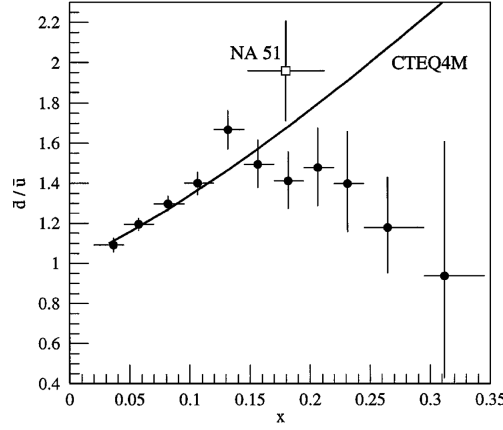


FIGURE 5.2 – Ratio of DY cross section between pd and pp collisions as a function of x_2 for data from E866 (filled circles) and NA51 (open circles) experiments, the black curve is from the CTEQ4M [261].

We notice that if the sea of quarks is symmetric (using $f_{\bar{d}}^n(x_2) = f_{\bar{u}}^n(x_2)$), the factor R_{DY}^{pd} in Equation 5.14 is equal to 1. This assumption has been also tested from the following expression:

$$\int_0^1 [F_2^p(x) - F_2^n(x)] \frac{dx}{x} = \frac{1}{3} - \frac{2}{3} \int_0^1 [f_{\bar{d}}^n(x) - f_{\bar{u}}^n(x)] dx, \quad (5.15)$$

where, $F_2^p(x)$ and $F_2^n(x)$ are the structure functions of the proton and neutron, $\bar{d}_p(x)$ and $\bar{u}_p(x)$ the antidown and antiup quark distributions as a function of Bjorken x . If the integral is equal to $1/3$ (Gottfried sum rule – GSR) [262], there is isospin symmetry, as mentioned in equation 5.4. The derivation of equation 5.15 can be found in appendix A. The E866/NuSea data showed evidence of violation of GSR [261].

The result obtained with the constraint of the d/u asymmetry in the $0.015 < x < 0.35$ range is:

$$\int_0^1 [f_{\bar{d}}^n(x) - f_{\bar{u}}^n(x)] dx = 0.118 \pm 0.012. \quad (5.16)$$

This indicates that in the nucleon sea of a deuteron nucleus, there are more anti-down quarks than anti-up quarks. However, this asymmetry is not dominant in the parton distribution functions (PDFs) of heavier nuclei such as lead (Pb), where nuclear effects like gluon shadowing take place.

5.1.3 Gluon shadowing in pPb collisions

At forward rapidity in pPb collisions at the LHC, where $x_1 \gg x_2$, the DY cross section at LO is dominated by the valence quarks from the proton (large x_1) interacting with sea antiquarks from the Pb nucleus (small x_2). The DY cross section in pPb collisions can be approximated as:

$$\sigma^{p\text{Pb}} \sim \frac{4}{9} f_u^p(x_1) f_{\bar{u}}^{\text{Pb}}(x_2) + \frac{1}{9} f_d^p(x_1) f_{\bar{d}}^{\text{Pb}}(x_2). \quad (5.17)$$

At forward rapidity (i.e. $x_1 \sim 10^{-1}$), the following approximation can be used: $f_u^p(x_1) \approx 2f_d^p(x_1)$ and the cross section becomes:

$$\sigma^{p\text{Pb}} \sim \frac{8}{9} f_d^p(x_1) f_{\bar{u}}^{\text{Pb}}(x_2) + \frac{1}{9} f_d^p(x_1) f_{\bar{d}}^{\text{Pb}}(x_2) = \frac{f_d^p(x_1)}{9} \left(8 f_{\bar{u}}^{\text{Pb}}(x_2) + f_{\bar{d}}^{\text{Pb}}(x_2) \right). \quad (5.18)$$

To quantify nuclear effects, we evaluate R_{pA} . Since the factor $f_d^p(x_1)/9$ is common to both numerator and denominator, it cancels, yielding:

$$R_{p\text{Pb}}^{DY} \sim \frac{1}{208} \cdot \frac{8 f_{\bar{u}}^{\text{Pb}}(x_2) + f_{\bar{d}}^{\text{Pb}}(x_2)}{8 f_{\bar{u}}^p(x_2) + f_{\bar{d}}^p(x_2)}. \quad (5.19)$$

This equation shows how the $R_{p\text{Pb}}^{DY}$ reflects the modification of antiquark distributions in the nucleus relative to the proton. A key observation for motivating the role of Drell-Yan in constraining gluon shadowing is that, in different nPDF fits, the nuclear modifications of gluons and sea of antiquarks track each other rather closely. If this is true, the double ratio $R_g(x, Q)/R_{\bar{u}}(x, Q)$ should be nearly flat and close to unity across the small- x region at forward rapidity in pPb collisions.

In Figure 5.3, we present the nuclear modification ratios for gluons (left panel) and \bar{u} -quarks (right panel) in Pb nuclei performed by François Arleo and Stéphane Peigné in Ref. [55]. Three different global NLO nPDF fits have been used: EPS09 [263], DSSZ [264], and nCTEQ15 [265]. The factorization scale was set to $Q = 3$ GeV when evaluating R_g and $Q = 10$ GeV for $R_{\bar{u}}$, the x -axis ranges from 10^{-5} to 10^{-2} , which corresponds to the rapidity window $0 < y < 5$ in pPb collisions at the LHC. The shaded bands in the figure represent the uncertainties derived from the different replicas of each nPDF set. At $x = 10^{-5}$, DSSZ indicates almost no modification of the gluon distribution ($R_g \approx 0.95\text{--}1.05$), while nCTEQ15 suggests a much stronger suppression ($R_g \approx 0.5\text{--}0.6$). The associated error bands hardly overlap across the

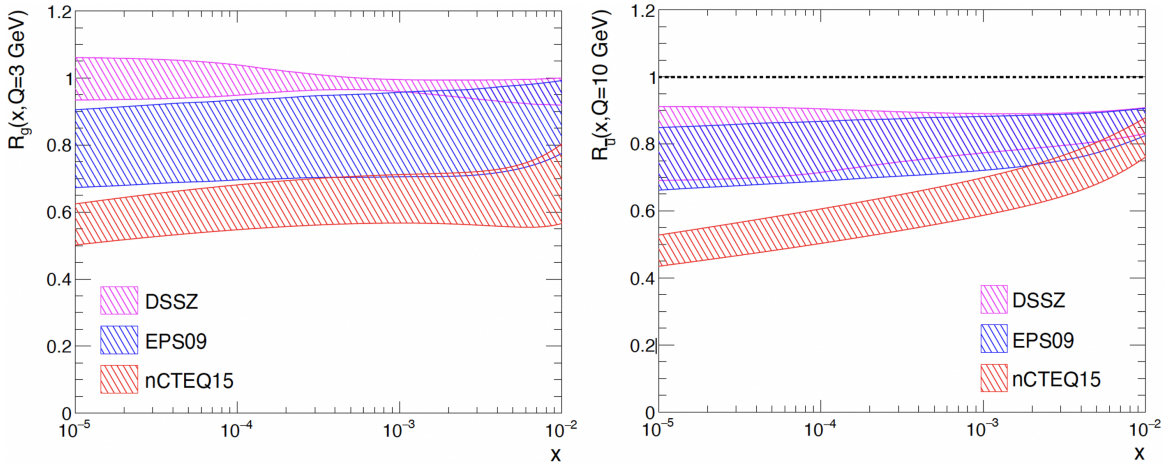


FIGURE 5.3 – Nuclear modification ratios in Pb nuclei: $R_g^{\text{Pb}}(x, Q = 3\text{GeV})$ (left) and $R_{\bar{u}}^{\text{Pb}}(x, Q = 10\text{GeV})$ (right), from various nPDF sets. Figure taken from [55].

studied x range. For EPS09 and nCTEQ15, the shadowing of sea antiquarks is found to be of a similar magnitude to that of gluons. Even though this feature is not apparent from the combined uncertainty envelopes in Figure 5.3, it is clearly visible in the individual error sets. As a result, the double ratio $R_g/R_{\bar{u}} \sim 1$, with much smaller uncertainty than in the single ratios.⁴ Using this approximation, one can say that DY (even at LO) can constrain the gluon contribution.

In addition, the R_{pA}^{DY} factor has also been calculated in Ref [55], as shown in Figure 5.4. The black curve correspond to the estimation without nuclear matter effects in PDF, in this case, the backward suppression is well explained with the isospin effects (see section 5.1.1).

The same nPDF sets detailed in Figure 5.3 are also shown in Figure 5.4. However, given the current bands and the different trends observed across nPDF sets, it is hard to draw firm conclusions. In this context, precise DY measurements at forward rapidity at the LHC would be particularly valuable, since they directly probe small- x partons in the nucleus and could provide strong constraints on shadowing effects.

4. DSSZ, however, predicts a different pattern: gluons are barely modified ($R_g \approx 0.95\text{--}1.05$), whereas sea antiquarks show stronger suppression ($R_{\bar{u}} \approx 0.7\text{--}0.9$).

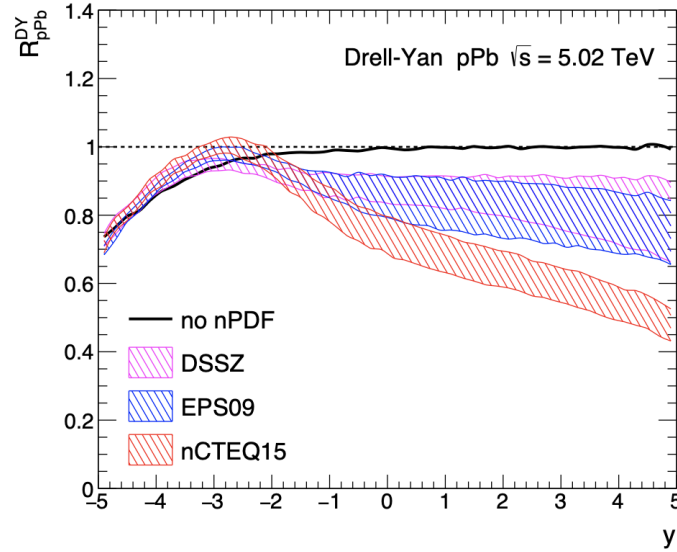


FIGURE 5.4 – R_{pPb}^{DY} as function of rapidity. Figure taken from [55].

5.2 Drell-Yan analysis

In this chapter, we show the detailed analysis, using DY pseudo-data to mimic LHCb conditions (see Section 3.1) in order to constrain the nuclear shadowing effects. We generate pseudodata for the nuclear modification factor $R_{pPb}(y)$ at a nucleon-nucleon center-of-mass energy of $\sqrt{s_{NN}} = 5.02$ TeV [266]. We also explain in detail how to constrain an observable using a detailed bayesian reweighting technique.

As already mentioned, LHCb is particularly well suited for constraining the nuclear shadowing effects at small values of Bjorken- x , thanks to its unique forward rapidity coverage ($2 < y < 5$). While the ALICE experiment also features a forward muon spectrometer ($2.5 < y < 4$), its measurements are limited by degraded momentum resolution due to the thick front absorber⁵, explained in detail in chapter 3. LHCb instead provides superior dimuon resolution and extends to higher rapidities, offering a cleaner and broader kinematic reach. In addition, the excellent vertexing capabilities of LHCb allow for an efficient separation of prompt signals from background processes, in particular by eliminating the contributions from heavy-flavour decays. These features make LHCb an ideal experiment for studying nuclear modifications in pA collisions at the LHC. In the forward rapidity

5. The front absorber of ALICE was designed to enable ultra-central Pb–Pb measurements, which LHCb cannot perform.

region of LHCb detector, values of x_2 are given approximately by $x_2 = \frac{Me^{-y}}{\sqrt{s_{NN}}}$ and are probed in the range:

$$x_2^{\max} \simeq \frac{20 e^{-2}}{8.8 \times 10^3} \sim 10^{-4}, \quad x_2^{\min} \simeq \frac{10.5 e^{-4}}{8.8 \times 10^3} \sim 10^{-5}. \quad (5.20)$$

This should serve as strong motivation for the LHCb collaboration to pursue forward Drell-Yan measurements in pA collisions. In this analysis, two different frameworks are used: Les Houches Accord Parton Distribution Function (LHAPDF) [267] and Drell-yan Turbo⁶ (DYTurbo) [268]. The LHAPDF library is used for accessing and interpolating parton distribution functions (PDFs). It provides a unified and consistent interface to a broad range of PDF sets developed by various collaborations (e.g., CT, MMHT, NNPDF, EPPS, nCTEQ), encompassing both proton and nuclear PDFs. These functions serve as input to DYTurbo, which is used to compute Drell-Yan cross sections.

5.2.1 From PDF to cross sections and R_{pA}

The DYTurbo relates the non-measurable PDF sets (in a proton or in nuclei) to a measurable cross section, through a pQCD calculation in a specific setup (order of the calculation, choice of scales, etc.).

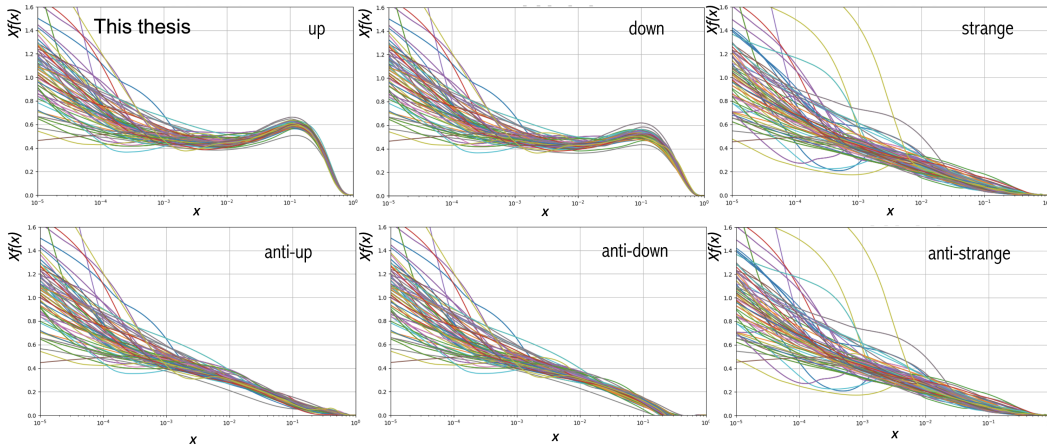


FIGURE 5.5 – Each line in the plot corresponds to a different replica f_i of the nPDF (Set nNNPDF30_nlo_as_0118_A208_-Z82 at $Q = 10$ GeV) for up, down, and strange quarks and their antiquarks.

6. DYTurbo program calculates the Drell-Yan cross sections up to approximate netx-to-next-to-next-to-next-to-leading (N4LLa) logarithmic accuracy.

We define a PDF set $\{f_i\}$ ($i = 1, \dots, N$) with N members (or replicas). In this analysis, the nPDF are probed at a momentum scale of $Q = 10$ GeV, corresponding to the momentum transfer in the scattering process. In Figure 5.5, the top panels show the nPDFs for up, down, and strange quarks in Pb nuclei (f_i^u, f_i^d, f_i^s), while the bottom panels present the corresponding distributions for their antiquark counterparts ($f_i^{\bar{u}}, f_i^{\bar{d}}, f_i^{\bar{s}}$). These nPDFs were obtained using the LHAPDF framework. The spread among the lines reflects the uncertainty in the nPDF determination for each flavor, illustrating both the flavor dependence and the statistical variation within the nNNPDF set. To avoid possible bias from energy loss in hadronic observables, the following nPDF sets are chosen.

- EPPS16nlo_CT14nlo_Pb208 [269, 270]:
 $i = 1, 2, 3, \dots, 95, 96$ (eigenvalue sets, 90% CL)
- nCTEQ15WZ_208_82 [271]:
 $i = 1, 2, 3, \dots, 38, 39$ (eigenvalue sets, 90% CL)
- nNNPDF30_nlo_as_0118_noLHCbD_A208_Z82 [272]:
 $i = 1, 2, 3, \dots, 250$ (Bayesian replicas, 68% CL)

In all cases, the member with $i = 0$ corresponds to the average of all members, denoted as central member. The first two sets use the **Hessian method**, where uncertainties are estimated using variations along eigenvectors of the fit's error matrix. Each pair of eigenvalue sets corresponds to positive and negative shifts along a specific uncertainty direction, and the total uncertainty is obtained by combining these contributions. The given confidence level (90%) reflects the range within which the true value is expected to lie. The last set follows a **Bayesian approach**, where a large number of Monte Carlo replicas are generated by sampling from the probability distribution of PDFs. Statistical measures (e.g., mean and standard deviation) over these replicas provide the central value and uncertainty, typically quoted at 68% confidence level. From $\{f_i\}$, we obtain a collection of cross sections $\{\sigma_i\}$ ⁷:

$$\{f_i\} \xrightarrow{\text{DYTurbo}} \{\sigma_i\}. \quad (5.21)$$

If we neglect the uncertainties in the proton PDF set, we can define a collection of

7. We always use rapidity differential quantities, i.e., $\sigma_i = \frac{d\sigma_i}{dy}$. Letter i denotes the (n)PDF member set, and j the rapidity y_j , $\sigma_i(j) = \frac{d\sigma_i(y_j)}{dy}$. We also write R instead of R_{pA} .

R_{pA} with N elements by dividing by the proton central member:

$$\frac{\{\sigma_i\}}{\sigma_0(pp)} \rightarrow \{R^i\}. \quad (5.22)$$

In this study, we focus on the mass window $5 < M < 120$ GeV in order to optimize the statistics, integrating over p_T to avoid complications such as the Cronin effect⁸, as initially proposed in [55].

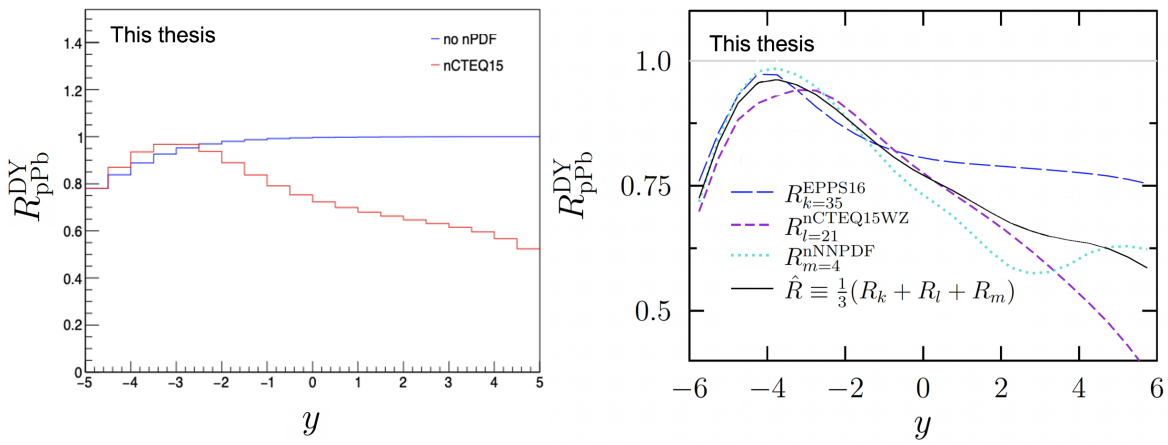


FIGURE 5.6 – Left panel: Nuclear modification factor R^0 associated to the central nPDF member. Right panel: 3 random replicas are shown, each from a different nPDF set.

In Figure 5.6, the left panel shows the nuclear modification factor R calculated using the central nPDF member f_0 from the nCTEQ set, as well as the baseline scenario where no nuclear modifications are included (this baseline reflects only the isospin effect, without any nPDF corrections). This comparison highlights the additional suppression or enhancement introduced by genuine nuclear effects beyond simple isospin considerations. Notice that the central member f_0 should not be confused with the average over all replicas, it corresponds to a single best-fit solution from the global analysis. Both curves in Figure 5.6 are consistent with Figure 5.4 (though not strictly comparable, since f_0 is a specific fit rather than an ensemble mean of all replicas), confirming the correct implementation of asymmetric collisions at NLO within DYTurbo. The right panel of Figure 5.6 presents three R curves. Each of these curves corresponds to a randomly selected replica from a different nPDF collaboration: one from EPPS, one from nCTEQ, and one from nNNPDF.

8. The Cronin effect refers to the enhancement of particle yields at intermediate p_T in pA collisions compared to pp collisions, attributed to multiple initial-state scatterings of partons.

5.2.2 Model and DY pseudo-data

At present, no experimental DY measurements in pA collisions are available in the kinematic region of interest ($x \sim 10^{-5}$). To assess their potential impact, we generate pseudo-data for this process, since DY provides a clean probe to constrain cold nuclear matter effects.

In this section, we explain in detail how we generate the pseudo-measurements R_{data} of DY. For this, we first define a "truth" R_{pA} denoted \hat{R} . In our model, it is defined as an average of R_{pA} computed with three arbitrary nPDF member sets (e.g., R_1 given by the replica $k = 12$ of EPPS21, R_2 given by $k = 26$ of nCTEQ15 and R_3 given by $k = 2$ of nNNPDF):

$$\hat{R} = \frac{1}{3}(R_1 + R_2 + R_3). \quad (5.23)$$

Once \hat{R} is known, we have to generate a data sample according to \hat{R} . Let us say we generate 8 data points ($j = 1, \dots, 8$) in the LHCb acceptance corresponding to the rapidity binning:

$$[-5, -4.5], [-4.5, -4], [-4, -3.5], [-3.5, -3], [2, 2.5], [2.5, 3], [3, 3.5], [3.5, 4]. \quad (5.24)$$

Assuming gaussian fluctuations, the data points should be given by:

$$R_{\text{data}}(j) = \hat{R}(j) + G(0, \delta R(j)), \quad (5.25)$$

where G is a random number from a Gaussian distribution centered at 0 with width $\delta R(j)$. This uncertainty can be calculated in the following way [266]:

$$\frac{\delta R(j)}{R(j)} = \sqrt{\left(\frac{1}{N_{\text{pp}}^{(j)}} + \frac{1}{N_{\text{pA}}^{(j)}} \right) \left(1 + \frac{1}{(N/B)_{\text{eff}}} \right)}. \quad (5.26)$$

Here, $N_{\text{pp}}^{(j)}$ and $N_{\text{pA}}^{(j)}$ represent the number of events in bin j for proton-proton and proton-nucleus collisions, respectively. The factor $\left[1 + \frac{1}{(N/B)_{\text{eff}}} \right]$ accounts for background fluctuations, with an effective signal-to-background ratio $(N/B)_{\text{eff}} \sim \frac{1}{30}$. In an ideal case without background, i.e., $(N/B)_{\text{eff}} \rightarrow \infty$, the statistical uncertainty simplifies to $\frac{\delta R(j)}{R(j)} \rightarrow \sqrt{\frac{1}{N_{\text{pp}}^{(j)}} + \frac{1}{N_{\text{pA}}^{(j)}}}$. This ideal limit corresponds to pure Poisson

statistics where the uncertainty is driven solely by the signal yield. To evaluate the expected number of DY events in each bin, the DYTurbo program was used. The DY yield $N^{(j)}$ can be estimated as:

$$N^{(j)} = A\epsilon \cdot L \cdot \sigma^{(j)}, \quad (5.27)$$

where the acceptance A , efficiency ϵ , and luminosity L are provided in Ref [266]. The projected integrated luminosities for LHCb during Runs 3 and 4 are:

$$\mathcal{L}_{pp} = 104 \text{ pb}^{-1}, \quad (5.28)$$

$$\mathcal{L}_{p\text{Pb}} \simeq 170 \text{ nb}^{-1} \leftrightarrow 500 \text{ nb}^{-1}. \quad (5.29)$$

We adopt $\mathcal{L}_{p\text{Pb}} = 250 \text{ nb}^{-1}$ in our analysis. An optimistic value of $A\epsilon = 0.9$ was adopted, following Ref. [273], leading to an estimated $N^{(j)} = \mathcal{O}(10^4)$. In Figure 5.7, the generated DY pseudodata points are shown together with three representative theoretical curves from different nPDF sets. The pseudodata are distributed around the black curve \hat{R} , which corresponds to the theoretical prediction used as the central value for generating the data. This illustrates how the simulated measurements fluctuate statistically. The pseudodata values are also reported in table 5.1.

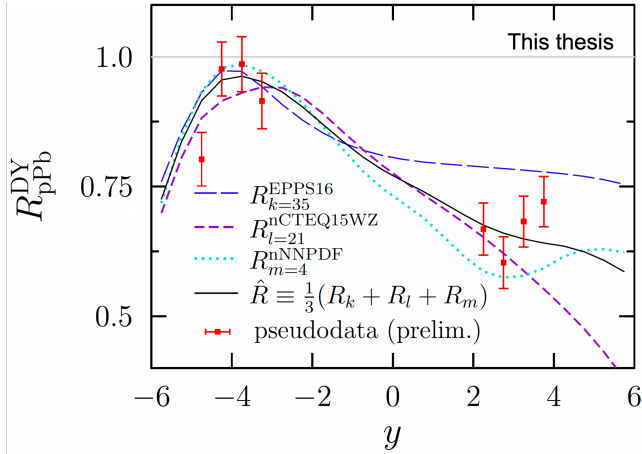


FIGURE 5.7 – R_{pA}^{DY} pseudo-data vs y , compared with 3 random replicas from different collaborations: EPPS, nCTEQ, and nNNPDF.

y	R_{pA}^{DY}	δR_{pA}^{DY}
-4.75	0.8026	0.0515
-4.25	0.9765	0.0522
-3.75	0.9860	0.0530
-3.25	0.9150	0.0536
2.25	0.6679	0.0503
2.75	0.6034	0.0497
3.25	0.6826	0.0490
3.75	0.7209	0.0482

TABLE 5.1 – Pseudodata values of R_{pA}^{DY} .

5.2.3 Reweighting nuclear PDFs using DY pseudo-data

The impact of new data on our knowledge of nuclear parton distribution functions (nPDFs) can be systematically quantified using a bayesian reweighting procedure [274]. This approach is general and can be formulated for any observable O that depends on the nPDFs. For the set of N_{rep} replicas $\{f_k\}$ from the nNNPDF collaboration, each predicting a value $O[f_k]$. The original (prior) expectation value and uncertainty for O are given by:

$$\langle O \rangle_{\text{old}} = \frac{1}{N_{\text{rep}}} \sum_{k=1}^{N_{\text{rep}}} O[f_k], \quad (5.30)$$

$$\delta \langle O \rangle_{\text{old}} = \sqrt{\frac{1}{N_{\text{rep}}} \sum_{k=1}^{N_{\text{rep}}} (O[f_k] - \langle O \rangle_{\text{old}})^2}. \quad (5.31)$$

Given new measurements, the χ_i^2 for each replica can be calculated, providing a quantitative measure of how well that replica reproduces the data. For uncorrelated data points, the chi-squared for replica i is given by:

$$\chi_i^2 = \sum_{j=1}^{N_{\text{data}}} \left(\frac{R_{\text{data}}(j) - R^i(j)}{\delta R_{\text{data}}(j)} \right)^2, \quad (5.32)$$

where, $R_{\text{data}}(j)$ and $\delta R_{\text{data}}(j)$ are the measured nuclear modification factor and its associated uncertainty in bin j , and $R^i(j)$ denotes the theoretical prediction from replica i . This chi-squared value forms the basis for constructing the likelihood of each replica, which is central to updating the probability distribution for the nPDFs in light of the new data. According to Bayes' theorem, the updated (posterior) probability distribution is given by:

$$P_{\text{new}}(f) \propto P(\vec{y}|f)P_{\text{old}}(f), \quad (5.33)$$

where, $P_{\text{old}}(f)$ is the prior distribution for the nPDF f , $P(\vec{y}|f)$ is the likelihood derived from the agreement between the data and the predictions, and $P_{\text{new}}(f)$ is the resulting posterior distribution. Following this procedure, the Bayesian reweighting allows one to compute an updated expectation value for any observable O that depends on the PDFs:

$$\langle O \rangle_{\text{new}} = \frac{1}{N_{\text{rep}}} \sum_{k=1}^{N_{\text{rep}}} \omega_k O[f_k], \quad (5.34)$$

$$\delta \langle O \rangle_{\text{new}} = \sqrt{\frac{1}{N_{\text{rep}}} \sum_{k=1}^{N_{\text{rep}}} \omega_k (O[f_k] - \langle O \rangle_{\text{new}})^2}, \quad (5.35)$$

where the weights ω_k are determined by the likelihood assigned to each replica f_k . There are several ways to define the likelihood function, each leading to a different form for the weights. One widely used approach, originally proposed by Giele and Keller (GK) [275], interprets the likelihood as the probability density for the data to fall within a small region around the observed values.

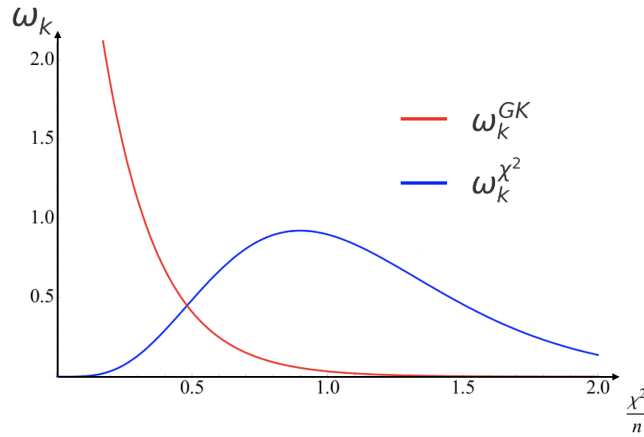


FIGURE 5.8 – Comparison of weights ω_k^{GK} for the original re-weighting method by Giele and Keller (GK) (red) and $\omega_k^{\chi^2}$ for the alternative approach based on the χ^2 distribution (blue).

The GK approach yields to the following weights:

$$\omega_k^{\text{GK}} = \frac{\exp(-\chi_k^2/2)}{(1/N_{\text{rep}}) \sum_{k=1}^{N_{\text{rep}}} \exp(-\chi_k^2/2)}, \quad (5.36)$$

Alternatively, the NNPDF collaboration has advocated for a likelihood based on the probability density in χ^2 space [276], leading to weights of the form:

$$\omega_k^{\chi^2} = \frac{\chi_k^{2(N_{\text{data}}-1)/2} \exp(-\chi_k^2/2)}{(1/N_{\text{rep}}) \sum_{k=1}^{N_{\text{rep}}} \chi_k^{2(N_{\text{data}}-1)/2} \exp(-\chi_k^2/2)}. \quad (5.37)$$

It is important to note that the choice of likelihood affects the sensitivity of the reweighting procedure. As shown in Figure 5.8, the GK likelihood leads to a more pronounced weighting toward replicas with smaller χ^2 values, thereby placing greater emphasis on those that better fit the new data. In comparison, the χ^2 -based likelihood tends to favor replicas with χ^2/N_{data} values close to one, offering less selectivity when the new data aligns well with the prior. While various approaches have been explored in the literature, there remains no consensus on a universally optimal reweighting prescription.

5.2.4 Results

In our analysis, the observable O can be the nuclear modification factor R_{pA} (given by Equation 5.22) or the PDF ratio $R_f^{(A)}$. The results presented in this chapter are derived solely from the bayesian reweighting procedure applied to the nNNPDF set.

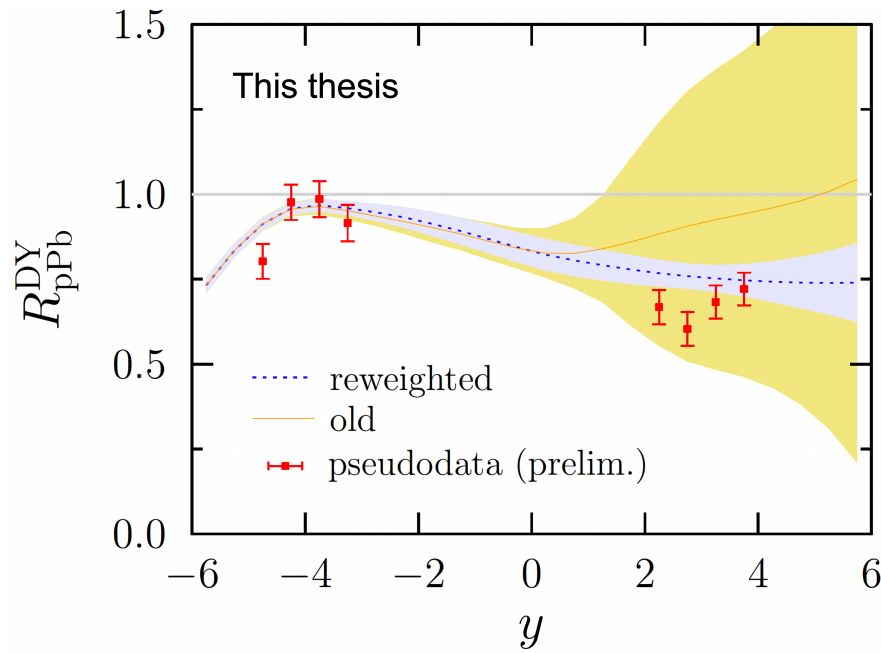


FIGURE 5.9 – Impact of reweighting on R_{pA} for Drell-Yan. The band shows the uncertainty before and after including the DY pseudo-data using the Bayesian reweighting method described above.

Figure 5.9 shows the nuclear modification factor R_{pA} , both before and after the inclusion of the new DY pseudo-data. The reduction in the uncertainty band after reweighting demonstrates how new measurements can significantly constrain the

theoretical predictions for R_{pA} , leading to improved precision in the extraction of nuclear effects. Similarly, we can constrain the ratio $R_f^{(A)}$, defined as:

$$R_f^{(A)}(x, Q) = \frac{f^{(N/A)}(x, Q)}{\frac{Z}{A}f^{(p)}(x, Q) + \frac{A-Z}{A}f^{(n)}(x, Q)}, \quad (5.38)$$

where, $f^{(N/A)}(x, Q)$ is the parton distribution function of flavor f in a bound nucleon inside a nucleus, and $f^{(p)}(x, Q)$, $f^{(n)}(x, Q)$ are the PDFs in a free proton and neutron, respectively. In this analysis, the nPDFs were evaluated at a momentum scale of $Q = 10$ GeV. Figure 5.10 presents the effect of reweighting on $R_f^{(A)}$. This figure displays the uncertainty band for each specific parton flavor, highlighting how the inclusion of new data narrows the allowed range for the nPDFs themselves.

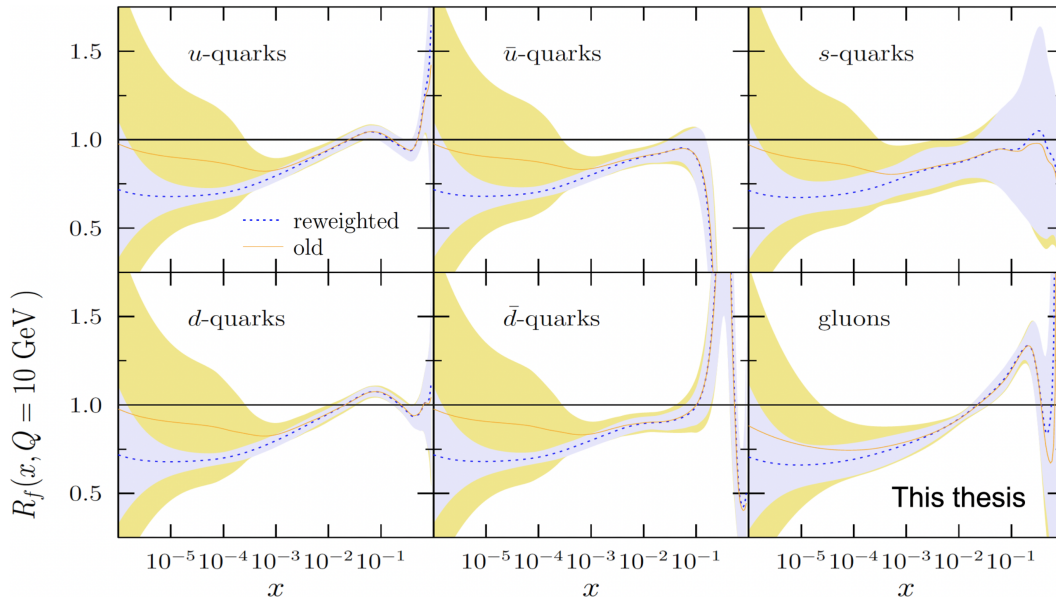


FIGURE 5.10 – Ratios of PDFs $R_f^{(A)}$, before and after reweighting. The PDFs are evaluated at $Q = 10$ GeV.

The comparison before and after reweighting clearly shows the enhanced constraining power provided by the new Drell-Yan pseudodata. Together, Figures 5.9 and 5.10 exemplify the strength of the reweighting approach, by incorporating additional data, we can achieve a more accurate and reliable determination of both R_{pA} and $R_f^{(A)}$, deepening our understanding of the partonic structure of nuclei. Future real data would supplant our pseudodata and give experimental constraints.

Chapter 6

Conclusion and perspectives

J/ψ collectivity in Pb-Pb collisions

The measurement of J/ψ elliptic flow (v_2) using multi-particle cumulants represents a crucial probe of the soft-hard interplay in heavy-ion collisions. This approach is particularly valuable because it provides direct access to the collective behavior of heavy quarks in the QGP medium, while being sensitive to flow fluctuations that arise from event-by-event variations in the initial collision geometry. Unlike light hadrons, which are predominantly produced through soft processes and directly reflect the bulk medium properties, J/ψ production involves both initial-state hard processes (perturbative QCD) and medium-induced effects (suppression, regeneration, and energy loss). The multi-particle cumulant method allows us to probe this soft-hard interplay by measuring how the collective flow of the bulk medium influences the azimuthal distribution of heavy quarkonia. Specifically, $v_2\{2\}$ captures both the average flow and its fluctuations, while $v_2\{4\}$ provides a more robust measurement of the average flow by suppressing non-flow correlations and flow fluctuations. This measurement is especially sensitive to flow fluctuations in the soft sector because the J/ψ v_2 reflects how the initial geometric anisotropy (ϵ_2) is transferred to the final state through the medium response (κ_2). The difference between $v_2\{2\}$ and $v_2\{4\}$ measurements can reveal the magnitude of these fluctuations, providing insights into the event-by-event variations in the initial geometry and the subsequent hydrodynamic evolution of the QGP. This thesis reports the first measurements of J/ψ elliptic flow and event-by-event fluctuations obtained with the multi-particle cumulant technique. The presented analysis demonstrates the successful application of the cumulant method to quarkonia, providing a robust approach that effectively suppresses non-flow effects through the natural pseudo-rapidity gap between the central barrel and muon spectrometer. In the schematic

illustration shown in Figure 6.1, the difference between $v_2\{SP\}$ and $v_2\{4\}$ in the left panel reflects the trends obtained in this analysis, highlighting the contributions of event-by-event fluctuations. The right panel illustrates the different types of fluctuations depending on the trend of the fluctuation ratio versus p_T . While the contributions to the elliptic flow from initial eccentricity fluctuations are expected to be independent of p_T [259], fluctuations from later-stage processes are expected to depend on the kinematics of the considered particles (as well as on the particle species). More statistics are needed to draw firm conclusions, however, a p_T dependence of the fluctuation ratio cannot be excluded, as reported in Chapter 4.

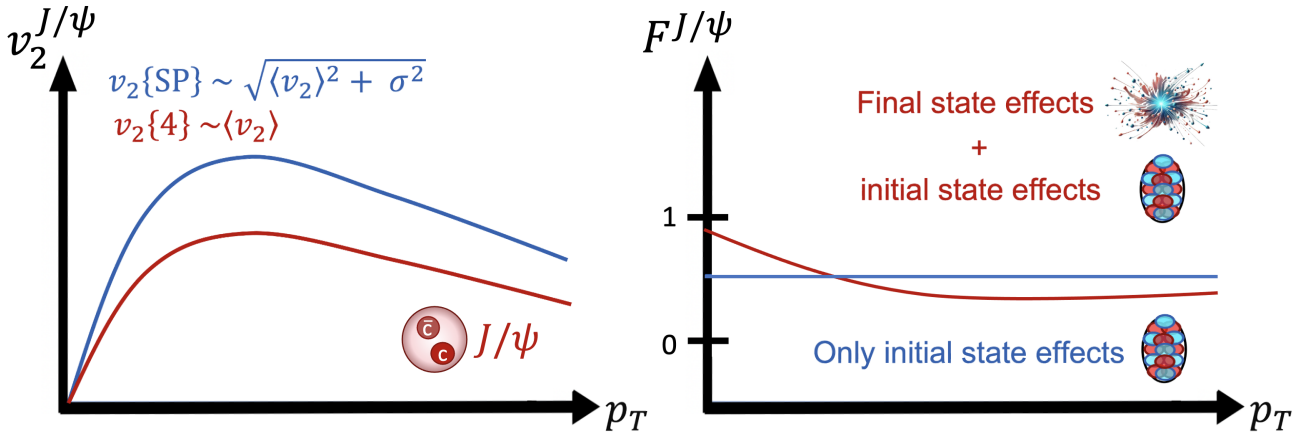


FIGURE 6.1 – Schematic illustration of $v_2^{J/\psi}\{SP\}$, $v_2^{J/\psi}\{4\}$ (left) and fluctuation ratio $F^{J/\psi}$ (right) as a function of p_T . The difference between $v_2^{J/\psi}\{SP\}$ and $v_2^{J/\psi}\{4\}$ reflects the contribution of flow fluctuations, while the right panel indicates the type of flow fluctuations expected depending on the p_T shape. The respective measurements can be found in Figures 4.21 and 4.24.

The agreement between $v_2\{SP\}$ and $v_2\{2\}$ flow measurement methods validates our analysis approach and provides confidence in the robustness of the flow measurements with cumulants.

In addition, Figure 6.2 shows schematic sketches that qualitatively reproduce the comparison of the measured J/ψ flow coefficients from ALICE with the strange-hadron results from CMS, as presented in this thesis. The left panel illustrates the transverse-momentum (p_T) dependence of the elliptic flow coefficient ($v_2\{4\} = \langle v_2 \rangle$), highlighting the characteristic hierarchy among particle species. The middle panel shows the flow fluctuations σ . The right panel displays the average flow vector components in the (v_x, v_y) plane. The positions of the dots and the circle

radii correspond to the observed mean values and fluctuation widths, respectively. This illustration highlights the stronger collectivity and larger fluctuations of Λ , the intermediate behavior of K_S^0 , and the weaker collectivity of J/ψ . Notably, for J/ψ , the flow fluctuations $\sigma^{J/\psi}$ are of the same order as the mean elliptic flow $\langle v_2^{J/\psi} \rangle$.

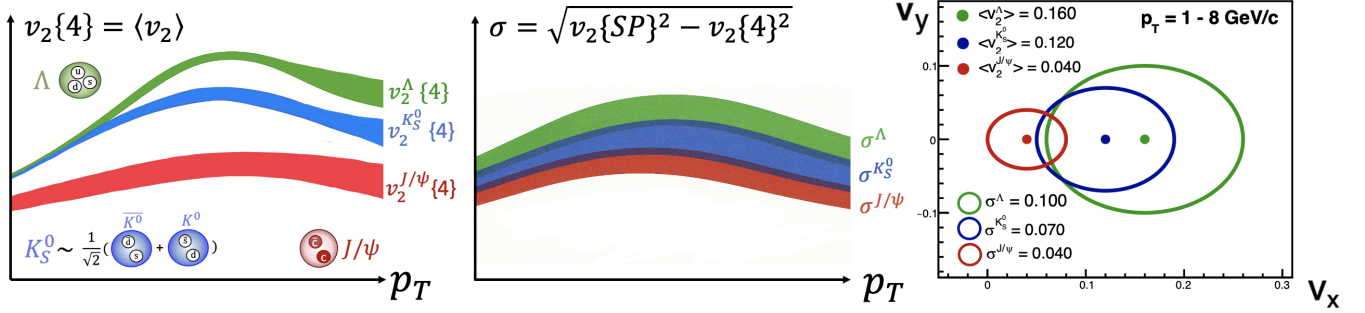


FIGURE 6.2 – Schematic illustration of $v_2\{4\}$ and flow fluctuations for J/ψ , K_S^0 and Λ . The respective measurements can be found in Figures 4.25 and 4.27.

Several areas for future improvement have been identified:

- Extension to other centrality classes to study the centrality dependence of J/ψ flow.
- Improved systematic uncertainty evaluation, particularly for sources not quantitatively assessed in this work.
- Comparison with additional theoretical models to better understand the underlying physics.

The upcoming high-statistics Pb–Pb data from 2024 will provide significant improvements in statistical precision and enable more detailed studies of the p_T and centrality dependence of J/ψ flow. Such measurements are not only crucial for more stringent tests of theoretical models and for providing deeper insights into the production mechanisms of quarkonia in the QGP medium, but they will also help to clarify the origin of event-by-event fluctuations. In particular, the centrality dependence study may shed light on whether these fluctuations are dominated by initial-state effects or arise primarily from final-state dynamics. In summary, this analysis shows that the multi-particle cumulant method is a powerful tool for studying quarkonia flow, offering unique sensitivity to collective behavior. For the first time, it is demonstrated that the flow fluctuations of J/ψ are quite significant, with magnitudes comparable to the mean flow itself.

Constraining cold nuclear matter effects with Drell-Yan

The second physics analysis of this thesis (see Chapter 5) focused on constraining cold nuclear matter (CNM) effects through the study of Drell–Yan (DY) production in p–Pb collisions. A central aspect of this investigation is the role of nuclear parton distribution functions (nPDFs), which are essential for describing particle production in nuclear environments. At low Bjorken- x in lead nuclei, where gluon shadowing and saturation effects remain poorly constrained, DY production offers a particularly clean probe to constrain nPDF. To enable this study, several methodological developments were carried out.

- Implementation of asymmetric collisions in DY Turbo, enabling reliable predictions for proton–lead kinematics at the LHC.
- Rapidity-differential cross-section and nuclear modification factor R_{pA} calculations at NLO.
- Generation of Drell–Yan pseudo-data using a Gaussian smearing approach, providing realistic uncertainty estimates for reweighting studies.
- Development and validation of a reweighting procedure for nPDFs, allowing the incorporation of DY pseudo-data to reweight a given observable.

Phenomenological predictions of DY in the LHCb kinematic region were provided, together with a study of the impact of nPDF reweighting techniques. We have tested the sensitivity of observables such as R_{pA} and parton density ratios (f_i^A / f_i^p) to new pseudo-data, thereby quantifying the constraining power of DY measurements.

The analysis highlights how pseudo-data in the LHCb phase space can significantly reduce the current uncertainties on nPDFs, especially at small x , complementing global fits that are otherwise limited by the scarcity of data in this regime.

Chapter 7

Résumé en français

Cette thèse présente deux analyses complémentaires visant à sonder les propriétés de la matière nucléaire dans les collisions d'ions lourds au LHC. La première analyse, réalisée avec le détecteur ALICE, utilise la méthode des cumulants multi-particules pour mesurer le flot elliptique du J/ψ et ses fluctuations événement par événement dans les collisions Pb-Pb à $\sqrt{s_{NN}} = 5.36$ TeV (voir Chapitre 4). La seconde analyse explore les effets de matière nucléaire froide via une étude phénoménologique de la production Drell-Yan dans les collisions p-Pb, en développant des techniques de repondération pour contraindre les fonctions de distribution partoniques nucléaires (nPDF) à petit x de Bjorken (voir Chapitre 5).

7.1 Flot elliptique du J/ψ dans les collisions Pb-Pb

La mesure du flot elliptique v_2 du J/ψ constitue une sonde essentielle pour comprendre les mécanismes de production des quarkonia dans le plasma de quarks et de gluons (QGP). Le J/ψ est sensible à la fois aux processus durs initiaux (production primordiale via fusion de gluons) et aux effets induits par le milieu (suppression par écrantage de couleur, régénération par recombinaison de quarks charm, etc.). Le coefficient de flot elliptique permet donc de sonder le degré de thermalisation des quarks charms dans le QGP produits dans les collisions d'ions lourds. La méthode des cumulants multi-particules présente plusieurs avantages décisifs par rapport aux méthodes traditionnelles du plan d'événement (EP) et du produit scalaire (SP). Elle supprime naturellement les corrélations de non-flot grâce aux corrélations d'ordre supérieur, offre une sensibilité directe aux fluctuations événement par événement du flot, et présente une robustesse accrue face aux effets instrumentaux tels que l'acceptance inhomogène ou le dédoublement de traces. Dans le détecteur

ALICE, la séparation naturelle en pseudo-rapacité d'environ 1.7 unités entre le tonneau central et le spectromètre à muons renforce encore la suppression des effets de non-flot, notamment ceux provenant de jets dont les corrélations à courte portée s'étendent typiquement sur $\Delta\eta \lesssim 1$. Cette analyse étend pour la première fois la technique des cumulants multi-particules, déjà validée pour les particules chargées du tonneau central, aux mesures de quarkonia à rapidité avant.

Échantillon de données et sélection

L'analyse utilise les données de collisions Pb-Pb collectées en novembre 2023 durant le Run 3 du LHC (voir Section 4.1). La reconstruction la plus récente (pass4) est adoptée, incluant les derniers alignements des détecteurs. Une procédure de streaming via le framework O2Physics a permis de réduire efficacement la taille des données de 2.3 pétaoctets à 7.1 téraoctets, tout en conservant l'information pertinente pour l'analyse de flot. Les événements sont sélectionnés selon plusieurs critères physiques rigoureux pour assurer la qualité des données et minimiser les biais systématiques. Le vertex primaire doit être situé à moins de 10 cm du point d'interaction nominal le long de l'axe du faisceau. Le déclenchement TVX (T0 Vertex) doit être actif, garantissant un signal de collision valide grâce aux informations de timing du détecteur FT0. Les événements situés aux frontières des time frames sont exclus pour éviter les problèmes de reconstruction. Une cohérence entre les positions du vertex reconstruites par les traces et par coïncidence temporelle FT0A-C est exigée (écart inférieur à 1 cm). Les événements présentant une occupation très élevée en nombre de traces dans la TPC sont rejetés afin d'éviter les inefficacités de reconstruction susceptibles d'introduire des biais dans les mesures de flot. La centralité des collisions est déterminée par ajustement de l'amplitude FT0C mesurée sur la distribution attendue d'un modèle de Glauber Monte Carlo couplé à une distribution binomiale négative. Cette analyse se concentre sur la classe de centralité semi-centrale 10-30% qui offre un compromis optimal entre statistique suffisante et anisotropie géométrique initiale significative, permettant des mesures de flot non-négligeables avec la méthode des cumulants multi-particules. Pour le tonneau central, les traces de particules chargées sont sélectionnées (avec une correspondance entre les détecteurs ITS et TPC), une acceptation en pseudo-rapacité de $-0.8 < \eta < 0.8$ pour assurer la couverture correcte du TPC, et un intervalle en impulsion transverse de $0.2 < p_T < 3.0 \text{ GeV}/c$. Cette gamme en p_T permet

de se concentrer sur les traces issues principalement de la physique du bulk. La limite inférieure de $0.2 \text{ GeV}/c$ garantit la capture du maximum de particules tout en maintenant une bonne efficacité de reconstruction, tandis que la limite supérieure de $3.0 \text{ GeV}/c$ aide à supprimer les contributions des jets et processus à haut p_T qui pourraient introduire des corrélations de non-flot. Pour les muons individuels, seules les traces appariées entre les détecteurs MCH et MID sont considérées, assurant une identification complète à travers tout le spectromètre. L'acceptance requise est $-4 < \eta < -2.5$, correspondant à la couverture du spectromètre à muons. L'impulsion transverse des muons individuels doit être supérieure à $1 \text{ GeV}/c$, critère crucial pour supprimer les muons de basse impulsion qui contribuent significativement au bruit de fond combinatoire dans le spectre de dimuons. Le rayon de la trace à la sortie de l'absorbeur doit se situer entre 17.6 et 89.5 cm pour exclure les muons traversant la région de l'absorbeur à haut Z où se produisent des diffusions multiples importantes. Le produit de l'impulsion de la trace et de sa distance d'approche minimale au vertex (pDCA) doit être inférieur à 6σ pour supprimer le bruit de fond provenant des interactions faisceau-gaz. Les paires de muons de signes opposés satisfaisant ces critères sont combinées pour former des candidats J/ψ . Seuls les candidats tombant dans la couverture en rapidité du spectromètre ($2.5 < y < 4.0$) sont considérés dans l'analyse.

Méthode des cumulants multi-particules

La méthode repose sur la construction de vecteurs de flot (Q-vectors) pour l'harmonique n , définis comme la somme complexe pondérée sur toutes les traces de particules chargées dans un événement (voir Section 4.3). Les poids de correction d'acceptance non uniforme (NUA) sont obtenus à partir des données expérimentales, afin de tenir compte des inhomogénéités du détecteur. Deux types de vecteurs de flot sont définis : le vecteur de référence (REF) construit à partir des particules chargées du tonneau central, et le vecteur des particules d'intérêt (POI) construit à partir des dimuons. Les corrélateurs à 2 et 4 particules sont calculés événement par événement en utilisant des combinaisons des Q-vectors. Pour les corrélateurs de référence, les calculs impliquent uniquement les particules chargées du tonneau central. Pour les corrélateurs POI, des corrélateurs mixtes sont construits, impliquant un dimuon et une ou trois particules de référence pour les corrélations à 2 et 4 particules respectivement. Un aspect important de l'analyse concerne le calcul de l'angle azimutal

du système dimuon. Contrairement aux analyses de flot de référence où l'angle φ est pris directement de la trajectoire des particules chargées, ici le système dimuon est traité comme un objet composite. L'angle azimutal de la paire de dimuons est calculé à partir de son quadri-vecteur impulsion total, obtenu en sommant les quadri-vecteurs des deux muons individuels. Cette approche garantit que l'angle reflète la cinématique réelle du système dimuon. Tous ces corrélateurs sont ensuite moyennés sur tous les événements, ou plus précisément sur toutes les paires de dimuons. Les cumulants REF et POI sont construits en combinant ces corrélateurs moyennés. Les coefficients de flot elliptique de référence sont obtenus en prenant la racine carrée du cumulant à 2 particules ou la racine quatrième (avec un signe négatif) du cumulant à 4 particules. Pour les dimuons, les coefficients de flot sont obtenus par le rapport des cumulants POI sur les cumulants REF appropriés. Cette procédure permet d'extraire à la fois $v_2^{\mu\mu}\{2\}$ et $v_2^{\mu\mu}\{4\}$ en fonction de la masse invariante et de l'impulsion transverse des dimuons.

Flot de référence à mi-rapidité

Le flot de référence v_2^{REF} des particules chargées a été extrait en fonction de la centralité, fournissant une validation cruciale de la méthode (voir Section 4.5). Une comparaison run par run de $v_2^{REF}\{2\}$ pour tous les événements de biais minimal collectés dans l'ensemble de données Pb-Pb 2023 montre une excellente stabilité sur les différentes périodes de prise de données, confirmant la robustesse de la mesure et la qualité de l'échantillon. La comparaison entre $v_2^{REF}\{2\}$ mesuré dans les événements de biais minimal et celui extrait des événements contenant au moins une paire de dimuons montre un excellent accord. Cet accord démontre que les événements avec un dimuon sont représentatifs de l'échantillon inclusif de biais minimal, validant ainsi la procédure de moyenne sur les événements où l'on moyenne sur toutes les paires de dimuons plutôt que sur tous les événements. La comparaison avec les résultats du Run 2 est également présentée. On observe que $v_2^{REF}\{2, |\Delta\eta| > 1\}$ est systématiquement plus grand que $v_2^{REF}\{2\}$ en raison de la suppression des effets de non-flot par l'exigence du gap en η , la différence étant plus prononcée dans les collisions périphériques. La différence entre $v_2^{REF}\{2\}$ et $v_2^{REF}\{4\}$ reflète la présence de fluctuations de flot en plus des effets résiduels de non-flot, conformément aux observations du Run 2. L'accord dans les tendances générales entre Run 2 et Run 3 souligne à la fois la stabilité de la mesure et la fiabilité de la méthode des cumulants

multi-particules dans le cadre du Run 3.

Procédure de mélange d'événements

L'extraction du signal v_2 du J/ψ nécessite une estimation précise du bruit de fond combinatoire en fonction de la masse invariante (voir Section 4.6.1). Une technique de mélange d'événements est employée pour construire ce bruit de fond combinatoire. Les événements sont regroupés en pools caractérisés par des bins de centralité et la position du vertex primaire. Cette approche implique de combiner des particules (muons) provenant d'événements différents, éliminant efficacement la contribution du signal tout en préservant les propriétés statistiques du bruit de fond. Le spectre de masse invariante des paires de même signe et de signes opposés est construit en utilisant deux muons provenant du même événement ou d'événements différents, respectivement. Les coefficients de flot des muons individuels sont extraits de manière similaire à ceux des dimuons, en construisant les cumulants POI et REF appropriés. Dans ce cas, les événements considérés contiennent au moins un muon individuel, et les coefficients $v_2^{\mu\pm}\{2\}$ et $v_2^{\mu\pm}\{4\}$ sont calculés en fonction de l'impulsion transverse des muons. Ces coefficients contribuent ensuite à la construction du bruit de fond combinatoire du v_2 des dimuons. La comparaison du v_2 des paires de dimuons (SEPM) et du v_2 du bruit de fond estimé via la méthode de mélange d'événements (MEPM) montre un bon accord dans les régions de bandes latérales, confirmant que la procédure implémentée reproduit correctement la forme du bruit de fond de flot.

Extraction du signal et incertitudes systématiques

L'extraction du coefficient v_2 du J/ψ s'effectue par une procédure d'ajustement en deux étapes appliquée à la distribution de masse invariante des dimuons et au $v_2^{\mu\mu}$ correspondant en fonction de la masse invariante (voir Sections 4.7 et 4.7.1). Dans la première étape, le spectre de masse invariante est ajusté pour déterminer le rapport signal sur bruit. La fraction signal sur bruit en fonction de la masse invariante est ensuite utilisée pour ajuster le $v_2^{\mu\mu}$ en fonction de la masse invariante. Le comportement du v_2 du bruit de fond varie significativement avec p_T . Dans toutes les gammes de p_T , une valeur significative de v_2 est observée à haute masse invariante. Au LHC, ces paires proviennent principalement de désintégrations semi-leptoniques de hadrons de saveur lourde, la contribution dom-

inante provenant des hadrons de charm ouvert. Les incertitudes systématiques sont évaluées en faisant varier les configurations d'ajustement. Pour les incertitudes sur le nombre total de J/ψ , différentes formes de signal sont testées (CB2 avec paramètres de queue fixés par les données ou MC, fonction NA60), ainsi que différents intervalles d'ajustement de masse. Pour les incertitudes sur l'extraction de $v_2^{J/\psi}$, un paramètre libre β est introduit pour modéliser la contribution du flot de bruit de fond corrélé, soit fixé à zéro (pas de contribution de flot corrélé) soit laissé libre de varier de 0 à 1 (contribution de flot corrélé indéterminée). La procédure d'ajustement a été répétée avec différentes combinaisons d'options disponibles, conduisant à un ensemble d'essais. La valeur finale du flot du J/ψ est prise comme la moyenne sur toutes les estimations, les erreurs statistiques résultantes étant données comme la moyenne sur les erreurs statistiques de tous les essais. L'incertitude systématique est évaluée en faisant la valeur quadratique moyenne de toutes les estimations. Une incertitude systématique supplémentaire est introduite pour tenir compte du choix du binning en masse invariante. L'analyse montre que la source dominante d'incertitude systématique provient du choix de l'intervalle d'ajustement de masse, reflétant la sensibilité à la modélisation du bruit de fond combinatoire. Cela représente l'impact de la description du bruit de fond combinatoire, qui change significativement lorsque l'intervalle d'ajustement est modifié.

Résultats du flot et des fluctuations du J/ψ

Cette thèse présente les premières mesures de $v_2^{J/\psi}\{2\}$ et $v_2^{J/\psi}\{4\}$ en fonction de p_T dans les collisions Pb-Pb à $\sqrt{s_{NN}} = 5.36$ TeV pour la classe de centralité 10-30% (voir Section 4.8). Comme montré dans la figure 7.1, un v_2 positif est observé sur une large gamme de p_T , de 0 à 10 GeV/c.

À bas p_T , un v_2 significatif dans la classe de centralité 10-30% est attribué au mécanisme de régénération. À plus haut p_T , le v_2 semble relativement plat avec des valeurs légèrement positives. Cependant, en raison des grandes incertitudes statistiques au-delà de 10 GeV/c, aucune conclusion définitive ne peut être tirée dans cette région. La bonne concordance entre les coefficients v_2 obtenus par les méthodes Event Plane ($v_2\{EP\}$), Scalar Product ($v_2\{SP\}$) et corrélations à deux particules ($v_2\{2\}$) atteste de la robustesse de l'anisotropie observée du J/ψ . Les différentes méthodes d'extraction du flot présentent des résultats cohérents dans la limite des incertitudes statistiques. La comparaison avec les résultats du Run 2

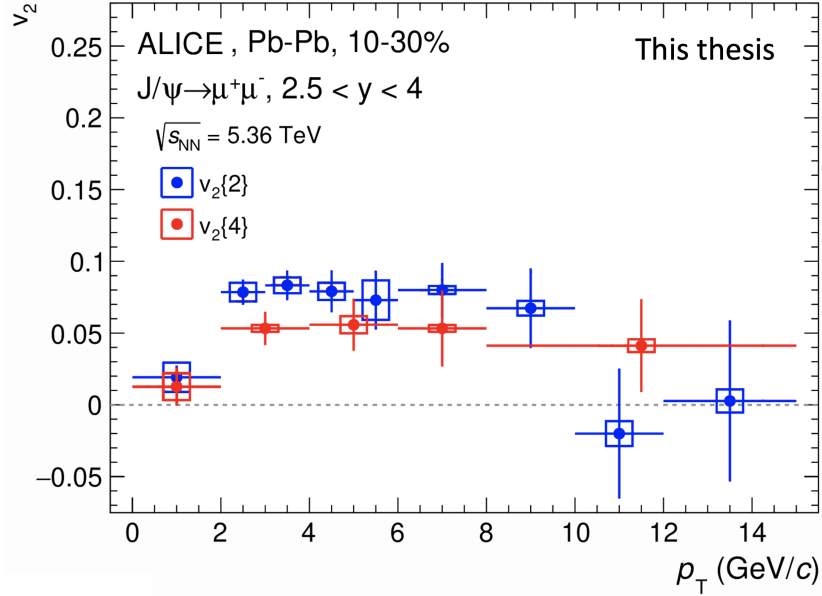


FIGURE 7.1 – Premières mesures de $v_2^{J/\psi}\{2\}$ et $v_2^{J/\psi}\{4\}$ dans les collisions Pb-Pb à $\sqrt{s_{NN}} = 5,36$ TeV pour la classe de centralité 10–30%.

à $\sqrt{s_{NN}} = 5.02$ TeV montre une cohérence, attendue étant donné les énergies de collision très similaires. Les résultats sont également comparés aux prédictions théoriques (Tsinghua et TAMU). Le coefficient $v_2^{J/\psi}\{4\}$ mesuré montre un accord plus proche avec les prédictions de Tsinghua qu'avec celles de TAMU. Il est important de noter qu'aucun des modèles ne tient compte des fluctuations événement par événement, leurs prédictions devraient donc suivre $v_2\{4\}$. Une signification de 2.7σ est observée pour $v_2\{4\} < v_2\{SP\}$. Cette observation représente la première démonstration directe que les fluctuations de flot jouent un rôle significatif dans le flot elliptique du J/ψ . Le ratio de fluctuation $F^{J/\psi}$ a été calculé et comparé à F^Λ et $F^{K_s^0}$ mesurés par CMS. Il a été affirmé que si F montre une dépendance significative en p_T , les fluctuations observées sont principalement pilotées par des variations de la géométrie de l'état initial et des effets dynamiques de l'état final. Le ratio $F^{J/\psi}$ est relativement plat à haut p_T , similaire aux valeurs pour Λ et K_s^0 . Le ratio du premier bin de p_T est proche de 1, signifiant que les fluctuations de flot sont très significatives. Pour évaluer correctement la magnitude des fluctuations de flot, la dépendance en p_T de la différence $\sigma = \sqrt{v_2\{SP\}^2 - v_2\{4\}^2}$ a été évaluée.

À très bas p_T , une hiérarchie est observée : $v_2^K > v_2^\Lambda > v_2^{J/\psi}$, cohérente avec le scaling en masse des hadrons légers et le scénario de recombinaison des quarks charm. À p_T intermédiaire-élevé, le J/ψ est produit principalement dans les pre-

miers stades de la collision. Une hiérarchie claire émerge : $v_2^{J/\psi} < v_2^{K_S^0} < v_2^\Lambda$. Pour K_S^0 et Λ , cette hiérarchie peut être qualitativement comprise en termes de scaling par le nombre de quarks constituants (NCQ). Les quarks légers peuvent être considérés comme pleinement thermalisés dans le QGP, tandis que le quark charm, avec sa masse bien plus grande, ne subit qu'une thermalisation cinématique partielle. Une observation frappante concerne le premier bin de p_T du J/ψ : on trouve $\langle v_2^{J/\psi} \rangle < \sigma^{J/\psi}$, conséquence de $v_2\{4\} \sim 0$ et $v_2\{SP\} > 0$ dans ce bin. Cela montre pour la première fois une indication que, à bas p_T , les fluctuations de flot peuvent être encore plus importantes que le flot attendu des mécanismes de régénération. Le fait que les fluctuations de flot $\sigma^{J/\psi}$ soient assez grandes dans toute la région de p_T , comparables au flot moyen, suggère que les fluctuations événement par événement peuvent jouer un rôle important dans le $v_2\{SP\}$ observé. Une faible dépendance en p_T de $\sigma^{J/\psi}$ et $F^{J/\psi}$ ne peut être exclue. Pour illustrer les résultats de fluctuations de flot événement par événement, un cadre de représentation 2D (dans le système de coordonnées EP) est utilisé, employant un échantillonnage aléatoire avec des distributions de Bessel-Gaussien. Les nuages pour le J/ψ , K_S^0 et Λ visualisent directement les hiérarchies observées.

7.2 Étude des effets de matière nucléaire froide avec le processus Drell-Yan

Cette analyse phénoménologique vise à prédire la distribution des partons nucléaires (nPDF) à petit x de Bjorken dans les noyaux de plomb, où les effets de matière nucléaire froide tels que la saturation de gluons ou le "shadowing" restent mal compris. L'analyse utilise des pseudo-données DY pour simuler les conditions de LHCb afin de contraindre les nPDF. Dans la région de rapidité avant du détecteur LHCb, les valeurs de x_2 sont sondées dans la gamme de 10^{-5} à 10^{-4} . Des pseudo-données sont générées pour le facteur de modification nucléaire $R_{pPb}(y)$ à $\sqrt{s_{NN}} = 5.02$ TeV.

Des PDF aux sections efficaces et R_{pA}

Deux frameworks différents sont utilisés dans cette analyse : Les Houches Accord Parton Distribution Function (LHAPDF) et Drell-Yan Turbo (DYTurbo) (voir

Section 5.2). La bibliothèque LHAPDF est utilisée pour accéder et interpoler les fonctions de distribution partoniques. Elle fournit une interface unifiée et cohérente avec un ensemble de PDF développés par diverses collaborations, englobant à la fois les PDF de proton et nucléaires. Ces fonctions servent d'entrée à DYTurbo, qui est utilisé pour calculer les sections efficaces Drell-Yan. Une implémentation des collisions asymétriques a été réalisée dans DYTurbo, permettant de calculer les sections efficaces Drell-Yan. DYTurbo relie les ensembles de PDF à une section efficace mesurable via un calcul pQCD. Les nPDF sont sondées à une échelle d'impulsion de $Q = 10$ GeV. Trois ensembles de nPDF différents sont utilisés : EPPS16nlo (96 membres, méthode hessienne, 90% CL), nCTEQ15WZ (39 membres, méthode hessienne, 90% CL), et nNNPDF30 (250 répliques bayésiennes, 68% CL). La méthode hessienne utilise des variations le long des vecteurs propres de la matrice d'erreur, tandis que l'approche bayésienne génère de nombreuses répliques Monte Carlo. À partir de ces ensembles, on obtient une collection de sections efficaces via DYTurbo, puis une collection de R_{pA} . Cette étude se concentre sur la fenêtre de masse $5 < M < 120$ GeV, en intégrant sur p_T pour éviter l'effet Cronin.

Modèle et génération de pseudo-données DY

Aucune mesure expérimentale DY n'étant disponible dans la région cinématique d'intérêt ($x \sim 10^{-5}$), des pseudo-données sont générées (voir Section 5.2.2). On définit \hat{R} (la "vérité") comme une moyenne de R_{pA} calculée avec trois membres arbitraires d'ensembles nPDF. Huit points de données sont générés dans l'acceptance de LHCb selon des bins de rapidité couvrant les régions avant et arrière, avec des fluctuations gaussiennes ajoutées. Les incertitudes tiennent compte du nombre d'événements dans chaque bin (calculé via DYTurbo) et d'un rapport signal sur bruit effectif d'environ 1/30. Avec les luminosités intégrées projetées pour les Runs 3 et 4 (104 pb⁻¹ pour pp et 250 nb⁻¹ pour p-Pb) et une acceptance fois efficacité de 0.9.

Repondération des nPDF

L'impact de nouvelles données sur les nPDF est quantifié par une procédure de repondération bayésienne appliquée à l'ensemble nNNPDF (voir Section 5.2.3). Chaque réplique prédit une valeur pour un observable donné, et la valeur d'espérance a priori est calculée comme la moyenne sur toutes les répliques. Pour chaque réplique, le χ^2 est calculé à partir des nouvelles mesures (somme des différences

quadratiques normalisées pour des données non corrélées). Cette valeur forme la base de la vraisemblance, centrale pour mettre à jour la distribution des nPDF. Selon le théorème de Bayes, la distribution postérieure est proportionnelle au produit de la vraisemblance et de la distribution a priori, permettant de calculer une valeur d'espérance mise à jour où les poids sont déterminés par la vraisemblance assignée à chaque réplique. La fonction de vraisemblance ω^{χ^2} est utilisée (approche NNPDF), qui favorise les valeurs de $\chi^2/N_{\text{données}}$ proches de un.

Résultats

Dans cette analyse, les observables étudiés sont le facteur de modification nucléaire R_{pA} et le rapport $R_f^{(A)}$ qui compare la distribution d'un parton de saveur (f) donnée dans un nucléon lié au sein d'un noyau à la distribution attendue dans un ensemble incohérent de nucléons libres (voir Section 5.2.4). Le facteur de modification nucléaire R_{pA} est présenté avant et après l'inclusion des nouvelles pseudo-données DY. La réduction de la bande d'incertitude après repondération démontre comment de nouvelles mesures peuvent contraindre significativement les prédictions théoriques pour R_{pA} . De même, le rapport $R_f^{(A)}$ est contraint (les nPDF sont évaluées à $Q = 10$ GeV), mettant en évidence comment l'inclusion de nouvelles données resserre la gamme autorisée pour chaque saveur partonique spécifique.

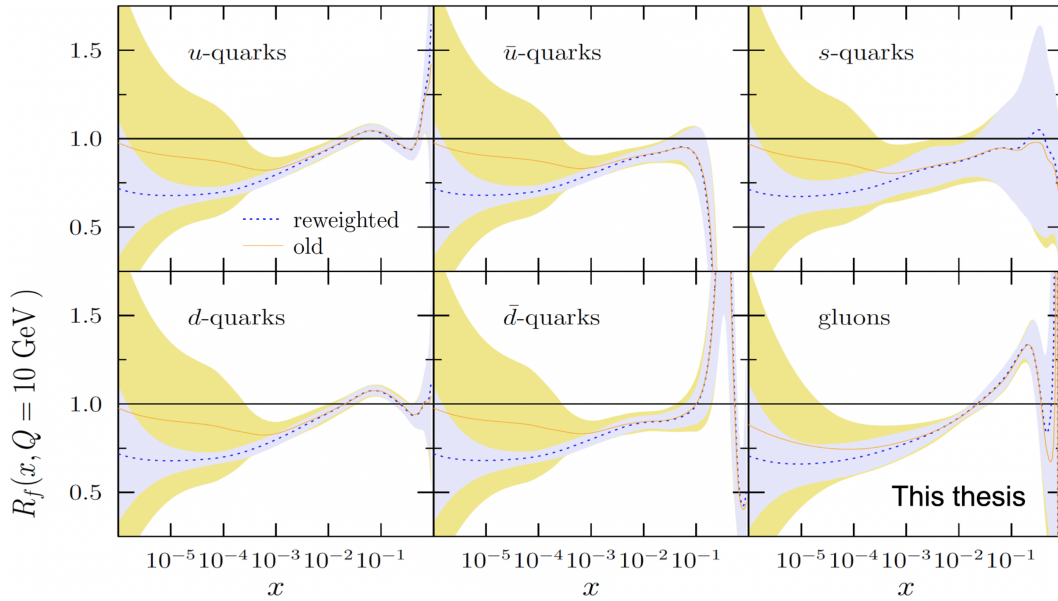


FIGURE 7.2 – Rapports de PDF $R_f^{(A)}$, avant et après réajustement. Les PDF sont évalués à $Q = 10\text{GeV}$.

La comparaison avant et après repondération montre le pouvoir de contrainte amélioré des pseudo-données Drell-Yan, conduisant à une détermination plus précise de la structure partonique des noyaux à petit x (voir Figure 7.2). Les futures données réelles de LHCb remplaceraient ces pseudo-données et fourniraient des contraintes expérimentales réduisant significativement les incertitudes actuelles sur les nPDF.

Conclusion

Cette thèse apporte des contributions significatives à deux domaines complémentaires de la physique des ions lourds. Pour la première fois, les fluctuations de flot du J/ψ sont mesurées, avec des magnitudes comparables au flot moyen lui-même, révélant que les fluctuations événement par événement jouent un rôle crucial. L'étude phénoménologique Drell-Yan démontre comment de futures mesures dans la région cinématique de LHCb pourraient réduire significativement les incertitudes actuelles sur les nPDF à petit x .

Appendix A

Mathematical framework

Chiral condensate derivation

Step-by-step derivation of the $\langle \bar{\psi} \psi \rangle$ term, using the chiral projectors of the following equation:

$$\langle \bar{\psi} \psi \rangle = \langle \bar{\psi} \mathbf{1} \mathbf{1} \psi \rangle = \langle \bar{\psi} (P_L + P_R) (P_L + P_R) \psi \rangle, \quad (\text{A.1})$$

with $P_{L,R} = \frac{1}{2}(1 \mp \gamma^5)$, $P_L + P_R = \mathbf{1}$, $P_{L,R}^2 = P_{L,R}$, and $P_L P_R = P_R P_L = 0$.
Expand:

$$\langle \bar{\psi} \psi \rangle = \langle \bar{\psi} P_L P_L \psi + \bar{\psi} P_L P_R \psi + \bar{\psi} P_R P_L \psi + \bar{\psi} P_R P_R \psi \rangle. \quad (\text{A.2})$$

We can write:

$$\bar{\psi} P_L P_L \psi = \bar{\psi}_R \psi_L, \quad \bar{\psi} P_R P_R \psi = \bar{\psi}_L \psi_R, \quad (\text{A.3})$$

while the mixed terms vanish:

$$\bar{\psi} P_L P_R \psi = \bar{\psi} P_R P_L \psi = 0. \quad (\text{A.4})$$

Therefore,

$$\langle \bar{\psi} \psi \rangle = \langle \bar{\psi}_L \psi_R + \bar{\psi}_R \psi_L \rangle. \quad (\text{A.5})$$

Rapidity and x-Bjorken in hadronic collisions

The kinematics of the structure of the beam particles can be expressed as function of x-Bjorken: [277]

$$p_{parton}^\mu = x E_{hadron} (1, 0, 0, \pm 1) \quad (\text{A.6})$$

$$s_{hadron} = (P_1 + P_2)^2 = (E + E, 0, 0, E - E)^2 = 4E^2 \quad (A.7)$$

Equation A.7 represents the square of the hadron center-of-mass energy, s_{hadron} , solely in terms of the total energy E of the colliding hadrons. It shows that s_{hadron} is four times the square of the total energy:

$$s_{parton} = (p_1 + p_2)^2 = E(x_1 + x_2, 0, 0, x_1 - x_2)^2 = 4x_1x_2E^2 \quad (A.8)$$

Equation A.8 characterizes the square of the parton center-of-mass energy, s_{parton} , in relation to the momentum fractions x_1 and x_2 of the colliding partons. This expression demonstrates that s_{parton} is proportional to the product of these momentum fractions.

Combinning equations A.7 and A.8 we obtain: Equation A.9:

$$\frac{s_{parton}}{s_{hadron}} = x_1x_2 \quad (A.9)$$

The ratio s_{parton}/s_{hadron} is simplified to the product x_1x_2 , indicating that the fraction of the hadron's energy carried by the partons is determined by their momentum fractions. [278]

$$y = \frac{1}{2} \ln \frac{E + p_z}{E - p_z} = \frac{1}{2} \ln \frac{E(x_1 + x_2 + x_1 - x_2)}{E(x_1 + x_2 - x_1 + x_2)} = \frac{1}{2} \ln \frac{x_1}{x_2} \quad (A.10)$$

Equation A.10 introduces the concept of rapidity (y), a measure of parton velocity. It showcases the relation between rapidity and momentum fractions, illustrating that y is half the natural logarithm of the ratio of x_1 to x_2 :

$$e^y = \sqrt{\frac{x_1}{x_2}} = x_1 \sqrt{\frac{s_{hadron}}{s_{parton}}} = x_1 \frac{2E}{\sqrt{s_{parton}}} \quad (A.11)$$

$$x_1 = \frac{\sqrt{s_{parton}}}{2E} e^{+y} \quad (A.12)$$

$$x_{1,2} = \frac{\sqrt{s_{parton}}}{2E} e^{\pm y} \quad (A.13)$$

Finally, equation A.13 express momentum fractions x_1 and x_2 in terms of the rapidity (y)

Boltzmann equation

Understanding how a physical system evolves toward equilibrium requires a microscopic, dynamical description. The Boltzmann equation provides this framework, describing the statistical behavior of a system out of equilibrium [279]. Specifically, it governs the time evolution of the single-particle distribution function $f(\mathbf{r}, \mathbf{p}, t)$ in phase space:

$$\frac{\partial}{\partial t}f + \frac{\mathbf{p}}{m} \cdot \nabla_r f - \nabla_r U \cdot \nabla_p f = C[f] \quad (\text{A.14})$$

Here, $C[f]$ is the collisional term for particle interactions, while the other terms describe free particle motion and the influence of external forces. Macroscopic quantities, which are crucial for fluid dynamics, are derived from this distribution function through integrals over momentum space. For instance, particle density $n(\mathbf{r}, t)$ is defined as:

$$n(\mathbf{r}, t) = \int \frac{d^3p}{(2\pi)^3} f(\mathbf{r}, \mathbf{p}, t) \quad (\text{A.15})$$

the velocity field $n\mathbf{v}(\mathbf{r}, t)$ is obtained as:

$$n\mathbf{v}(\mathbf{r}, t) = \int \frac{d^3p}{(2\pi)^3} \frac{\mathbf{p}}{m} f(\mathbf{r}, \mathbf{p}, t) \quad (\text{A.16})$$

and the pressure tensor $P_{ij}(\mathbf{r}, t)$ is calculated as:

$$P_{ij}(\mathbf{r}, t) = \int \frac{d^3p}{(2\pi)^3} \frac{p_i p_j}{m} f(\mathbf{r}, \mathbf{p}, t) \quad (\text{A.17})$$

When the single-particle distribution function is locally isotropic in momentum space, the Boltzmann equation reduces to the equations of hydrodynamics [85]. In this limit, the pressure tensor becomes isotropic and the macroscopic evolution of the system is governed by conservation laws. Specifically, the conservation of mass is expressed as

$$\partial_t n + \nabla_r \cdot (n\mathbf{v}) = 0 \quad (\text{A.18})$$

and the momentum balance equation:

$$m\partial_t \mathbf{v} + (\mathbf{v} \cdot \nabla_r) \mathbf{v} + \nabla_r U + \frac{1}{n} \nabla_r P = 0 \quad (\text{A.19})$$

Phase transition

A phase transition describes a fundamental change in the macroscopic system behavior. This process implies a spontaneous symmetry breaking (SSB) mechanism [280]. In ferromagnetism, as the system cools below the Curie temperature, individual atomic spins spontaneously align in a common direction, breaking the underlying rotational symmetry of the magnetic interactions. In the Higgs mechanism, the vacuum selects a specific configuration of the Higgs field, breaking the electroweak gauge symmetry and giving mass to fundamental particles. In quantum chromodynamics (QCD), chiral symmetry is approximately spontaneously broken in the vacuum, leading to the emergence of massive hadrons from nearly massless quarks. In each case, the transition is characterized by the emergence of an order parameter, a quantity that is zero in the symmetric phase and acquires a non-zero value once the symmetry is broken, signaling the onset of a new macroscopic order. In thermodynamics, macroscopic variables define the equation of state, which determines the equilibrium state of matter through a relation like:

$$f(P, V, T, \dots) = 0 \quad (\text{A.20})$$

This equation defines a hypersurface in thermodynamic space, where reversible transformations correspond to continuous paths, and metastable states, conversely, lie outside this hypersurface [281]. Phase transitions are identified by points where derivatives such as $\partial V/\partial T|_P$, $\partial P/\partial T|_V$, or $\partial V/\partial P|_T$ become undefined or discontinuous. These derivatives are related to physical coefficients like the coefficient of thermal expansion $\alpha = \frac{1}{V} \frac{\partial V}{\partial T} \Big|_P$, the isothermal compressibility $K = \frac{1}{V} \frac{\partial V}{\partial P} \Big|_T$, and the specific heat at constant pressure $C_P = T \frac{\partial S}{\partial T} \Big|_P$.

If these coefficients diverge, the system undergoes a first-order phase transition, characterized by distinct entropy and volume for coexisting phases A and B ($S_A \neq S_B, V_A \neq V_B$), leading to infinite α , K , and C_P [282]. In such transitions, a mixed state exists with properties that are weighted averages of the individual phases, like $V = x_A V_A + x_B V_B$ where $x_A + x_B = 1$. The Clausius-Clapeyron relation connects the slope of the phase boundary to the discontinuities in entropy and volume:

$$\frac{dP}{dT} = \frac{S_B - S_A}{V_B - V_A} = \frac{L}{T \Delta V} \quad (\text{A.21})$$

where L is the latent heat of transition. In contrast, second-order phase transitions

occur when α , K , and C_P are defined but exhibit finite discontinuities, meaning $S_A = S_B$ and $V_A = V_B$ but their derivatives are different. These transitions are instantaneous, without latent heat or phase coexistence, and can mark a critical point where a first-order transition line ends. Exotic λ -transitions, such as the superfluid transition of helium, present a unique case where α and K diverge while $S_A = S_B$ and $V_A = V_B$. Furthermore, a system may exhibit a unique triple point (P_t, V_t, T_t) where three phases coexist, satisfying Gibbs' phase rule, as seen in substances like water near 0°C and 6×10^{-3} atm.

Flow coefficients derivation

The azimuthal distribution of particles in heavy ion collisions is a periodic function and can therefore be expanded in a Fourier series. We express the distribution function $r(\psi)$ as:

$$r(\psi) = \frac{x_0}{2\pi} + \frac{1}{\pi} \sum_{n=1}^{\infty} [x_n \cos(n\psi) + y_n \sin(n\psi)] \quad (\text{A.22})$$

where the Fourier coefficients are given by:

$$x_n = \langle \cos(n\psi) \rangle = \int_0^{2\pi} r(\psi) \cos(n\psi) d\psi \quad (\text{A.23})$$

$$y_n = \langle \sin(n\psi) \rangle = \int_0^{2\pi} r(\psi) \sin(n\psi) d\psi \quad (\text{A.24})$$

The following quantity can be defined:

$$v_n^2 = x_n^2 + y_n^2 \quad (\text{A.25})$$

It is called the flow harmonic and plays a central role in the characterization of collective motion in the transverse plane.

We now turn to the exponential form of the Fourier expansion. Using Euler's formulas: $\cos(n\psi) = \frac{e^{in\psi} + e^{-in\psi}}{2}$, $\sin(n\psi) = \frac{e^{in\psi} - e^{-in\psi}}{2i}$. We rewrite the series as:

$$r(\psi) = \frac{x_0}{2\pi} + \frac{1}{2\pi} \sum_{n=1}^{\infty} \left[(x_n - iy_n) e^{in\psi} + (x_n + iy_n) e^{-in\psi} \right] \quad (\text{A.26})$$

Introducing the complex flow coefficients:

$v_n = x_n - iy_n$ for $n > 0$ and $V_{-n} = x_n + iy_n$ for $n < 0$. We obtain the compact exponential form:

$$r(\psi) = \frac{1}{2\pi} \sum_{n=-\infty}^{+\infty} v_n e^{-in\psi} \quad (\text{A.27})$$

Since the distribution $r(\psi)$ is real-valued, it follows that $r(\psi) = r(\psi)^*$, which implies: $v_n = V_{-n}^*$ and thus the distribution can also be written as:

$$r(\psi) = \frac{v_0}{2\pi} + \frac{1}{\pi} \sum_{n=1}^{\infty} |v_n| \cos[n(\psi - \Phi_n)] \quad (\text{A.28})$$

where the phase Φ_n is defined by writing $v_n = |v_n|e^{in\Phi_n}$.

If we normalize such that $v_0 = 1$, the expression simplifies to:

$$r(\psi) = \frac{1}{2\pi} \left(1 + \sum_{n=1}^{\infty} 2|v_n| \cos[n(\psi - \Phi_n)] \right) \quad (\text{A.29})$$

In the case of symmetric collisions, such as Pb–Pb or p–p, the symmetry under reflection implies that all sine coefficients vanish:

$$\sin(n\psi) + \sin(n(-\psi)) = \sin(n\psi) - \sin(n\psi) = 0 \quad (\text{A.30})$$

Hence, $y_n = 0$ and the flow harmonics reduce to $v_n = x_n$.

This shows that the magnitude $|v_n|$ is the average value:

$$|v_n| = \langle \cos[n(\psi - \Phi_n)] \rangle \quad (\text{A.31})$$

and allows a physical interpretation in terms of anisotropic flow components:

$$\begin{aligned} v_1 &\rightarrow \text{Directed Flow} \\ v_2 &\rightarrow \text{Elliptic Flow} \\ v_3 &\rightarrow \text{Triangular Flow} \\ &\vdots \end{aligned}$$

Inviscid relativistic and energy-momentum tensor derivation

The fluid equations derived under the assumption of local thermodynamic equilibrium are called inviscid, or ideal-fluid, equations [283].

$$T_{ideal}^{\mu\nu} = (\epsilon + P)u^\mu u^\nu - Pg^{\mu\nu}, \quad (\text{A.32})$$

where u^μ is the four-velocity of the fluid and $g^{\mu\nu} = \text{diag}(1, -1, -1, -1)$ is the Minkowski metric. The energy-momentum tensor encapsulates the densities and fluxes of energy and momentum in spacetime. This ideal form neglects dissipative effects such as viscosity and heat conduction.

This tensor satisfies the continuity equation, which ensures the conservation of energy and momentum:

$$\partial_\mu T^{\mu\nu} = 0 \quad (\text{A.33})$$

We define the following $T^{\mu\nu}$, is written as a 2×2 block matrix, reflecting the $(0) \oplus (i)$ decomposition of spacetime:

$$T^{\mu\nu} = \begin{pmatrix} T^{00} & T^{0j} \\ T^{i0} & T^{ij} \end{pmatrix}, \quad (\text{A.34})$$

In the fluid rest frame, assuming local equilibrium, the energy flux T^{i0} and momentum density T^{0j} vanish. Additionally, the pressure tensor simplifies to $T^{ij} = P\delta_{ij}$, leading to the rest-frame energy-momentum tensor:

$$T_{(0)}^{\mu\nu} = \begin{pmatrix} \epsilon & 0 & 0 & 0 \\ 0 & P & 0 & 0 \\ 0 & 0 & P & 0 \\ 0 & 0 & 0 & P \end{pmatrix} = \begin{pmatrix} \epsilon & 0 \\ 0 & P\delta^{ij} \end{pmatrix}, \quad (\text{A.35})$$

where ϵ is the energy density and P the isotropic pressure.

To boost this tensor to a frame where the fluid moves with small velocity $\mathbf{v} = (v_x, v_y, v_z)$, we apply a Lorentz transformation valid to first order in $|\mathbf{v}| \ll 1$. The transformation matrix is:

$$\Lambda = \begin{pmatrix} 1 & v_x & v_y & v_z \\ v_x & 1 & 0 & 0 \\ v_y & 0 & 1 & 0 \\ v_z & 0 & 0 & 1 \end{pmatrix} = \begin{pmatrix} 1 & \mathbf{v}^T \\ \mathbf{v} & \mathbb{1} \end{pmatrix}, \quad (\text{A.36})$$

where $\mathbb{1}$ is the 3×3 identity matrix.

The boosted energy–momentum tensor is given by:

$$T^{\mu\nu} = \Lambda^\mu{}_\alpha \Lambda^\nu{}_\beta T_{(0)}^{\alpha\beta} = \begin{pmatrix} 1 & \mathbf{v}^T \\ \mathbf{v} & \mathbb{1} \end{pmatrix} \begin{pmatrix} \epsilon & 0 \\ 0 & P\delta^{ij} \end{pmatrix} \begin{pmatrix} 1 & \mathbf{v}^T \\ \mathbf{v} & \mathbb{1} \end{pmatrix}. \quad (\text{A.37})$$

Keeping terms only to first order in the velocity \mathbf{v} , the ideal energy-momentum tensor, valid in any frame:

$$T^{\mu\nu} = \begin{pmatrix} \epsilon & (\epsilon + P)\mathbf{v}^T \\ (\epsilon + P)\mathbf{v} & P\delta^{ij} \end{pmatrix}, \quad (\text{A.38})$$

To understand the physical content of this tensor more concretely, it is useful to examine its components in a given reference frame. In particular, the time and spatial components of $T^{\mu\nu}$ have the following physical meanings:

- T^{00} : energy density,
- T^{0j} : density of the j^{th} component of momentum,
- T^{i0} : energy flux along axis i ,
- T^{ij} : pressure tensor.

Coalescence model

In the coalescence (or recombination) model, hadronization occurs via the combination of constituent quarks—assumed to be the relevant degrees of freedom after gluons convert into quark pairs [284]. The collective anisotropic flow of hadrons thus reflects the flow of their constituents, built from the convolution of individual quark azimuthal distributions. Assuming collinear coalescence and setting the reaction plane angle $\Psi_{\text{RP}} = 0$, the elliptic flow of a meson such as the open charm

$D^0 = c\bar{u}$ can be written as:

$$\begin{aligned}
 v_n^{D^0} &= \int d\phi_c d\phi_{\bar{u}} d\phi_{D^0} \cos(n\phi_{D^0}) (1 + 2v_n^c \cos(n\phi_c)) (1 + 2v_n^{\bar{u}} \cos(n\phi_{\bar{u}})) \\
 &\quad \times \delta(\phi_{D^0} - \phi_c) \delta(\phi_{D^0} - \phi_{\bar{u}}) \\
 &= \int d\phi_{D^0} \cos(n\phi_{D^0}) (1 + 2v_n^c \cos(n\phi_{D^0})) (1 + 2v_n^{\bar{u}} \cos(n\phi_{D^0})) \\
 &\approx \int d\phi_{D^0} \cos(n\phi_{D^0}) \cdot (2v_n^c + 2v_n^{\bar{u}}) \cos(n\phi_{D^0}) \\
 &= (2v_n^c + 2v_n^{\bar{u}}) \cdot \int d\phi_{D^0} \cos^2(n\phi_{D^0}) \\
 &= (v_n^c + v_n^{\bar{u}})
 \end{aligned} \tag{A.39}$$

The delta functions $\delta(\phi_{D^0} - \phi_c)\delta(\phi_{D^0} - \phi_{\bar{u}})$ in equation A.39 enforce the collinear coalescence condition, i.e., that the meson is formed only when the constituent quarks move in the same azimuthal direction as the hadron. They collapse the integrals over ϕ_c and $\phi_{\bar{u}}$ to ϕ_{D^0} , yielding a single-variable expression that reflects the assumption that the hadron inherits the collective anisotropy of its constituents.

Experiments at RHIC and LHC reveal that v_n approximately scales with the number of constituent light quarks (NCQ scaling).

Riemann Zeta function, Gamma function, Bose-Einstein Integrals, Bessel-Gaussian function and flow fluctuation derivation

Before introducing Bessel-Gaussian function to compute flow fluctuations, we first recall the Riemann zeta function $\zeta(s)$ and the Gamma function $\Gamma(z)$, both of which frequently arise in integrals involving powers and exponentials. We then show how Bose-Einstein integrals can be expressed as products of Gamma and zeta functions. Finally, we derive the Bessel-Gaussian distribution and use it to compute event-by-event fluctuations in the two-dimensional case.

Gamma function $\Gamma(z)$

For complex numbers with $\text{Re}(z) > 0$, the Gamma function is defined by the improper integral

$$\Gamma(z) = \int_0^\infty t^{z-1} e^{-t} dt. \quad (\text{A.40})$$

It generalizes the factorial, since for natural numbers n , we have:

$$\Gamma(n) = (n-1)!. \quad (\text{A.41})$$

Notice the Gamma function plays an essential role in computing the volume of an n -dimensional ball (hypersphere). Let $B^n(R)$ denote the ball of radius R in \mathbb{R}^n . Its volume is

$$V_n(R) = \frac{\pi^{n/2}}{\Gamma(\frac{n}{2} + 1)} R^n \quad \begin{cases} = 2R & \text{if } n = 1 \quad (\text{diameter of a circle}), \\ = \pi R^2 & \text{if } n = 2 \quad (\text{area of a disk}), \\ = \frac{4}{3} \pi R^3 & \text{if } n = 3 \quad (\text{volume of a sphere}). \end{cases} \quad (\text{A.42})$$

Similarly the surface of a hypersphere:

$$S_n(R) = \frac{d}{dR} V_n(R) = \frac{d}{dR} \left(\frac{\pi^{n/2}}{\Gamma(\frac{n}{2} + 1)} R^n \right) = \frac{\pi^{n/2}}{\Gamma(\frac{n}{2} + 1)} \cdot n R^{n-1} = \frac{2\pi^{n/2}}{\Gamma(\frac{n}{2})} R^{n-1}, \quad (\text{A.43})$$

where in the last step we used the Gamma identity $\Gamma(\frac{n}{2} + 1) = \frac{n}{2} \Gamma(\frac{n}{2})$.

$$S_n(R) = \frac{2\pi^{n/2}}{\Gamma(\frac{n}{2})} R^{n-1} \quad \begin{cases} 2\pi R & n = 2, \\ 4\pi R^2 & n = 3. \end{cases} \quad (\text{A.44})$$

Riemann Zeta Function $\zeta(s)$

The Riemann zeta function is one of the most important special functions in analysis and number theory. For a complex number s with $\text{Re}(s) > 1$, it is defined by the infinite series

$$\zeta(s) = \sum_{n=1}^{\infty} \frac{1}{n^s}. \quad (\text{A.45})$$

This series converges absolutely in the half-plane $\text{Re}(s) > 1$. In particular, the famous *Basel problem* corresponds to the case $s = 2$:

$$\zeta(2) = \sum_{n=1}^{\infty} \frac{1}{n^2} = \frac{\pi^2}{6}. \quad (\text{A.46})$$

Euler found this solution remarkable at the time, since it revealed a deep connection between an infinite series of rational numbers and the geometry of the circle (via π).

Gamma–Riemann structure of the Bose–Einstein integral

The Bose–Einstein integral of order s can be expressed in terms of two classical special functions:

$$I_s = \underbrace{\int_0^{\infty} t^{s-1} e^{-t} dt}_{\Gamma(s)} \cdot \underbrace{\sum_{k=1}^{\infty} \frac{1}{k^s}}_{\zeta(s)} = \int_0^{\infty} \frac{x^{s-1}}{e^x - 1} dx, \quad \text{Re}(s) > 1. \quad (\text{A.47})$$

Evaluation at $s = 4$ and the ultraviolet catastrophe:

$$I_4 = \Gamma(4) \zeta(4) = 6 \cdot \frac{\pi^4}{90} = \frac{\pi^4}{15}. \quad (\text{A.48})$$

In black-body radiation, this integral controls the total energy density, leading to $u(T) \propto T^4$ and the Stefan–Boltzmann law. The exact Bose–Einstein denominator $(e^x - 1)^{-1}$ suppresses ultraviolet modes and makes the integral finite, whereas the classical Rayleigh–Jeans law $(e^x - 1) \approx x$ predicts a divergent $\int_0^{\infty} \nu^2 d\nu$ —the *ultraviolet catastrophe*.

Bessel functions

Bessel functions arise naturally as solutions of Bessel’s differential equation,

$$x^2 \frac{d^2 y}{dx^2} + x \frac{dy}{dx} + (x^2 - n^2) y = 0, \quad (\text{A.49})$$

where n is a real (often integer) parameter called the *order* of the Bessel function.

The solutions that remain finite at the origin are called *Bessel functions of the first kind*, denoted by $J_n(x)$.

They can be expressed as a power series:

$$J_n(x) = \sum_{m=0}^{\infty} \frac{(-1)^m}{m! \Gamma(m+n+1)} \left(\frac{x}{2}\right)^{2m+n}, \quad (\text{A.50})$$

where $\Gamma(z)$ is the Gamma function, a generalization of the factorial.

An equivalent representation is given by the real integral form (valid for real x and integer n):

$$J_n(x) = \frac{1}{\pi} \int_0^\pi \cos(n\theta - x \sin \theta) d\theta. \quad (\text{A.51})$$

More generally, for complex analysis, Bessel functions admit the contour integral representation:

$$J_n(x) = \frac{1}{2\pi i} \int_C t^{-n-1} \exp\left(\frac{x}{2} \left(t - \frac{1}{t}\right)\right) dt, \quad (\text{A.52})$$

where C is a closed contour encircling the origin counterclockwise in the complex plane.

Closely related to the Bessel functions $J_n(x)$ are the *modified Bessel functions* $I_n(x)$. They can be defined by

$$I_n(x) = i^{-n} J_n(ix). \quad (\text{A.53})$$

In particular, for $n = 0$ one has the integral identity

$$\int_0^{2\pi} \exp(z \cos \theta) d\theta = 2\pi I_0(z). \quad (\text{A.54})$$

Derivation of the Bessel-Gaussian \mathcal{BG} distribution

We define the random vector (x, y) that follows a two-dimensional Gaussian distribution:

$$(x, y) \sim \mathcal{N}^2(v; \mu, \sigma^2)(x, y) = \mathcal{N}(x; v_0, \sigma^2) \mathcal{N}(y; 0, \sigma^2). \quad (\text{A.55})$$

with mean $\mu = (v_0, 0)$ and isotropic variance σ^2 . So the associated density distribution is:

$$f(x, y) = \frac{1}{2\pi\sigma^2} \exp\left(-\frac{(x - v_0)^2 + y^2}{2\sigma^2}\right). \quad (\text{A.56})$$

We define polar coordinates:

$$x = v \cos \theta, \quad y = v \sin \theta, \quad (\text{A.57})$$

where $v \geq 0$ is the radius (magnitude) and $\theta \in [0, 2\pi)$ is the angle. The determinant of the Jacobian is $dx dy = v dv d\theta$. So the joint density in polar coordinates is:

$$f(v, \theta) = \frac{v}{2\pi\sigma^2} \exp\left(-\frac{(v \cos \theta - v_0)^2 + (v \sin \theta)^2}{2\sigma^2}\right). \quad (\text{A.58})$$

Expand the exponent:

$$(v \cos \theta - v_0)^2 + (v \sin \theta)^2 = v^2 - 2vv_0 \cos \theta + v_0^2. \quad (\text{A.59})$$

We can write:

$$f(v, \theta) = \frac{v}{2\pi\sigma^2} \exp\left(-\frac{v^2 + v_0^2}{2\sigma^2} + \frac{vv_0 \cos \theta}{\sigma^2}\right). \quad (\text{A.60})$$

We want just the distribution of the radius v , so we integrate over all angles: $f(v) = \int_0^{2\pi} f(v, \theta) d\theta$. That gives:

$$f(v) = \frac{v}{2\pi\sigma^2} \exp\left(-\frac{v^2 + v_0^2}{2\sigma^2}\right) \int_0^{2\pi} \exp\left(\frac{vv_0}{\sigma^2} \cos \theta\right) d\theta. \quad (\text{A.61})$$

The integral $\int_0^{2\pi} \exp(z \cos \theta) d\theta = 2\pi I_0(z)$, is the defining identity of the modified Bessel function $I_0(z)$. The final probability is:

$$f(v) = \frac{v}{\sigma^2} \exp\left(-\frac{v^2 + v_0^2}{2\sigma^2}\right) I_0\left(\frac{vv_0}{\sigma^2}\right). \quad (\text{A.62})$$

Detailed derivation of flow moments, $v_2\{2\}$ and $v_2\{4\}$ assuming 2D Gaussian fluctuations

We start from the flow vector $\mathbf{v} = (v_x, v_y)$, whose Cartesian components are assumed to be independent Gaussian random variables:

$$v_x \sim \mathcal{N}(v_{RP}, \sigma^2), \quad v_y \sim \mathcal{N}(0, \sigma^2). \quad (\text{A.63})$$

Here v_{RP} is the flow coefficient respect to the reaction plane, while σ quantifies event-by-event fluctuations. The experimentally measured flow magnitude is

$$v = \sqrt{v_x^2 + v_y^2}. \quad (\text{A.64})$$

We first compute the moments $\langle v^2 \rangle$ and $\langle v^4 \rangle$, then extract the cumulants

$$c_2\{2\} = \langle v^2 \rangle, \quad c_2\{4\} = \langle v^4 \rangle - 2\langle v^2 \rangle^2. \quad (\text{A.65})$$

By definition, the second moment is

$$\langle v^2 \rangle = \langle v_x^2 \rangle + \langle v_y^2 \rangle. \quad (\text{A.66})$$

Using the Gaussian density for v_x ,

$$\langle v_x^2 \rangle = \frac{1}{\sqrt{2\pi}\sigma} \int_{-\infty}^{\infty} v_x^2 \exp\left(-\frac{(v_x - v_{RP})^2}{2\sigma^2}\right) dv_x. \quad (\text{A.67})$$

Shifting variables $v_x = v_{RP} + \sigma u$, the integral reduces to a standard Gaussian moment, yielding

$$\langle v_x^2 \rangle = v_{RP}^2 + \sigma^2. \quad (\text{A.68})$$

Similarly,

$$\langle v_y^2 \rangle = \frac{1}{\sqrt{2\pi}\sigma} \int_{-\infty}^{\infty} v_y^2 e^{-v_y^2/(2\sigma^2)} dv_y = \sigma^2. \quad (\text{A.69})$$

Therefore, **the second moment** is

$$\langle v^2 \rangle = v_{RP}^2 + 2\sigma^2. \quad (\text{A.70})$$

Expanding the fourth moment:

$$\langle v^4 \rangle = \langle (v_x^2 + v_y^2)^2 \rangle = \langle v_x^4 \rangle + \langle v_y^4 \rangle + 2\langle v_x^2 v_y^2 \rangle. \quad (\text{A.71})$$

The first term of equation (A.71) can be written as

$$\langle v_x^4 \rangle = \frac{1}{\sqrt{2\pi}\sigma} \int_{-\infty}^{\infty} v_x^4 \exp\left(-\frac{(v_x - v_{RP})^2}{2\sigma^2}\right) dv_x. \quad (\text{A.72})$$

Shifting again to the dimensionless variable: $u = \frac{1}{\sigma} (v_x - v_{RP})$, we can write:

$$\langle v_x^4 \rangle = \frac{1}{\sqrt{2\pi}} \int_{-\infty}^{\infty} (v_{RP} + \sigma u)^4 e^{-u^2/2} du. \quad (\text{A.73})$$

Expanding the fourth power,

$$(v_{RP} + \sigma u)^4 = v_{RP}^4 + 4v_{RP}^3\sigma u + 6v_{RP}^2\sigma^2 u^2 + 4v_{RP}\sigma^3 u^3 + \sigma^4 u^4,$$

and noting that the odd terms vanish upon integration, we obtain

$$\langle v_x^4 \rangle = \frac{1}{\sqrt{2\pi}} \int_{-\infty}^{\infty} (v_{RP}^4 + 6v_{RP}^2\sigma^2 u^2 + \sigma^4 u^4) e^{-u^2/2} du. \quad (\text{A.74})$$

Using the Gaussian integrals

$$\int_{-\infty}^{\infty} e^{-u^2/2} du = \sqrt{2\pi}, \quad \int_{-\infty}^{\infty} u^2 e^{-u^2/2} du = \sqrt{2\pi}, \quad \int_{-\infty}^{\infty} u^4 e^{-u^2/2} du = 3\sqrt{2\pi},$$

we finally obtain

$$\langle v_x^4 \rangle = v_{RP}^4 + 6v_{RP}^2\sigma^2 + 3\sigma^4. \quad (\text{A.75})$$

The second term of equation (A.71) is

$$\langle v_y^4 \rangle = \frac{1}{\sqrt{2\pi}\sigma} \int_{-\infty}^{\infty} v_y^4 e^{-v_y^2/(2\sigma^2)} dv_y = 3\sigma^4. \quad (\text{A.76})$$

The last term of equation (A.71) is obtained from the independence of v_x and v_y :

$$2\langle v_x^2 v_y^2 \rangle = 2\langle v_x^2 \rangle \langle v_y^2 \rangle = 2(v_{RP}^2 + \sigma^2)(\sigma^2) = 2v_{RP}^2\sigma^2 + 2\sigma^4. \quad (\text{A.77})$$

Finally, **the fourth moment** becomes

$$\langle v^4 \rangle = v_{RP}^4 + 8v_{RP}^2\sigma^2 + 8\sigma^4. \quad (\text{A.78})$$

Using equations A.70 and A.78, the cumulants are

$$c_2\{2\} = \langle v^2 \rangle = v_{RP}^2 + 2\sigma^2, \quad (\text{A.79})$$

$$c_2\{4\} = \langle v^4 \rangle - 2\langle v^2 \rangle^2 = (v_{RP}^4 + 8v_{RP}^2\sigma^2 + 8\sigma^4) - 2(v_{RP}^2 + 2\sigma^2)^2 = -v_{RP}^4. \quad (\text{A.80})$$

Finally, we have prove:

$$v_2\{2\}^2 \equiv c_2\{2\} = v_{RP}^2 + 2\sigma^2, \quad (\text{A.81})$$

$$v_2\{4\}^4 \equiv -c_2\{4\} = v_{RP}^4. \quad (\text{A.82})$$

Therefore, the fourth-order cumulant exactly recovers the flow coefficient v_{RP} respect to the reaction plane, independent of fluctuations σ .

Appendix B

Flow analysis with cumulants

POI $\mu+$ / $\mu-$ correlators of single muons

The muon and anti-muon flow vectors $p_2^{\mu-}$ and $p_2^{\mu+}$ needs to be computed. The 2-particle correlation calculations for $\mu+$ and $\mu-$:

$$\langle 2'^{\mu\pm} \rangle = \frac{p_{2,0}^{\mu\pm} Q_{2,1}^*}{m_p^{\pm} S_{1,1}} \quad (\text{B.1})$$

$$\langle\langle 2'^{\mu\pm} \rangle\rangle = \frac{\sum_{i=1}^N (M_{01}'^{\pm} / m_p^{\pm})_i \langle 2'^{\mu\pm} \rangle_i}{\sum_{i=1}^N (M_{01}'^{\pm} / m_p^{\pm})_i}, \quad (\text{B.2})$$

$$M_{01}'^{\pm} = \sum_{i=1}^{m_p^{\pm}} \sum_{j=1}^M w_j = m_p^{\pm} S_{1,1}. \quad (\text{B.3})$$

The four-particle correlators for $\mu+$ and $\mu-$ are expressed as:

$$\begin{aligned} \langle 4'^{\mu\pm} \rangle = \frac{1}{M_{0111}'^{\pm}} & \left(p_{2,0}^{\mu\pm} Q_{2,1}^3 - p_{2,0}^{\mu\pm} Q_{2,1} Q_{4,2} - 2S_{1,2} p_{2,0}^{\mu\pm} Q_{2,1} \right. \\ & \left. - 2S_{1,1} Q_{2,1}^2 + 2p_{2,0}^{\mu\pm} Q_{2,3} + 2S_{1,1} S_{1,2} - 6S_{1,3} \right) \end{aligned} \quad (\text{B.4})$$

$$\langle\langle 4'^{\mu\pm} \rangle\rangle = \frac{\sum_{i=1}^N (M_{0111}'^{\pm} / m_p^{\pm})_i \langle 4'^{\mu\pm} \rangle_i}{\sum_{i=1}^N (M_{0111}'^{\pm} / m_p^{\pm})_i}, \quad (\text{B.5})$$

$$M_{0111}'^{\pm} = \sum_{i=1}^{m_p^{\pm}} \sum_{j,k,l=1}^{M_{0jkl}} w_j w_k w_l = m_p^{\pm} [S_{3,1} - 3S_{1,1} S_{1,2} + 2S_{1,3}]. \quad (\text{B.6})$$

Invariant mass fit functions

Signal functions:

- **Double Crystal Ball (CB2):** A Gaussian core with two power-law tails, described by 7 parameters ($N, \bar{x}, \sigma, \alpha, \alpha', n, n'$):

$$CB2(x) = N \cdot \begin{cases} \exp\left(-\frac{(x - \bar{x})^2}{2\sigma^2}\right) & \text{for } \alpha' > \frac{x - \bar{x}}{\sigma} > -\alpha \\ A \cdot \left(B - \frac{x - \bar{x}}{\sigma}\right)^{-n} & \text{for } \frac{x - \bar{x}}{\sigma} \leq -\alpha \\ C \cdot \left(D + \frac{x - \bar{x}}{\sigma}\right)^{-n'} & \text{for } \frac{x - \bar{x}}{\sigma} \geq \alpha' \end{cases} \quad (B.7)$$

with

$$A = \left(\frac{n}{|\alpha|}\right)^n \cdot \exp\left(-\frac{|\alpha|^2}{2}\right), \quad B = \frac{n}{|\alpha|} - |\alpha| \quad (B.8)$$

$$C = \left(\frac{n'}{|\alpha'|}\right)^{n'} \cdot \exp\left(-\frac{|\alpha'|^2}{2}\right), \quad D = \frac{n'}{|\alpha'|} - |\alpha'| \quad (B.9)$$

A sketch of the CB2 function is shown in Figure B.1, where the asymmetric Gaussian core is depicted in red and the two power-law tails on the left and right are illustrated in blue.

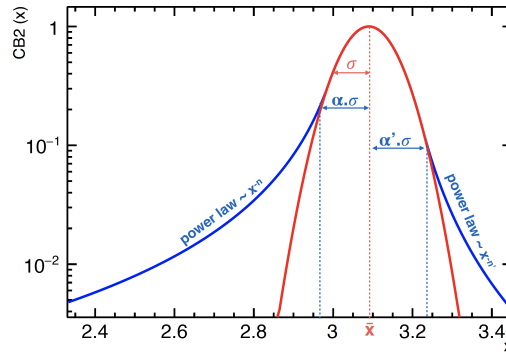


FIGURE B.1 – CB2(x) function with parameters $N, \bar{x}, \sigma, \alpha, \alpha', n, n'$ [285].

Similarly, the NA60 function is a Gaussian core with a power-law tail, described by 11 parameters:

— **NA60:**

$$f(x; N, \bar{x}, \sigma, t_1, t_2, p_1, p_2, p_3, p_4, p_5, p_6) = N \cdot \exp \left(-\frac{1}{2} \left(\frac{t}{t_0} \right)^2 \right), \quad (\text{B.10})$$

where $t = \frac{x - \bar{x}}{\sigma}$ and

$$t_0 = \begin{cases} 1 + (p_1(t_1 - t))^{p_2 - p_3 \sqrt{t_1 - t}} & , t \leq t_1 \\ 1 & , t_1 < t < t_2 \\ 1 + (p_4(t - t_2))^{p_5 - p_6 \sqrt{t - t_2}} & , t \geq t_2 \end{cases}$$

Background function:

— **Chebyshev polynomial (degree 3):** The background is modeled with a third-order Chebyshev polynomial, expressed in terms of the normalized variable

$$t(x) = -1 + 2 \frac{x - m_{\min}}{m_{\max} - m_{\min}}, \quad t \in [-1, 1], \quad (\text{B.11})$$

which maps the fitted mass range $[m_{\min}, m_{\max}]$ onto the standard Chebyshev domain $[-1, 1]$. The Chebyshev background function is written as:

$$B_{\text{Cheb3}}(x; c_0, c_1, c_2, c_3) = \sum_{k=0}^3 c_k T_k(t(x)), \quad (\text{B.12})$$

where the coefficients (c_0, c_1, c_2, c_3) are free fit parameters, and $T_k(t)$ denote the Chebyshev polynomials. Up to degree three, they are explicitly given by

$$T_0(t) = 1, \quad T_1(t) = t, \quad T_2(t) = 2t^2 - 1, \quad T_3(t) = 4t^3 - 3t. \quad (\text{B.13})$$

Significance of $\Delta v_2 = v_2\{SP\} - v_2\{4\}$

To quantify the significance of the difference between the two flow coefficients, $v_2\{SP\}$ and $v_2\{4\}$, we define for each transverse momentum bin, indexed by i , the quantity:

$$\Delta v_2^i = v_2\{SP\}^i - v_2\{4\}^i \quad (\text{B.14})$$

The total uncertainty associated with this difference is calculated as the quadrature sum of the statistical and systematic uncertainties of both measurements:

$$\sigma_{\text{tot}}^i = \sqrt{\left(\sigma_{\text{stat},v2sp}^i\right)^2 + \left(\sigma_{\text{sys},v2sp}^i\right)^2 + \left(\sigma_{\text{stat},v24}^i\right)^2 + \left(\sigma_{\text{sys},v24}^i\right)^2} \quad (\text{B.15})$$

Using these values, the statistical significance of the difference in each p_T bin is given by:

$$S^i = \frac{\Delta v_2^i}{\sigma_{\text{tot}}^i} \quad (\text{B.16})$$

To compute an overall weighted average of Δv_2 , weights are assigned to each bin as:

$$w^i = \frac{1}{\left(\sigma_{\text{tot}}^i\right)^2} \quad (\text{B.17})$$

The weighted average of Δv_2 is then given by:

$$\langle \Delta v_2 \rangle = \frac{\sum_i w^i \Delta v_2^i}{\sum_i w^i} \quad (\text{B.18})$$

and its associated uncertainty is:

$$\sigma_{\langle \Delta v_2 \rangle} = \frac{1}{\sqrt{\sum_i w^i}} \quad (\text{B.19})$$

Finally, the integrated significance of the observed deviation from zero is computed as:

$$S_{\text{total}} = \frac{\langle \Delta v_2 \rangle}{\sigma_{\langle \Delta v_2 \rangle}} \quad (\text{B.20})$$

Error propagation on fluctuation ratio and flow fluctuations

The second-order expansion provides a more accurate estimate of uncertainties, especially when the function has significant curvature or when the relative errors are large.

For a function $f(x, y)$, the second-order Taylor expansion around the point (x_0, y_0) is:

$$f(x, y) \approx f(x_0, y_0) + \frac{\partial f}{\partial x} \Delta x + \frac{\partial f}{\partial y} \Delta y + \frac{1}{2} \frac{\partial^2 f}{\partial x^2} (\Delta x)^2 + \frac{1}{2} \frac{\partial^2 f}{\partial y^2} (\Delta y)^2 + \frac{\partial^2 f}{\partial x \partial y} \Delta x \Delta y \quad (\text{B.21})$$

The variance of f can be expressed as:

$$\sigma_f^2 = \left(\frac{\partial f}{\partial x} \right)^2 \sigma_x^2 + \left(\frac{\partial f}{\partial y} \right)^2 \sigma_y^2 + \frac{1}{2} \left[\left(\frac{\partial^2 f}{\partial x^2} \right)^2 \sigma_x^4 + \left(\frac{\partial^2 f}{\partial y^2} \right)^2 \sigma_y^4 + 2 \left(\frac{\partial^2 f}{\partial x \partial y} \right)^2 \sigma_x^2 \sigma_y^2 \right] \quad (\text{B.22})$$

Error propagation on flow fluctuations

In our analysis, we study the function:

$$f(v_2\{SP\}, v_2\{4\}) = \sqrt{v_2\{SP\}^2 - v_2\{4\}^2} \quad (\text{B.23})$$

where:

- $v_2\{SP\}$ is the single-particle elliptic flow coefficient,
- $v_2\{4\}$ is the four-particle cumulant elliptic flow coefficient,
- the expression is real only if $v_2\{SP\}^2 \geq v_2\{4\}^2$.

This function represents the root-mean-square fluctuations of the anisotropic flow coefficient v_2 .

The first partial derivatives are:

$$\frac{\partial f}{\partial v_2\{SP\}} = \frac{v_2\{SP\}}{\sqrt{v_2\{SP\}^2 - v_2\{4\}^2}} = \frac{v_2\{SP\}}{f} \quad (\text{B.24})$$

$$\frac{\partial f}{\partial v_2\{4\}} = \frac{-v_2\{4\}}{\sqrt{v_2\{SP\}^2 - v_2\{4\}^2}} = \frac{-v_2\{4\}}{f} \quad (\text{B.25})$$

The second partial derivatives are:

$$\frac{\partial^2 f}{\partial v_2\{\text{SP}\}^2} = \frac{v_2\{4\}^2}{(v_2\{\text{SP}\}^2 - v_2\{4\}^2)^{3/2}} = \frac{v_2\{4\}^2}{f^3} \quad (\text{B.26})$$

$$\frac{\partial^2 f}{\partial v_2\{4\}^2} = \frac{v_2\{\text{SP}\}^2}{(v_2\{\text{SP}\}^2 - v_2\{4\}^2)^{3/2}} = \frac{v_2\{\text{SP}\}^2}{f^3} \quad (\text{B.27})$$

$$\frac{\partial^2 f}{\partial v_2\{\text{SP}\} \partial v_2\{4\}} = \frac{v_2\{\text{SP}\} v_2\{4\}}{(v_2\{\text{SP}\}^2 - v_2\{4\}^2)^{3/2}} = \frac{v_2\{\text{SP}\} v_2\{4\}}{f^3} \quad (\text{B.28})$$

Substituting these derivatives into the second-order formula:

$$\begin{aligned} \sigma_f^2 = & \left(\frac{v_2\{\text{SP}\}}{f} \right)^2 \sigma_{v_2\{\text{SP}\}}^2 + \left(\frac{-v_2\{4\}}{f} \right)^2 \sigma_{v_2\{4\}}^2 \\ & + \frac{1}{2} \left[\left(\frac{v_2\{4\}^2}{f^3} \right)^2 \sigma_{v_2\{\text{SP}\}}^4 + \left(\frac{v_2\{\text{SP}\}^2}{f^3} \right)^2 \sigma_{v_2\{4\}}^4 + 2 \left(\frac{v_2\{\text{SP}\} v_2\{4\}}{f^3} \right)^2 \sigma_{v_2\{\text{SP}\}}^2 \sigma_{v_2\{4\}}^2 \right] \end{aligned} \quad (\text{B.29})$$

Simplifying:

$$\begin{aligned} \sigma_f^2 = & \frac{v_2\{\text{SP}\}^2 \sigma_{v_2\{\text{SP}\}}^2 + v_2\{4\}^2 \sigma_{v_2\{4\}}^2}{f^2} \\ & + \frac{1}{2f^6} \left[v_2\{4\}^4 \sigma_{v_2\{\text{SP}\}}^4 + v_2\{\text{SP}\}^4 \sigma_{v_2\{4\}}^4 + 2v_2\{\text{SP}\}^2 v_2\{4\}^2 \sigma_{v_2\{\text{SP}\}}^2 \sigma_{v_2\{4\}}^2 \right] \end{aligned} \quad (\text{B.30})$$

Error propagation of the Fluctuation Ratio

The fluctuation ratio is defined as

$$F(v_2\{\text{SP}\}, v_2\{4\}) = \sqrt{\frac{v_2\{\text{SP}\}^2 - v_2\{4\}^2}{v_2\{\text{SP}\}^2 + v_2\{4\}^2}}. \quad (\text{B.31})$$

The first partial derivatives are:

$$\frac{\partial F}{\partial v_2\{\text{SP}\}} = \frac{1}{2F} \left(\frac{2v_2\{\text{SP}\} (v_2\{\text{SP}\}^2 + v_2\{4\}^2)}{(v_2\{\text{SP}\}^2 + v_2\{4\}^2)^2} - \frac{2v_2\{\text{SP}\} (v_2\{\text{SP}\}^2 - v_2\{4\}^2)}{(v_2\{\text{SP}\}^2 + v_2\{4\}^2)^2} \right). \quad (\text{B.32})$$

$$\frac{\partial F}{\partial v_2\{4\}} = \frac{1}{2F} \left(\frac{-2v_2\{4\} (v_2\{SP\}^2 + v_2\{4\}^2)}{(v_2\{SP\}^2 + v_2\{4\}^2)^2} - \frac{2v_2\{4\} (v_2\{SP\}^2 - v_2\{4\}^2)}{(v_2\{SP\}^2 + v_2\{4\}^2)^2} \right). \quad (\text{B.33})$$

Second derivatives are:

$$\begin{aligned} \frac{\partial^2 F}{\partial v_2\{SP\}^2} &= \frac{1}{2F} \left(\frac{2(v_2\{SP\}^2 + v_2\{4\}^2)}{(v_2\{SP\}^2 + v_2\{4\}^2)^2} - \frac{8v_2\{SP\}^2}{(v_2\{SP\}^2 + v_2\{4\}^2)^2} \right) \\ &\quad - \frac{1}{4F^3} \left(\frac{2v_2\{SP\} (v_2\{SP\}^2 + v_2\{4\}^2)}{(v_2\{SP\}^2 + v_2\{4\}^2)^2} - \frac{2v_2\{SP\} (v_2\{SP\}^2 - v_2\{4\}^2)}{(v_2\{SP\}^2 + v_2\{4\}^2)^2} \right)^2. \end{aligned} \quad (\text{B.34})$$

$$\begin{aligned} \frac{\partial^2 F}{\partial v_2\{4\}^2} &= \frac{1}{2F} \left(\frac{-2(v_2\{SP\}^2 + v_2\{4\}^2)}{(v_2\{SP\}^2 + v_2\{4\}^2)^2} - \frac{8v_2\{4\}^2}{(v_2\{SP\}^2 + v_2\{4\}^2)^2} \right) \\ &\quad - \frac{1}{4F^3} \left(\frac{-2v_2\{4\} (v_2\{SP\}^2 + v_2\{4\}^2)}{(v_2\{SP\}^2 + v_2\{4\}^2)^2} - \frac{2v_2\{4\} (v_2\{SP\}^2 - v_2\{4\}^2)}{(v_2\{SP\}^2 + v_2\{4\}^2)^2} \right)^2. \end{aligned} \quad (\text{B.35})$$

$$\begin{aligned} \frac{\partial^2 F}{\partial v_2\{SP\} \partial v_2\{4\}} &= \frac{1}{2F} \frac{-8v_2\{SP\} v_2\{4\}}{(v_2\{SP\}^2 + v_2\{4\}^2)^2} \\ &\quad - \frac{1}{4F^3} \left(\frac{2v_2\{SP\} (v_2\{SP\}^2 + v_2\{4\}^2)}{(v_2\{SP\}^2 + v_2\{4\}^2)^2} - \frac{2v_2\{SP\} (v_2\{SP\}^2 - v_2\{4\}^2)}{(v_2\{SP\}^2 + v_2\{4\}^2)^2} \right) \\ &\quad \times \left(\frac{-2v_2\{4\} (v_2\{SP\}^2 + v_2\{4\}^2)}{(v_2\{SP\}^2 + v_2\{4\}^2)^2} - \frac{2v_2\{4\} (v_2\{SP\}^2 - v_2\{4\}^2)}{(v_2\{SP\}^2 + v_2\{4\}^2)^2} \right). \end{aligned} \quad (\text{B.36})$$

Finally, the error propagation on the fluctuation ratio is given by:

$$\begin{aligned} \sigma_F^2 &= \left(\frac{\partial F}{\partial v_2\{SP\}} \right)^2 \sigma_{v_2\{SP\}}^2 + \left(\frac{\partial F}{\partial v_2\{4\}} \right)^2 \sigma_{v_2\{4\}}^2 \\ &\quad + \frac{1}{2} \left[\left(\frac{\partial^2 F}{\partial v_2\{SP\}^2} \right)^2 \sigma_{v_2\{SP\}}^4 + \left(\frac{\partial^2 F}{\partial v_2\{4\}^2} \right)^2 \sigma_{v_2\{4\}}^4 \right. \\ &\quad \left. + 2 \left(\frac{\partial^2 F}{\partial v_2\{SP\} \partial v_2\{4\}} \right)^2 \sigma_{v_2\{SP\}}^2 \sigma_{v_2\{4\}}^2 \right]. \end{aligned} \quad (\text{B.37})$$

Additional plots of the $v_2\{2\}$ and $v_2\{4\}$ signal extraction

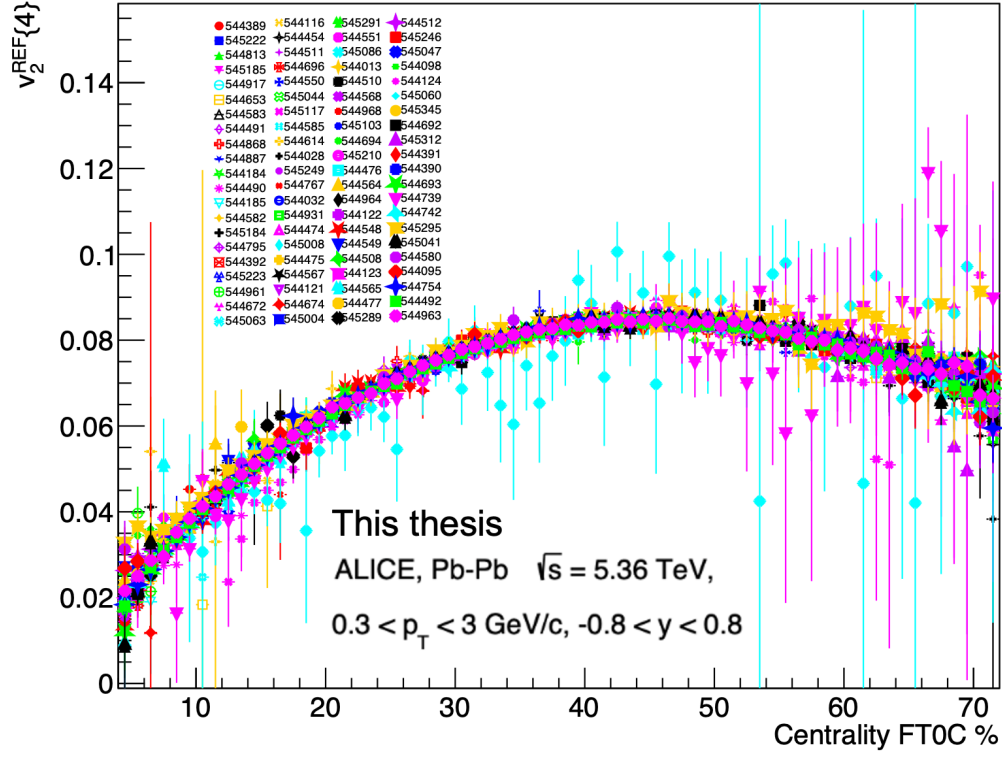


FIGURE B.2 – Run-by-run comparison of Run 3 data. Elliptic flow of charged particles at mid-rapidity $v_2^{\text{REF}\{4\}}$ as a function of centrality.

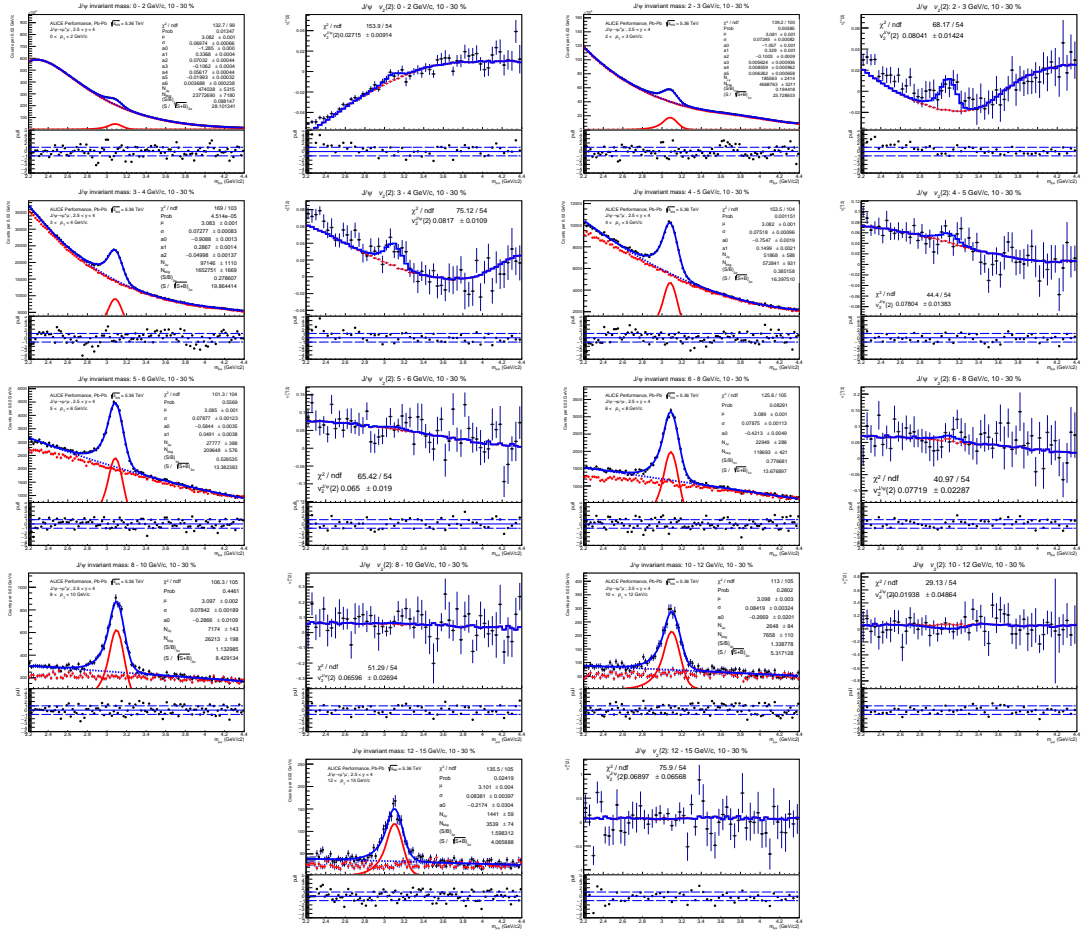


FIGURE B.3 – Example of fitting results for dimuon invariant mass spectra and $v_2\{2\}$ as a function of the invariant mass for the p_T bins: 0-2, 2-3, 3-4, 4-5, 5-6, 6-8, 8-10, 10-12, and 12-15 GeV/c. (from left to right, from top to bottom, respectively) within the centrality class 10-50%. The fit results use CB2 as the signal and Chebychev as the background for the mass fit, and event-mixing with one free parameter β modeling the correlated background flow contribution for v_2 background.

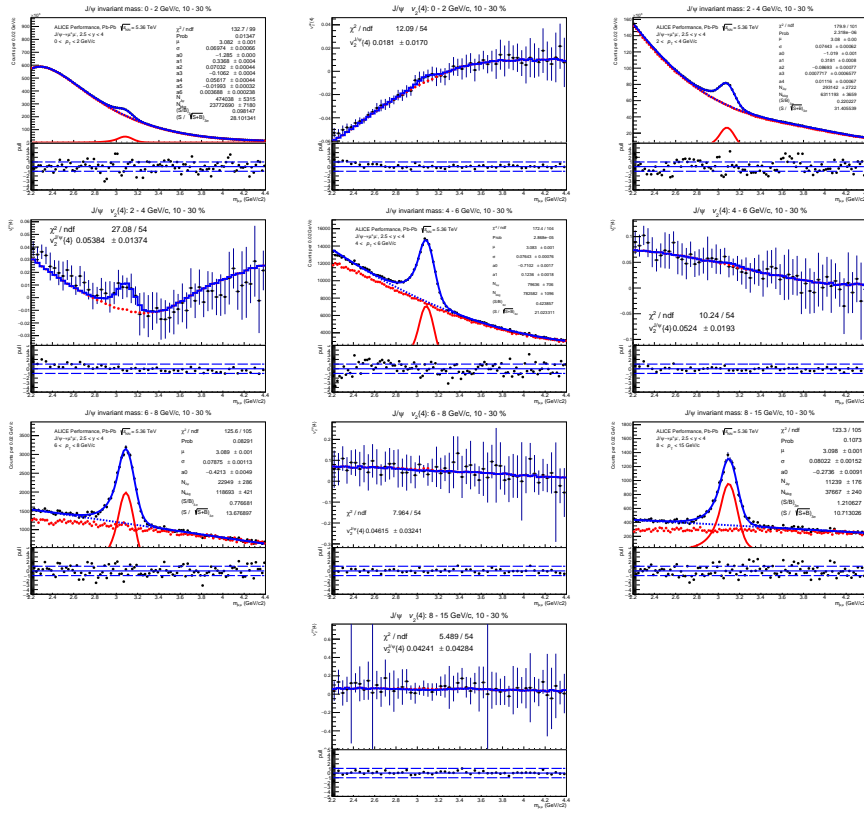


FIGURE B.4 – Example of fitting results for dimuon invariant mass spectra and $v_2\{4\}$ as a function of the invariant mass for the p_T bins: 0-2, 2-4, 4-6, 6-8 and 8-15 GeV/c. (from left to right, from top to bottom, respectively) within the centrality class 10-30%. The fit results use CB2 as the signal and event mixing as background for the mass fit, and event mixing for the v_2 background with one free parameter β modeling the correlated background flow contribution for v_2 background.

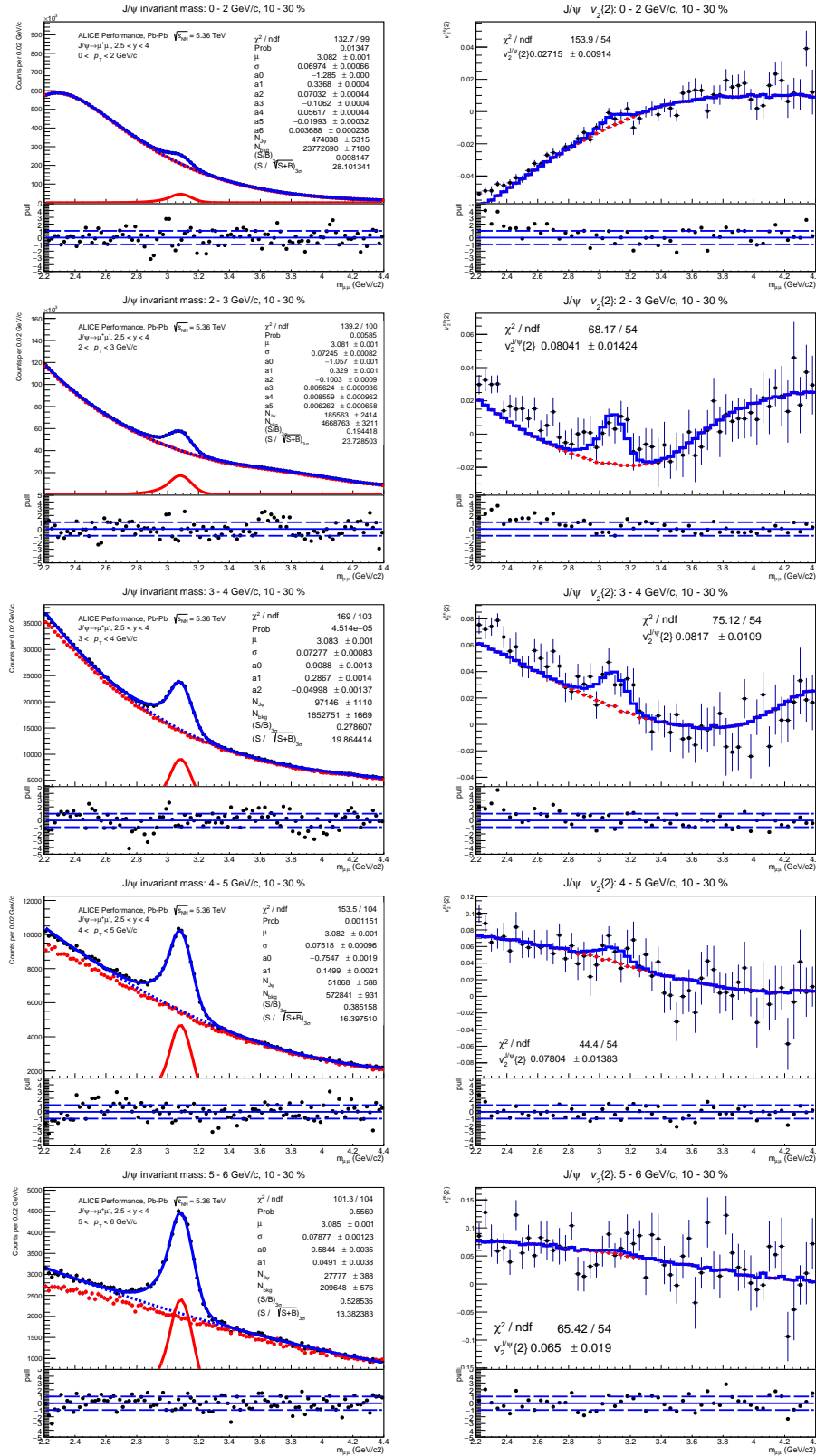


FIGURE B.5 – Example of fitting results for dimuon invariant mass spectra and $v_2\{2\}$ as a function of the invariant mass for the p_T bins: 0-2, 2-3, 3-4, 4-5, and 5-6 GeV/c. (from left to right, from top to bottom, respectively) within the centrality class 10-30%. The fit results use CB2 as the signal and event mixing as background for the mass fit, and event mixing for the v_2 background with one free parameter β modeling the correlated background flow contribution for v_2 background.

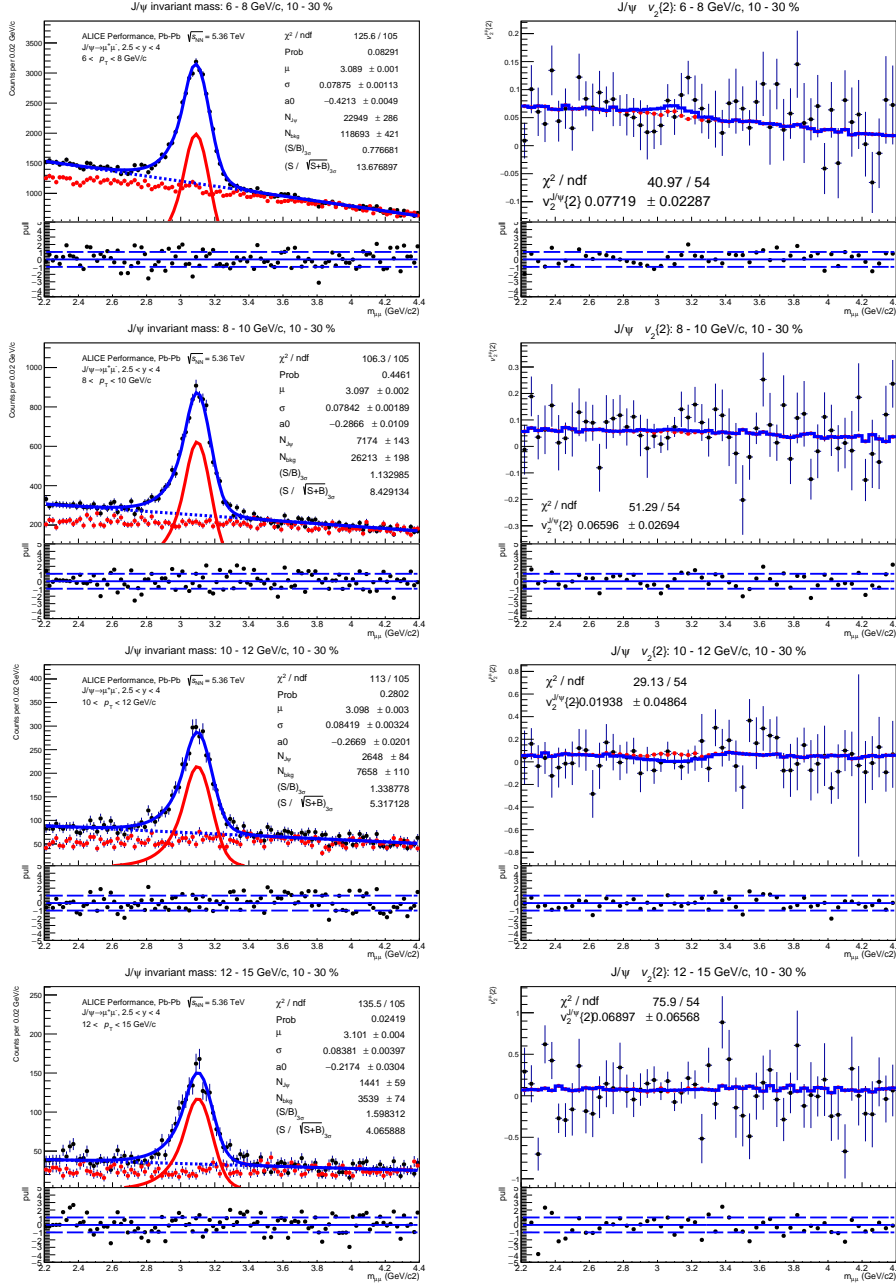


FIGURE B.6 – Example of fitting results for dimuon invariant mass spectra and $v_2\{2\}$ as a function of the invariant mass for the p_T bins: 6-8, 8-10, 10-12 and 12-15 GeV/c. (from left to right, from top to bottom, respectively) within the centrality class 10-30%. The fit results use CB2 as the signal and event mixing as background for the mass fit, and event mixing for the v_2 background with one free parameter β modeling the correlated background flow contribution for v_2 background.

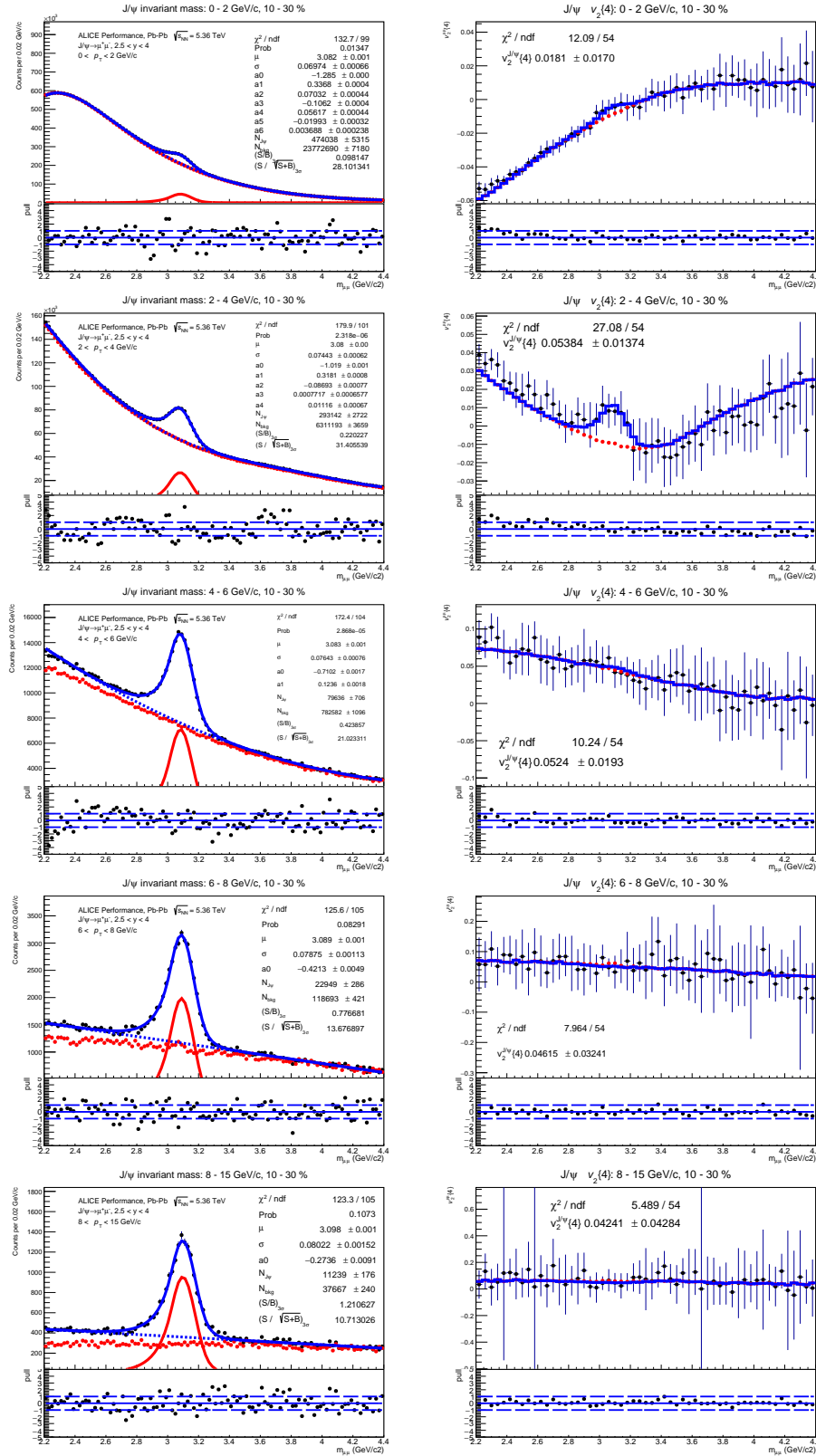


FIGURE B.7 – Example of fitting results for dimuon invariant mass spectra and $v_2\{4\}$ as a function of the invariant mass for the p_T bins: 0-2, 2-4, 4-6, 6-8 and 8-15 GeV/c. (from left to right, from top to bottom, respectively) within the centrality class 10-30%. The fit results use CB2 as the signal and event mixing as background for the mass fit, and event mixing for the v_2 background with one free parameter β modeling the correlated background flow contribution for v_2 background.

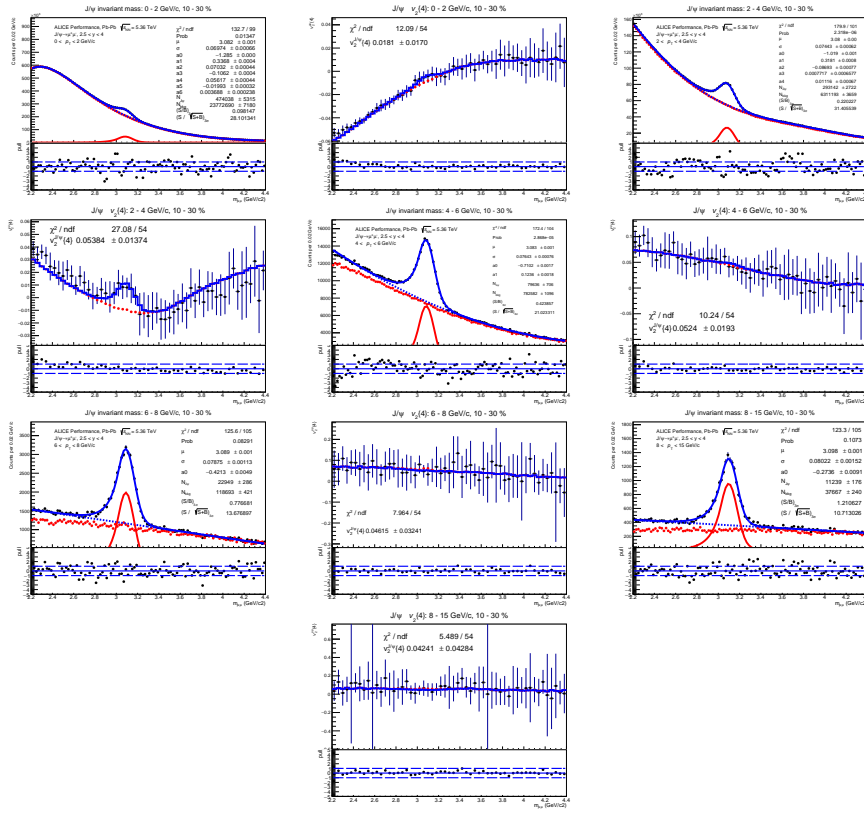


FIGURE B.8 – Example of fitting results for dimuon invariant mass spectra and $v_2\{4\}$ as a function of the invariant mass for the p_T bins: 0-2, 2-4, 4-6, 6-8 and 8-15 GeV/c. (from left to right, from top to bottom, respectively) within the centrality class 10-30%. The fit results use CB2 as the signal and event mixing as background for the mass fit, and event mixing for the v_2 background with one free parameter β modeling the correlated background flow contribution for v_2 background.

Systematic uncertainties study for yield extraction

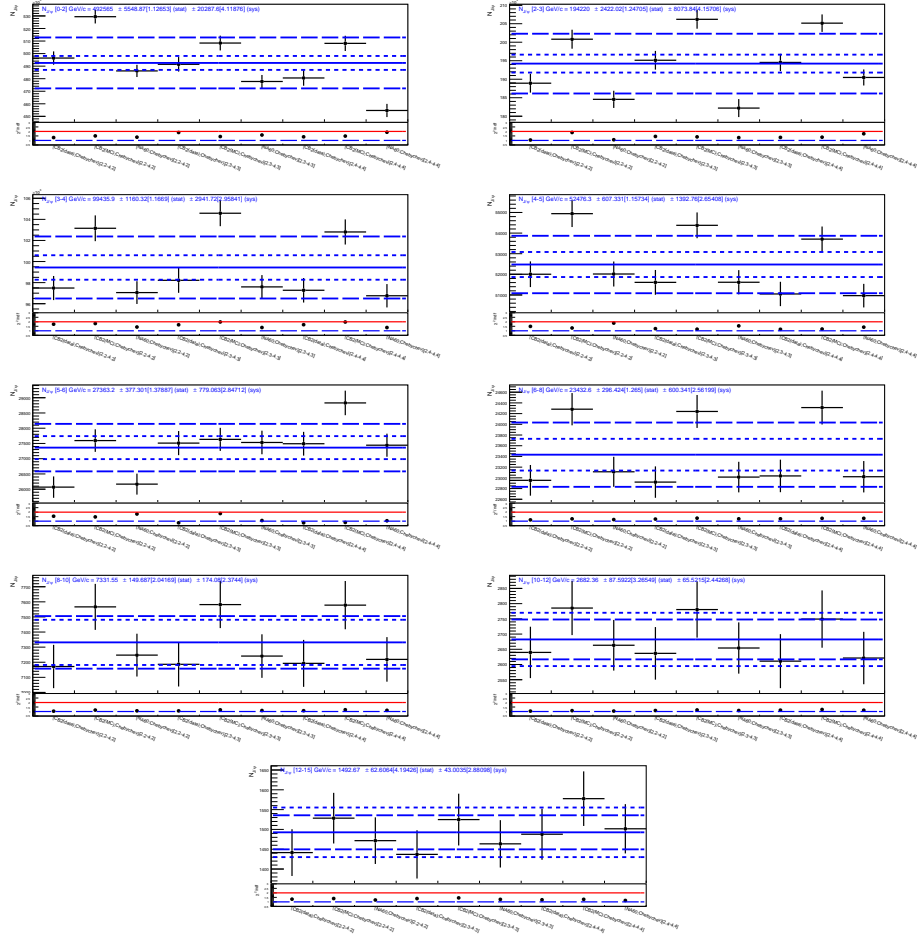


FIGURE B.9 – Systematic results of N^I/Ψ for the p_T bins: 0-2, 2-3, 3-4, 4-5, 5-6, 6-8, 8-10, 10-12, and 12-15 GeV/c. (from left to right, from top to bottom, respectively) within the centrality class 10-30%.

Systematic uncertainties study for cumulant

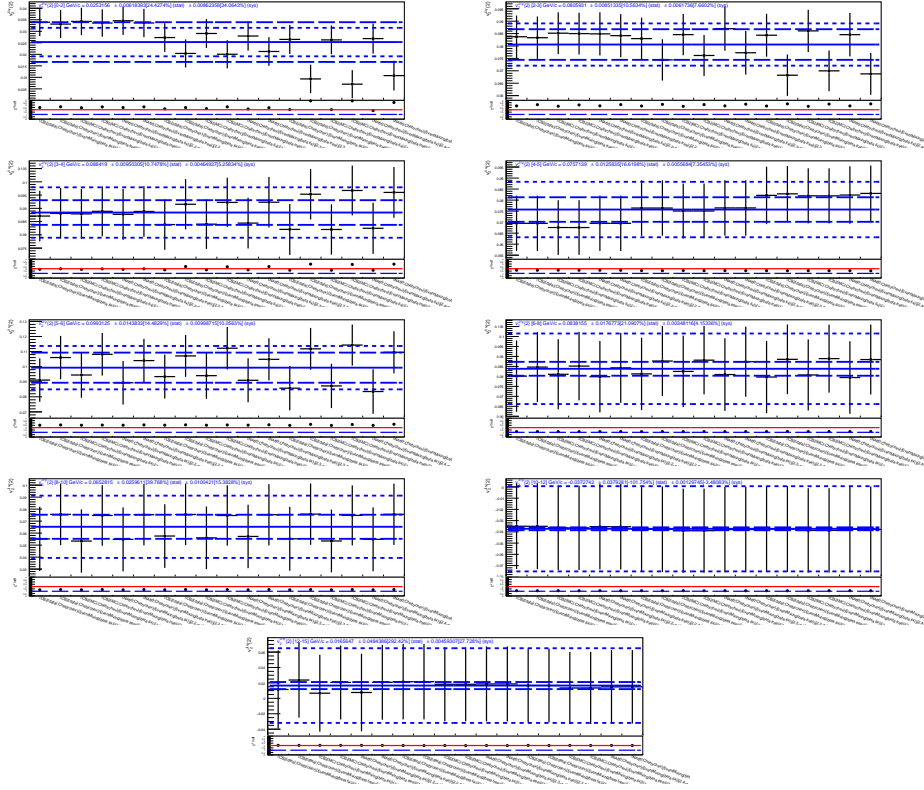


FIGURE B.10 – Systematic results of $v_2\{2\}$ for the p_T bins: 0-2, 2-3, 3-4, 4-5, 5-6, 6-8, 8-10, 10-12, and 12-15 GeV/c. (from left to right, from top to bottom, respectively) within the centrality class 10-30%. Event-mixing with parameter β modeling the correlated background flow contribution for v_2 background.

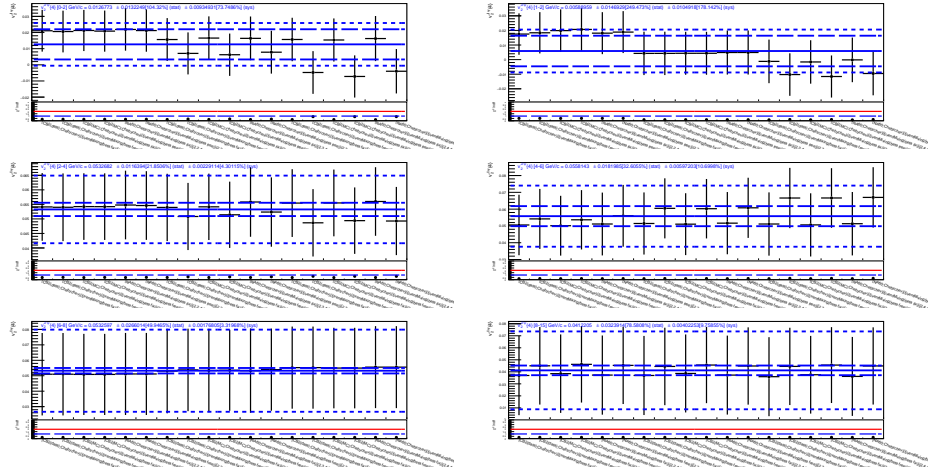


FIGURE B.11 – Systematic results of $v_2\{4\}$ for the p_T bins: 0-2, 1-2, 2-4, 4-6, 6-8, 8-10 and 8-15 GeV/c.(from left to right, from top to bottom, respectively) within the centrality class 10-30%. Event-mixing with parameter β modeling the correlated background flow contribution for v_2 background.

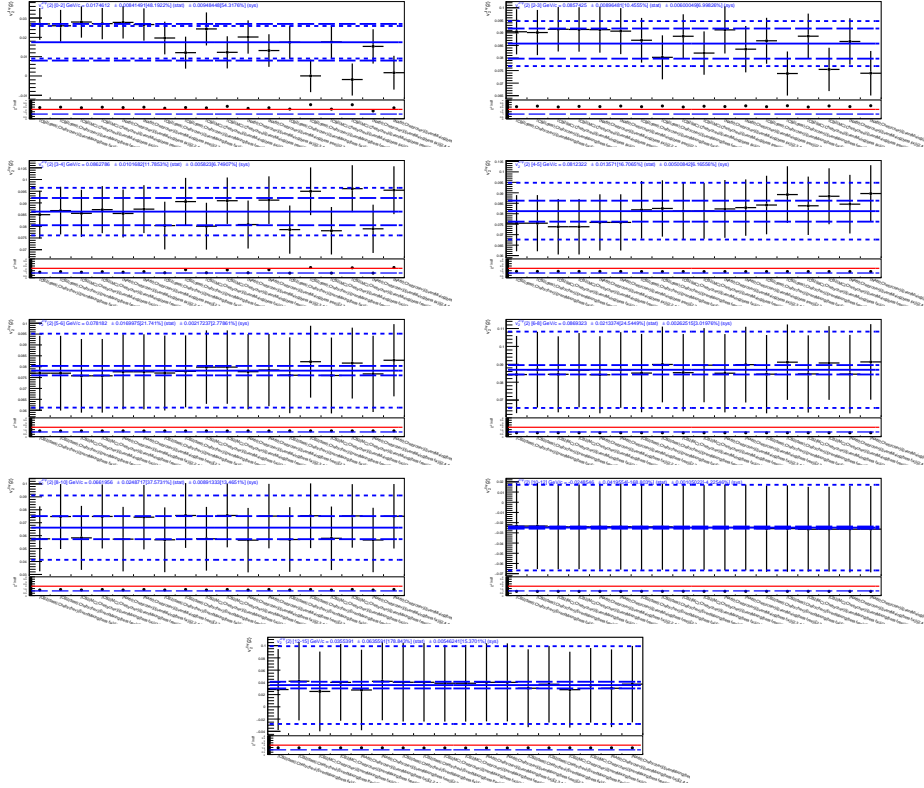


FIGURE B.12 – Systematic fit results from of $v_2\{4\}$ rebinned distributions for the p_T bins: 0-2, 2-3, 3-4, 4-5, 5-6, 6-8, 8-10, 10-12, and 12-15 GeV/c. (from left to right, from top to bottom, respectively) within the centrality class 10-30%. Event-mixing with parameter β modeling the correlated background flow contribution for v_2 background.

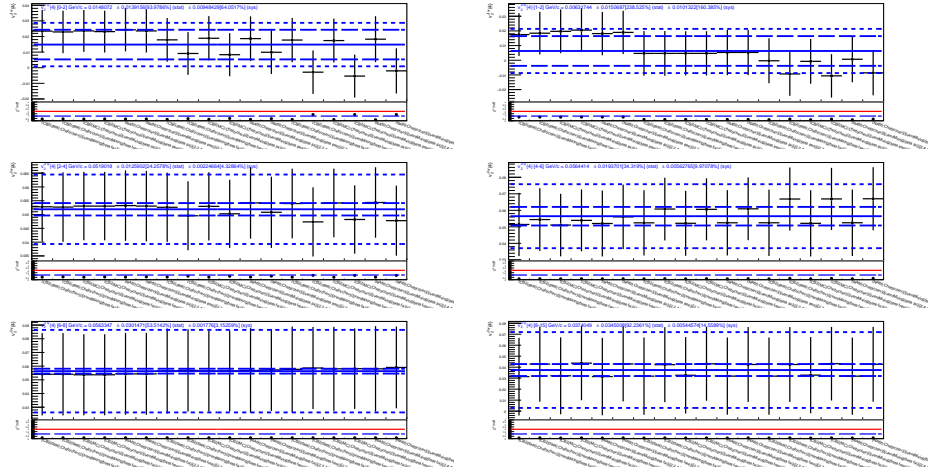


FIGURE B.13 – Systematic fit results from of $v_2\{4\}$ rebinned distributions for the p_T bins: 0-2, 1-2, 2-4, 4-6, 6-8 and 8-15 GeV/c.(from left to right, from top to bottom, respectively) within the centrality class 10-30%. Event-mixing with parameter β modeling the correlated background flow contribution for v_2 background.

J/ψ v_2 values

p_T (GeV/c)	$v_2^{J/\psi}\{2\}$	Stat.	Syst.
0.00 - 2.00	0.0192	± 0.0082	± 0.0102
2.00 - 3.00	0.0785	± 0.0088	± 0.0065
3.00 - 4.00	0.0833	± 0.0104	± 0.0055
4.00 - 5.00	0.0791	± 0.0147	± 0.0060
5.00 - 6.00	0.0730	± 0.0206	± 0.0138
6.00 - 8.00	0.0800	± 0.0189	± 0.0027
8.00 - 10.00	0.0673	± 0.0278	± 0.0051
10.00 - 12.00	-0.0201	± 0.0453	± 0.0087
12.00 - 15.00	0.0027	± 0.0562	± 0.0081

TABLE B.1 – J/ψ $v_2\{2\}$
vs. p_T in 10-30%.

p_T (GeV/c)	$v_2^{J/\psi}\{4\}$	Stat.	Syst.
0.00 - 2.00	0.0127	± 0.0132	± 0.0094
2.00 - 4.00	0.0533	± 0.0116	± 0.0024
4.00 - 6.00	0.0558	± 0.0182	± 0.0060
6.00 - 8.00	0.0533	± 0.0266	± 0.0023
8.00 - 15.00	0.0412	± 0.0324	± 0.0045

TABLE B.2 – J/ψ $v_2\{4\}$
vs. p_T in 10-30%.

p_T (GeV/c)	$v_2\{SP\}$	Stat.	Syst.
0.00 - 0.50	0.0076	± 0.0111	± 0.0065
0.50 - 1.00	0.0155	± 0.0096	± 0.0069
1.00 - 1.50	0.0228	± 0.0059	± 0.0043
1.50 - 2.00	0.0533	± 0.0081	± 0.0057
2.00 - 2.50	0.0654	± 0.0067	± 0.0077
2.50 - 3.00	0.0867	± 0.0073	± 0.0032
3.00 - 4.00	0.0884	± 0.0060	± 0.0013
4.00 - 5.00	0.0792	± 0.0075	± 0.0050
5.00 - 6.00	0.0944	± 0.0094	± 0.0039
6.00 - 8.00	0.0664	± 0.0091	± 0.0060
8.00 - 10.00	0.0824	± 0.0156	± 0.0052
10.00 - 12.00	0.1003	± 0.0247	± 0.0102
12.00 - 15.00	0.0770	± 0.0304	± 0.0077

TABLE B.3 – v_2 vs. p_T for given bins.

p_T (GeV/ c)	$v_2\{4\}$	Stat.	Syst.
0.00 - 2.00	0.0127	± 0.0132	± 0.0094
2.00 - 3.00	0.0602	± 0.0144	± 0.0058
3.00 - 4.00	0.0610	± 0.0226	± 0.0051
4.00 - 5.00	0.0380	± 0.0284	± 0.0054
5.00 - 6.00	0.0477	± 0.0354	± 0.0030
6.00 - 8.00	0.0533	± 0.0266	± 0.0023
8.00 - 10.00	0.0286	± 0.0513	± 0.0034

TABLE B.4 – v_2 vs. p_T with finer p_T binning.

p_T (GeV/ c)	$v_2\{SP\}$	Stat.	Syst.
1 - 2	0.0343	± 0.0047	± 0.0028
2 - 3	0.0749	± 0.0049	± 0.0048
3 - 5	0.0855	± 0.0047	± 0.0013
5 - 15	0.0814	± 0.0058	± 0.0035

TABLE B.5 – $v_2\{2\}$ vs.
 p_T intervals.

p_T (GeV/ c)	$v_2\{4\}$	Stat.	Syst.
1 - 2	0.0103	± 0.0127	± 0.0106
2 - 3	0.0602	± 0.0144	± 0.0058
3 - 5	0.0634	± 0.0135	± 0.0061
5 - 15	0.0506	± 0.0179	± 0.0026

TABLE B.6 – $v_2\{4\}$ vs.
 p_T intervals.**Values of the fluctuation ratio and flow fluctuations**

Pb-Pb collisions, 10-30% centrality									
p_T [GeV/ c]	$v_2\{SP\}$	Stat	Sys	$v_2\{4\}$	Stat	Sys	F	Stat	Sys
Kaon (CMS) - $\sqrt{s_{NN}} = 5.02$ TeV, $ y < 1.0$									
1.0 - 1.4	0.1090	0.0005	0.0038	0.0917	0.0002	0.0039	0.6417	0.0100	0.1045
1.4 - 1.8	0.1329	0.0003	0.0047	0.1163	0.0002	0.0049	0.5517	0.0068	0.1148
1.8 - 2.2	0.1503	0.0003	0.0053	0.1330	0.0001	0.0056	0.5266	0.0059	0.1185
2.2 - 2.8	0.1673	0.0004	0.0059	0.1466	0.0002	0.0062	0.5508	0.0056	0.1150
2.8 - 3.6	0.1762	0.0006	0.0062	0.1538	0.0002	0.0065	0.5588	0.0079	0.1138
3.6 - 4.6	0.1675	0.0010	0.0059	0.1444	0.0004	0.0061	0.5868	0.0140	0.1103
4.6 - 6.0	0.1402	0.0017	0.0049	0.1176	0.0007	0.0049	0.6491	0.0274	0.1040
6.0 - 7.0	0.1214	0.0035	0.0043	0.0934	0.0021	0.0039	0.8306	0.0665	0.0940
7.0 - 8.5	0.1056	0.0043	0.0037	0.0772	0.0018	0.0032	0.9329	0.0880	0.0922
Λ (CMS) - $\sqrt{s_{NN}} = 5.02$ TeV, $ y < 1.0$									
1.8 - 2.2	0.1521	0.0009	0.0087	0.1179	0.0005	0.0065	0.8140	0.0131	0.1419
2.2 - 2.8	0.1850	0.0006	0.0105	0.1529	0.0003	0.0084	0.6807	0.0076	0.1515
2.8 - 3.6	0.2241	0.0007	0.0128	0.1881	0.0002	0.0103	0.6478	0.0070	0.1551
3.6 - 4.6	0.2420	0.0010	0.0138	0.2061	0.0005	0.0113	0.6147	0.0103	0.1596
4.6 - 6.0	0.2259	0.0019	0.0129	0.2002	0.0008	0.0110	0.5222	0.0219	0.1767
6.0 - 7.0	0.1809	0.0047	0.0103	0.1642	0.0019	0.0090	0.4625	0.0731	0.1928
7.0 - 8.5	0.1492	0.0068	0.0085	0.1187	0.0045	0.0065	0.7623	0.1105	0.1447
J/ψ (ALICE) - $\sqrt{s_{NN}} = 5.36$ TeV, $2.5 < y < 4$									This thesis
1.0 - 2.0	0.0343	0.0047	0.0028	0.0063	0.0151	0.0101	0.9666	0.1570	0.1055
2.0 - 3.0	0.0749	0.0049	0.0048	0.0571	0.0157	0.0052	0.5153	0.2551	0.1000
3.0 - 5.0	0.0855	0.0047	0.0013	0.0598	0.0161	0.0070	0.5859	0.2067	0.0886
5.0 - 15.0	0.0814	0.0058	0.0035	0.0551	0.0209	0.0027	0.6091	0.2728	0.0460

TABLE B.7 – Combined measurements: $v_{2\{SP\}}$ (single-particle), $v_{2\{4\}}$ (4-particle cumulant), and F (fluctuation ratio) with statistical and systematic uncertainties. Data from CMS (Kaon & Λ at $\sqrt{s_{NN}} = 5.02$ TeV) and ALICE (J/ψ at $\sqrt{s_{NN}} = 5.36$ TeV) for 10–30% centrality.

Pb-Pb collisions, 10-30% centrality			
p_T [GeV/c]	σ	Stat	Sys
Kaon (CMS) - $\sqrt{s_{NN}} = 5.02$ TeV, $y < 1.0$			
1.0 - 1.4	0.058856	0.000907	0.009261
1.4 - 1.8	0.064183	0.000784	0.013086
1.8 - 2.2	0.070022	0.000777	0.015483
2.2 - 2.8	0.080723	0.000814	0.016511
2.8 - 3.6	0.085967	0.001207	0.017135
3.6 - 4.6	0.084752	0.002012	0.015526
4.6 - 6.0	0.076327	0.003192	0.011800
6.0 - 7.0	0.077561	0.005962	0.008156
7.0 - 8.5	0.072023	0.006577	0.006440
Λ (CMS) - $\sqrt{s_{NN}} = 5.02$ TeV, $y < 1.0$			
1.8 - 2.2	0.095994	0.001494	0.015880
2.2 - 2.8	0.104073	0.001148	0.022439
2.8 - 3.6	0.121829	0.001305	0.028400
3.6 - 4.6	0.126711	0.002099	0.032153
4.6 - 6.0	0.104569	0.004368	0.034910
6.0 - 7.0	0.075942	0.011972	0.031378
7.0 - 8.5	0.090442	0.012657	0.016431
J/ψ (ALICE) - $\sqrt{s_{NN}} = 5.36$ TeV, $2.5 < y < 4$			This thesis
1.0 - 2.0	0.033701	0.005596	0.003438
2.0 - 3.0	0.048511	0.019974	0.009541
3.0 - 5.0	0.061105	0.017048	0.007072
5.0 - 15.0	0.059849	0.020763	0.005328

TABLE B.8 – Combined flow fluctuation measurements σ calculated as $\sigma \equiv \sqrt{v_{2\{SP\}}^2 - v_{2\{4\}}^2}$ with statistical and systematic uncertainties. Data from CMS (Kaon & Λ at $\sqrt{s_{NN}} = 5.02$ TeV) and ALICE (J/ ψ at $\sqrt{s_{NN}} = 5.36$ TeV) for 10–30% centrality.

Appendix C

Cold nuclear matter effects and nPDF

Structure function calculation

The structure function $F_2(x)$ for a nucleon is given by:

$$F_2(x) = x \sum_q e_q^2 [f_q(x) + f_{\bar{q}}(x)] \quad (\text{C.1})$$

where $f_q(x)$, $f_{\bar{q}}(x)$ are the parton distribution functions (PDFs) for quarks and antiquarks, and e_q is the quark charge fraction in units of e . For the proton:

$$F_2^p(x) = x \left[\frac{4}{9}(f_u(x) + f_{\bar{u}}(x)) + \frac{1}{9}(f_d(x) + f_{\bar{d}}(x)) + \frac{1}{9}(f_s(x) + f_{\bar{s}}(x)) \right] \quad (\text{C.2})$$

and for the neutron (using isospin symmetry):

$$F_2^n(x) = x \left[\frac{4}{9}(f_d(x) + f_{\bar{d}}(x)) + \frac{1}{9}(f_u(x) + f_{\bar{u}}(x)) + \frac{1}{9}(f_s(x) + f_{\bar{s}}(x)) \right] \quad (\text{C.3})$$

Subtracting the two gives:

$$F_2^p(x) - F_2^n(x) = \frac{1}{3}x [f_u(x) - f_d(x) + f_{\bar{u}}(x) - f_{\bar{d}}(x)] \quad (\text{C.4})$$

Dividing by x and integrating over $x \in [0, 1]$:

$$\int_0^1 [F_2^p(x) - F_2^n(x)] \frac{dx}{x} = \frac{1}{3} \int_0^1 [f_u(x) - f_d(x) + f_{\bar{u}}(x) - f_{\bar{d}}(x)] dx \quad (\text{C.5})$$

Apply the valence quark number sum rules (for the proton: $\int f_u(x)dx = 2$ and $\int f_d(x)dx = 1$). Thus the expression becomes:

$$\int_0^1 [F_2^p(x) - F_2^n(x)] \frac{dx}{x} = \frac{1}{3} - \frac{2}{3} \int_0^1 [f_{\bar{d}}(x) - f_{\bar{u}}(x)] dx \quad (\text{C.6})$$

This is the modified Gottfried sum rule [262], which shows that any deviation of the left-hand side from $\frac{1}{3}$ (a quantity that can be experimentally measured) indicates a sea quark asymmetry, $f_{\bar{d}}(x) \neq f_{\bar{u}}(x)$.

Additional nPDF figures

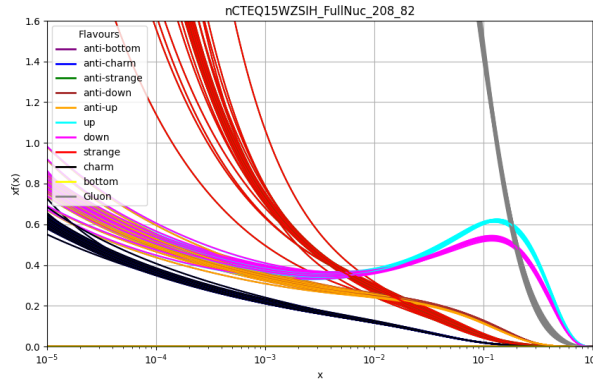
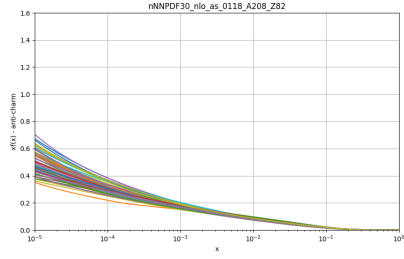
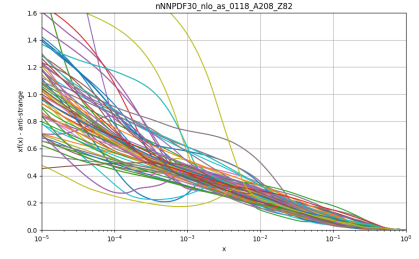


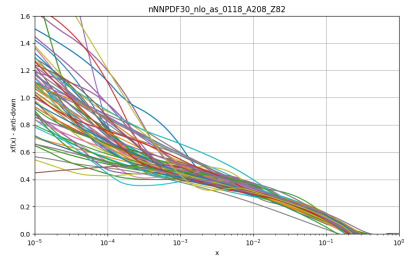
FIGURE C.1 – Each line in the plot represents a different replica of the nCTEQ nPDFs for Pb (evaluated at $Q = 10$ GeV). The curves correspond to nPDFs for various parton flavors, illustrating the spread and uncertainty associated with the nPDF determination for each flavor.



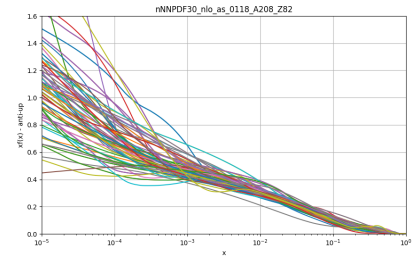
(A) Anticharm



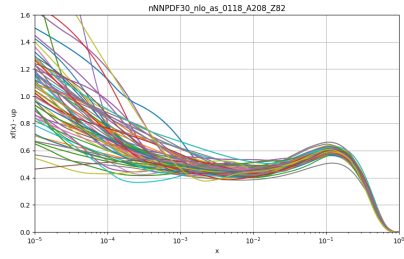
(B) Antistrange



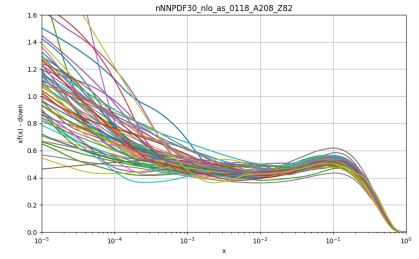
(C) Antidown



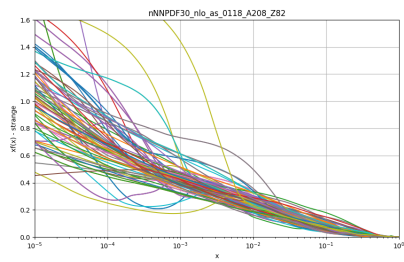
(D) Antiup



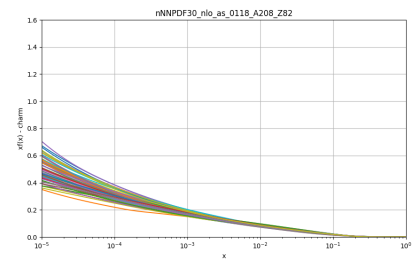
(E) Up



(F) Down



(G) Strange



(H) Charm

FIGURE C.2 – nNNPDF nuclear PDFs (nNNPDF30_nlo_as_0118_A208_Z82) for various quark flavors at $Q = 10$ GeV. Each panel shows the distribution for one flavor.

Bibliography

- [1] S. et al.(Particle Data Group) Navas. *Phys. Rev. D* 030001.110 (2024).
- [2] S. Weinberg. “A Model of Leptons”. *Phys. Rev. Lett.* 19 (1967), 1264–1266. DOI: [10.1103/PhysRevLett.19.1264](https://doi.org/10.1103/PhysRevLett.19.1264).
- [3] C. N. Yang and R. L. Mills. “Conservation of Isotopic Spin and Isotopic Gauge Invariance”. *Phys. Rev.* 96 (1954), 191–195. DOI: [10.1103/PhysRev.96.191](https://doi.org/10.1103/PhysRev.96.191).
- [4] A. Salam. “Weak and Electromagnetic Interactions”. *Conf. Proc. C* 680519 (1968), 367–377.
- [5] P. W. Higgs. “Broken Symmetries and the Masses of Gauge Bosons”. *Phys. Rev. Lett.* 13 (1964), 508–509. DOI: [10.1103/PhysRevLett.13.508](https://doi.org/10.1103/PhysRevLett.13.508).
- [6] J. Goldstone. “Broken Symmetries”. *Phys. Rev.* 127.3 (Aug. 1962), 965–970. DOI: [10.1103/PhysRev.127.965](https://doi.org/10.1103/PhysRev.127.965). URL: <https://link.aps.org/doi/10.1103/PhysRev.127.965>.
- [7] J. M. Butterworth. “The Standard Model: how far can it go and how can we tell?” *Philosophical Transactions of the Royal Society A* 374.2075 (2016), 20150249. DOI: [10.1098/rsta.2015.0249](https://doi.org/10.1098/rsta.2015.0249).
- [8] Walter Greiner, Stefan Schramm, and Eckhart Stein. *Quantum Chromodynamics; 3rd ed.* Berlin: Springer, 2007.
- [9] Michael E. Peskin and Daniel V. Schroeder. *An Introduction to Quantum Field Theory*. Includes exercises. Boulder, CO: Westview, 1995.
- [10] M. Gell-Mann. “A Schematic Model of Baryons and Mesons”. *Phys. Lett.* 8 (1964), 214–215. DOI: [10.1016/S0031-9163\(64\)92001-3](https://doi.org/10.1016/S0031-9163(64)92001-3).
- [11] C. N. Yang and R. L. Mills. “Conservation of Isotopic Spin and Isotopic Gauge Invariance”. *Phys. Rev.* 96 (1954), 191–195. DOI: [10.1103/PhysRev.96.191](https://doi.org/10.1103/PhysRev.96.191).
- [12] R. Katz. *Thesis on QCD and Particle Physics*. PhD Thesis. 2015.
- [13] H. D. Politzer. “Reliable Perturbative Results for Strong Interactions?” *Phys. Rev. Lett.* 30 (1973), 1346–1349. DOI: [10.1103/PhysRevLett.30.1346](https://doi.org/10.1103/PhysRevLett.30.1346).

- [14] K. G. Wilson. “Confinement of Quarks”. *Phys. Rev. D* 10 (1974), 2445–2459. DOI: [10.1103/PhysRevD.10.2445](https://doi.org/10.1103/PhysRevD.10.2445).
- [15] M. Tanabashi. et al. “Review of Particle Physics”. *Phys. Rev. D* 98 (3 Aug. 2018), 030001. DOI: [10.1103/PhysRevD.98.030001](https://doi.org/10.1103/PhysRevD.98.030001). URL: <https://link.aps.org/doi/10.1103/PhysRevD.98.030001>.
- [16] R. Aaij et al. “Observation of an exotic narrow doubly charmed tetraquark”. *Nature Physics* 18.7 (June 2022), 751–754. ISSN: 1745-2481. DOI: [10.1038/s41567-022-01614-y](https://doi.org/10.1038/s41567-022-01614-y). URL: <http://dx.doi.org/10.1038/s41567-022-01614-y>.
- [17] R. Aaij et al. “Observation of $J/\psi p$ Resonances Consistent with Pentaquark States in $\Lambda_b^0 \rightarrow J/\psi K^- p$ Decays”. *Phys. Rev. Lett.* 115 (7 Aug. 2015), 072001. DOI: [10.1103/PhysRevLett.115.072001](https://doi.org/10.1103/PhysRevLett.115.072001). URL: <https://link.aps.org/doi/10.1103/PhysRevLett.115.072001>.
- [18] CMS Collaboration. “Observation of a pseudoscalar excess at the top quark pair production threshold”. *Reports on Progress in Physics* 88.8 (Aug. 2025), 087801. ISSN: 1361-6633. DOI: [10.1088/1361-6633/adf7d3](https://doi.org/10.1088/1361-6633/adf7d3). URL: <http://dx.doi.org/10.1088/1361-6633/adf7d3>.
- [19] A. Bazavov et al. “Chiral and deconfinement aspects of the QCD transition”. *Phys. Rev. D* 85 (2012), 054503. DOI: [10.1103/PhysRevD.85.054503](https://doi.org/10.1103/PhysRevD.85.054503).
- [20] Owe Philipsen. “The QCD equation of state from the lattice”. *Progress in Particle and Nuclear Physics* 70 (May 2013), 55–107. ISSN: 0146-6410. DOI: [10.1016/j.pnpnp.2012.09.003](https://doi.org/10.1016/j.pnpnp.2012.09.003). URL: <http://dx.doi.org/10.1016/j.pnpnp.2012.09.003>.
- [21] K. Fukushima and T. Hatsuda. “The phase diagram of dense QCD”. *Rept. Prog. Phys.* 74 (2011), 014001. DOI: [10.1088/0034-4885/74/1/014001](https://doi.org/10.1088/0034-4885/74/1/014001).
- [22] N. Cabibbo and G. Parisi. “Exponential hadronic spectrum and quark liberation”. *Physics Letters B* 59.1 (1975), 67–69. ISSN: 0370-2693. DOI: [10.1016/0370-2693\(75\)90158-6](https://doi.org/10.1016/0370-2693(75)90158-6). URL: <https://www.sciencedirect.com/science/article/pii/0370269375901586>.
- [23] N. Cabibbo and G. Parisi. “Exponential hadronic spectrum and quark liberation”. *Phys. Lett. B* 59 (1975), 67.
- [24] Tapan K. Nayak. *Quark-Gluon Plasma: Present and Future*. 2008. arXiv: [0804.1368](https://arxiv.org/abs/0804.1368) [nucl-ex]. URL: <https://arxiv.org/abs/0804.1368>.

- [25] B. Author. *QCD phase diagram*. Reference for phase diagram. 2020.
- [26] P. Braun-Munzinger, V. Koch, T. Schaefer, and J. Stachel. “Properties of hot and dense matter from relativistic heavy ion collisions”. *Phys. Rept.* 621 (2016), 76–126. DOI: [10.1016/j.physrep.2015.12.003](https://doi.org/10.1016/j.physrep.2015.12.003).
- [27] E. Shuryak. “Strongly coupled quark-gluon plasma in heavy ion collisions”. *Rev. Mod. Phys.* 89 (2017), 035001. DOI: [10.1103/RevModPhys.89.035001](https://doi.org/10.1103/RevModPhys.89.035001).
- [28] S. Borsanyi et al. “Is there still any T_c mystery in lattice QCD? Results with physical masses in the continuum limit III”. *JHEP* 09 (2010), 073. DOI: [10.1007/JHEP09\(2010\)073](https://doi.org/10.1007/JHEP09(2010)073).
- [29] Fernando G. Gardim, Giuliano Giacalone, Matthew Luzum, and Jean-Yves Ollitrault. “Thermodynamics of hot strong-interaction matter from ultrarelativistic nuclear collisions”. *Nature Physics* 16.6 (Mar. 2020), 615–619. ISSN: 1745-2481. DOI: [10.1038/s41567-020-0846-4](https://doi.org/10.1038/s41567-020-0846-4). URL: <http://dx.doi.org/10.1038/s41567-020-0846-4>.
- [30] Marek Gazdzicki and Mark I. Gorenstein. *On the Early Stage of Nucleus–Nucleus Collisions*. 1998. arXiv: [hep-ph/9803462](https://arxiv.org/abs/hep-ph/9803462) [hep-ph]. URL: <https://arxiv.org/abs/hep-ph/9803462>.
- [31] Mark I. Gorenstein. *Signals of Deconfinement Transition in Nucleus-Nucleus Collisions*. 2003. arXiv: [hep-ph/0310269](https://arxiv.org/abs/hep-ph/0310269) [hep-ph]. URL: <https://arxiv.org/abs/hep-ph/0310269>.
- [32] J. Adams et al. (STAR Collaboration). “Experimental and theoretical challenges in the search for the quark–gluon plasma: The STAR Collaboration’s critical assessment of the evidence from RHIC collisions”. *Nucl. Phys. A* 757 (2005), 102–183. DOI: [10.1016/j.nuclphysa.2005.03.085](https://doi.org/10.1016/j.nuclphysa.2005.03.085).
- [33] K. Adcox et al. (PHENIX Collaboration). “Formation of dense partonic matter in relativistic nucleus–nucleus collisions at RHIC: Experimental evaluation by the PHENIX Collaboration”. *Nucl. Phys. A* 757 (2005), 184–283. DOI: [10.1016/j.nuclphysa.2005.03.086](https://doi.org/10.1016/j.nuclphysa.2005.03.086).
- [34] I. Arsene et al. “Quark gluon plasma and color glass condensate at RHIC? The Perspective from the BRAHMS experiment”. *Nucl. Phys. A* 757 (2005), 1–27. DOI: [10.1016/j.nuclphysa.2005.02.130](https://doi.org/10.1016/j.nuclphysa.2005.02.130).

- [35] ALICE collaboration. “Charged-Particle Multiplicity Density at Midrapidity in Central Pb-Pb Collisions at $\sqrt{s_{NN}} = 2.76$ TeV”. *Physical Review Letters* 105.25 (Dec. 2010). ISSN: 1079-7114. DOI: [10.1103/physrevlett.105.252301](https://doi.org/10.1103/physrevlett.105.252301). URL: <http://dx.doi.org/10.1103/PhysRevLett.105.252301>.
- [36] ALICE collaboration. “Elliptic flow of charged particles in Pb–Pb collisions at $\sqrt{s_{NN}} = 2.76$ TeV”. *Physical Review Letters* 105.25 (Dec. 2010). ISSN: 1079-7114. DOI: [10.1103/physrevlett.105.252302](https://doi.org/10.1103/physrevlett.105.252302). URL: <http://dx.doi.org/10.1103/PhysRevLett.105.252302>.
- [37] Michael L. Miller, Klaus Reygers, Stephen J. Sanders, and Peter Steinberg. “Glauber Modeling in High-Energy Nuclear Collisions”. *Annual Review of Nuclear and Particle Science* 1 (Nov. 2007), 205–243. DOI: [10.1146/annurev.nucl.57.090506.123020](https://doi.org/10.1146/annurev.nucl.57.090506.123020). URL: <https://arxiv.org/abs/nucl-ex/0701025>.
- [38] Larry McLerran and Raju Venugopalan. “Computing quark and gluon distribution functions for very large nuclei”. *Phys. Rev. D* 49 (1994), 2233–2241. DOI: [10.1103/PhysRevD.49.2233](https://doi.org/10.1103/PhysRevD.49.2233). arXiv: [hep-ph/9309289](https://arxiv.org/abs/hep-ph/9309289) [hep-ph].
- [39] J. J. Ethier and E. R. Nocera. “Parton Distributions in Nucleons and Nuclei”. *Ann. Rev. Nucl. Part. Sci.* 70 (2020), 43–76. DOI: [10.1146/annurev-nucl-011720-042725](https://doi.org/10.1146/annurev-nucl-011720-042725).
- [40] V. N. Gribov and L. N. Lipatov. “Deep inelastic e p scattering in perturbation theory”. *Sov. J. Nucl. Phys.* 15 (1972). IPTI-381-71, 438–450.
- [41] M. B. Einhorn and S. D. Ellis. “Hadronic Production of the New Resonances: Probing Gluon Distributions”. *Phys. Rev. D* 12 (1975), 2007. DOI: [10.1103/PhysRevD.12.2007](https://doi.org/10.1103/PhysRevD.12.2007).
- [42] L. A. Harland-Lang, A. D. Martin, P. Motylinski, and R. S. Thorne. “Parton distributions in the LHC era: MMHT 2014 PDFs”. *Eur. Phys. J. C* 75 (2015), 204. DOI: [10.1140/epjc/s10052-015-3397-6](https://doi.org/10.1140/epjc/s10052-015-3397-6). arXiv: [1412.3989](https://arxiv.org/abs/1412.3989).
- [43] J. Pumplin, D. R. Stump, J. Huston, H. L. Lai, P. M. Nadolsky, and W. K. Tung. “New generation of parton distributions with uncertainties from global QCD analysis”. *JHEP* 07 (2002), 012. DOI: [10.1088/1126-6708/2002/07/012](https://doi.org/10.1088/1126-6708/2002/07/012). arXiv: [hep-ph/0201195](https://arxiv.org/abs/hep-ph/0201195).
- [44] S. Dulat et al. “New parton distribution functions from a global analysis of quantum chromodynamics”. *Phys. Rev. D* 93 (2016), 033006. DOI: [10.1103/PhysRevD.93.033006](https://doi.org/10.1103/PhysRevD.93.033006). arXiv: [1506.07443](https://arxiv.org/abs/1506.07443).

- [45] R. D. Ball et al. [NNPDF Collaboration]. “Parton distributions from high-precision collider data”. *Eur. Phys. J. C* 77 (2017), 663. DOI: [10.1140/epjc/s10052-017-5199-5](https://doi.org/10.1140/epjc/s10052-017-5199-5). arXiv: [1706.00428](https://arxiv.org/abs/1706.00428).
- [46] Tie-Jiun Hou et al. “New CTEQ global analysis of quantum chromodynamics with high-precision data from the LHC”. *Phys. Rev. D* 103.1 (2021), 014013. DOI: [10.1103/PhysRevD.103.014013](https://doi.org/10.1103/PhysRevD.103.014013). arXiv: [1912.10053](https://arxiv.org/abs/1912.10053) [hep-ph].
- [47] Y. L. Dokshitzer. “Calculation of the Structure Functions for Deep Inelastic Scattering and e^+e^- Annihilation by Perturbation Theory in Quantum Chromodynamics”. *Sov. Phys. JETP* 46 (1977), 641–653.
- [48] V. N. Gribov and L. N. Lipatov. “Deep inelastic $e p$ scattering in perturbation theory”. *Sov. J. Nucl. Phys.* 15 (1972). IPTI-381-71, 438–450.
- [49] G. Altarelli and G. Parisi. “Asymptotic Freedom in Parton Language”. *Nucl. Phys. B* 126 (1977), 298–318. DOI: [10.1016/0550-3213\(77\)90384-4](https://doi.org/10.1016/0550-3213(77)90384-4).
- [50] N. Armesto. “Nuclear shadowing”. *J. Phys. G* 32 (2006), R367–R394. DOI: [10.1088/0954-3899/32/11/R01](https://doi.org/10.1088/0954-3899/32/11/R01).
- [51] Rabah Abdul Khalek, Rhorry Gauld, Tommaso Giani, Emanuele R. Nocera, Tanjona R. Rabemananjara, and Juan Rojo. *NNPDF3.0: Evidence for a modified partonic structure in heavy nuclei*. 2022. arXiv: [2201.12363](https://arxiv.org/abs/2201.12363) [hep-ph]. URL: <https://arxiv.org/abs/2201.12363>.
- [52] LHCb Collaboration. “Study of prompt D^0 meson production in pPb collisions at $\sqrt{s_{NN}} = 5$ TeV”. *Journal of High Energy Physics* 2017.10 (Oct. 2017), 90. ISSN: 1029-8479. DOI: [10.1007/JHEP10\(2017\)090](https://doi.org/10.1007/JHEP10(2017)090). URL: [http://dx.doi.org/10.1007/JHEP10\(2017\)090](http://dx.doi.org/10.1007/JHEP10(2017)090).
- [53] François Arleo, Greg Jackson, and Stéphane Peigné. “Impact of fully coherent energy loss on heavy meson production in pA collisions”. *Journal of High Energy Physics* 2022.1 (Jan. 2022). ISSN: 1029-8479. DOI: [10.1007/jhep01\(2022\)164](https://doi.org/10.1007/jhep01(2022)164). URL: [http://dx.doi.org/10.1007/JHEP01\(2022\)164](http://dx.doi.org/10.1007/JHEP01(2022)164).
- [54] François Arleo, Stéphane Peigné, and Taklit Sami. “Revisiting scaling properties of medium-induced gluon radiation”. *Physical Review D* 83.11 (June 2011). ISSN: 1550-2368. DOI: [10.1103/physrevd.83.114036](https://doi.org/10.1103/physrevd.83.114036). URL: <http://dx.doi.org/10.1103/PhysRevD.83.114036>.

- [55] F. Arleo and S. Peigné. “Disentangling Shadowing from Coherent Energy Loss using the Drell-Yan Process”. *Phys. Rev. D* 95 (2017), 011502. DOI: [10.1103/PhysRevD.95.011502](#). arXiv: [1512.01794 \[hep-ph\]](#).
- [56] Nicolas Bize. “Étude de la production de charmonia dans les collisions pp et études de performances du spectromètre à muons et du MFT avec le détecteur ALICE”. Theses. Nantes Université, Oct. 2024. URL: <https://theses.hal.science/tel-05017971>.
- [57] J. D. Bjorken. “Highly Relativistic Nucleus-Nucleus Collisions: The Central Rapidity Region”. *Phys. Rev. D* 27 (1983), 140–151. DOI: [10.1103/PhysRevD.27.140](#).
- [58] G. Altarelli and G. Parisi. “Asymptotic Freedom in Parton Language”. *Nucl. Phys. B* 126 (1977), 298–318. DOI: [10.1016/0550-3213\(77\)90384-4](#).
- [59] B. Hippolyte. “Production de hadrons légers et Plasma de Quarks et de Gluons au LHC (2005).” ().
- [60] Y. Mehtar-Tani, J. G. Milhano, and K. Tywoniuk. “Jet physics in heavy-ion collisions”. *Int. J. Mod. Phys. A* 28 (2013), 1340013. DOI: [10.1142/S0217751X13400137](#).
- [61] D. H. Rischke. “The Quark gluon plasma in equilibrium”. *Prog. Part. Nucl. Phys.* 52 (2004), 197–296. DOI: [10.1016/j.pnpnp.2003.09.002](#).
- [62] MADAI Collaboration, Hannah Petersen, and Jonah Bernhard.
- [63] T. Lappi and L. McLerran. “Some features of the glasma”. *Nucl. Phys. A* 772 (2006), 200–212. DOI: [10.1016/j.nuclphysa.2006.04.001](#).
- [64] Rainer J Fries. “Early time evolution of high-energy heavy-ion collisions”. *Journal of Physics G: Nuclear and Particle Physics* 34.8 (July 2007), S851–S854. ISSN: 1361-6471. DOI: [10.1088/0954-3899/34/8/s111](#). URL: <http://dx.doi.org/10.1088/0954-3899/34/8/S111>.
- [65] J. Rafelski and B. Müller. “Strangeness Production in the Quark-Gluon Plasma”. *Phys. Rev. Lett.* 48 (1982), 1066. DOI: [10.1103/PhysRevLett.48.1066](#).
- [66] J. Adam et al. (ALICE Collaboration). “Enhanced production of multi-strange hadrons in high-multiplicity proton–proton collisions”. *Nature Phys.* 13 (2017), 535–539. DOI: [10.1038/nphys4111](#).

- [67] M. Gyulassy, I. Vitev, X.-N. Wang, and B.-W. Zhang. “Jet quenching and radiative energy loss in dense nuclear matter”. *Quark Gluon Plasma* 3 (2003), 123–191. DOI: [10.1142/9789812795533_0003](https://doi.org/10.1142/9789812795533_0003).
- [68] A. Andronic et al. “Heavy-flavour and quarkonium production in the LHC era: from proton–proton to heavy-ion collisions”. *Eur. Phys. J. C* 76 (2016), 107. DOI: [10.1140/epjc/s10052-015-3819-5](https://doi.org/10.1140/epjc/s10052-015-3819-5).
- [69] Edward Shuryak. “Theory of hadron plasma”. *Sov. Phys. JETP* 47.2 (1978), 212–219.
- [70] L. D. Landau. “On the multiparticle production in high-energy collisions”. *Izv. Akad. Nauk Ser. Fiz.* 17 (1953), 51–64.
- [71] Satyendra Nath Bose. “Plancks Gesetz und Lichtquantenhypothese”. *Zeitschrift für Physik* 26 (1924), 178–181. DOI: [10.1007/BF01327326](https://doi.org/10.1007/BF01327326).
- [72] Albert Einstein. “Quantentheorie des einatomigen idealen Gases”. *Sitzungsberichte der Preußischen Akademie der Wissenschaften* (1924), 261–267.
- [73] Enrico Fermi. “Zur Quantelung des idealen einatomigen Gases”. *Zeitschrift für Physik* 36 (1926), 902–912. DOI: [10.1007/BF01400221](https://doi.org/10.1007/BF01400221).
- [74] Paul A. M. Dirac. “On the Theory of Quantum Mechanics”. *Proc. R. Soc. Lond. A* 112 (1926), 661–677. DOI: [10.1098/rspa.1926.0133](https://doi.org/10.1098/rspa.1926.0133).
- [75] R. K. Pathria and Paul D. Beale. *Statistical Mechanics*. 3rd. Elsevier, 2011.
- [76] Steven Weinberg. *Gravitation and Cosmology: Principles and Applications of the General Theory of Relativity*. Wiley, 1972.
- [77] Paul Romatschke and Ulrike Romatschke. *Relativistic Fluid Dynamics In and Out of Equilibrium – Ten Years of Progress in Theory and Numerical Simulations of Nuclear Collisions*. 2019. arXiv: [1712.05815 \[nucl-th\]](https://arxiv.org/abs/1712.05815). URL: <https://arxiv.org/abs/1712.05815>.
- [78] Jean-Yves Ollitrault. “Relativistic hydrodynamics for heavy-ion collisions”. *European Journal of Physics* 29.2 (Jan. 2008), 275–302. DOI: [10.1088/0143-0807/29/2/010](https://doi.org/10.1088/0143-0807/29/2/010). URL: <https://arxiv.org/abs/0708.2433>.
- [79] Carlo Cercignani. *The Boltzmann Equation and Its Applications*. Berlin: Springer, 1988.

- [80] W. Israel and J. M. Stewart. “Transient relativistic thermodynamics and kinetic theory”. *Ann. Phys.* 118 (1979), 341–372. DOI: [10.1016/0003-4916\(79\)90130-1](https://doi.org/10.1016/0003-4916(79)90130-1).
- [81] R. E. Tribble. *NSAC Long Range Plan*. NSAC reference. 2013.
- [82] P. Danielewicz and M. Gyulassy. “Dissipative phenomena in quark-gluon plasmas”. *Phys. Rev. D* 31 (1 Jan. 1985), 53–62. DOI: [10.1103/PhysRevD.31.53](https://doi.org/10.1103/PhysRevD.31.53). URL: <https://link.aps.org/doi/10.1103/PhysRevD.31.53>.
- [83] Pavel Kovtun, Dam T. Son, and Andrei O. Starinets. “Viscosity in strongly interacting quantum field theories from black hole physics”. *Phys. Rev. Lett.* 94 (2005), 111601. DOI: [10.1103/PhysRevLett.94.111601](https://doi.org/10.1103/PhysRevLett.94.111601). arXiv: [hep-th/0405231](https://arxiv.org/abs/hep-th/0405231) [hep-th].
- [84] U. Heinz and R. Snellings. “Collective flow and viscosity in relativistic heavy-ion collisions”. *Ann. Rev. Nucl. Part. Sci.* 63 (2013), 123–151. DOI: [10.1146/annurev-nucl-102212-170540](https://doi.org/10.1146/annurev-nucl-102212-170540).
- [85] Aleksi Kurkela and Yan Zhu. “Isotropization and hydrodynamization in weakly coupled heavy-ion collisions”. *Phys. Rev. Lett.* 115.18 (2015), 182301. DOI: [10.1103/PhysRevLett.115.182301](https://doi.org/10.1103/PhysRevLett.115.182301).
- [86] G Jackson and A Peshier. “Re-running the QCD shear viscosity”. *Journal of Physics G: Nuclear and Particle Physics* 45.9 (July 2018), 095001. ISSN: 1361-6471. DOI: [10.1088/1361-6471/aad374](https://doi.org/10.1088/1361-6471/aad374). URL: <http://dx.doi.org/10.1088/1361-6471/aad374>.
- [87] K. H. Ackermann et al. “Elliptic Flow in Au+Au Collisions at $\sqrt{s_{NN}} = 130$ GeV”. *Physical Review Letters* 86.3 (Jan. 2001), 402–407. ISSN: 1079-7114. DOI: [10.1103/physrevlett.86.402](https://doi.org/10.1103/physrevlett.86.402). URL: <http://dx.doi.org/10.1103/PhysRevLett.86.402>.
- [88] J. Berges, M. P. Heller, A. Mazeliauskas, and R. Venugopalan. “QCD thermalization: Ab initio approaches and interdisciplinary connections”. *Rev. Mod. Phys.* 93.3 (2021), 035003. DOI: [10.1103/RevModPhys.93.035003](https://doi.org/10.1103/RevModPhys.93.035003).
- [89] Chun Shen and Li Yan. “Recent development of hydrodynamic modeling in heavy-ion collisions”. *Nucl. Sci. Tech.* 31.12 (Oct. 2020), 122. DOI: [10.1007/s41365-020-00829-z](https://doi.org/10.1007/s41365-020-00829-z).
- [90] L. D. Landau and E. M. Lifshitz. *Fluid Mechanics*. Vol. 6. Pergamon Press, 1987.

- [91] “Extracting the speed of sound in quark–gluon plasma with ultrarelativistic lead–lead collisions at the LHC”. *Reports on Progress in Physics* 87.7 (June 2024), 077801. ISSN: 1361-6633. DOI: [10.1088/1361-6633/ad4b9b](https://doi.org/10.1088/1361-6633/ad4b9b). URL: <http://dx.doi.org/10.1088/1361-6633/ad4b9b>.
- [92] “Assessing the speed of sound in Pb–Pb collisions with ALICE” (2024).
- [93] Govert Nijs and Wilke van der Schee. *Predictions and postdictions for relativistic lead and oxygen collisions with Trajectum*. 2021. arXiv: [2110.13153](https://arxiv.org/abs/2110.13153) [nucl-th]. URL: <https://arxiv.org/abs/2110.13153>.
- [94] A. Bazavov et al. “Equation of state in (2+1)-flavor QCD”. *Phys. Rev. D* 90 (2014), 094503. DOI: [10.1103/PhysRevD.90.094503](https://doi.org/10.1103/PhysRevD.90.094503).
- [95] S. Voloshin and Y. Zhang. “Flow study in relativistic nuclear collisions by Fourier expansion of Azimuthal particle distributions”. *Z. Phys. C* 70 (1996), 665–672. DOI: [10.1007/s002880050141](https://doi.org/10.1007/s002880050141).
- [96] ALICE Collaboration. *Long-range transverse momentum correlations and radial flow in Pb–Pb collisions at the LHC*. 2025. arXiv: [2504.04796](https://arxiv.org/abs/2504.04796) [nucl-ex]. URL: <https://arxiv.org/abs/2504.04796>.
- [97] E. Schnedermann, J. Sollfrank, and U. Heinz. “Thermal phenomenology of hadrons from 200-A/GeV S+S collisions”. *Phys. Rev. C* 48 (1993), 2462–2475. DOI: [10.1103/PhysRevC.48.2462](https://doi.org/10.1103/PhysRevC.48.2462). arXiv: [nuc1-th/9307020](https://arxiv.org/abs/nuc1-th/9307020). URL: <https://journals.aps.org/prc/abstract/10.1103/PhysRevC.48.2462>.
- [98] J.-Y. Ollitrault. “Anisotropy as a signature of transverse collective flow”. *Phys. Rev. D* 46 (1992), 229–245. DOI: [10.1103/PhysRevD.46.229](https://doi.org/10.1103/PhysRevD.46.229).
- [99] Derek Teaney and Li Yan. “Triangularity and dipole asymmetry in relativistic heavy ion collisions”. *Physical Review C* 83.6 (June 2011). ISSN: 1089-490X. DOI: [10.1103/physrevc.83.064904](https://doi.org/10.1103/physrevc.83.064904). URL: <http://dx.doi.org/10.1103/PhysRevC.83.064904>.
- [100] Zhi Qiu and Ulrich Heinz. “Event-by-event shape and flow fluctuations of relativistic heavy-ion collision fireballs”. *Phys. Rev. C* 84 (2 Aug. 2011), 024911. DOI: [10.1103/PhysRevC.84.024911](https://doi.org/10.1103/PhysRevC.84.024911). URL: <https://link.aps.org/doi/10.1103/PhysRevC.84.024911>.
- [101] John W. Harris. “Exploring matter 10 microseconds after the Big Bang”. *Innovation News Network* (Dec. 2020). Accessed: 2024. URL: <https://www.innovationnewsnetwork.com/exploring-matter-after-the-big-bang/8120/>.

- [102] S. Voloshin A. Bilandzic R. Snellings. “Flow analysis with cumulants: Direct calculations”. *Phys. Rev. C* 83 (2011), 044913. DOI: [10.1103/PhysRevC.83.044913](https://doi.org/10.1103/PhysRevC.83.044913).
- [103] A. M. Poskanzer and S. A. Voloshin. “Methods for analyzing anisotropic flow in relativistic nuclear collisions”. *Physical Review C* 58.3 (Sept. 1998), 1671–1678. ISSN: 1089-490X. DOI: [10.1103/physrevc.58.1671](https://doi.org/10.1103/physrevc.58.1671). URL: <http://dx.doi.org/10.1103/PhysRevC.58.1671>.
- [104] Sergei A. Voloshin, Arthur M. Poskanzer, and Raimond Snellings. *Collective phenomena in non-central nuclear collisions*. 2008. arXiv: [0809.2949](https://arxiv.org/abs/0809.2949) [nucl-ex]. URL: <https://arxiv.org/abs/0809.2949>.
- [105] C. et al. Adler. “Elliptic flow from two- and four-particle correlations in Au+Au collisions at $\sqrt{s_{NN}} = 130$ GeV”. *Physical Review C* 66.3 (Sept. 2002). ISSN: 1089-490X. DOI: [10.1103/physrevc.66.034904](https://doi.org/10.1103/physrevc.66.034904). URL: <http://dx.doi.org/10.1103/PhysRevC.66.034904>.
- [106] Matthew Luzum and Jean-Yves Ollitrault. “Eliminating experimental bias in anisotropic-flow measurements of high-energy nuclear collisions”. *Physical Review C* 87.4 (Apr. 2013). ISSN: 1089-490X. DOI: [10.1103/physrevc.87.044907](https://doi.org/10.1103/physrevc.87.044907). URL: <http://dx.doi.org/10.1103/PhysRevC.87.044907>.
- [107] R.S. Bhalerao, N. Borghini, and J.-Y. Ollitrault. “Analysis of anisotropic flow with Lee–Yang zeroes”. *Nuclear Physics A* 727.3–4 (Nov. 2003), 373–426. ISSN: 0375-9474. DOI: [10.1016/j.nuclphysa.2003.08.007](https://doi.org/10.1016/j.nuclphysa.2003.08.007). URL: <http://dx.doi.org/10.1016/j.nuclphysa.2003.08.007>.
- [108] Ante Bilandzic, Naomi van der Kolk, Jean-Yves Ollitrault, and Raimond Snellings. “Event-plane flow analysis without nonflow effects”. *Physical Review C* 83.1 (Jan. 2011). ISSN: 1089-490X. DOI: [10.1103/physrevc.83.014909](https://doi.org/10.1103/physrevc.83.014909). URL: <http://dx.doi.org/10.1103/PhysRevC.83.014909>.
- [109] Nicolas Borghini, Phuong Mai Dinh, and Jean-Yves Ollitrault. “Flow analysis from multiparticle azimuthal correlations”. *Phys. Rev. C* 64 (5 Sept. 2001), 054901. DOI: [10.1103/PhysRevC.64.054901](https://doi.org/10.1103/PhysRevC.64.054901). URL: <https://link.aps.org/doi/10.1103/PhysRevC.64.054901>.

- [110] Henning Heiselberg and Anne-Marie Levy. “Elliptic flow and Hanbury-Brown–Twiss correlations in noncentral nuclear collisions”. *Phys. Rev. C* 59 (5 May 1999), 2716–2727. DOI: [10.1103/PhysRevC.59.2716](https://doi.org/10.1103/PhysRevC.59.2716). URL: <https://link.aps.org/doi/10.1103/PhysRevC.59.2716>.
- [111] Rajeev S. Bhalerao and Jean-Yves Ollitrault. “Eccentricity fluctuations and elliptic flow at RHIC”. *Physics Letters B* 641.3–4 (Oct. 2006), 260–264. ISSN: 0370-2693. DOI: [10.1016/j.physletb.2006.08.055](https://doi.org/10.1016/j.physletb.2006.08.055). URL: <http://dx.doi.org/10.1016/j.physletb.2006.08.055>.
- [112] H. Sorge. “Elliptical flow: A signature for early pressure in ultrarelativistic nucleus-nucleus collisions”. *Physical Review Letters* 82 (1999), 2048–2051. DOI: [10.1103/PhysRevLett.82.2048](https://doi.org/10.1103/PhysRevLett.82.2048).
- [113] S. Manly. “System size, energy and pseudorapidity dependence of directed and elliptic flow at RHIC”. *Nuclear Physics A* 774 (Aug. 2006), 523–526. ISSN: 0375-9474. DOI: [10.1016/j.nuclphysa.2006.06.079](https://doi.org/10.1016/j.nuclphysa.2006.06.079). URL: <http://dx.doi.org/10.1016/j.nuclphysa.2006.06.079>.
- [114] Sergei A. Voloshin, Arthur M. Poskanzer, Aihong Tang, and Gang Wang. “Elliptic flow in the Gaussian model of eccentricity fluctuations”. *Physics Letters B* 659.3 (Jan. 2008), 537–541. ISSN: 0370-2693. DOI: [10.1016/j.physletb.2007.11.043](https://doi.org/10.1016/j.physletb.2007.11.043). URL: <http://dx.doi.org/10.1016/j.physletb.2007.11.043>.
- [115] Mike Miller and Raimond Snellings. *Eccentricity fluctuations and its possible effect on elliptic flow measurements*. 2003. arXiv: [nuc1-ex/0312008](https://arxiv.org/abs/nuc1-ex/0312008) [nuc1-ex]. URL: <https://arxiv.org/abs/nuc1-ex/0312008>.
- [116] Sergei A. Voloshin. *Toward the energy and the system size dependence of elliptic flow: working on flow fluctuations*. 2006. arXiv: [nuc1-th/0606022](https://arxiv.org/abs/nuc1-th/0606022) [nuc1-th]. URL: <https://arxiv.org/abs/nuc1-th/0606022>.
- [117] ALICE Collaboration. “Anisotropic flow of identified particles in Pb-Pb collisions at $\sqrt{s_{\text{NN}}} = 5.02$ TeV”. *Journal of High Energy Physics* 2018.9 (Sept. 2018). ISSN: 1029-8479. DOI: [10.1007/jhep09\(2018\)006](https://doi.org/10.1007/jhep09(2018)006). URL: [http://dx.doi.org/10.1007/JHEP09\(2018\)006](http://dx.doi.org/10.1007/JHEP09(2018)006).
- [118] CMS Collaboration. “Higher-order moments of the elliptic flow distribution in PbPb collisions at $\sqrt{s_{\text{NN}}} = 5.02$ TeV”. *Journal of High Energy Physics* 2024.2 (Feb. 2024). ISSN: 1029-8479. DOI: [10.1007/jhep02\(2024\)106](https://doi.org/10.1007/jhep02(2024)106). URL: [http://dx.doi.org/10.1007/JHEP02\(2024\)106](http://dx.doi.org/10.1007/JHEP02(2024)106).

- [119] Sergei A. Voloshin. “Transverse radial expansion and directed flow”. *Phys. Rev. C* 55 (1997), R1630–R1632. DOI: [10.1103/PhysRevC.55.R1630](https://doi.org/10.1103/PhysRevC.55.R1630). arXiv: [nuc1-th/9611038](https://arxiv.org/abs/nuc1-th/9611038).
- [120] Dénes Molnár and Sergei A. Voloshin. “Elliptic Flow at Large Transverse Momenta from Quark Coalescence”. *Physical Review Letters* 91.9 (Aug. 2003). ISSN: 1079-7114. DOI: [10.1103/physrevlett.91.092301](https://doi.org/10.1103/physrevlett.91.092301). URL: <http://dx.doi.org/10.1103/PhysRevLett.91.092301>.
- [121] V. Greco, C. M. Ko, and P. Lévai. “Partonic coalescence in relativistic heavy ion collisions”. *Physical Review C* 68.3 (Sept. 2003). ISSN: 1089-490X. DOI: [10.1103/physrevc.68.034904](https://doi.org/10.1103/physrevc.68.034904). URL: <http://dx.doi.org/10.1103/PhysRevC.68.034904>.
- [122] ALICE Collaboration. *Evidence of nuclear geometry-driven anisotropic flow in OO and Ne–Ne collisions at $\sqrt{s_{\text{NN}}} = 5.36$ TeV*. 2025. arXiv: [2509.06428](https://arxiv.org/abs/2509.06428) [nuc1-ex]. URL: <https://arxiv.org/abs/2509.06428>.
- [123] Giuliano Giacalone et al. *The unexpected uses of a bowling pin: exploiting ^{20}Ne isotopes for precision characterizations of collectivity in small systems*. 2024. arXiv: [2402.05995](https://arxiv.org/abs/2402.05995) [nuc1-th]. URL: <https://arxiv.org/abs/2402.05995>.
- [124] Govert Nijs, Wilke van der Schee, Umut Gürsoy, and Raimond Snellings. “Bayesian analysis of heavy ion collisions with the heavy ion computational framework Trajectum”. *Physical Review C* 103.5 (May 2021). ISSN: 2469-9993. DOI: [10.1103/physrevc.103.054909](https://doi.org/10.1103/physrevc.103.054909). URL: <http://dx.doi.org/10.1103/PhysRevC.103.054909>.
- [125] Dean Lee. *Lattice Effective Field Theory Simulations of Nuclei*. 2025. arXiv: [2501.03303](https://arxiv.org/abs/2501.03303) [nuc1-th]. URL: <https://arxiv.org/abs/2501.03303>.
- [126] Mikael Frosini, Thomas Duguet, Jean-Paul Ebran, and Vittorio Somà. *Multi-reference many-body perturbation theory for nuclei I – Novel PGCM-PT formalism*. 2022. arXiv: [2110.15737](https://arxiv.org/abs/2110.15737) [nuc1-th]. URL: <https://arxiv.org/abs/2110.15737>.
- [127] M. Frosini, T. Duguet, J.-P. Ebran, B. Bally, T. Mongelli, T. R. Rodríguez, R. Roth, and V. Somà. “Multi-reference many-body perturbation theory for nuclei: II. Ab initio study of neon isotopes via PGCM and IM-NCSM calculations”. *The European Physical Journal A* 58.4 (Apr. 2022). ISSN: 1434-601X. DOI:

- 10.1140/epja/s10050-022-00693-y. URL: <http://dx.doi.org/10.1140/epja/s10050-022-00693-y>.
- [128] L. Adamczyk et al. (STAR Collaboration). “Elliptic flow of identified hadrons in Au+Au collisions at $\sqrt{s_{NN}} = 7.7\text{--}62.4\text{ GeV}$ ”. *Phys. Rev. C* 88 (2015), 014902. DOI: [10.1103/PhysRevC.88.014902](https://doi.org/10.1103/PhysRevC.88.014902).
- [129] J. Scott Moreland, Jonah E. Bernhard, and Steffen A. Bass. “Alternative ansatz to wounded nucleon and binary collision scaling in high-energy nuclear collisions”. *Physical Review C* 92.1 (July 2015). ISSN: 1089-490X. DOI: [10.1103/PhysRevC.92.011901](https://doi.org/10.1103/PhysRevC.92.011901). URL: <http://dx.doi.org/10.1103/PhysRevC.92.011901>.
- [130] CMS Collaboration. “Strange hadron collectivity in pPb and PbPb collisions”. *JHEP* 2023.5 (May 2023), 007. DOI: [10.1007/JHEP05\(2023\)007](https://doi.org/10.1007/JHEP05(2023)007). URL: [http://dx.doi.org/10.1007/JHEP05\(2023\)007](http://dx.doi.org/10.1007/JHEP05(2023)007).
- [131] T. Matsui and H. Satz. “J/psi Suppression by Quark-Gluon Plasma Formation”. *Phys. Lett. B* 178 (1986), 416–422. DOI: [10.1016/0370-2693\(86\)91404-8](https://doi.org/10.1016/0370-2693(86)91404-8).
- [132] Nathan Isgur and H. B. Thacker. “Origin of the Okubo-Zweig-Iizuka (OZI) rule in QCD”. *Physical Review D* 64.9 (Oct. 2001). DOI: [10.1103/PhysRevD.64.094507](https://doi.org/10.1103/PhysRevD.64.094507). URL: <https://doi.org/10.1103/PhysRevD.64.094507>.
- [133] R. Baier and R. Ruckl. “Hadronic Collisions: A Quarkonium Factory”. *Z. Phys. C* 19 (1983), 251. DOI: [10.1007/BF01572254](https://doi.org/10.1007/BF01572254).
- [134] G. Sterman J. C. Collins D. E. Soper. “Factorization of Hard Processes in QCD”. *Adv. Ser. Direct. High Energy Phys.* 5 (1989), 1–91. DOI: [10.1142/9789814503266_0001](https://doi.org/10.1142/9789814503266_0001).
- [135] A. V. Lipatov and N. P. Zotov. “Study of the color singlet model with k_T factorization in inclusive J/ψ production at CERN LEP-2” (Feb. 2003). arXiv: [hep-ph/0304181](https://arxiv.org/abs/hep-ph/0304181).
- [136] Daekyoung Kang, Jong-Wan Lee, Jungil Lee, Taewon Kim, and Pyungwon Ko. “Color-evaporation-model calculation of $e^+e^- \rightarrow J/\psi + c\bar{c} + X$ at $\sqrt{s} = 10.6\text{ GeV}$ ”. *Physical Review D* 71.9 (May 2005). DOI: [10.1103/PhysRevD.71.094019](https://doi.org/10.1103/PhysRevD.71.094019). URL: <http://dx.doi.org/10.1103/PhysRevD.71.094019>.

- [137] Geoffrey T. Bodwin, Eric Braaten, and Jungil Lee. “Comparison of the color-evaporation model and the nonrelativistic QCD factorization approach in charmonium production”. *Physical Review D* 72.1 (July 2005). ISSN: 1550-2368. DOI: [10.1103/PhysRevD.72.014004](https://doi.org/10.1103/PhysRevD.72.014004). URL: <http://dx.doi.org/10.1103/PhysRevD.72.014004>.
- [138] Jean-Philippe Lansberg. “New Observables in Inclusive Production of Quarkonia”. *Phys. Rept.* 889 (2020), 1–106.
- [139] A.M. Sirunyan et al. “Measurement of quarkonium production cross sections in pp collisions at $\sqrt{s} = 13$ TeV”. *Physics Letters B* 780 (May 2018), 251–272. ISSN: 0370-2693. DOI: [10.1016/j.physletb.2018.02.033](https://doi.org/10.1016/j.physletb.2018.02.033). URL: <http://dx.doi.org/10.1016/j.physletb.2018.02.033>.
- [140] LHCb collaboration. “Production of J/ψ and Υ mesons in pp collisions at $\sqrt{s} = 8$ TeV”. *Journal of High Energy Physics* 2013.6 (June 2013). ISSN: 1029-8479. DOI: [10.1007/jhep06\(2013\)064](https://doi.org/10.1007/jhep06(2013)064). URL: [http://dx.doi.org/10.1007/JHEP06\(2013\)064](http://dx.doi.org/10.1007/JHEP06(2013)064).
- [141] ALICE Collaboration. *Measurement of quarkonium production at forward rapidity in pp collisions at $\sqrt{s} = 7$ TeV*. 2014. arXiv: [1403.3648](https://arxiv.org/abs/1403.3648) [nucl-ex]. URL: <https://arxiv.org/abs/1403.3648>.
- [142] ATLAS Collaboration. “ATLAS reach for Quarkonium production and polarization measurements”. *Nuclear Physics B - Proceedings Supplements* 187 (Feb. 2009), 136–144. ISSN: 0920-5632. DOI: [10.1016/j.nuclphysbps.2009.01.020](https://doi.org/10.1016/j.nuclphysbps.2009.01.020). URL: <http://dx.doi.org/10.1016/j.nuclphysbps.2009.01.020>.
- [143] Marek Walczak. “Ultra-peripheral J/ψ Production in PbPb Collisions in CMS”. *Acta Phys. Polon. B* 48 (2017), 1231–1236. DOI: [10.5506/APhysPolB.48.1231](https://doi.org/10.5506/APhysPolB.48.1231).
- [144] Enrico Fermi. “Über die Theorie des Stoßes zwischen Atomen und elektrisch geladenen Teilchen”. *Zeitschrift für Physik* 29 (1924), 315–327. DOI: [10.1007/BF03184853](https://doi.org/10.1007/BF03184853).
- [145] Carl Friedrich von Weizsäcker. “Ausstrahlung bei Stößen sehr schneller Elektronen”. *Zeitschrift für Physik* 88 (1934), 612–625. DOI: [10.1007/BF01333110](https://doi.org/10.1007/BF01333110).
- [146] R. Vogt. “Cold Nuclear Matter Effects on J/ψ and Υ Production at the LHC”. *Phys. Rev. C* 81 (2010), 044903. DOI: [10.1103/PhysRevC.81.044903](https://doi.org/10.1103/PhysRevC.81.044903).

- [147] K. J. Eskola, P. Paakkinen, H. Paukkunen, and C. A. Salgado. “EPPS16: Nuclear parton distributions with LHC data”. *Eur. Phys. J. C* 77 (2017), 163. DOI: [10.1140/epjc/s10052-017-4725-9](https://doi.org/10.1140/epjc/s10052-017-4725-9).
- [148] D. Antreasyan, J. Cronin, H. Frisch, M. Shochet, L. Kluberg, P. Piroué, and R. Sumner. “Production of hadrons at large transverse momentum in 200-, 300-, and 400-GeV pp and p–nucleus collisions”. *Physical Review D* 19 (1979), 764–778. DOI: [10.1103/PhysRevD.19.764](https://doi.org/10.1103/PhysRevD.19.764).
- [149] A. Accardi. *Cronin effect in proton nucleus collisions: A Survey of theoretical models*. 2002. arXiv: [hep-ph/0212148](https://arxiv.org/abs/hep-ph/0212148).
- [150] J. Hüfner, Y. Kurihara, and H. Pirner. “Gluon multiple scattering and the transverse momentum dependence of J/ψ production in nucleus–nucleus collisions”. *Physics Letters B* 215.2 (1988), 218–222. DOI: [10.1016/0370-2693\(88\)91032-6](https://doi.org/10.1016/0370-2693(88)91032-6).
- [151] F. Arleo and S. Peigné. “Heavy-quarkonium suppression in p-A collisions from parton energy loss in cold QCD matter”. *JHEP* 03 (2013), 122. DOI: [10.1007/JHEP03\(2013\)122](https://doi.org/10.1007/JHEP03(2013)122).
- [152] François Arleo, Gavin Jackson, and Stéphane Peigné. “Coherent energy loss effects in quarkonium production”. *JHEP* 01 (2022), 164. DOI: [10.1007/JHEP01\(2022\)164](https://doi.org/10.1007/JHEP01(2022)164). arXiv: [2111.07276](https://arxiv.org/abs/2111.07276) [hep-ph].
- [153] Cheuk-Yin Wong and Chun Wa Wong. “Color-Octet Fraction in J/ψ Production and Absorption”. *Physical Review D* 57.3 (Feb. 1998), 1838–1845. ISSN: 1089-4918. DOI: [10.1103/physrevd.57.1838](https://doi.org/10.1103/physrevd.57.1838). URL: <http://dx.doi.org/10.1103/PhysRevD.57.1838>.
- [154] E. G. Ferreira. “Excited charmonium suppression in proton–nucleus collisions as a consequence of comovers”. *Phys. Lett. B* 731 (2014), 57–63. DOI: [10.1016/j.physletb.2014.02.011](https://doi.org/10.1016/j.physletb.2014.02.011).
- [155] E. G. Ferreira, F. Fleuret, J. P. Lansberg, and A. Rakotozafindrabe. “Impact of the Nuclear Modification of the Gluon Densities on J/ψ production in pPb collisions at $\sqrt{s_{NN}} = 5$ TeV”. *Physical Review C* 88.4 (Oct. 2013). DOI: [10.1103/physrevc.88.047901](https://doi.org/10.1103/physrevc.88.047901). URL: <https://arxiv.org/abs/1305.4569>.

- [156] François Arleo and Stéphane Peigné. “Disentangling shadowing from coherent energy loss using the Drell-Yan process”. *Physical Review D* 95.1 (Jan. 2017). ISSN: 2470-0029. DOI: [10.1103/PhysRevD.95.011502](https://doi.org/10.1103/PhysRevD.95.011502). URL: <http://dx.doi.org/10.1103/PhysRevD.95.011502>.
- [157] S. Brodsky and A. Mueller. “Using nuclei to probe hadronization in QCD”. *Physics Letters B* 206.4 (1988), 685–690. DOI: [10.1016/0370-2693\(88\)90719-8](https://doi.org/10.1016/0370-2693(88)90719-8).
- [158] B. Kopeliovich and B. Zakharov. “Quantum effects and color transparency in charmonium photoproduction on nuclei”. *Physical Review D* 44 (1991), 3466–3472. DOI: [10.1103/PhysRevD.44.3466](https://doi.org/10.1103/PhysRevD.44.3466).
- [159] D. Kharzeev and R. Thews. “Quarkonium formation time in a model independent approach”. *Physical Review C* 60 (1999), 041901. DOI: [10.1103/PhysRevC.60.041901](https://doi.org/10.1103/PhysRevC.60.041901).
- [160] A. Andronic, P. Braun-Munzinger, M. K. Köhler, A. Mazeliauskas, K. Redlich, J. Stachel, and V. Viskovitch. “The multiple-charm hierarchy in the statistical hadronization model”. *JHEP* 07 (2021), 035. DOI: [10.1007/JHEP07\(2021\)035](https://doi.org/10.1007/JHEP07(2021)035). arXiv: [2104.12754](https://arxiv.org/abs/2104.12754).
- [161] L. Altenkort, O. Kaczmarek, R. Larsen, S. Mukherjee, P. Petreczky, H. T. Shu, and S. Stendebach. “Heavy Quark Diffusion from 2+1 Flavor Lattice QCD with 320 MeV Pion Mass”. *Phys. Rev. Lett.* 130 (2023), 231902. DOI: [10.1103/PhysRevLett.130.231902](https://doi.org/10.1103/PhysRevLett.130.231902). arXiv: [2302.08501](https://arxiv.org/abs/2302.08501) [hep-lat].
- [162] R. Rapp and H. van Hees. “Heavy Quark Diffusion as a Probe of the Quark-Gluon Plasma”. *Eur. Phys. J. A* 52 (2017), 257. DOI: [10.1140/epja/i2016-16257-4](https://doi.org/10.1140/epja/i2016-16257-4).
- [163] F. Karsch, M. T. Mehr, and H. Satz. “Color Screening and Deconfinement for Bound States of Heavy Quarks”. *Z. Phys. C* 37 (1988), 617. DOI: [10.1007/BF01549722](https://doi.org/10.1007/BF01549722).
- [164] H. Satz. “Quarkonium Binding and Dissociation: The Spectral Analysis of the QGP”. *J. Phys. G* 40 (2013), 093003. DOI: [10.1088/0954-3899/40/9/093003](https://doi.org/10.1088/0954-3899/40/9/093003).
- [165] Xingbo Zhao and Ralf Rapp. “Medium modifications and production of charmonia at LHC”. *Nuclear Physics A* 859.1 (June 2011), 114–125. ISSN: 0375-9474. DOI: [10.1016/j.nuclphysa.2011.05.001](https://doi.org/10.1016/j.nuclphysa.2011.05.001). URL: <http://dx.doi.org/10.1016/j.nuclphysa.2011.05.001>.

- [166] Peter Braun-Munzinger and Johanna Stachel. “The quest for the quark-gluon plasma”. *Nature* 448 (2007), 302–309. DOI: [10.1038/nature06080](https://doi.org/10.1038/nature06080).
- [167] A. et al. Andronic. “Heavy-flavour and quarkonium production in the LHC era: from proton–proton to heavy-ion collisions”. *The European Physical Journal C* 76.3 (Feb. 2016). ISSN: 1434-6052. DOI: [10.1140/epjc/s10052-015-3819-5](https://doi.org/10.1140/epjc/s10052-015-3819-5). URL: <http://dx.doi.org/10.1140/epjc/s10052-015-3819-5>.
- [168] PHENIX Collaboration. “ J/ψ suppression at forward rapidity in Au+Au collisions at $\sqrt{s_{NN}} = 200$ GeV”. *Physical Review C* 84.5 (Nov. 2011). ISSN: 1089-490X. DOI: [10.1103/physrevc.84.054912](https://doi.org/10.1103/physrevc.84.054912). URL: <http://dx.doi.org/10.1103/PhysRevC.84.054912>.
- [169] ALICE Collaboration. “ J/ψ Suppression at Forward Rapidity in Pb-Pb Collisions at $\sqrt{s_{NN}} = 2.76$ TeV”. *Phys. Rev. Lett.* 109 (7 Aug. 2012), 072301. DOI: [10.1103/PhysRevLett.109.072301](https://doi.org/10.1103/PhysRevLett.109.072301). URL: <https://link.aps.org/doi/10.1103/PhysRevLett.109.072301>.
- [170] Shreyasi Acharya et al. “Studies of J/ψ production at forward rapidity in Pb-Pb collisions at $\sqrt{s_{NN}} = 5.02$ TeV”. *JHEP* 02 (2020), 041. DOI: [10.1007/JHEP02\(2020\)041](https://doi.org/10.1007/JHEP02(2020)041). arXiv: [1909.03158](https://arxiv.org/abs/1909.03158) [nucl-ex].
- [171] ALICE Collaboration. “Differential studies of inclusive J/ψ and $\psi(2S)$ production at forward rapidity in Pb-Pb collisions at $\sqrt{s_{NN}} = 2.76$ TeV”. *Journal of High Energy Physics* 2016.5 (May 2016). ISSN: 1029-8479. DOI: [10.1007/jhep05\(2016\)179](https://doi.org/10.1007/jhep05(2016)179). URL: [http://dx.doi.org/10.1007/JHEP05\(2016\)179](http://dx.doi.org/10.1007/JHEP05(2016)179).
- [172] Xiaojian Du and Ralf Rapp. “Sequential regeneration of charmonia in heavy-ion collisions”. *Nuclear Physics A* 943 (Nov. 2015), 147–158. ISSN: 0375-9474. DOI: [10.1016/j.nuclphysa.2015.09.006](https://doi.org/10.1016/j.nuclphysa.2015.09.006). URL: <http://dx.doi.org/10.1016/j.nuclphysa.2015.09.006>.
- [173] Anton Andronic, Peter Braun-Munzinger, Markus K. Köhler, Krzysztof Redlich, and Johanna Stachel. “Transverse momentum distributions of charmonium states with the statistical hadronization model”. *Phys. Lett. B* 797 (2019), 134836. DOI: [10.1016/j.physletb.2019.134836](https://doi.org/10.1016/j.physletb.2019.134836).
- [174] Jiaying Zhao and Baoyi Chen. “Strong diffusion effect of charm quarks on J/ψ production in Pb–Pb collisions at the LHC”. *Physics Letters B* 776 (Jan. 2018), 17–21. ISSN: 0370-2693. DOI: [10.1016/j.physletb.2017.11.014](https://doi.org/10.1016/j.physletb.2017.11.014). URL: <http://dx.doi.org/10.1016/j.physletb.2017.11.014>.

- [175] L. Grandchamp and R. Rapp. “Thermal versus direct J/ψ production in ultrarelativistic heavy ion collisions”. *Phys. Lett. B* 523 (2001), 60–66. DOI: [10.1016/S0370-2693\(01\)01311-9](https://doi.org/10.1016/S0370-2693(01)01311-9).
- [176] A. Mocsy, P. Petreczky, and M. Strickland. “Quarkonia in the Quark Gluon Plasma”. *Int. J. Mod. Phys. A* 28 (2013), 1340012. DOI: [10.1142/S0217751X13400125](https://doi.org/10.1142/S0217751X13400125).
- [177] Yukinao Akamatsu. “Heavy quark master equations in the Lindblad form at high temperatures”. *Phys. Rev. D* 91.5 (2015), 056002. DOI: [10.1103/PhysRevD.91.056002](https://doi.org/10.1103/PhysRevD.91.056002).
- [178] ALICE collaboration. “ J/ψ elliptic and triangular flow in Pb-Pb collisions at $\sqrt{s_{NN}} = 5.02$ TeV”. *Journal of High Energy Physics* 2020.10 (Oct. 2020). ISSN: 1029-8479. DOI: [10.1007/jhep10\(2020\)141](https://doi.org/10.1007/jhep10(2020)141). URL: [http://dx.doi.org/10.1007/JHEP10\(2020\)141](http://dx.doi.org/10.1007/JHEP10(2020)141).
- [179] STAR Collaboration. “Measurement of J/ψ Azimuthal Anisotropy in Au+Au Collisions at $\sqrt{s_{NN}} = 200$ GeV”. *Physical Review Letters* 111.5 (Aug. 2013), 052301. ISSN: 1079-7114. DOI: [10.1103/PhysRevLett.111.052301](https://doi.org/10.1103/PhysRevLett.111.052301). URL: <http://dx.doi.org/10.1103/PhysRevLett.111.052301>.
- [180] Luis Bichon III. “Forward rapidity elliptic flow measurements in PHENIX Au+Au collisions at 200 GeV”. Presentation at SQM 2024 (International Conference on Strangeness in Quark Matter), 5–9 June 2024. On behalf of the PHENIX Collaboration. Slide deck: “SQM2024_Bichon.pdf”. 2024. URL: https://indico.in2p3.fr/event/29792/contributions/137205/attachments/85216/127618/SQM2024_Bichon.pdf.
- [181] Min He, Biaogang Wu, and Ralf Rapp. “Collectivity of J/ψ Mesons in Heavy-Ion Collisions”. *Physical Review Letters* 128.16 (Apr. 2022). ISSN: 1079-7114. DOI: [10.1103/physrevlett.128.162301](https://doi.org/10.1103/physrevlett.128.162301). URL: <http://dx.doi.org/10.1103/PhysRevLett.128.162301>.
- [182] Min He, Rainer J. Fries, and Ralf Rapp. “Scaling of elliptic flow, recombination, and sequential freeze-out of hadrons in heavy-ion collisions”. *Physical Review C* 82.3 (Sept. 2010). ISSN: 1089-490X. DOI: [10.1103/physrevc.82.034907](https://doi.org/10.1103/physrevc.82.034907). URL: <http://dx.doi.org/10.1103/PhysRevC.82.034907>.

- [183] A. M. Sirunyan et al. (CMS Collaboration). “Measurement of the elliptic flow of prompt and nonprompt J/ψ mesons in PbPb collisions at $\sqrt{s_{NN}} = 5.02$ TeV”. *Phys. Rev. Lett.* 128 (2021), 032301. DOI: [10.1103/PhysRevLett.128.032301](https://doi.org/10.1103/PhysRevLett.128.032301).
- [184] Guillaume Falmagne. “The B+c meson in heavy-ion collisions with the CMS detector”. Theses. Institut Polytechnique de Paris, Dec. 2021. URL: <https://theses.hal.science/tel-03619850>.
- [185] S. Acharya et al. (ALICE Collaboration). “ J/ψ elliptic and triangular flow in Pb-Pb collisions at $\sqrt{s_{NN}} = 5.02$ TeV”. *JHEP* 10 (2020), 141. DOI: [10.1007/JHEP10\(2020\)141](https://doi.org/10.1007/JHEP10(2020)141).
- [186] “LHC Design Report Vol.1: The LHC Main Ring” (June 2004). Ed. by Oliver S. Bruning, P. Collier, P. Lebrun, S. Myers, R. Ostojic, J. Poole, and P. Proudlock. DOI: [10.5170/CERN-2004-003-V-1](https://doi.org/10.5170/CERN-2004-003-V-1).
- [187] Thomas Taylor and Daniel Treille. “The Large Electron Positron Collider (LEP): Probing the Standard Model”. *Adv. Ser. Direct. High Energy Phys.* 27 (2017), 217–261.
- [188] *High-Luminosity Large Hadron Collider (HL-LHC): Technical Design Report*. Technical Design Report. View Vol. 10 (2020). CERN, 2020.
- [189] Esma Mobs. “The CERN Accelerator Complex”. *Open-Pho-Accel* 2016.009 (2018).
- [190] M. Vretenar et al. “Linac4 design report”. *CERN Yellow Reports: Monographs* (2020), 1–230. DOI: [10.23731/CYRM-2020-006](https://doi.org/10.23731/CYRM-2020-006).
- [191] K. H. Reich. “The CERN Proton Synchrotron Booster”. *IEEE Trans. Nucl. Sci.* 16 (1969), 959–961. DOI: [10.1109/TNS.1969.4325414](https://doi.org/10.1109/TNS.1969.4325414).
- [192] W. Fischer and J. M. Jowett. “Ion Colliders”. *Rev. Accel. Sci. Tech.* 7 (2014), 49–76. DOI: [10.1142/S1793626814300047](https://doi.org/10.1142/S1793626814300047).
- [193] G. Aad et al. “The ATLAS Experiment at the CERN Large Hadron Collider”. *JINST* 3 (2008), S08003. DOI: [10.1088/1748-0221/3/08/S08003](https://doi.org/10.1088/1748-0221/3/08/S08003).
- [194] K. Aamodt et al. “The ALICE experiment at the CERN LHC”. *JINST* 3 (2008), S08002. DOI: [10.1088/1748-0221/3/08/S08002](https://doi.org/10.1088/1748-0221/3/08/S08002).
- [195] S. Chatrchyan et al. “The CMS Experiment at the CERN LHC”. *JINST* 3 (2008), S08004. DOI: [10.1088/1748-0221/3/08/S08004](https://doi.org/10.1088/1748-0221/3/08/S08004).

- [196] A. Augusto Alves Jr. et al. “The LHCb Detector at the LHC”. *JINST* 3 (2008), S08005. DOI: [10.1088/1748-0221/3/08/S08005](https://doi.org/10.1088/1748-0221/3/08/S08005).
- [197] *LHCb SMOG Upgrade*. Tech. rep. Geneva: CERN, 2019. DOI: [10.17181/CERN.SAQC.EOWH](https://doi.org/10.17181/CERN.SAQC.EOWH). URL: <https://cds.cern.ch/record/2673690>.
- [198] G. Anelli et al. “The TOTEM experiment at the CERN Large Hadron Collider”. *JINST* 3 (2008), S08007. DOI: [10.1088/1748-0221/3/08/S08007](https://doi.org/10.1088/1748-0221/3/08/S08007).
- [199] Eugenio Berti. *The LHCf experiment: present status and physics results*. 2017. arXiv: [1710.03991](https://arxiv.org/abs/1710.03991) [hep-ex]. URL: <https://arxiv.org/abs/1710.03991>.
- [200] James L. Pinfold. “The MoEDAL experiment at the LHC — a new light on the high energy frontier”. *Conference in Honor of the 90th Birthday of Freeman Dyson*. 2014, 173–178. DOI: [10.1142/9789814590112_0008](https://doi.org/10.1142/9789814590112_0008).
- [201] Henso et al. Abreu. “The FASER detector”. *Journal of Instrumentation* 19.05 (May 2024), P05066. ISSN: 1748-0221. DOI: [10.1088/1748-0221/19/05/P05066](https://doi.org/10.1088/1748-0221/19/05/P05066). URL: <http://dx.doi.org/10.1088/1748-0221/19/05/P05066>.
- [202] CERN. *Concept of Luminosity*. <https://cds.cern.ch/record/941318/files/p361.pdf>. CERN-2006-002, pp. 361–378, Accessed: 2025-05-30. 2006.
- [203] J. Gareyte. “LHC main parameters”. *Part. Accel.* 50 (1995). Ed. by E. Keil, 61–68.
- [204] *Site web du LHC*. URL: <http://lhc-commissioning.web.cern.ch/schedule/LHC-long-term.htm>.
- [205] Shreyasi Acharya et al. “Performance of the ALICE Electromagnetic Calorimeter”. *JINST* 18.08 (2023), P08007. DOI: [10.1088/1748-0221/18/08/P08007](https://doi.org/10.1088/1748-0221/18/08/P08007). arXiv: [2209.04216](https://arxiv.org/abs/2209.04216) [physics.ins-det].
- [206] B Abelev et al. “Technical Design Report for the Upgrade of the ALICE Inner Tracking System”. *J. Phys. G* 41 (2014), 087002. DOI: [10.1088/0954-3899/41/8/087002](https://doi.org/10.1088/0954-3899/41/8/087002).
- [207] Felix Reidt. “Upgrade of the ALICE ITS detector”. *Nucl. Instrum. Meth. A* 1032 (2022), 166632. DOI: [10.1016/j.nima.2022.166632](https://doi.org/10.1016/j.nima.2022.166632). arXiv: [2111.08301](https://arxiv.org/abs/2111.08301) [physics.ins-det].
- [208] Andrea Sofia Triolo. *Calibration and Performance of the Upgraded ALICE Inner Tracking System*. 2024. arXiv: [2409.19810](https://arxiv.org/abs/2409.19810) [physics.ins-det]. URL: <https://arxiv.org/abs/2409.19810>.

- [209] Christian Lippmann. “Upgrade of the ALICE Time Projection Chamber” (Mar. 2014).
- [210] F. Sauli. “GEM: A new concept for electron amplification in gas detectors”. *Nucl. Instrum. Meth. A* 386 (1997), 531–534. DOI: [10.1016/S0168-9002\(96\)01172-2](https://doi.org/10.1016/S0168-9002(96)01172-2).
- [211] Christian Lippmann. “Upgrade of the ALICE Time Projection Chamber” (Mar. 2014).
- [212] G. Dellacasa et al. “ALICE technical design report of the time-of-flight system (TOF)” (Feb. 2000).
- [213] G. Dellacasa et al. “ALICE technical design report of the Transition Radiation Detector (TRD)” (Oct. 2001).
- [214] P. Cortese et al. “ALICE Electromagnetic Calorimeter Technical Design Report” (May 2008).
- [215] *ALICE DCal: An Addendum to the EMCal Technical Design Report Di-Jet and Hadron-Jet correlation measurements in ALICE*. Tech. rep. June 2010. URL: <http://cds.cern.ch/record/1272952/files/ALICE-TDR-014-ADD-1.pdf>.
- [216] J. Allen et al. *ALICE DCal: An Addendum to the EMCal Technical Design Report Di-Jet and Hadron-Jet correlation measurements in ALICE*. Tech. rep. 2010. URL: <https://cds.cern.ch/record/1272952>.
- [217] François Piuz, W Klempt, L Leistam, J De Groot, and Jürgen Schükraft. *ALICE high-momentum particle identification: Technical Design Report*. Technical design report. ALICE. Geneva: CERN, 1998. URL: <https://cds.cern.ch/record/381431>.
- [218] J. Seguinot and T. Ypsilantis. “Photo-ionization and Cherenkov ring imaging”. *Nuclear Instruments and Methods* 142.3 (1977), 377–391. ISSN: 0029-554X. DOI: [https://doi.org/10.1016/0029-554X\(77\)90671-1](https://doi.org/10.1016/0029-554X(77)90671-1). URL: <https://www.sciencedirect.com/science/article/pii/0029554X77906711>.
- [219] Giacomo Volpe. “The High Momentum Particle IDentification (HMPID) detector PID performance and its contribution to the ALICE physics program”. *Nucl. Instrum. Meth. A* 876 (2017). Ed. by P. Krizan, S. Korpar, G. Hallewell, W. Hofmann, and E. Nappi, 133–136. DOI: [10.1016/j.nima.2017.02.037](https://doi.org/10.1016/j.nima.2017.02.037).
- [220] G. Dellacasa et al. “ALICE technical design report of the photon spectrometer (PHOS)” (Mar. 1999).

- [221] S. Evdokimov, V. Izucheev, Yu. Kharlov, E. Kondratyuk, S. Sadovsky, and A. Shangaraev. “The ALICE CPV Detector”. *KnE Energ. Phys.* 3 (2018), 260–267. DOI: [10.18502/ken.v3i1.1752](https://doi.org/10.18502/ken.v3i1.1752). URL: <http://cds.cern.ch/record/2658138/files/4048.pdf>.
- [222] *Technical Design Report for the Upgrade of the ALICE Read-out & Trigger System*. Tech. rep. July 2014. URL: <https://cds.cern.ch/record/1603472/files/ALICE-TDR-015.pdf>.
- [223] P Antonioli, A Kluge, and W Riegler. *Upgrade of the ALICE Readout amp; Trigger System*. Tech. rep. Presently we require a LHCC-TDR reference number.a later stage we will fill the required information. 2013. URL: <https://cds.cern.ch/record/1603472>.
- [224] G. Dellacasa et al. “ALICE technical design report of the zero degree calorimeter (ZDC)” (Mar. 1999).
- [225] S.C. Zugravel et al. “ALICE Zero Degree Calorimeters. The new readout system in LHC Run 3”. *Journal of Instrumentation* 18.02 (Feb. 2023), C02009. DOI: [10.1088/1748-0221/18/02/C02009](https://doi.org/10.1088/1748-0221/18/02/C02009). URL: <https://dx.doi.org/10.1088/1748-0221/18/02/C02009>.
- [226] “ALICE technical design report of the dimuon forward spectrometer” (Aug. 1999).
- [227] “ALICE addendum to the technical design report of the dimuon forward spectrometer” (Dec. 2000).
- [228] “Dimuon Forward Spectrometer: Tracking Chambers” (). URL: <https://twiki.cern.ch/twiki/bin/viewauth/ALICE/MuonTracking>.
- [229] Mohamad Tarhini. “Measurement of Z-boson and J/ψ Production in p-Pb and Pb-Pb Collisions at $\sqrt{s_{NN}} = 5.02$ TeV with ALICE at the LHC”. 2017SACLS283 (Jun 2017). URL: <https://theses.hal.science/tel-01691725>.
- [230] *Technical Design Report for the Muon Forward Tracker*. Tech. rep. 2015. URL: <https://cds.cern.ch/record/1981898>.
- [231] ALICE Collaboration. “ALICE upgrades during the LHC Long Shutdown 2”. *Journal of Instrumentation* 19.05 (May 2024), P05062. DOI: [10.1088/1748-0221/19/05/p05062](https://doi.org/10.1088/1748-0221/19/05/p05062). URL: <https://arxiv.org/abs/2302.01238>.
- [232] P. Buncic, M. Krzewicki, and P. Vande Vyvre. “Technical Design Report for the Upgrade of the Online-Offline Computing System” (Apr. 2015).

- [233] Rene Brun and Fons Rademakers. *ROOT — An object-oriented data analysis framework*. Proceedings AIHENP’96 Workshop, Lausanne, Sep. 1996. Nucl. Inst. & Meth. in Phys. Res. A 389 (1997) 81-86. 1997. DOI: [10.1016/S0168-9002\(97\)00048-X](https://doi.org/10.1016/S0168-9002(97)00048-X).
- [234] Apache Software Foundation. *Apache Arrow: A cross-language development platform for in-memory data*. <https://arrow.apache.org/>. Accessed: 2025-05-30. 2016.
- [235] Anton Alkin, Giulio Eulisse, Jan Fiete Grosse-Oetringhaus, Peter Hristov, and Maja Kabus. “ALICE Run 3 Analysis Framework”. *EPJ Web Conf.* 251 (2021), 03063. DOI: [10.1051/epjconf/202125103063](https://doi.org/10.1051/epjconf/202125103063). URL: <https://cds.cern.ch/record/2814355>.
- [236] Raquel Quishpe, Jan Fiete Grosse-Oetringhaus, Raluca Cruceru, and Costin Grigoras. “Hyperloop – The ALICE analysis train system for Run 3”. *PoS LHCP2021* (2021), 250. DOI: [10.22323/1.397.0250](https://doi.org/10.22323/1.397.0250). arXiv: [2109.09594](https://arxiv.org/abs/2109.09594) [physics.ins-det].
- [237] Raquel Quishpe, Jan Fiete Grosse-Oetringhaus, Raluca Cruceru, and Costin Grigoras. “Hyperloop – The ALICE analysis train system for Run 3”. *arXiv e-prints* 2021.arXiv:2109.09594 (2021). URL: <https://arxiv.org/abs/2109.09594>.
- [238] P. Saiz, J. Templon, P. Buncic, and F. Carminati. “AliEn: ALICE Environment on the GRID”. *Nucl. Instrum. Meth. A* 502.2-3 (2003), 437–440. DOI: [10.1016/S0168-9002\(03\)00462-5](https://doi.org/10.1016/S0168-9002(03)00462-5).
- [239] ALICE Collaboration. “ALICE upgrades during the LHC Long Shutdown 2”. *Journal of Instrumentation* 19.05 (May 2024), P05062. ISSN: 1748-0221. DOI: [10.1088/1748-0221/19/05/p05062](https://doi.org/10.1088/1748-0221/19/05/p05062). URL: <http://dx.doi.org/10.1088/1748-0221/19/05/P05062>.
- [240] Livia Terlizzi and ALICE Collaboration. “Upgrade and commissioning of the ALICE muon spectrometer for LHC Run 3”. *Proceedings of the 7th FAIRness Workshop (FAIRness2022)* (2022). arXiv:2210.12431. DOI: [10.22323/1.450.0052](https://doi.org/10.22323/1.450.0052).

- [241] ALICE Collaboration, P. Buncic, M. Krzewicki, and P. Vande Vyvre. *Technical Design Report for the Upgrade of the Online–Offline Computing System (O²)*. Tech. rep. CERN-LHCC-2015-006 / ALICE-TDR-019. CERN, 2015. URL: <https://cds.cern.ch/record/2011297>.
- [242] ALICE Collaboration. “Centrality determination of Pb–Pb collisions at $\sqrt{s_{NN}} = 2.76$ TeV with ALICE”. *Physical Review C* 88.4 (Oct. 2013), 044909. ISSN: 1089-490X. DOI: [10.1103/PhysRevC.88.044909](https://doi.org/10.1103/PhysRevC.88.044909). URL: <http://dx.doi.org/10.1103/PhysRevC.88.044909>.
- [243] Ante Bilandzic, Raimond Snellings, and Sergei Voloshin. “Flow analysis with cumulants: Direct calculations”. *Phys. Rev. C* 83.4 (Apr. 2011), 044913. DOI: [10.1103/PhysRevC.83.044913](https://doi.org/10.1103/PhysRevC.83.044913). URL: <http://dx.doi.org/10.1103/PhysRevC.83.044913>.
- [244] ALICE Collaboration. “Elliptic flow of charged particles in Pb-Pb collisions at $\sqrt{s_{NN}} = 2.76$ TeV”. *Phys. Rev. Lett.* 105 (2010), 252302. DOI: [10.1103/PhysRevLett.105.252302](https://doi.org/10.1103/PhysRevLett.105.252302).
- [245] ALICE Collaboration. “Elliptic flow of charged particles in Pb-Pb collisions at $\sqrt{s_{NN}} = 5.02$ TeV”. *Phys. Rev. Lett.* 116 (2016), 132302. DOI: [10.1103/PhysRevLett.116.132302](https://doi.org/10.1103/PhysRevLett.116.132302).
- [246] Nicolas Borghini, Phuong Mai Dinh, and Jean-Yves Ollitrault. “New method for measuring azimuthal distributions in nucleus-nucleus collisions”. *Phys. Rev. C* 63 (5 Apr. 2001), 054906. DOI: [10.1103/PhysRevC.63.054906](https://doi.org/10.1103/PhysRevC.63.054906). URL: <https://link.aps.org/doi/10.1103/PhysRevC.63.054906>.
- [247] Sergei A. Voloshin, Arthur M. Poskanzer, Aihong Tang, and Gang Wang. “Elliptic flow in the Gaussian model of eccentricity fluctuations”. *Phys. Lett. B* 659.3 (Jan. 2008), 537–541. DOI: [10.1016/j.physletb.2007.11.043](https://doi.org/10.1016/j.physletb.2007.11.043). URL: <http://dx.doi.org/10.1016/j.physletb.2007.11.043>.
- [248] J. Gaiser. “Charmonium Spectroscopy From Radiative Decays of the J/ψ and $\psi(2S)$ ”. SLAC-R-255. PhD thesis. Stanford Linear Accelerator Center (SLAC), 1982. URL: <http://www.slac.stanford.edu/cgi-wrap/getdoc/slac-r-255.pdf>.
- [249] Ruben Shahoyan. “ J/ψ and ψ -prime production in 450 GeV pA interactions and its dependence on the rapidity and x_F ”. PhD thesis. Lisboa U., 2001.

- [250] sPHENIX Collaboration. *Measurement of π^0 v_2 in Au+Au Collisions at 200 GeV with the sPHENIX Detector*. Tech. rep. sPH-CONF-BULK-2024-01. sPHENIX, May 2024. URL: <https://www.sphenix.bnl.gov/sites/default/files/2024-06/sPH-CONF-BULK-2024-01.pdf>.
- [251] S. Acharya et al. “Study of J/ψ azimuthal anisotropy at forward rapidity in Pb-Pb collisions at $\sqrt{s_{\text{NN}}} = 5.02$ TeV”. *Journal of High Energy Physics* 2019.2 (Feb. 2019). URL: <https://arxiv.org/abs/1811.12727>.
- [252] “Quarkonium signal extraction in ALICE” (2015). URL: <https://cds.cern.ch/record/2060096>.
- [253] Michele Pennisi (on behalf of the ALICE Collaboration). “Charm and beauty production at forward rapidity with ALICE”. *Hard Probes 2024*. Presentation on 23 September 2024. Nagasaki, Japan, Sept. 2024. URL: https://indico.cern.ch/event/1339555/contributions/6040879/attachments/2932254/5149656/HP2024_MPennisi_v6.pdf.
- [254] Jean-Yves Ollitrault. “Anisotropy as a signature of transverse collective flow”. *Phys. Rev. D* 46 (1992), 229–245. DOI: [10.1103/PhysRevD.46.229](https://doi.org/10.1103/PhysRevD.46.229).
- [255] Xiaojian Du and Ralf Rapp. “Sequential regeneration of charmonia in heavy-ion collisions”. *arXiv* (2015). DOI: [10.48550/arXiv.1504.00670](https://doi.org/10.48550/arXiv.1504.00670). eprint: 1504.00670. URL: <https://doi.org/10.48550/arXiv.1504.00670>.
- [256] Chi Zhang. *Quarkonia collectivity in large collision systems with ALICE*. 2025. arXiv: 2509.06240 [nucl-ex]. URL: <https://arxiv.org/abs/2509.06240>.
- [257] Jiaxing et al. Zhao. “Charmonium triangular flow in high energy nuclear collisions”. *Phys. Rev. C* 105.3 (Mar. 2022), 034902. DOI: [10.1103/PhysRevC.105.034902](https://doi.org/10.1103/PhysRevC.105.034902). URL: <https://link.aps.org/doi/10.1103/PhysRevC.105.034902>.
- [258] ALICE collaboration. “Anisotropic flow and flow fluctuations of identified hadrons in Pb–Pb collisions at $\sqrt{s_{\text{NN}}} = 5.02$ TeV”. *Journal of High Energy Physics* 2023.5 (May 2023). ISSN: 1029-8479. DOI: [10.1007/jhep05\(2023\)243](https://doi.org/10.1007/jhep05(2023)243). URL: [http://dx.doi.org/10.1007/JHEP05\(2023\)243](http://dx.doi.org/10.1007/JHEP05(2023)243).
- [259] Mauricio Martinez, Matthew D. Sievert, Douglas E. Wertepny, and Jacquelyn Noronha-Hostler. *Initial state fluctuations of QCD conserved charges in heavy-ion collisions*. 2019. arXiv: 1911.10272 [nucl-th]. URL: <https://arxiv.org/abs/1911.10272>.

- [260] Liang Zheng, Hui Li, Hong Qin, Qi-Ye Shou, and Zhong-Bao Yin. “Investigating the NCQ scaling of elliptic flow at LHC with a multiphase transport model”. *The European Physical Journal A* 53.6 (June 2017). ISSN: 1434-601X. DOI: [10.1140/epja/i2017-12312-8](https://doi.org/10.1140/epja/i2017-12312-8). URL: <http://dx.doi.org/10.1140/epja/i2017-12312-8>.
- [261] E. A. Hawker et al. “Measurement of the Light Antiquark Flavor Asymmetry in the Nucleon Sea”. *Physical Review Letters* 80.17 (Apr. 1998), 3715–3718. ISSN: 1079-7114. DOI: [10.1103/physrevlett.80.3715](https://doi.org/10.1103/physrevlett.80.3715). URL: <http://dx.doi.org/10.1103/PhysRevLett.80.3715>.
- [262] Kurt Gottfried. “Sum Rule for High-Energy Electron-Proton Scattering”. *Physical Review Letters* 18 (June 1967), 1174–1177. DOI: [10.1103/PhysRevLett.18.1174](https://doi.org/10.1103/PhysRevLett.18.1174).
- [263] K.J Eskola, H Paukkunen, and C.A Salgado. “EPS09 — A new generation of NLO and LO nuclear parton distribution functions”. *Journal of High Energy Physics* 2009.04 (Apr. 2009), 065–065. ISSN: 1029-8479. DOI: [10.1088/1126-6708/2009/04/065](https://doi.org/10.1088/1126-6708/2009/04/065). URL: <http://dx.doi.org/10.1088/1126-6708/2009/04/065>.
- [264] Daniel de Florian, Rodolfo Sassot, Pia Zurita, and Marco Stratmann. “Global analysis of nuclear parton distributions”. *Physical Review D* 85.7 (Apr. 2012). ISSN: 1550-2368. DOI: [10.1103/physrevd.85.074028](https://doi.org/10.1103/physrevd.85.074028). URL: <http://dx.doi.org/10.1103/PhysRevD.85.074028>.
- [265] K. Kovarik et al. “nCTEQ15: Global analysis of nuclear parton distributions with uncertainties in the CTEQ framework”. *Physical Review D* 93.8 (Apr. 2016). ISSN: 2470-0029. DOI: [10.1103/physrevd.93.085037](https://doi.org/10.1103/physrevd.93.085037). URL: <http://dx.doi.org/10.1103/PhysRevD.93.085037>.
- [266] M. Winn. *LHCb projections for proton-lead collisions during LHC Runs 3 and 4*. <http://cds.cern.ch/record/2648625>. CERN Report. 2018.
- [267] A. Buckley, J. Ferrando, S. Lloyd, K. Nordström, B. Page, M. Ruefenacht, M. Schönherr, and G. Watt. “LHAPDF6: parton density access in the LHC precision era”. *Eur. Phys. J. C* 75.3 (2015), 132. DOI: [10.1140/epjc/s10052-015-3318-8](https://doi.org/10.1140/epjc/s10052-015-3318-8). arXiv: [arXiv:1412.7420](https://arxiv.org/abs/1412.7420) [hep-ph].

- [268] Stefano Camarda et al. “DYTurbo: Fast predictions for Drell–Yan processes”. *Eur. Phys. J. C* 80 (2020), 251. DOI: [10.1140/epjc/s10052-020-7757-5](https://doi.org/10.1140/epjc/s10052-020-7757-5). arXiv: [arXiv:1910.07049](https://arxiv.org/abs/1910.07049) [hep-ph].
- [269] K. J. Eskola, P. Paakkinen, H. Paukkunen, and C. A. Salgado. “EPPS16: Nuclear parton distributions with LHC data”. *Eur. Phys. J. C* 77 (2017), 163. DOI: [10.1140/epjc/s10052-017-4725-9](https://doi.org/10.1140/epjc/s10052-017-4725-9). arXiv: [1612.05741](https://arxiv.org/abs/1612.05741) [hep-ph].
- [270] S. Dulat et al. “New parton distribution functions from a global analysis of quantum chromodynamics”. *Phys. Rev. D* 93 (2016), 033006. DOI: [10.1103/PhysRevD.93.033006](https://doi.org/10.1103/PhysRevD.93.033006). arXiv: [1506.07443](https://arxiv.org/abs/1506.07443) [hep-ph].
- [271] A. Kusina et al. “Impact of LHC vector boson production in heavy ion collisions on strange PDFs”. *Eur. Phys. J. C* 80 (2020), 968. DOI: [10.1140/epjc/s10052-020-08490-0](https://doi.org/10.1140/epjc/s10052-020-08490-0). arXiv: [2007.09100](https://arxiv.org/abs/2007.09100) [hep-ph].
- [272] R. Abdul Khalek, R. Gauld, T. Giani, E. R. Nocera, T. R. Rabemananjara, and J. Rojo. “nNNPDF3.0: evidence for a modified partonic structure in heavy nuclei”. *Eur. Phys. J. C* 82 (2022), 507. DOI: [10.1140/epjc/s10052-022-10441-8](https://doi.org/10.1140/epjc/s10052-022-10441-8). arXiv: [2201.12363](https://arxiv.org/abs/2201.12363) [hep-ph].
- [273] *LHCb projections for proton-lead collisions during LHC Runs 3 and 4*. Tech. rep. Geneva: CERN, 2018. URL: <https://cds.cern.ch/record/2648625>.
- [274] NNPDF Collaboration: Richard D. Ball et al. “Reweight- ing of Parton Distributions and the LHC W lepton asymmetry data”. *arXiv e-prints* (2011). arXiv:1108.1758 [hep-ph]. arXiv: [1108.1758](https://arxiv.org/abs/1108.1758) [hep-ph].
- [275] W. T. Giele and S. Keller. “Implications of hadron collider observables on parton distribution function uncertainties”. *Phys. Rev. D* 58 (1998), 094023. DOI: [10.1103/PhysRevD.58.094023](https://doi.org/10.1103/PhysRevD.58.094023). arXiv: [hep-ph/9803393](https://arxiv.org/abs/hep-ph/9803393).
- [276] Hannu Paukkunen and Pia Zurita. “PDF reweighting in the Hessian matrix approach”. *arXiv e-prints* (2014). arXiv:1402.6623 [hep-ph]. arXiv: [1402.6623](https://arxiv.org/abs/1402.6623) [hep-ph].
- [277] J. D. Bjorken. “Asymptotic Sum Rules at Infinite Momentum”. *Phys. Rev.* 179 (1969), 1547–1553. DOI: [10.1103/PhysRev.179.1547](https://doi.org/10.1103/PhysRev.179.1547).
- [278] R. P. Feynman. *Statistical Mechanics: A Set of Lectures*. W. A. Benjamin, 1969.
- [279] Peter Brockway Arnold, Guy D. Moore, and Laurence G. Yaffe. “Effective kinetic theory for high temperature gauge theories”. *JHEP* 01 (2003), 030. DOI: [10.1088/1126-6708/2003/01/030](https://doi.org/10.1088/1126-6708/2003/01/030).

- [280] Y. Nambu and G. Jona-Lasinio. “Dynamical Model of Elementary Particles Based on an Analogy with Superconductivity. I”. *Phys. Rev.* 122 (1961), 345–358. DOI: [10.1103/PhysRev.122.345](https://doi.org/10.1103/PhysRev.122.345).
- [281] L. D. Landau and E. M. Lifshitz. *Statistical Physics, Part 1*. Vol. 5. Pergamon Press, 1980.
- [282] Gines Martinez Garcia. “Introduction à l’étude expérimentale de la matière hadronique dans les collisions entre ions lourds. Le Plasma de Quarks et de Gluons.” Habilitation à diriger des recherches. Université de Nantes, Dec. 2006. URL: <https://tel.archives-ouvertes.fr/tel-00370481>.
- [283] L. D. Landau and E. M. Lifshitz. *Fluid Mechanics*. Pergamon Press, 1987.
- [284] Denes Molnar and Sergei A. Voloshin. “Elliptic flow at large transverse momenta from quark coalescence”. *Phys. Rev. Lett.* 91 (2003), 092301. DOI: [10.1103/PhysRevLett.91.092301](https://doi.org/10.1103/PhysRevLett.91.092301).
- [285] Mohamad Tarhini. “Measurement of Z-boson and J/ψ Production in p-Pb and Pb-Pb Collisions at $\sqrt{s_{NN}}=5.02$ TeV with ALICE at the LHC”. Theses. Université Paris-Saclay, June 2017. URL: <https://tel.archives-ouvertes.fr/tel-01691725>.

Titre : Étude de la collectivité du J/ψ dans les collisions Pb-Pb utilisant la technique des cumulants multiparticules avec le détecteur ALICE et exploration des effets de matière nucléaire froide avec la production Drell-Yan.

Mot clés : Physique nucléaire, Physique des particules, Ions lourds, État initial, Plasma de quarks et de gluons, Flot, Saveurs lourdes, Quarkonium, Drell-Yan, LHC, CERN, ALICE, Spectromètre à muons.

Résumé : Cette thèse présente deux analyses complémentaires qui améliorent notre compréhension de la dynamique des collisions d'ions lourds et de la structure nucléaire à hautes énergies. La première partie rapporte une mesure pionnière du flot elliptique (v_2) du J/ψ dans les collisions Pb-Pb à $\sqrt{s_{NN}} = 5.36$ TeV avec le détecteur ALICE, employant pour la première fois la technique des cumulants multiparticules. Cette méthode fournit une sensibilité directe aux fluctuations de flot événement par événement. Les résultats montrent que $v_2\{4\}$

est systématiquement plus faible que $v_2\{2\}$ et $v_2\{SP\}$, indiquant des fluctuations de flot substantielles d'une magnitude comparable au flot elliptique moyen. La deuxième partie présente une étude phénoménologique de la production Drell-Yan (DY) dans les collisions proton-plomb. En appliquant des techniques de repondération à des pseudo-données DY dans la région cinématique de LHCb, l'analyse démontre le fort potentiel de telles mesures pour contraindre les fonctions de distribution de partons nucléaires (nPDFs) à bas Bjorken- x .

Title: Investigation of J/ψ collectivity in Pb-Pb collisions using multi-particle cumulants technique with ALICE detector and exploration of cold nuclear matter effects with Drell-Yan production.

Keywords: Nuclear Physics, Particle Physics, Heavy-Ions, Initial State, Quark-Gluon Plasma, Flow, Heavy flavours, Quarkonium, Drell-Yan, LHC, CERN, ALICE, Muon Spectrometer.

Abstract: This thesis presents two complementary analyses that enhance our understanding of heavy-ion collision dynamics and nuclear structure at high energies. The first part reports a pioneering measurement of J/ψ elliptic flow (v_2) in Pb-Pb collisions at $\sqrt{s_{NN}} = 5.36$ TeV with the ALICE detector, employing for the first time the multi-particle cumulant technique. This method provides direct sensitivity to event-by-event flow fluctuations. The results show that $v_2\{4\}$ is systematically

lower than both $v_2\{2\}$ and $v_2\{SP\}$, indicating substantial flow fluctuations of a magnitude comparable to the mean elliptic flow. The second part presents a phenomenological study of Drell-Yan (DY) production in proton-lead collisions. By applying reweighting techniques to DY pseudo-data in the LHCb kinematic region, the analysis demonstrates the strong potential of such measurements to constrain nuclear parton distribution functions (nPDFs) at low Bjorken- x .